The Environmental Dependence of Galaxy Evolution

By

Christopher Steven Burton

Submitted to the University of Hertfordshire
in partial fulfilment of the requirements of the degree of
Doctor of Philosophy.
School of Physics, Astronomy and Mathematics

July 2013

Typeset in LaTeX 2_ε.

Acknowledgements

First and foremost, I thank Dr Matt Jarvis, without whom, the thesis you are currently holding would simply not exist. I thank him for his unwavering support, motivation and genius over the last four years, and for not giving up on me when, no doubt, that would have been the easier option. For that I will always be grateful.

I also thank Dr Dan Smith, for stepping into the breach early in my third year, for always being willing to help solve technical issues, and for providing guidance through the gauntlet that was publishing my paper.

I also sincerely thank my examiners, Prof. Omar Almaini and Prof. Elias Brinks, for giving their time to read this thesis, and for providing useful comments and criticisms. I have no doubt that this thesis is all the better for it.

When not buried under journals of papers, I have been lucky enough to socialise with a very fine bunch of people: Niall, Sam H, James, José, Sam L, Phil, Mahesh, Frith and Gemma. I thank you all for providing quality banter, regular laughter and insightful discussion over countless mugs of tea. This, beyond doubt, preserved my sanity throughout this madness!

I wholeheartedly thank my family for their truly endless love and support that I have received throughout my life, and especially for the continual encouragement during the last four years. I simply would not, and could not, have done this without them.

Finally, I thank Jenny. Thank you for putting up with all my long hours, and for all of the lost weekends. Thank you for always supporting me, and for being there to remind me there was light at the end of the tunnel.

Abstract

Observations of galaxy environments have revealed numerous correlations associated with their intrinsic properties. It is therefore clear that if we are to understand the processes by which galaxies form and evolve, we have to consider the role of their immediate environment and how these trends change across cosmic time. In this thesis, I investigate the relationship between the environmental densities of galaxies and their associated properties by developing and implementing a novel approach to measuring galaxy environments on individual galaxy scales with Voronoi tessellations. Using optical spectroscopy and photometry from GAMA and SDSS, with 250μm far-infrared observations from the *Herschel*-ATLAS SDP and Phase-One fields, the environmental and star formation properties of far-infrared detected and non–far-infrared detected galaxies are compared out to $z \sim 0.5$. Applying statistical analyses to colour, magnitude and redshift-matched samples, I show there to be significant differences between the normalised density distributions of the optical and far-infrared selected samples, at the 3.5σ level for the SDP increasing to $> 5\sigma$ when combined with the Phase-One data. This is such that infrared emission (a tracer of star formation activity) favours underdense regions, in agreement with previous studies that have proposed such a correlation. I then apply my method to synthetic light cones generated from semi-analytic models (SAMs), finding that over the whole redshift distribution the same correlations between star-formation rate and environmental density are found. However, as the SAMs restrict the role of ram-pressure stripping, the fact that we find the same qualitative results may preclude ram-pressure as a key mechanism in truncating star formation. I also find significant correlations between isothermal dust temperature

and environment, such that the coldest sources reside in the densest regions at the 3.9σ level, indicating that the observed far-infrared emission in these densest regions is the product of ISM heating by the older stellar populations.

I then extend my analysis to a deeper sample of galaxies out to $z \sim 2.2$, combining near-infrared and optical photometry from the VIDEO and CFHTLS-D1 observations, cross-matched in colour, magnitude and redshift against 1.4 GHz VLA radio observations. Across the entire radio sample, galaxies with radio detected emission are found to reside in more overdense environments at a 4.0σ significance level. I then divide my radio sample to investigate environmental dependence on both radio detected star-forming galaxies and radio detected AGN individually, based upon a luminosity selection defined as $L = 10^{23}$ W Hz^{-1}. The same trends with environment are shown by my Radio-AGN sample ($L > 10^{23}$ W Hz^{-1}) which favour overdense regions at the 4.5σ level, suggestive of the interaction processes (i.e. major mergers) that are believed to trigger accretion, in agreement with earlier work that has suggested such a relationship. At lower radio luminosities, my Radio-SF sample ($L < 10^{23}$ W Hz^{-1}) also display a significant trend towards overdense regions in comparison to my non-radio detected sample, at the less significant level of 2.7σ. This is suggestive of the low overall bolometric luminosity of radio emission in star forming galaxies, leading to only the brightest radio emitting star forming galaxies being observed and a bias towards overdense regions. This is in addition to the fact that the luminosity selection used to separate AGN from star forming galaxies is not a perfect selection and open to AGN contamination in the low-luminosity sample. I conclude that the next generation of deep radio surveys, which are expected to reach many orders of magnitude deeper than current observations, will remove radio-loud AGN contamination and allow for the detection of low-luminosity star forming galaxies via radio emission out to high redshifts.

This work has allowed for the environments of galaxies to be probed on smaller-scales and across both wider and deeper samples than previous studies. With significant environmental correlations being returned, this indicates that the established processes responsible for such trends must have influence on the most local of scales.

Contents

List of Figures

List of Tables

1

Introduction

1.1 Discovery of the Extra-Galactic Universe

The understanding of how our universe formed and the processes that have shaped and changed its evolution over time have fascinated humans for millennia. However, it has only been within the last few centuries, with the gradual advancement of astronomical methods and techniques, that a more detailed picture of the true structure of our universe has begun to be understood. The earliest astronomical observations established little in terms of extra-galactic theory, with the prevailing view that the entire universe consisted of only the Milky Way. Until as recently as the beginning of the last century, there was no solid theory as to the structure or content of space beyond our own galaxy and as such, the initial classification of extra-galactic objects was subject to some controversy.

In the late 18th century the French astronomer Charles Messier catalogued more than 100 deep sky objects (Messier, 1781), found while attempting to measure local transient comets. This catalogue marked the first categorisation of extra-galactic structure, later found to contain 39 of the brightest galaxies visible in the Northern hemisphere, although initially all objects within the catalogue were erroneously classified together as galactic nebulae. By the late 19th century, studies of these 'nebulae' had advanced such that it was understood that these objects differed significantly from the galactic stellar content, lacking the point-like observational qualities of stars. William Herschel published his *General Catalogue* (Herschel, 1864) containing observations of $5,079$ nebular objects and within a few decades this number had increased three-fold with the publication of the *New General Catalogue of Nebulae and Clusters of Stars* by Dreyer (1888). This expansion of Herschel's catalogue contained over $15,000$ nebulae, yet at the time there was much disagreement as to whether these objects were galactic structure associated with the Milky Way or some extra-galactic, individual 'island universe' separate from our own galaxy. This argument persisted well into the 20th century when Edwin Hubble confirmed, through analysis of the tight luminosity-period correlation of Cepheid variable stars in the Andromeda galaxy (Hubble, 1925), that these nebulous objects were too distant to belong to our galaxy and were themselves individual galaxy systems beyond our own.

This discovery signalled the beginning of the age of extra-galactic astronomy and heralded an increased desire for deeper and more detailed observations. Since then, a great deal of technological advancement in astronomical techniques has been achieved, particularly in the field of CCD technology and in the commissioning of large-scale telescopic facilities. In the last few decades, large-area galaxy surveys have led to vast numbers of these galaxies to be observed and catalogued. For example; between 1997 and 2002 the Two-Degree-Field Galaxy Redshift Survey (2dFGRS; Colless et al. 2001), observing at visible wavelengths out to $z \sim 0.3$, catalogued $\sim 232,000$ galaxy spectra. This was followed more recently by the Sloan Digital Sky Survey (SDSS; York et al. 2000), observing across 5 optical bands, which catalogued $\sim 1,000,000$ galaxy spectra over 35 per cent of the sky, out to a median redshift of $z = 0.1$.

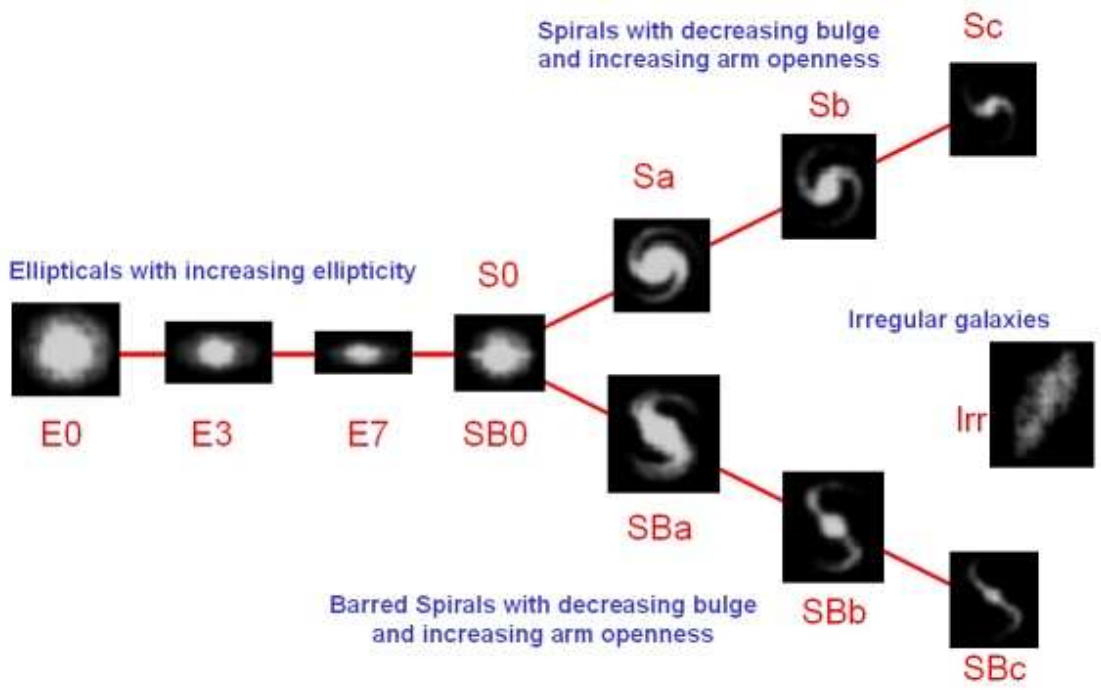

Figure 1.1: The Hubble Sequence illustrating the different morphological classifications of galaxies. From 'early-type' morphologies on the far left moving to progressively more 'late-type' morphologies further right [Image from Swinburne University of Technology].

1.2 The Hubble Sequence

Following Hubble's confirmation of extra-galactic structure, it became apparent that these objects could be classified into particular morphological groups. Using some of the earliest astrophotography of these objects, Hubble established his 'Hubble Sequence' of galaxies (Hubble, 1926) - a morphological classification system still widely used to label galactic structure today. A contemporary version of this sequence is illustrated in Figure 1.1, presenting the main morphological classifications of galaxies and examples of the different sub-classifications within them.

All galaxies on the Hubble sequence are divided into one of four classifications, initially based entirely on their morphological appearance. These are elliptical, spiral, irregular and lenticular type morphologies, which are detailed in the following sections. Many studies of galaxy evolution have shown, based on large-area galaxy survey catalogues (such as the 2dFGS and SDSS), that there are also a number of intrinsic galaxy

properties that correlate well with morphology and can themselves be used to classify galaxy populations. In establishing the relationships between these parameters, a picture of the evolutionary history of these different galaxy types can begin to be understood.

1.2.1 Elliptical Morphologies

Elliptical galaxies are defined as having a smooth and featureless morphology with no distinct features. They are shown to have generally low rotation velocities in comparison with other morphologies, which correlates with increased surface brightness and mass (e.g. Davies et al. 1983; Halliday et al. 2001; Caimmi 2009). These galaxies, situated at the left-hand side of Figure 1.1, are sub-divided into eight separate morphology classifications (E0−E7), commonly labelled as part of the broader 'early-type' galaxy classification. These sub-classifications are a measure of the degree of their ellipticity, defined by Hubble (1926) as the relationship between their semi-major (a) and semi-minor (b) axes. This is such that

$$n = 10(1 - a/b) \ , \tag{1.1}$$

where the closest integer to n between 0 and 7 gives the the sub-category for that galaxy (En).

Elliptical galaxies were once believed to contain no gas and dust, however observations of these galaxies have since shown that they do contain a significant amount of inter-stellar medium (ISM) (Roberts et al. 1991; Buson et al. 1993; Goudfrooij et al. 1994; Goudfrooij 1999), dominated by hot (10^7K) X-ray emitting gas which can contribute up to $10^{10}\,\mathrm{M}_\odot$ in the most luminous galaxies (Fabbiano 1989; Mathews & Brighenti 2003). In addition, there are small amounts of warm (10^4K) ionized gas, contributing between $10^2 - 10^4\,\mathrm{M}_\odot$ and a cold (< 100K) atomic and molecular gas component contributing between $10^6 - 10^8\,\mathrm{M}_\odot$ (Phillips et al. 1986; Bregman et al. 1992; van Dokkum & Franx 1995; Tran et al. 2001; Ferrarese et al. 2006).

Many observations have shown that elliptical galaxies are predominantly found to have redder photometric colours and lower star formation rates (SFRs) than other

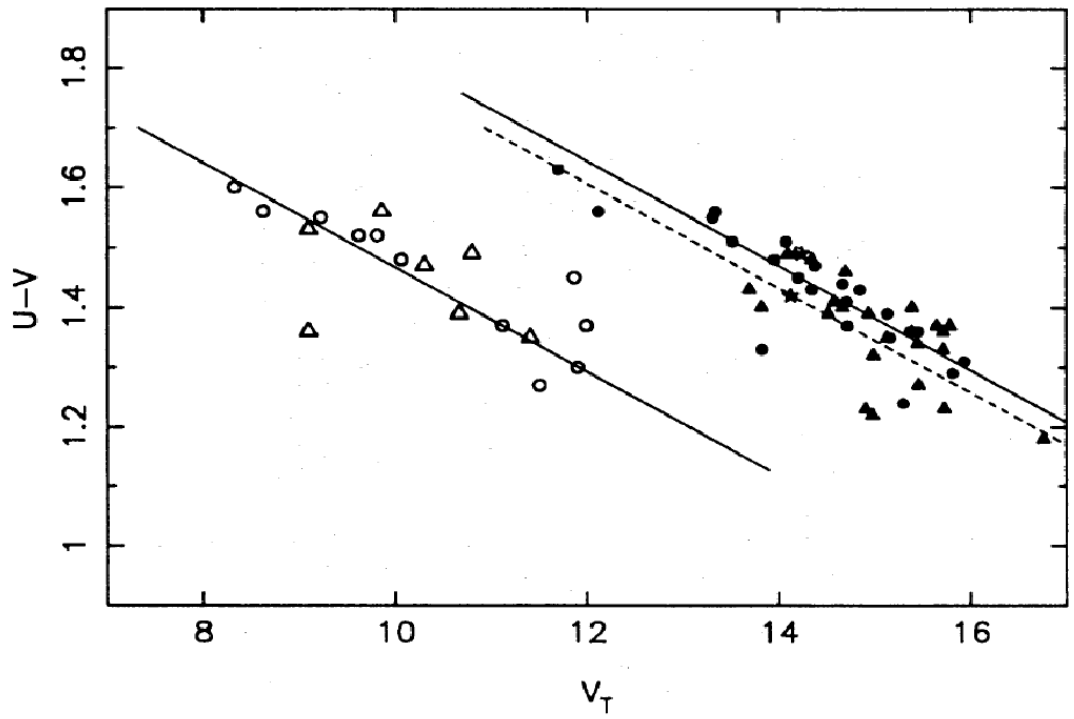

Figure 1.2: The colour-magnitude relationship between two samples of early-type galaxies, adapted from Bower et al. (1992a), with open and closed symbols representing galaxies from the Virgo and Coma clusters respectively. Circles denote elliptical galaxies whereas triangles represent lenticular (S0) types, defined in Section 1.2.3. There is a clear correlation such that the brightest galaxies have redder colours.

galaxy morphologies, and that this redness is found to strongly correlate with both increasing luminosity and mass (e.g. Baum 1959; Visvanathan & Sandage 1977; Sandage & Visvanathan 1978; Bower et al. 1992a; Schweizer & Seitzer 1992; Kauffmann 1996; Kauffmann & Charlot 1998; Terlevich et al. 2001; Bernardi et al. 2003; Baldry et al. 2004; Schombert & Rakos 2009). Figure 1.2 shows this colour-magnitude relation of two samples of early-type galaxies, taken from Bower et al. (1992a), illustrating the clear positive correlation between these two parameters.

Initially there was some uncertainty as to the cause for such reddening with increasing magnitude. This was due to the fact that changes in photometric colour can be driven by changes in both the age or metallicity of a galaxy's stellar population, thus leading to potential confusion known as the age-metallicity degeneracy. However, this

degeneracy can be overcome with the adoption of spectral diagnostics that are not sensitive to attenuation by dust and yet have different sensitivities to age and metallicity. Studies in this area have focused predominantly on the Lick indices (Faber et al., 1985), a set of 25 absorption features based upon the spectra of 460 nearby galaxies. It has been shown that of these spectral features, the Balmer lines, such as H_β and H_γ, are sensitive to the age of the stellar population, whereas more metallic lines, such as Fe_1, Fe_2 and Mgb, are sensitive to metallicity (Worthey et al. 1994; Worthey & Ottaviani 1997). Using these spectra it was therefore established that this increased redness is associated with the fact that the stellar populations of more massive elliptical galaxies are found to be both older and more metal-rich than less massive ellipticals (e.g. Ellis et al. 1997; Stanford et al. 1998; Maraston & Thomas 2000; De Lucia et al. 2006; Zhu et al. 2010; Koleva et al. 2011). These galaxies also display a slight colour gradient, such that they exhibit their most reddest areas towards their central regions and bluer colours at their outer radii. This therefore constrains the age and metallicity of the ISM as being older towards the central galactic regions (e.g. Peletier et al. 1990; Davies et al. 1993; Trager et al. 2000; Kuntschner et al. 2006).

1.2.2 Spiral Morphologies

Spiral galaxies have far more complex morphological structures than elliptical galaxies. Typically, these galaxies have a rotationally supported disk structure with spiral arms and a pronounced central bulge. Situated to the right of the Hubble sequence in Figure 1.1, they constitute part of the 'late-type' galaxy classification. These galaxies are initially classified into either the lower or upper branch of the Hubble sequence, depending on the presence (SBn) or absence (Sn) of bar-like structure within the central part of the galaxy. Many studies have shown that between 20 to 60 per cent of spiral galaxies out to $z \sim 1$ exhibit bar-like structure (e.g. Eskridge et al. 2000; Elmegreen et al. 2004; Jogee et al. 2004; Nair & Abraham 2010; Masters et al. 2011) believed to be formed through either dynamical instability (Sellwood 1981) or interaction processes such as mergers or tidal forces (Noguchi 1987), this is detailed further in Section 1.4. These branches are further sub-divided into three separate morphology classifications

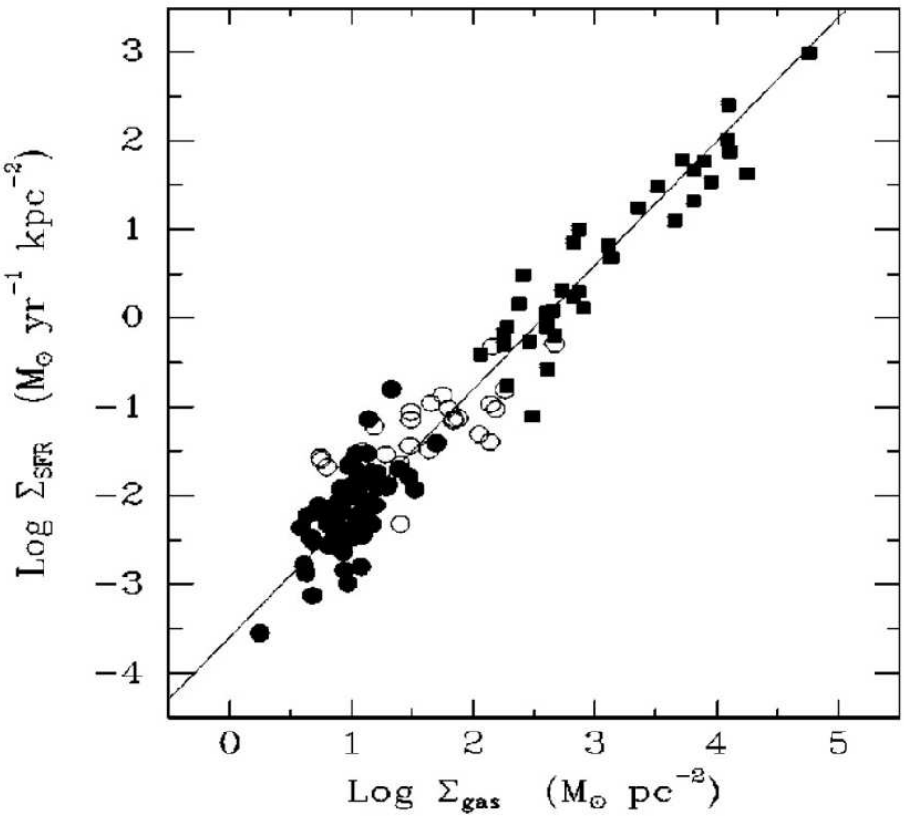

Figure 1.3: The Schmidt-Kennicutt relation between gas surface density and SFR surface density. Figure taken from Kennicutt (1998) where filled circles represent normal disk galaxies, open circles represent centres of normal disk galaxies and filled squares denote starburst galaxies. The solid line shows the least-squares fit between the data points where $N = 1.4$.

$(n = a, b, c)$ dependent upon: the fraction of light in the central bulge; the tightness of the spiral arms in the disk; the degree to which the spiral arms are resolved into stars, HII regions and ordered dust lanes.

Studies of spiral galaxies have established many intrinsic properties associated with this morphological classification. The spiral disk structure has been shown to be defined as gas-rich (e.g. Bothun et al. 1982; Huchtmeier & Richter 1985; Young & Knezek 1989; Thakar & Ryden 1996; Immeli et al. 2004; Pelupessy & Papadopoulos 2009), with HII regions tracing young stellar populations (e.g. Frogel 1985; Young et al. 1996; Ferguson et al. 1998; Battinelli et al. 2000; Barnes et al. 2012). Unlike elliptical galaxies whose ISM consists of significant quantities of hot, highly ionised gas; the gaseous component of spiral galaxies are predominantly HI and molecular H_2. In addition, the gas-mass

fraction has been shown to increase from ~ 5 per cent in the most massive early-type spirals (Sa/SBa) to over ~ 80 per cent in the lowest mass late-type spirals (McGaugh & de Blok, 1997a).

In contrast to elliptical galaxies, a large fraction of the star formation within the local universe occurs within these spiral systems, as indicated by the Schmidt-Kennicutt (SK) relation, which compares the SFR to the observable gas surface/volume density at kpc scales (Schmidt 1959; Kennicutt 1989). This is such that

$$\Sigma_{SFR} = \epsilon_{SF} \Sigma_{gas}^{N} \ , \tag{1.2}$$

where Σ_{SFR} represents the SFR surface density, ϵ_{SF} represents the star formation efficiency, Σ_{gas} represents the surface density of the gas and N is the index of the power law. Schmidt (1959) showed that $N \sim 2$ was adequate for the distribution of HI from observations of our galaxy. Numerous observations have since showed this relation to be a good description of global SFRs averaged across the entire disk (e.g. Kennicutt et al. 2007; Bigiel et al. 2008; Monaco et al. 2012; Bonnell et al. 2013), with best-fit values of the index typically between $N \sim 1 - 2$. Kennicutt (1998) demonstrated that the relation holds over 5 orders of magnitude in gas density and 6 orders of magnitude in SFR, with $N \sim 1.4$ as shown in Figure 1.3.

As well as exhibiting more complex morphological features, spiral galaxies have been found to possess generally bluer photometric colours than elliptical galaxies of equal luminosity, as a consequence of the young stellar populations within their disks (e.g. Wilson et al. 1990; Terndrup et al. 1994; Matthews et al. 1999; Strateva et al. 2001; Tojeiro et al. 2013). However, it has been shown that the same colour-magnitude relation, as followed by elliptical morphologies, is found for spiral galaxies. This is such that brighter, more massive spirals have slightly redder colours, although this relation suffers from increased scatter due to inclination effects and extinction within the disk (e.g. Tully et al. 1982, 1998; Peletier & de Grijs 1998; Fioc & Rocca-Volmerange 1999; Baldry et al. 2004; Wyder et al. 2007; Unterborn & Ryden 2008). In addition, there is also a colour gradient, as found with elliptical galaxies, such that the central regions of the spirals have redder colours than their outer disk regions, once more implying trends

with stellar age and metallicity with radius (e.g. de Jong 1996; Peletier & Balcells 1996; Kuchinski et al. 1998; Bell & de Jong 2000; MacArthur et al. 2004).

1.2.3 Lenticular Morphologies

Lenticular galaxies are defined as being an intermediate step between elliptical E7 and spiral Sa/SBa morphologies (Hubble 1936; de Vaucouleurs 1959; Sandage 1961) and are usually considered, along with elliptical galaxies, as part of the early-type galaxy classification. They are known to have smooth light distributions, no HII regions, and an absence of morphological features such as spiral arms; as found in elliptical galaxies. However, they also exhibit disk structure and a central bulge, as associated with spirals, although the bulge is more dominant than in a regular spiral (e.g. Tsikoudi 1980; Seifert & Scorza 1996; Bedregal et al. 2011). The intermediate properties of these galaxies marks their position on the Hubble sequence between the elliptical and spiral branches. They can be classified depending on the presence (SB0n) or absence (S0n) of bar-like structure, where $n = a, b, c$ is in parallel with the spiral Sa-Sc sequence with increasing bulge-to-disk ratio (Kormendy & Bender, 2012).

1.2.4 Irregular Morphologies

Irregular galaxies (Irr) have few features which would allow them to be easily classified along with either spiral or elliptical morphologies. They have neither a dominant bulge or a rotationally symmetric disk, and as such were not included in the original sequence by Hubble. However, later studies have shown that these galaxies have prominent HII regions and can therefore be associated with late-type morphologies (e.g. Stasińska et al. 1986; Hunter et al. 1993; Driver et al. 1995; Abraham et al. 1996; Brosch et al. 1998; Hunter & Elmegreen 2004).

1.3 The Origins of Structure

1.3.1 A Merging Scenario

As shown above, observations have revealed that intrinsic properties of galaxies (such as their morphology, luminosity, stellar age and colour) change across the different galaxy classifications. It is now well understood that a galaxy's position along the Hubble sequence, in conjunction with its morphology, is indicative of its formation history. However, although Hubble's spiral and elliptical galaxy types were well established by the 1930's, for several decades there was still great uncertainty as to the detailed physical mechanisms that produced such diverse structure, and whether there was any evolutionary connection between the different classifications.

Initially it was postulated that galaxies form from the collapse of primordial gas clouds, tracing initial density perturbations within the cloud. Eggen et al. (1962) suggested that it is the speed at which stars from, following this gas collapse, that determines the initial morphology of a galaxy. With a rapid collapse forming stars quickly, preventing the dissipation of gravitational energy and producing an elliptical morphology. Conversely, a slow collapse would allow for gravitational energy to be removed via shocks and radiative cooling until angular momentum within the cloud would act to prevent further contraction, supporting the cloud in a rotating disk. Gott & Thuan (1976) expanded upon this 'monolithic collapse' model, by suggesting that the rate of gas collapse would depend on the amplitude of the initial perturbation. This was based on the fact that star formation efficiency scales as Σ_{gas}^2 (Schmidt, 1959), such that larger amplitudes (and hence the most overdense regions) of the primordial gas cloud would collapse faster and generate stars more quickly, leading to elliptical morphologies. The advancement of numerical simulations allowed for this formation model to be tested in greater detail in a series of studies by Larson (1974a,b, 1975, 1976), who showed, in agreement with these earlier conclusions, that the resultant morphology of a galaxy was dependent on the ratio between star formation time-scales and the dissipation time of the collapsing progenitor gas cloud.

This monolithic model therefore predicts formation of elliptical galaxies through

a single violent burst of star formation during the initial collapse at high redshift ($z > 2$), followed by quiescent evolution to the present day. Chiosi & Carraro (2002) used N-body simulations to investigate whether the formation of elliptical galaxies from monolithic collapse would lead to comparable results with observation, they find that the basic structural properties of ellipticals of different mass (colours, mass-to-light ratios, colour-magnitude relation) can be reproduced at both local and high redshifts. Furthermore, the well known colour-magnitude relation of these elliptical galaxies has been widely used to constrain their star-formation histories (SFHs), with the lack of redshift evolution in the slope and scatter being consistent with high redshift formation ($z > 2$) followed by passive evolution as predicted by the monolithic model (e.g. Bower et al. 1992b, 1998; Ellis et al. 1997; Stanford et al. 1998; Gladders et al. 1998; van Dokkum et al. 2000).

Despite this, notable evidence exists for morphological evolution of galaxies towards the local universe. Kaviraj et al. (2007) study ~ 2100 early-type galaxies across the relatively low redshift range $0 < z < 0.11$. They find $\gtrsim 30$ per cent of galaxies have UV and optical colours consistent with recent star formation within the last Gyr. They find quantitative agreement between observations and model predictions, deducing that early-types in this redshift range have $1-3$ per cent of stars < 1 Gyr old. They conclude that under the monolithic collapse model, the continued star formation in these galaxies should only be driven by recycled gas from mass loss via stellar winds and supernovae at later times. They demonstrate that these processes under a monolithic collapse model would not be sufficient to reproduce the blue colours found in ~ 30 per cent of their sample.

An important and revolutionary model was proposed by Toomre & Toomre (1972), who identified that the different morphological classifications are connected through a process of merging. They investigated distinct tail-like features associated with perturbed galaxies with 'peculiar' morphologies; so named due to their disassociation with any of the main Hubble types. Using simple numerical simulations of the effects of tidal interactions between spiral galaxies, they demonstrated that such interactions would result in these distinct features, and that they are tidal relics of close encounters.

Based on the frequency of peculiar galaxies exhibiting disturbed features and estimates of the time-scales necessary to form them, they concluded that most elliptical morphologies were the result of the merging of two spiral galaxies. This was followed by numerous simulations supporting this merging formation model, with spiral merger remnants found to have morphologies and density profiles expected of elliptical galaxies (e.g. White 1978; Gerhard 1981; Farouki & Shapiro 1982; Negroponte & White 1983; Barnes 1988).

There is still a great deal of debate, however, as to which of these two formation models (monolithic or merging) may be responsible for the build up of the most massive elliptical galaxies observed in the local universe. Monolithic formation has been shown to reproduce the wide spectrum of chemo-photometric properties of large early types galaxies, and has in fact formed the basis of numerous studies into the photometric and chemical properties of elliptical galaxies (e.g. Arimoto & Yoshii 1987; Bruzual & Charlot 1993; Tantalo et al. 1998). However, it cannot account for the wide morphological and kinematical variety of ellipticals observed, such as counter-rotating cores, small disks, and recent stellar activity (e.g. Schweizer & Seitzer 1992; Longhetti et al. 1998a,b, 2000). Furthermore, simulations have shown that the efficient transfer of angular momentum achieved within a merging system can form spheroid-dominated ellipticals much more efficiently than disk-dominated galaxies (e.g. Katz & Gunn 1991; Katz et al. 1992). In addition to this, the number density of passively evolving galaxies has been observed to be a factor of approximately $3-4$ times lower at $z \sim 1$ than today, thus ~ 70 per cent of ellipticals where either star-forming at $z = 1$ or not actually assembled (e.g. Dressler 1980; van Dokkum et al. 2000; Kaviraj et al. 2007). This is suggestive of strong evolution in galaxy morphology.

For simulations of spiral mergers to produce such remnants, with observationally accurate rotation properties of elliptical galaxies, some fine-tuning of the initial mass within these progenitor systems was necessary. Initially, the disk progenitors were assumed to be embedded within low-mass haloes of dark matter. As such, the orbital angular momentum of these galaxies would be largely converted to internal spin, producing elliptical galaxies with rotational speeds much faster than those observed. It

was suggested by Barnes (1988) that, if the dark matter halo were extended, dynamical friction would act to transfer the orbital angular momentum of the disk progenitors into the more loosely bound dark matter halo. Therefore the resultant rotational velocity of the elliptical remnant would closely resemble observed quantities. In addition, if gas is able to cool, a new disk may form around the spheroidal merger remnant, giving rise to a disk-bulge (S0) type morphology (e.g. Kauffmann et al. 1993; Baugh et al. 1996). Subsequent simulations of disk galaxy mergers have shown that, accounting for this extended dark matter halo, merger remnants represent elliptical morphologies across a wide range of observed properties such as global kinematic and photometric properties and rotation velocities (e.g. Barnes 1992; Hernquist 1992, 1993; Heyl et al. 1994; Naab & Burkert 2003; Jesseit et al. 2005).

1.3.2 Dark Matter Haloes: Seeds of Formation

It is evident that the formation of galactic structure, through a process of hierarchical merging, is dependent on the clustering and build up of the dark matter haloes in which the baryonic matter resides. Numerous studies of the rotation curves of spiral galaxies have shown that these galaxies are embedded within a dark matter halo, which extends well beyond the radius of the visible matter (e.g. Roberts & Rots 1973; van Albada et al. 1985; Kent 1986, 1987; Persic et al. 1996; Salucci et al. 2007). This was established by equating the measured rotational velocity of a galaxy with its estimated mass and finding a discrepancy between the two parameters; with rotational velocities measured either through optical long-slit spectroscopy of HII emission lines (e.g. Rogstad & Shostak 1972; Bosma 1981; Keel 1996; Courteau 1997; Matthews & Gallagher 2002; Catinella et al. 2005) or via the resolved 21cm Hydrogen emission line (e.g. Begeman 1989; Begeman et al. 1991; Kirby et al. 2012).

Assuming the rotation to be circular, the gravitational force can be equated to the centrifugal force such that

$$\frac{v^2}{r} = G\frac{M(r)}{r^2} \quad , \tag{1.3}$$

where v is the rotational velocity, r is radius at which the v is measured, M is the

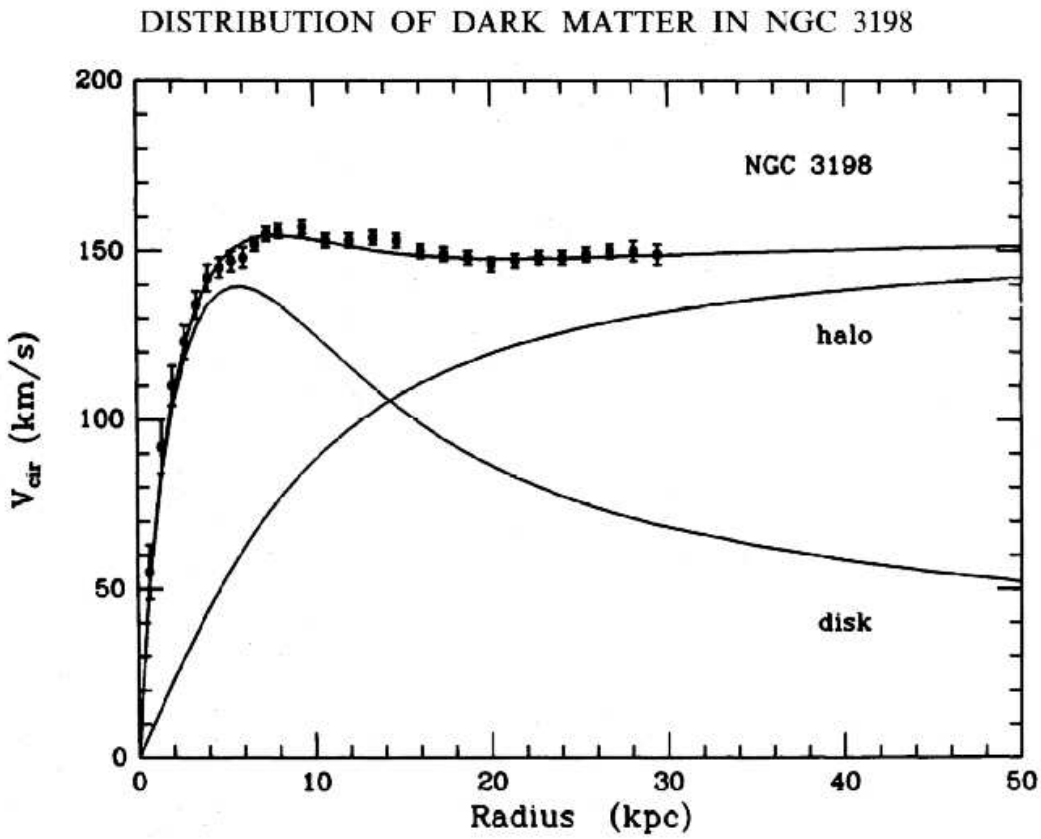

FIGURE 1.4: Example of a rotation curve showing the expected Keplerian fall-off assuming most of the galaxy's matter resides towards the central bulge of the system (disk). The actual observed rotation curve (for galaxy NGC 3198) remains flat, indicating the presence of an extended dark matter halo. Figure from van Albada et al. (1985).

mass within r and G is the gravitational constant. Therefore, rearranging to express the rotational velocity,

$$v = \sqrt{\frac{GM(r)}{r}} \ , \tag{1.4}$$

shows that the velocity is expected to fall as a Keplerian decrease $\propto r^{-1/2}$ for larger r beyond the radius of visible matter. This is illustrated in Figure 1.4, taken from van Albada et al. (1985), where the line (disk) shows the predicted fall in rotation velocity with increasing radius due to the majority of the mass being located at the core of the galaxy. However, observations of rotation curves, such as this example of NGC 3198, have conclusively demonstrated that towards larger radii the rotation curve flattens out. This indicates that these galaxies have massive dark matter haloes that extend well beyond the observable radius and dominate the total mass distribution

of the galaxy, given by line (halo). Guo et al. (2010), for example, show that the stellar mass constitutes at most ~ 3.5 per cent of the total halo mass. It is therefore apparent that in order to understand the origin of the observed hierarchical formation of galactic structure, the interactions between the dark matter haloes and the origins of structure formation must also be considered under the currently accepted constraints of a lambda cold dark matter (ΛCDM) cosmology (Planck Collaboration 2006; Planck Collaboration et al. 2013).

Cosmic inflation models of the universe state that this initial and rapid expansion amplified minute quantum fluctuations, present at the beginning of the universe, into an inhomogeneous distribution of slight overdensities within the coupled photon-baryon fluid (e.g. Dodelson et al. 1996; Brandenberger 2001; Das et al. 2013). At the epoch of decoupling ($z \sim 1100$), where the photons and baryons separate, the baryon-acoustic oscillations would cease and the universe became transparent for the first time as the photons were free to propagate as their mean free path becomes longer than the Hubble distance. The amplitude of the baryon-acoustic oscillations at the time of photon-baryon decoupling became fixed and these fluctuations mark the minute temperature/density anisotropies observed in the cosmic microwave background (CMB) radiation. Several instruments have mapped the CMB, such as the Cosmic Background Explorer (COBE; Smoot et al. 1992), the Wilkinson Microwave Anisotropy Probe (WMAP; Bennett et al. 2003; Hinshaw et al. 2007) and most recently, the *Planck Space Telescope* (Planck Collaboration 2006; Planck Collaboration et al. 2013), from which Figure 1.5 illustrates the fine structure of CMB anisotropies that form the foundations of the largest structures we see in the local universe.

With the removal of radiation pressure support, the baryonic matter would finally undergo gravitational collapse into the gravitational potential wells laid down by the already collapsed dark matter haloes, tracing these primordial gravitational instabilities. This was then followed by cooling and condensation of gas within these haloes to form the first galaxies. Under the standard model of galaxy formation, this initial collapse of baryonic matter acquires the same specific angular momentum as the dark matter halo into which it is falling via tidal torques (e.g. Fall & Efstathiou 1980; Efstathiou

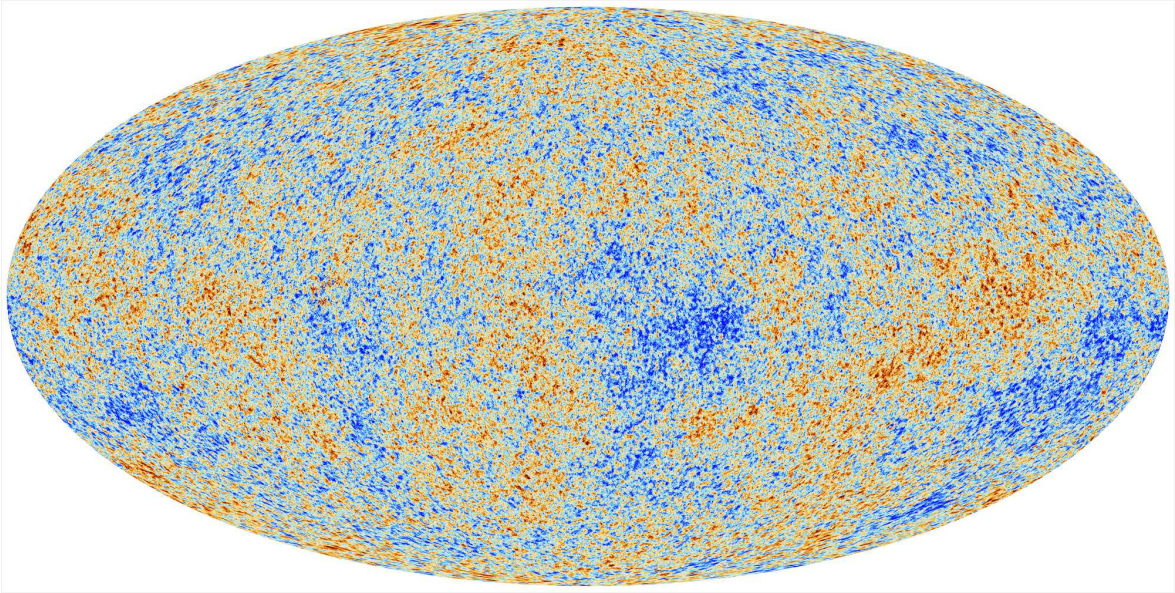

FIGURE 1.5: Anisotropies of the Cosmic Microwave Background (CMB) radiation as observed by the Planck space telescope. These slight temperature variations map the density distribution of the universe $\sim 380,000$ years after the Big Bang [Image from ESA and the Planck Collaboration].

& Silk 1983; Dalcanton et al. 1997; Mo et al. 1998; Fall 2002a). The cooled baryons then settle into a rotating, centrifugally supported disk at the centre of the dark matter potential well (Fall, 2002b). Some early numerical simulations of galaxy formation initially found a factor of ~ 30 loss of angular momentum in post collapse simulated galaxies; a discrepancy known as the 'angular momentum catastrophe' (e.g. Navarro & Benz 1991; Navarro & White 1994; Navarro & Steinmetz 2000). However these results have since been shown to have been due to a combination of a lack of resolution within these simulations (e.g. Governato et al. 2010; Brook et al. 2011; Brooks et al. 2011; Kimm et al. 2011), in addition to insufficient treatments of feedback effects, such as supernovae and stellar winds, preventing the cooling of baryons and delaying the formation of disks. More detailed, high resolution simulations that account for sufficient feedback effects have shown that gravitational collapse of baryonic matter into these primordial dark matter haloes will produce disk morphologies with an insignificant loss of angular momentum (e.g. Weil et al. 1998; Sommer-Larsen et al. 1999; Brook et al. 2004; Okamoto et al. 2005; Robertson et al. 2006; Scannapieco et al. 2008). Thus these dark matter haloes act as a universal head-start for structure formation in the universe.

1.3.3 Hierarchical Formation

White & Rees (1978) were first to suggest such a two-stage model of hierarchical galaxy formation, where the evolution of galactic structure is inherently linked to the build-up of dark matter haloes over time. Their work was based upon the analytical theory proposed by Press & Schechter (1974), who demonstrated how these initial density fluctuation will have evolved to form the mass distributions in the local universe. Further studies have since applied numerical simulations to investigate this hierarchical merging scenario: Davis et al. (1985) applied N-body simulations to show a bias in the formation of galaxies, such that they form from the highest peaks of the density perturbations and appear in the most overdense regions; Bower (1991) extended the model of Press & Schechter (1974), and earlier works on hierarchical formation, to show that hierarchical clustering between small haloes would lead to the large groups and clusters observed in the local universe; Kauffmann & White (1993) developed an algorithm that mapped the merging history of present-day dark matter haloes from high redshifts through to $z = 0$. These halo merging trees were used to investigate the formation and merging of galaxies, and were found to agree with those derived from earlier numerical simulations; a schematic of such a merging tree is displayed in Figure 1.6. This has been followed by a number of studies which have developed similar merger-tree analytical models to map this hierarchical formation, establishing that the largest dark matter haloes in the local universe have been built through a process of hierarchical merging (e.g. Lacey & Cole 1993; Sheth & Lemson 1999; Somerville & Kolatt 1999; Cole et al. 2000a; Neistein & Dekel 2008).

More advanced simulations, which have used semi-analytic and hydrodynamical models, have incorporated multiple processes associated with stellar and galaxy formation to reproduce galaxies representative of a locally observed population after a series of hierarchical merging (e.g. White & Frenk 1991; Kauffmann et al. 1993; Cole et al. 1994; Somerville & Primack 1999). In addition to dark matter halo mergers, these simulations have included treatments of gas cooling, stellar ISM heating, the transformation of disk morphologies to spheroids, and the regulation of star formation by feedback from evolved stars and supernovae. These models confirm that the

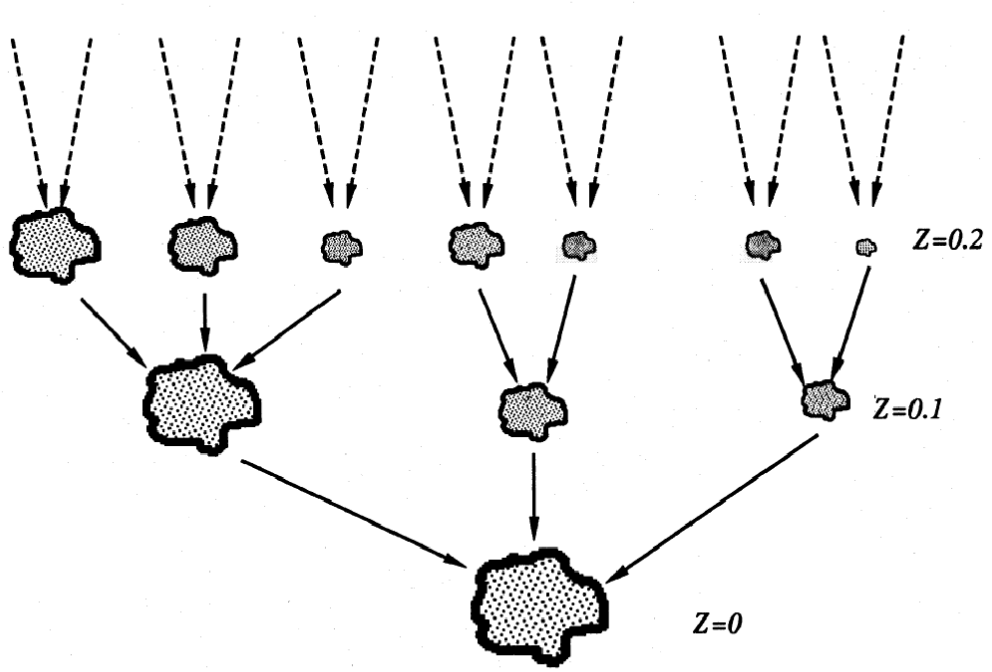

FIGURE 1.6: An illustration of a dark matter halo merging tree associated with galaxy formation. Figure taken from Kauffmann & White (1993).

hierarchical build-up of dark matter haloes will dramatically affect the gravitationally embedded baryonic content within them, leading to the merging scenario of galaxy formation introduced in Section 1.3.1. This indicates that the dark matter halo and baryonic matter content are inherently linked and this is further demonstrated by the tight correlation found between the stellar and dark matter halo masses (e.g. Moster et al. 2010; Wake et al. 2011; Munshi et al. 2013), despite the high mass ratio found between them (Guo et al., 2010).

It has been shown, predominantly through simulations of dark matter halo interactions, that the rate of galaxy mergers in the hierarchical model, increases with redshift (e.g. Carlberg 1992; Governato et al. 1999; Ellis 1997; Gottlöber et al. 2001; Berrier et al. 2006; Genel et al. 2009; Stewart et al. 2009; Wetzel et al. 2009). There has also been significant observational support for such a trend with redshift, with interactions and mergers shown to be more common at high redshifts (e.g. Carlberg et al. 2000; Somerville et al. 2001; Patton et al. 2002; Conselice et al. 2003); where merger rates

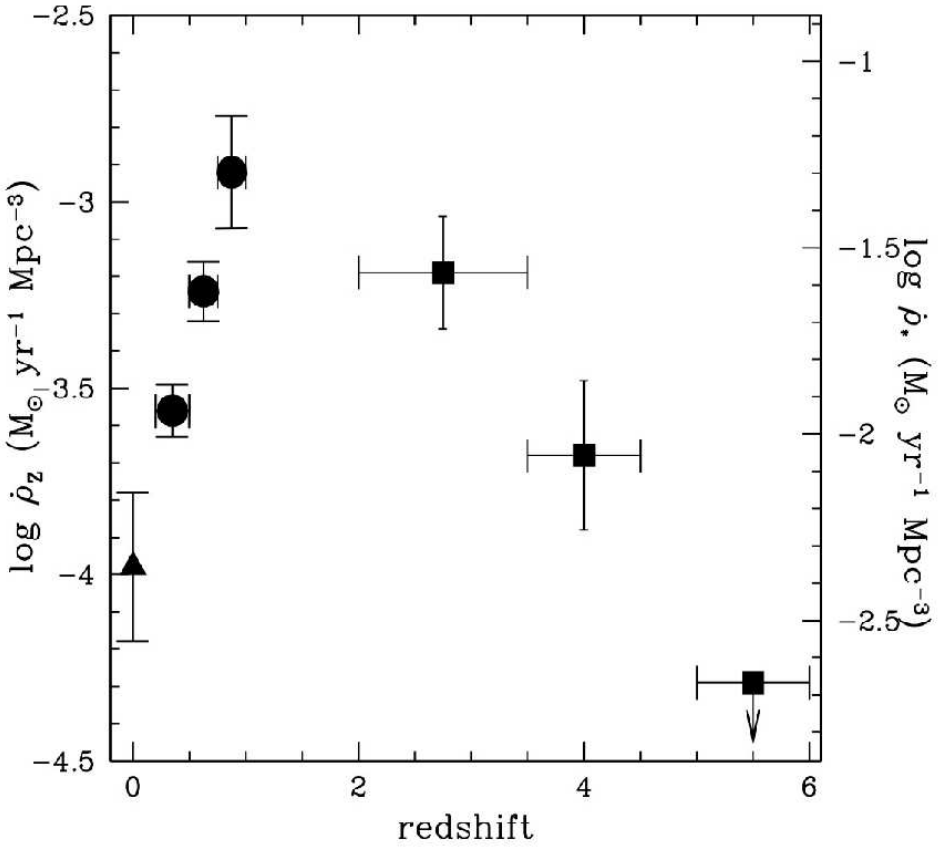

Figure 1.7: The SFR density as a function of redshift illustrating the peak between $z = 1 - 3$. Below this redshift the SFR falls dramatically. Figure taken from Madau (1997).

are calculated through either physical counting of close pairs, with the assumption that they will eventually merge (e.g. Le Fèvre et al. 2000; Lin et al. 2008; Bluck et al. 2009), or through identification of galaxies that exhibit merging morphologies (e.g. Conselice et al. 2003, 2008, 2009; Lotz et al. 2004, 2008). From these studies it has been shown that the merger fraction at $z \gtrsim 1$ is $\sim 0.1 - 0.3$ on average, compared to a fraction $\lesssim 0.1$ in the local universe. Furthermore, the peak in the volume averaged SFR within galaxies has been shown to occur between the redshift range $1 < z < 3$, corresponding with the known peak in merger fraction, and the rate has been found to be declining since this redshift (e.g. Lilly et al. 1996; Madau et al. 1996, 1998; Pérez-González et al. 2005; Daddi et al. 2007; Bell et al. 2007; Poggianti et al. 2008; Sobral et al. 2013; Stott et al. 2013). Figure 1.7, taken from Madau (1997), shows this peak with a sharp decline towards lower redshifts.

From these correlations between the SFR density and the galaxy merging rate, with respect to redshift, it is apparent that a relationship between these two parameters probably exists in terms of their impact on the evolution of galactic structure. This relationship was further strengthened by the discovery that the most massive galaxies in the local universe contain older stellar populations than lower mass galaxies (e.g. Cowie et al. 1996; Bower et al. 2006; Gilbank et al. 2010; De Lucia & Borgani 2012). This indicates that environmental influence has an important contribution to the evolution of a number of galaxy properties. These properties, and the evidence for environmental influence, are discussed in the following section.

1.4 Environmental Influences on Galaxy Properties

It is clear that if we are to understand the complex processes by which galaxies form and evolve, we must consider the role of their immediate environment on different galactic properties, in terms of their evolution. There are a number of techniques used to measure galaxy environment and these are discussed in detail in Chapter 2. Extragalactic observations have revealed a wide variety of observed galaxy characteristics and properties that suggest a varied evolutionary history and these relationships are discussed below.

1.4.1 Morphology Relations

There is a noted morphological difference between galaxy populations located within dense cluster regions compared to less dense field environments; first suggested by Gunn & Gott (1972) to be due to some internal dynamical process, changing the morphology from late-type disks to S0 and elliptical early-types with increasing density. Later, Oemler (1974) found that a galaxy's morphology was a function of both cluster structure and location within the cluster; with large populations of elliptical and S0 galaxies, with small fractions of spiral morphologies in clusters that appeared dynamically relaxed. He also showed that the ratio of early-to-late types increased towards the central regions of the dense cluster. This morphology-density (MD) relationship was

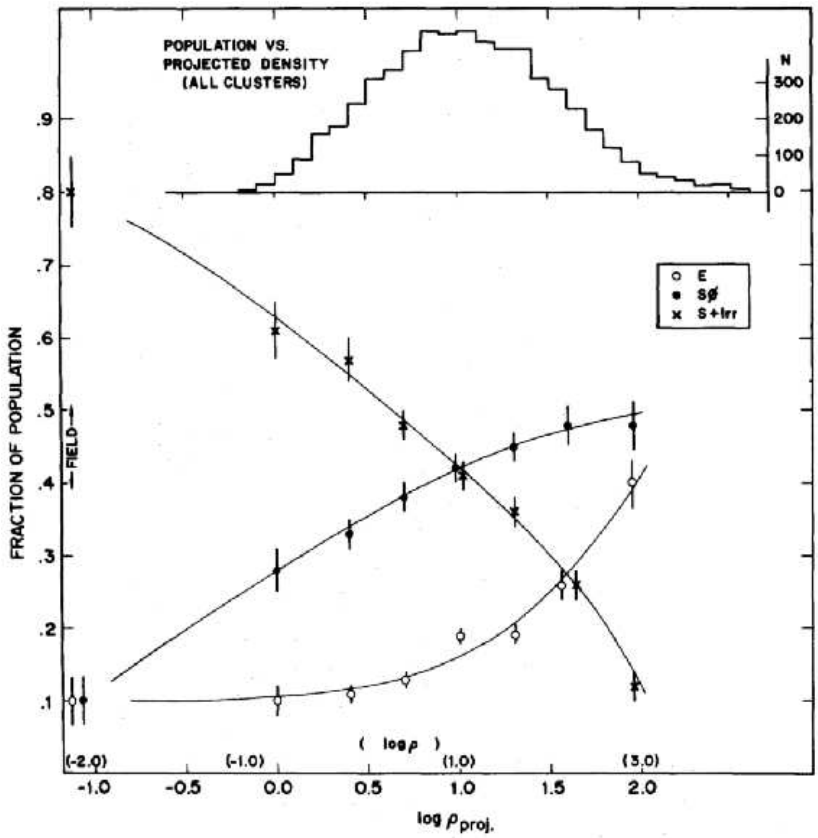

Figure 1.8: The Morphology-Density relation from Dressler (1980), showing the fraction of E and S0 types to be increasing with density while the fraction of S types reduces.

first conclusively shown by Dressler (1980), who showed that there is a good correlation between the morphology of a galaxy population and the density of its environment. Analysing the morphologies of ~ 6000 low-redshift ($z < 0.06$) galaxies across 55 clusters, he found that the fraction of late-type spiral morphologies decreased from ~ 60 per cent in underdense regions to < 10 per cent in overdense regions, with an opposite trend for elliptical morphologies (see Figure 1.8). Postman & Geller (1984), using a sample of 1312 galaxies with mean $z \lesssim 0.03$ from the CfA Redshift survey (Huchra et al., 1983), showed that the MD relation extends to galaxy group environments with the fraction of elliptical galaxies increasing rapidly in the most overdense cluster regions (~ 3000 galaxies Mpc^{-3}). Both Whitmore & Gilmore (1991) and Whitmore et al. (1993) re-examined the data of Dressler (1980) and found, in addition to the MD relation, that there is also a prominent trend in morphology with respect to cluster-centric radius. This was such that the fraction of elliptical morphologies rises rapidly at small

radii from the centre of the cluster, representing > 60 per cent of the galaxy fraction within 0.1Mpc. In comparison to the edges of the cluster, beyond 0.6Mpc, where the fraction can be as low as ~ 10 per cent. They state that this morphology-radius (MR) relation is stronger than the MD relation and conclude therefore that destructive environmental processes within the cluster centre must be the driving force for such correlations. Such environmental processes include major/minor mergers (Toomre & Toomre, 1972), galaxy harassment (Moore et al., 1996) and ram pressure stripping (Gunn & Gott, 1972). These processes are discussed in Section 1.5.

Dressler et al. (1997) expanded the analysis of the MD relation to intermediate redshifts ($z \sim 0.5$), using 10 clusters observed with the *Hubble Space Telescope* they found that the MD relation is strong for centrally-concentrated clusters, but almost absent for less concentrated clusters. Goto et al. (2003) used SDSS data out to similar redshifts, finding in agreement with these earlier studies such that the MD and MR relations are well defined. Smith et al. (2005) measure the MD relation out to high redshift, establishing that this relation has been in place since $z \sim 1$. They show that, for the highest density regions, the fraction of early-type (E+S0) morphologies have increased with redshift, from ~ 70 per cent at $z = 1$ to ~ 90 per cent at $z = 0$. They state that at intermediate densities, such as galaxy groups, there is only significant evolution after $z = 0.5$ and in the lowest density field regions, there is no evolution of the early-type fraction with redshift. In agreement with this work; Postman et al. (2005) also measure the MD relation out to $z = 1$ and find a change in the early-type fraction in dense regions with redshift. This is such that the fraction increases less rapidly with density at $z \sim 1$ than $z \sim 0$, in agreement with earlier studies.

It is therefore well established that a galaxy's morphology and its environment are inherently linked in terms of a galaxy's formation history. Considering that both the SFR density and merging rate are shown to correlate with redshift (Section 1.3.3), in addition to formation models of elliptical galaxies requiring spiral mergers (Section 1.3.1); it is subsequently expected that a relationship between galaxy morphology and SFR will exist. From Section 1.2, it is known that galaxies with different morphologies have broadly different star formation rates - with galaxies that have late-type spiral

morphologies exhibiting higher SFRs than early-type elliptical galaxies. This has been confirmed within a number of studies that have shown a strong correlation between a galaxy's morphology and its total SFR (e.g. Postman & Geller 1984; Wilson et al. 1990; Terndrup et al. 1994; Dressler et al. 1997; Matthews et al. 1999; Domínguez et al. 2001; Strateva et al. 2001; Goto et al. 2003; Kauffmann et al. 2004; O'Mill et al. 2008; Lee et al. 2010). These studies all propose a number of environmental influences on the SFR of galaxies which would drive such a correlation, and these are discussed in Section 1.5.

1.4.2 Colour Relations

It has also been shown, with the advent of large area surveys such as the SDSS, that galaxies can be categorised into two distinct optical colour populations, '*red*' and '*blue*', where the assigned colour given to a galaxy is dependent on several internal galaxy properties that represent the evolutionary history of the galaxy (e.g. Strateva et al. 2001; Baldry et al. 2004; Kauffmann et al. 2004). As shown from Figure 1.9, massive bright short-lived stars (e.g. O-B types) emit the largest fraction of their light at shorter wavelengths and are thus bluer than less massive older stars (e.g. M types), which emit primarily at redder wavelengths. In addition, increased metallicity, which reflects the amount of gas that has been reprocessed by stars, will act to increase reddening within the galaxy. A galaxy's colour therefore provides a good indication of its stellar content and constrains its recent star formation history. Recent observations have shown that this colour bimodality in the galaxy population is present out to at least $z \sim 1.5$ (e.g. Bell et al. 2004; Willmer et al. 2006; Cirasuolo et al. 2007; Cooper et al. 2007; Chuter et al. 2011).

As introduced in Section 1.2, a trend between galaxy morphology and colour, where early-type elliptical galaxies are predominantly redder than late-type spiral morphologies of similar luminosity, have been identified in a number of studies (e.g. Bernardi et al. 2003; Baldry et al. 2004; Schombert & Rakos 2009). Considering the correlations already discussed between morphology and both SFR and density; it is therefore unsurprising that both red and blue colour populations show, at a fixed luminosity, a

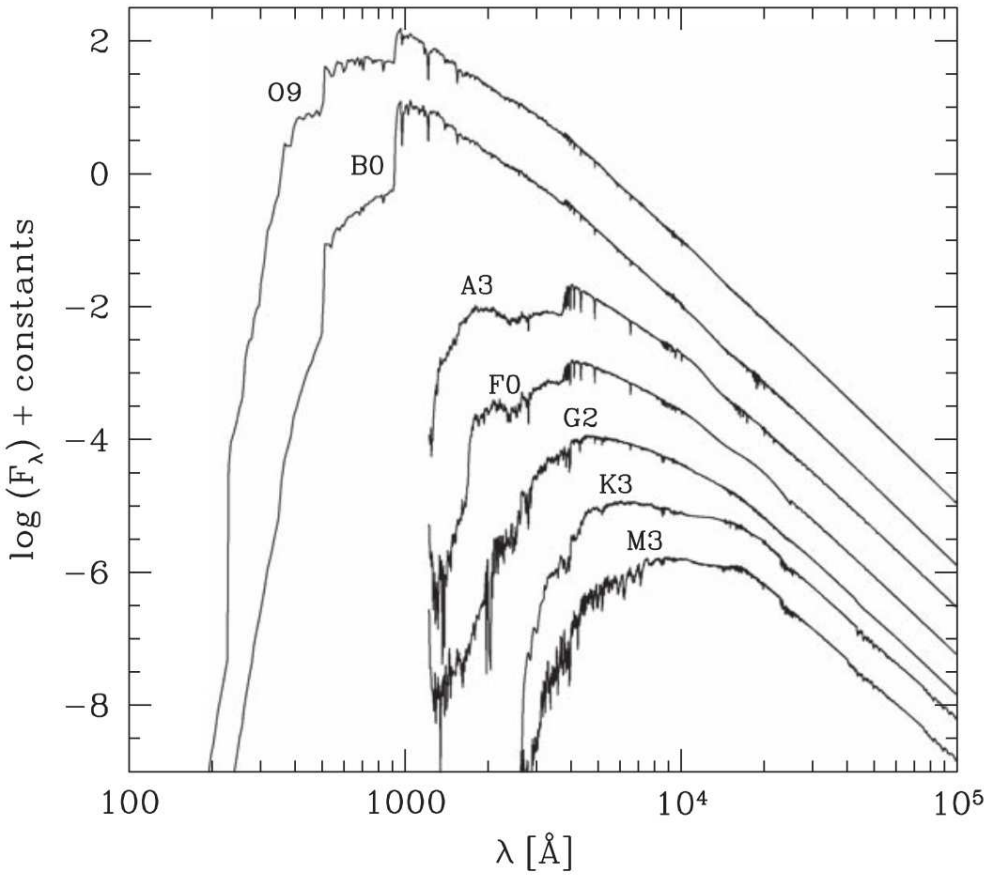

FIGURE 1.9: Spectra of stars for a variety of spectral types. F_λ is the flux per Ångstrom, with an arbitrary constant added to each spectrum for separation clarity. Figure taken from Mo et al. (2010).

correlation with environment. This is such that the densest regions are populated by the red, early-type passive galaxies with blue star forming late-types observed in less dense regions (e.g. Poggianti et al. 2006; Ball et al. 2008; O'Mill et al. 2008; Bamford et al. 2009).

However, the relation between galaxy morphology and colour is not an all encompassing correlation, suggested by observations of both red spirals (caused by dust reddening) and blue ellipticals (from recent periods of star formation) (e.g. Hughes & Cortese 2009; Masters et al. 2010; Tojeiro et al. 2013). For example, Bamford et al. (2009), who examined $\sim 10^5$ galaxies across a low-redshift range ($0.03 < z < 0.085$), demonstrate that at a fixed mass, the colour-density relation is more dominant than the morphology-density relation. They find that high mass galaxies are predominantly

red, regardless of morphology or density and that low mass galaxies are mainly blue in low-density regions but redder in high-density regions, again regardless of morphology. Despite finding that early-types do have a higher fraction of red colours, they infer that this is sub-dominant to the dependence of colour on mass and environment. They conclude that the transformation of galaxies from the blue to red population must occur on significantly shorter timescales than the morphology transformation from spirals to ellipticals.

As shown by Butcher & Oemler (1978), the cores of intermediate redshift clusters ($0.1 \lesssim z \lesssim 0.5$) contain a higher fraction of blue galaxies than low redshift cores. This blue fraction exhibits disturbed morphologies representative of recent merging activity (e.g. Couch et al. 1994; Lavery & Henry 1994; Wirth et al. 1994; Morris et al. 1998; Stanford et al. 1998); with spectroscopic data revealing strong Balmer lines which are indicative of recent active star formation (e.g Dressler & Gunn 1983; Poggianti et al. 1999). This suggests that there is considerable evolution within these dense regions over time, towards lower redshifts, once more driven by numerous environmental influences, as discussed in Section 1.5.

1.4.3 Mass Relations

With regard to the relationships previously mentioned, the overall mass of a galaxy is found to correlate well with a number of different galactic parameters, adding to the global picture of galaxy formation. From the accepted model that structure is assembled hierarchically with time, as described through Section 1.3, it is intuitive that the most massive galaxies in the local universe will have the highest environmental densities, and this mass-density relationship has been confirmed by numerous studies: Kauffmann et al. (2004), using a complete sample of galaxies taken from the SDSS between $0.03 < z < 0.1$, investigated how a number of galaxy properties depend on both environment and stellar mass. They show that the most massive galaxies reside within the most overdense regions, with mass increasing by a factor of two between low and high densities. Baldry et al. (2006), analysing a galaxy sample from the SDSS out to $z \sim 0.1$, find the same trend with mass, such that a density increase

across the range $0.1 - 10$ Mpc^{-2}, correlates with an increase in the characteristic mass between $\sim 5 - 9 \times 10^{10}\,\mathrm{M}_{\odot}$. This mass-density relation was further supported by Li et al. (2006), who showed that massive galaxies are more strongly clustered than less-massive galaxies, from a sample of $\sim 200,000$ SDSS galaxies out to $z < 0.3$.

Considering the previously discussed correlations with respect to both galaxy morphology and colour, in relation to both their environments and SFRs, additional correlations with galaxy stellar mass are expected. Subsequently, the most massive galaxies in the local universe are found to have redder colours and exhibit a higher fraction of elliptical morphologies with lower SFRs than lower mass galaxies, which show higher fractions of blue late-type morphologies and have higher SFRs. This has been confirmed in multiple observations (e.g. Brinchmann & Ellis 2000; Kauffmann et al. 2004; Deng et al. 2011; Grützbauch et al. 2011; Ideue et al. 2012).

The increased redness with increasing mass is suggestive of another correlation, associated with the metallicity content of the galaxy. As previously mentioned, increasing the metallicity content of a galaxy will act to increase the redness of its colour. Analyses of galaxy masses have revealed a distinct relationship between mass and gas-phase metallicity, such that the most massive galaxies are more metal rich. This relation was initially shown by Lequeux et al. (1979), using luminosity as a proxy for mass, and later by Garnett & Shields (1987) who showed the relation for blue galaxies. This work was then extended by various authors (e.g. Skillman et al. 1989; Brodie & Huchra 1991; Zaritsky et al. 1994) and the mass-metallicity relation has since become well established. More recently, Tremonti et al. (2004), find a positive correlation spanning three orders of magnitude in stellar mass and a factor of 10 in metallicity.

This tight relation gives an insight into the fundamental role galaxy mass must play in galaxy evolution. As it is understood, metallicity generally reflects the balance of several processes within the galaxy, principally: gas reprocessed by stars via supernovae and stellar winds; the ejection of gas from the galaxy in galactic outflows; and the accretion of gas onto the galaxy via inflows. Thus metallicity is strongly related to stellar evolution. Observations have shown that the gas-mass fraction of galaxies decreases with increasing stellar mass (e.g. McGaugh & de Blok 1997b; Bell & de Jong

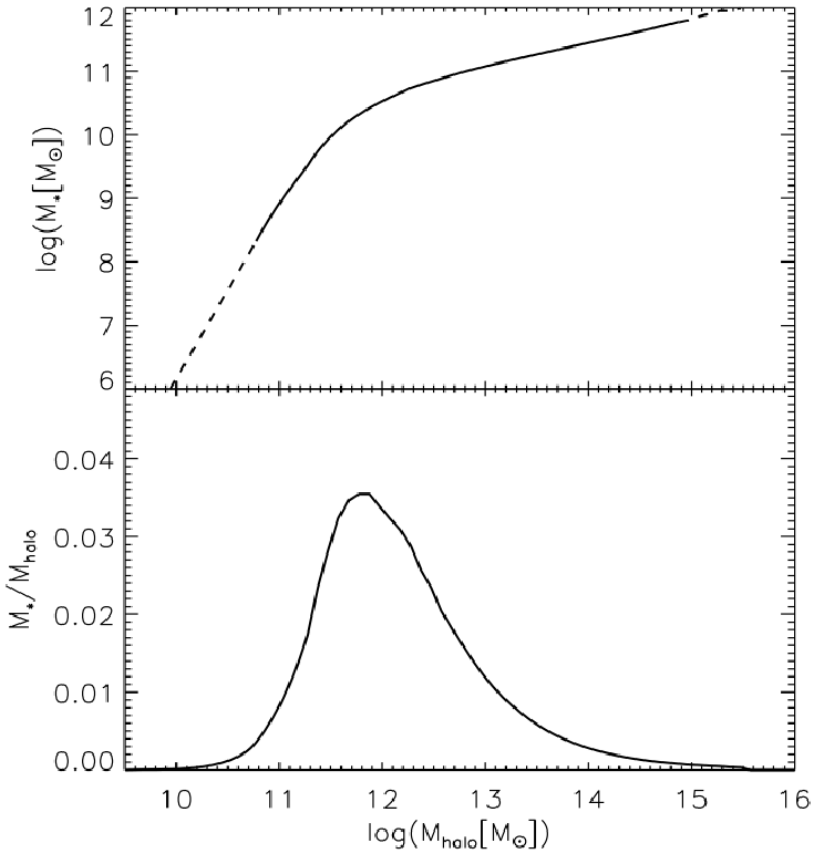

Figure 1.10: The stellar-halo mass relation, where the highest ratio between stellar and halo mass occurs at the characteristic mass M^* which in this example, taken from Guo et al. (2010), is found at $\sim 10^{11.7}\,\mathrm{M}_\odot$. At the peak, this equates to a stellar-halo mass ratio of just ~ 3.5 per cent.

2000; Boselli et al. 2001; Giodini et al. 2009; Catinella et al. 2010), indicating that the highest mass galaxies in the local universe are believed to have formed their stars earlier in a shorter, more intense period of star formation (Jimenez et al. 2005; Thomas et al. 2005). This is in agreement with the 'downsizing' scenario discussed earlier, where the most massive galaxies in the local universe contain older stellar populations than lower mass galaxies (e.g. Cowie et al. 1996; Bower et al. 2006; Gilbank et al. 2010; De Lucia & Borgani 2012). The relationship between mass and star formation rate is also shown to extend to high redshifts beyond $z = 1$ (Noeske et al. 2007a,b; Elbaz et al. 2007; Ilbert et al. 2010).

From Section 1.3, despite the evident high stellar-halo mass ratio, there is a strong positive correlation between these two parameters providing insight into the efficiency

of gas cooling and star formation over a wide range of halo mass (e.g. Somerville & Primack 1999; Moster et al. 2010; Wake et al. 2011; Munshi et al. 2013). The stellar-halo mass ratio is shown by Guo et al. (2010) to vary strongly with halo mass, indicating that baryons form stars with different efficiency in haloes of different mass. The highest stellar-halo mass ratio, and thus the peak in the star formation efficiency, corresponds with the characteristic mass (M^*), as shown in Figure 1.10. It is believed that the star formation efficiency is influenced by different processes associated with the local environment and the mass of the halo, leading to the change in the stellar-halo mass relation with halo mass. At halo masses below M^*, the decline in star formation efficiency is considered to be due to effects associated with UV photoionization, heating the ISM and preventing collapse to fuel future star formation (e.g. Quinn et al. 1996; Gnedin 2000; Okamoto et al. 2008; Nickerson et al. 2011). At halo masses above M^*, ISM heating is believed to be due primarily to various feedback effects such as from supernovae, winds or active galactic nuclei (AGN) feedback (e.g. Bower et al. 2006; Dekel & Birnboim 2006; Croton 2009; McCarthy et al. 2011; Johansson et al. 2012). These influence the galactic stellar content and are discussed further in Section 1.5.

1.4.4 Star Formation Trends

There are clearly numerous trends between a galaxy's environment and its star forming characteristics, indicating that both of these parameters are crucial tracers of galaxy formation. As shown above, the rate of star formation within a galaxy correlates with density, mass, morphology, colour and metallicity. Thus the most massive galaxies in the local universe are red ellipticals with low levels of star formation and high metallicity, residing in the most over dense regions. It has been demonstrated conclusively that galaxy properties that are associated with SFR, correlate strongly with environmental density (e.g. Hashimoto et al. 1998; Gómez et al. 2003; Kauffmann et al. 2004; Elbaz et al. 2007; Welikala et al. 2008; Patel et al. 2009, 2011). This correlation of SFR with environment has been shown, based on studies of mass-selected samples based on near-infrared selection, to hold out to $z \sim 2$, indicating that the correlations found in the local universe have been in place since this epoch (e.g. Chuter et al. 2011; Quadri

et al. 2012).

Due to the different processes affecting galaxies of different masses, it is often convenient to express SFR as a function of mass. Therefore both a galaxy's mass and its SFR can be described in terms of a its specific star formation rate (sSFR), representing the total SFR as a fraction of the total stellar mass of that galaxy. The sSFR has also been shown to correlate with both mass and environment, with the most massive galaxies having the lowest sSFRs. This implies, once more, that an environmental mechanism is actively influencing galaxy evolution within the densest environments through the truncation of star formation in the densest regions.

This raises an important consideration with respect to which correlations are actually dependent on environment and which reflect other correlations that are actually independent of environment. Work by Balogh et al. (1997, 1998), which compared galaxies with similar luminosities and morphologies from both dense cluster and low density field environments, found that SFRs were still lower in galaxies within dense cluster regions and thus the SFR-density correlation still held regardless of the morphology of the galaxy. This indicated that the observed SFR-density relation cannot be exclusively tied to the morphology-density relation alone, other processes must be influencing these observed correlations.

Furthermore, recent studies into the strong relationship between mass and environment have concluded that the quenching effects of environment on SFR are clearly separable from the quenching processes traced by stellar mass. Peng et al. (2010) argued that the quenching of star formation in passive red galaxies is distinct from the general decline in the global sSFR of star-forming galaxies since $z \sim 2$. They showed that the sSFRs of star-forming galaxies are, at most, a weak function of stellar mass and completely independent of environment. For passive galaxies however, they concluded that environment has little impact on the evolution of the most massive ($> 10^{10}\,\mathrm{M}_{\odot}$) galaxies, where stellar-mass related quenching dominates through feedback effects. For lower-mass passive galaxies ($< 10^{10}\,\mathrm{M}_{\odot}$), this quenching is the product of environmental interaction processes.

These interactions are believed to be associated with the hierarchical formation

model of galaxy structure (where galaxies accrete onto dense haloes from less dense environments) and will thus suppress star formation across both field and cluster environments (Cole et al., 2000b). There are several interaction models, associated with environmental influence, that may explain the aforementioned correlations between SFR and environment, and these are described in the following section.

1.5 Environmental Influences on Star Formation

1.5.1 Major Mergers

As already discussed, in hierarchical models of galaxy formation, it is the smallest structures that form first, merging with others over time forming larger structures. For a merging event to occur, a number of conditions must first be met, particularly in terms of the orbital energy between the two progenitor galaxies. Where the orbital energy of two galaxies is low, any bound orbit will eventually lead to a merging event, as tidal interactions between the two galaxies will gradually transfer orbital energy into internal energy (Barnes & Hernquist, 1992).

When two dark matter haloes of similar mass merge this is known as a major merger (with ratios $\lesssim 4:1$). Any orbital energy associated with the progenitor haloes is transformed by violent relaxation into internal binding energy within the merger remnant. In addition, any hot gas will be initially shock heated before settling back into hydrostatic equilibrium in the newly formed halo. Any central galaxies residing within the merging haloes will also undergo merging to produce a new central galaxy (Mo et al., 2010). Tidal perturbations between these two galaxies can affect the disk structure disrupting its stability, resulting in the formation of a pronounced bar-like structure. In this model, the gaseous and stellar-bar structures respond differently to tidal forces and thus develop different rotational phases. These phase differences give rise to torques that can remove angular momentum from the gas which is then able to fall toward the centre of the merger remnant (e.g. Barnes & Hernquist 1991; Heller & Shlosman 1994; Mihos & Hernquist 1996; Athanassoula 2003; Mo et al. 2010; Lee

et al. 2012).

This infall of gas increases the gas density within the centre of the merger remnant and, if the merging progenitors are gas-rich, containing a significant amount of cold gas (known as a wet merger), this will result in a burst of nuclear activity associated with a central starburst, with high levels of star formation (e.g. Kennicutt 1998; Freedman Woods et al. 2010; Patton et al. 2011; Lambas et al. 2012). Feedback from such starburst events, such as supernova winds, are able to prevent gas cooling, which as a result remains out of pressure equilibrium with its environment. Due to this pressure difference the gas expands out of the central regions of the galaxy sweeping up the ISM. This ejection of the ISM from the merger remnant can lead to further suppression of star formation (e.g. Mac Low & Ferrara 1999; Gay et al. 2010). Additionally, some of the nuclear gas can continue to lose angular momentum leading to accretion onto a putative central supermassive black hole (SMBH), possibly resulting in the formation of an AGN that may also contribute to the suppression of star formation via feedback processes of their own (e.g. Granato et al. 2004; Croton et al. 2006; Khalatyan et al. 2008; Teyssier et al. 2011; Bower et al. 2012). This AGN feedback can take two distinct forms: radiative feedback, where UV and X-ray photons emitted by the AGN, ionize and heat the neutral gas through photoionization increasing the IGM temperature to $\sim 10^4$ K, significantly suppressing gas cooling and truncating star formation in low mass haloes (e.g. Best et al. 2006; McCarthy et al. 2010); and mechanical feedback where, during the low-accretion mode of AGN, when the accretion rate of the SMBH is much lower that the Eddington rate, radio jets and lobes can further heat the IGM in the haloes of early-type galaxies, quenching radiative cooling and star formation in these systems (e.g. Bower et al. 2006; Croton et al. 2006). If, however, one or both of the merging galaxies do not have significant amounts of cold gas and are thus considered gas-poor (i.e. the merging of two early-type elliptical galaxies), this is known as a dry merger and there is little change in the overall SFR between the progenitors and merger remnant, although there will be significant build up in stellar mass (Bell et al. 2004, 2006; van Dokkum 2005; Bundy et al. 2009; Eliche-Moral et al. 2013).

The major merger model is supported by observations that have shown that the

peak in the SFR of the universe occurred around $z \sim 2$ and has been steadily decreasing since (e.g. Pérez-González et al. 2005; Daddi et al. 2007; Bell et al. 2007; Poggianti et al. 2008). This is in conjunction with the peak in the space density of massive star forming galaxies occurring across this epoch ($1 < z < 3$; Daddi et al. 2004; Ilbert et al. 2010) combined with the observed trend in the total stellar mass on the red sequence which has roughly doubled since $z \sim 2$, dominating the centre of local clusters (e.g. Lilly et al. 1996; Madau et al. 1998; Hopkins 2004; Bell et al. 2004; McIntosh et al. 2005; Poggianti et al. 2006; van den Bosch et al. 2008). In addition, some of the most luminous objects in the universe such as ultra-luminous infra-red galaxies (ULIRGs; $> 10^{12}\,L_{\odot}$), widely considered to be galaxies undergoing a massive star-burst (Sanders & Mirabel, 1996), show signs of recent disruption such as shells and tidal tails. These galaxies are dominant at $z \sim 2$ but rare in the local universe (e.g. Le Floc'h et al. 2005a; Seymour et al. 2008). With the expected lifespan of such a high luminosity galaxy to be around 10^8 years (Devriendt et al., 1999) this leads to the conclusion that these galaxies are the progenitors of local passive red-sequence ellipticals (e.g. Larson & Tinsley 1978; Le Floc'h et al. 2005b; Bridge et al. 2007; Elbaz et al. 2011; Magnelli et al. 2012).

1.5.2 Minor Mergers

Minor mergers, where a high mass ratio exists between the merging galaxies ($\gtrsim 4:1$), are the most common merging interaction due to the greater fractional abundance of low luminosity galaxies (Lambas et al., 2012). The dynamical processes involved are less violent compared to major merging events and consequently it is the smaller system only that undergoes any significant change to its structural and star formation properties. Woods & Geller (2007) show evidence for tidally triggered star formation in the faint galaxy member, whereas the primary larger merging galaxy shows no effect of the interaction. The smaller progenitor may orbit the main halo accreting its weakly bound material onto the larger galaxy (Naab et al., 2009).

In the densest cluster regions, smaller satellite galaxies orbiting the larger central galaxies towards the centre of the cluster may undergo a loss of energy and momentum

through dynamical friction. This will result in a satellite galaxy falling towards the centre of the large potential well, provided by the centre of the cluster. The central cluster galaxy will then begin to accrete material from the satellite, leading to an increase in mass of the central cluster galaxy, before finally merging with the galaxy in a process known as galaxy cannibalism (Ostriker & Tremaine 1975; Merritt 1983; Dubinski 1998; Nipoti et al. 2004). Both Oemler (1976) and Schombert (1986) showed such an effect through observations that central galaxies of clusters are typically the brightest and often display highly diffuse and extended outer envelopes (which consist of the tidally stripped material from the cannibalised satellite), categorised as an elliptical cD type morphology. Numerous further studies have shown that these elliptical cD galaxies are the product of galactic cannibalism and that this effect can explain the large masses and diffuse envelopes exhibited by the brightest central cluster galaxies. (e.g. White 1976; Hausman & Ostriker 1978; Malumuth & Richstone 1984; Aragon-Salamanca et al. 1998; De Lucia & Blaizot 2007).

1.5.3 Galaxy Harassment

As galaxy environmental density increases, the probability of interaction between galaxies is also increased due to the larger number of galaxies within a specific volume. However, with a greater number of galaxies within a specific environment, the associated increase in mass will result in a larger gravitational potential well. This leads to increased velocities between the gravitationally bound group members which reduces the cross-sectional area available for interaction. The maximum rate of galaxy interaction will therefore be obtained where the ideal conditions are met between the group and cluster regime. It is here that the internal energy of colliding galaxies is increased, causing them to heat up and become less bound and more susceptible to having their diffuse gas stripped, resulting in a lack of fuel for future star formation (e.g. Larson et al. 1980; Bekki et al. 2002).

The tidal interactions associated with galaxy harassment can destroy galactic disks, converting spiral galaxy structure into bulge dominated ellipticals or S0s (Larson et al. 1980; Bekki et al. 2002; Mihos 2004; Mo et al. 2010). Multiple close encounters with

large cluster galaxies achieve large scale mass-loss through impulsive heating, leading to a passive dwarf-elliptical morphology. The effects of galaxy harassment were first investigated by Farouki & Shapiro (1981) who showed through simulations that disk structure could be almost entirely destroyed by one or two passages through a cluster. This work was later extended by Moore et al. (1996, 1998) who highlighted the impact of harassment on the dynamically cold disk structure, leading to heating within the disk and a transformation into a spheroidal component resembling a dwarf elliptical. These passive dwarfs have since been observed to exist predominantly within dense cluster regions and are thus likely remnants of disk galaxies that have undergone harassment (e.g. Toomre & Toomre 1972; Moore et al. 1996, 1998; González-García et al. 2005; Haynes et al. 2007; Dutta et al. 2010).

1.5.4 Ram-Pressure Stripping

As a galaxy moves through the dense intra-cluster medium (ICM), the pressure from the ICM can strip the ISM from the galaxy if it exceeds the binding energy of the ISM to the disk. This can potentially prevent the galaxy from undergoing future episodes of star formation in a process called ram pressure stripping (Gunn & Gott 1972; Fujita & Nagashima 1999; Roediger & Brüggen 2008; Kapferer et al. 2009; Mo et al. 2010; Pappalardo et al. 2010).

The surface densities of stars and gas decline with galactocentric distance (Zasov & Khoperskov, 2008) and as such the efficiency of ram pressure stripping will increase towards the outer regions of the galaxy. The result is that the stripping of predominantly the highest radii disk gas may lead to the central regions being compressed continuing the star formation within the galaxy. Supernova feedback (SNe) from this star formation can create a hot gas reservoir within the outer atmosphere of the galaxy leading to sustained star formation through cooling flows of this material (e.g. Kronberger et al. 2008a,b; Kapferer et al. 2009; Smith et al. 2012c). Additionally, this loosely-bound hot gas reservoir may have contributions from gas that has either been shocked to high temperatures by infall but has yet to cool, or gas that has yet to fall into the host galaxy at all (e.g. Cole et al. 1994; Kauffmann et al. 1999; Nagashima

& Gouda 2001; Fujita 2004). The central region of the galaxy can maintain star formation via accretion of this gas until this reservoir is depleted by either further ram pressure stripping, tidal forces or the accretion of the host galaxy into a cluster. Once this supply of fuel has been severed, a slow reduction of star formation will occur, this is known as strangulation (Larson et al. 1980; Kawata & Mulchaey 2008; McGee et al. 2009; Bahé et al. 2012). The continuation of star formation within the central regions of these galaxies can last for several Gyr and may explain the greater number of blue star-forming galaxies found at intermediate redshifts than found in the local universe (Butcher & Oemler, 1978).

As previously discussed, it is well established that galaxies within underdense field regions have higher SFRs than galaxies of similar luminosity within overdense cluster regions. It is also known that this is partly a reflection of the morphology-density relation, where elliptical and S0 types have lower SFRs and are more abundant in denser regions than spiral late-type galaxies of similar mass. Considering observations that have shown the SFR-density relation to hold regardless of morphology, such that late-type disk galaxies within dense clusters have a lower gas content and form fewer stars than the same morphology within the field (Balogh et al., 1997, 1998), it is argued by several studies that strangulation must form a prominent mechanism for the environmental dependence of the SFR (e.g. Balogh et al. 2000; Balogh & Morris 2000; van den Bosch et al. 2008; Weinmann et al. 2009).

1.5.5 The Hot-Halo Model

As described above, the star formation within a galaxy is dependent upon the continuous supply of fuel through gas accretion. This process is governed by cold and hot two-mode accretion models (Kereš et al. 2005; Dekel & Birnboim 2006), which state that it is the dark matter halo-mass of a galaxy that is the key parameter in determining the rate of gas accretion. As such, a number of studies have investigated the role of galaxy halo-mass on accretion, and have concluded that the truncation of star formation is a result of gas temperature shock-heating, preventing further cooling flows.

Croton et al. (2006) show that, as in-falling gas is shocked to the virial temperature, for low-mass galaxies ($\lesssim 2-3\times10^{11}\,\mathrm{M}_{\odot}$), the post-shock cooling time is sufficiently short such that a quasi-static atmosphere cannot form. They find that as the cooling radius lies outside of the virial radius ($r_{cool} > r_{vir}$), the post-shocked gas can cool in less than one sound-crossing time. Therefore, this gas cannot maintain the required pressure to support an accretion shock at larger radii. This accretion shock will then move inwards as the post-shock temperature rises. The associated mass stored in the post-shock hot atmosphere will then decrease as it cools onto the central galaxy. For high-mass galaxies ($\gtrsim 2-3\times10^{11}\,\mathrm{M}_{\odot}$), they find that the gas is again shocked to the virial temperature and is added to the quasi-static hot atmosphere that extends to approximately the virial radius. From this halo, gas may still accrete onto the central galaxy in a cooling flow, however once the mass of hot halo exceeds that of the cold disk, the galaxy will form a static halo where cooling ceases.

Cen (2011) find in agreement with this result; halo-mass is the sole determinant of gas accretion, with larger haloes ($\gtrsim 10^{11}\,\mathrm{M}_{\odot}$) primarily accreting hot gas, while smaller haloes accrete cold gas. It is shown that the identified divisional mass between these two accretion regimes is roughly independent of redshift out to $z\sim6$. In further agreement with Croton et al. (2006) and also Bower et al. (2006), AGN feedback mechanisms are found to be the most likely candidate for the suppression of cooling flows, and thus the truncation of star formation in larger galaxies. This is further supported by the fact that these feedback mechanisms are increasingly effective with increasing virial temperature and decreasing redshift. These systems are thus found to be representative of groups and clusters typically associated with massive ellipticals. With the growth of large-scale structure under the hierarchical formation model, more massive galaxies will progressively become heated to higher temperatures, preventing further cooling. Therefore, under this hot-halo model, the most overdense regions will be starved of cold gas earlier than low density regions.

1.6 Star Formation Tracers

There is still a great deal of debate as to the extent that the SFRs of galaxies (particularly at high-mass) are dependent on interaction processes associated with their environments and whether it is these processes that drive galaxy evolution over cosmic time. A number of star formation tracers exist which have been used to examine these relationships, and in this section I outline the most common methods.

1.6.1 The Ultra-Violet Continuum

It is known that more massive stars ($> 5\,\mathrm{M}_{\odot}$) have much shorter main sequence lifetimes ($\sim 10^8$ yrs) than the typical age of a galaxy. As a consequence, the current SFR within a galaxy is directly proportional to the number of these massive stars that reside within it. These massive stars emit the majority of their radiation at short wavelengths (as shown in Figure 1.9), particularly in the ultraviolet (UV) regime, and as such, this emission can be used as a direct tracer of star formation. However, for the UV continuum to be successfully used as a star formation tracer, the optimal wavelength range must be short enough to avoid contamination by older stellar populations, while at the same time being long enough to avoid absorption due to neutral Hydrogen along the line of sight. This is achieved within the rest-frame wavelength range of $1250 - 2500$Å (Kennicutt, 1998) and a large number of studies have used the rest-frame UV continuum to measure galaxy SFRs (e.g. Smith & Cornett 1982; Donas & Deharveng 1984; Madau et al. 1998; Kennicutt 1998). Due to the transmission of the atmosphere and cosmological redshift effects, this technique is best suited for observing high redshift galaxies from ground observations between $1 < z < 5$, where this emission will have been redshifted into the optical and near-infrared regime (e.g. Lilly et al. 1996; Madau et al. 1996; Bouwens et al. 2007; Wilkins et al. 2010, 2011). Although space based observations, such as the *Galaxy Evolution Explorer* (GALEX; Martin et al. 2005), have allowed for the use of UV to trace SFRs at more local redshifts $z < 1$ (e.g. Heckman et al. 2005; Salim et al. 2007; Schiminovich et al. 2010; Robotham & Driver 2011).

The main drawbacks of using this technique as a measure of SFR are the fact

that UV is highly sensitive to dust extinction and therefore the SFR derived from the observable UV may be an underestimation. Therefore details of the dust extinction are necessary to calibrate the technique, however this is hampered by the very non-uniform spatial distributions associated with star forming regions (Calzetti et al., 1994). The use of spectral synthesis models (e.g. Bruzual & Charlot 1993) to calibrate between the UV continuum and SFR, introduce assumptions based upon the time-scales of star formation within the galaxy. It is commonly assumed that the SFR has remained constant over similar time-scales to the lifetimes of the dominant UV population ($> 10^8$ yrs), and therefore will be inaccurate for starburst galaxies (Kennicutt, 1998). An additional problem is related to the dependence of the calculated SFR on the assumed initial mass function (IMF). As UV emission is dominated by $> 5\,M_\odot$ stars, while the total mass of new stars is dominated by lower masses, the conversion of UV to SFR is sensitive to the selected IMF, usually assumed to be a Salpeter IMF (Salpeter, 1955) although others are used (e.g. Scalo 1986; Kroupa et al. 1990; Chabrier 2003). Independent of which IMF is used, SFR determination from the UV continuum often involves a large extrapolation to lower stellar masses.

1.6.2 Recombination Emission Lines

Any stellar luminosity from a galaxy shortward of 912Å (the Lyman limit) will be absorbed by the neutral ISM surrounding these young massive stars. This will ionise the ISM giving rise to HII regions which will exhibit hydrogen emission lines when the ionized gas recombines. As only the most massive ($> 10\,M_\odot$), short-lived ($\sim 10^7$ yrs) stars contribute significantly to Lyman continuum, there is very little contamination from older stars and these lines can thus return a SFR irrespective of the star formation history (Kennicutt, 1998) and can therefore be used as a direct tracer of star formation within a galaxy.

Hydrogen, being the most abundant material in the universe with a low ionisation potential, produces the brightest rest-frame emission line in the UV at ~ 1216Å, which represents the Lyman-α line (i.e. the transition from $n = 2$ to $n = 1$). However, the main drawback of this star formation tracer is the high efficiency of dust absorption of

UV emission, resulting in a potential underestimation of the SFR. The Lyman-α line is therefore biased towards young star-forming galaxies with the lowest dust content. To reduce this bias, it is common for the brightest rest-frame emission line in the optical to be used as a tracer of star formation. At 6563Å, which represents the first Balmer line transition from $n = 3$ to $n = 2$ (Hα), this has become the most commonly used emission line for this purpose within numerous surveys (e.g. Young et al. 1996; Bechtold et al. 1997; Moorwood et al. 2000; Twite et al. 2012). However, as with the UV continuum, this technique is still subject to systematic errors through dust extinction, as well as assumptions made with regard to the selection of an appropriate IMF and the assumption that all massive star formation is traced by ionised gas. In addition, for galaxies $z \gtrsim 0.4$, the Hα emission line is redshifted out of the optical passband and therefore optical spectroscopy becomes unavailable.

Because of this redshifting, a shorter wavelength emission line would be better suited. However, the next Balmer emission line Hβ (a transition from $n = 4$ to $n = 2$), although generated via the same processes, is significantly weaker, more strongly influenced by absorption and a poor SFR diagnostic (Jansen et al. 2001; Charlot et al. 2002). Therefore it is often the shorter wavelength [OII] forbidden-line doublet at 3727Å, that is used (e.g. Charlot et al. 2002; Rosa-González et al. 2002; Kewley et al. 2004). The [OII] line is an effective SFR tracer due to its intensity, but is not directly related to the UV luminosity produced by massive young stars and requires calibration with the Hα line which adds the same uncertainties associated with it (Kennicutt, 1998). In addition the [OII] line is also strongly dependent on metallicity (e.g. Kewley et al. 2004).

1.6.3 Far-Infrared Emission

The origin of dust within the ISM is known to be closely related to the stellar processes occurring within a galaxy. The primary source of this dust originates from post–main-sequence, asymptotic giant branch (AGB) stars, with initial main-sequence masses of the order $0.6 - 10\,\mathrm{M}_{\odot}$. These stars undergo a heavy mass-loss through ejection of their outer layers via low velocity stellar winds ($v \sim 10\,\mathrm{kms}^{-1}$), increasing the dust content

in their environments (e.g. Renzini & Voli 1981; Sedlmayr 1994; Dorschner & Henning 1995; Wachter et al. 2002; Winters et al. 2003; Matsuura et al. 2009). However, the time-scales involved for such low- to intermediate-mass main-sequence stars to evolve onto the AGB are of the order of several Gyr, and consequently a more rapid source of dust contribution is required to explain the far-infrared emission (a tracer of warm dust) observed at high redshifts, where the AGB mass-loss would not have had time to contribute.

A solution to this issue arises from the fact that star formation within a galaxy typically increases the dust content of the ISM through processes associated with the short-lived massive stars that inhabit these regions, such as core-collapse supernovae (Type II, Ib & Ic), which redistribute material into the surrounding ISM (e.g. Dunne et al. 2003; Sugerman et al. 2006; Dunne et al. 2009; Gomez et al. 2012). This dust then absorbs a significant fraction of the UV light emitted by the young O-B type stars associated with these regions and is heated to temperatures of around 20-40K, emitting thermal radiation at far-infrared wavelengths. This makes the use of far-infrared wavelengths from a galaxy a reliable diagnostic for the obscured star formation rate of a galaxy (e.g. Kennicutt 1998; Hirashita et al. 2003; Driver et al. 2007; Cortese et al. 2008; Nordon et al. 2010; Buat et al. 2010; Dunne et al. 2011; Smith et al. 2012a; Galametz et al. 2013).

Other contributions to the UV radiation field which heats the dust, such as AGN and older stellar populations within the galaxy, may lead to overestimates of the SFR using far-infrared emission (e.g. Schmitt et al. 2006; da Cunha et al. 2008; Nardini et al. 2008; Bendo et al. 2010, 2012; Groves et al. 2012; Smith et al. 2012a; Smith et al. 2012b). Conversely, in galaxies where the ISM is optically thin at UV wavelengths, the measured SFR will emerge directly from the UV and not in the far-infrared. In these galaxies, deriving the star formation from far-infrared emission may lead to an underestimation of the total SFR (Kennicutt, 1998).

However, in late-type star forming galaxies the far-infrared has been shown to correlate well with both Hα and UV luminosities (e.g. Lonsdale Persson & Helou 1987; Sauvage & Thuan 1992; Buat & Xu 1996; Kennicutt 1998). In addition, as more

than 50 per cent of energy ever radiated from stars has been absorbed by dust and re-radiated into the infrared (e.g. Puget et al. 1996; Fixsen et al. 1998; Adelberger & Steidel 2000; Finn et al. 2010), with the bulk of star formation $z < 1$ occurring in dust obscured galaxies (e.g. Calzetti & Heckman 1999; Le Floc'h et al. 2005a; Buat et al. 2010; Patel et al. 2013), it appears that only AGN, low metallicity systems and very passive but dusty galaxies will not lie on the far-infrared to SFR relation.

1.6.4 Radio Emission

An almost linear relationship exists between the far-infrared and radio luminosities of star-forming galaxies and has been shown, by numerous studies, to exist over 5 orders of magnitude in luminosity across a wide range of galaxy types and masses at all redshifts (e.g. de Jong et al. 1985; Condon et al. 1991; Condon 1992; Price & Duric 1992; Appleton et al. 2004; Ibar et al. 2008; Murphy 2009; Ivison et al. 2010; Jarvis et al. 2010; Lacki & Thompson 2010; Bourne et al. 2011). This tight far-infrared–radio correlation (FIRC) indicates that the observed radio emission can also be used as a diagnostic for ongoing star formation within a galaxy.

The radio continuum associated with star formation is generated predominantly via two processes: thermal bremsstrahlung (free-free) emission from HII regions (e.g. Duric et al. 1988; Richards 2000), and cosmic ray electrons being accelerated within supernovae remnants, resulting in non-thermal synchrotron emission (e.g. Condon 1992; Lacki & Thompson 2010). Both of these emission processes are associated with stars of masses $\gtrsim 8\,\mathrm{M}_{\odot}$ which dominate the ionisation of HII regions and lead to the Type II and Type Ib supernovae responsible for accelerating most of the relativistic electrons. Towards lower radio frequencies, the non-thermal synchrotron emission is expected to dominate the radio continuum of non-active 'normal' star forming galaxies. For example, at 1.4GHz, ~ 90 per cent of the total radio emission from normal star-forming galaxies is attributed to non-thermal radiation (Condon 1992; Bell 2003). Figure 1.11 shows the radio/far-infrared spectrum of a bright normal star-forming galaxy (M82), taken from Condon (1992), and shows the separate contributions of the different emission components: synchrotron (dot-dashed line), free-free (dashed line),

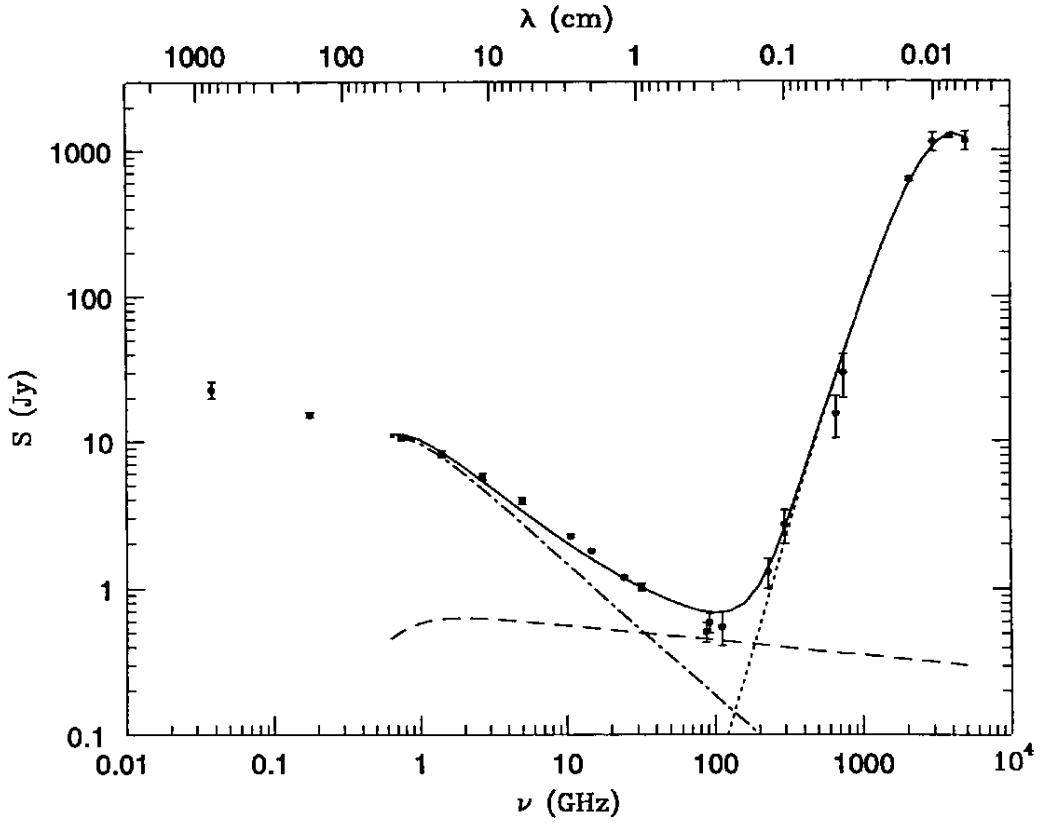

FIGURE 1.11: Observed radio/FIR spectrum of M82 presenting the different constituents of star formation driven emission. The *dashed* line represents free-free emission, the *dotted* line represents emission from dust, the *dot-dashed* line represents synchrotron emission and the *solid* line represents the sum. Figure taken from Condon (1992).

dust (dotted line) and the sum (solid line). It is clear that the thermal radiation from dust emission vastly exceeds the total radio emission at higher frequencies, becoming dominant at $\gtrsim$ 200GHz and signalling an upper boundary to the radio as a tracer of star formation. It is also apparent that the total star formation related radio component represents only a small proportion of the overall emission of a normal galaxy, accounting for $< 10^{-4}$ of the bolometric luminosity. Therefore, the observations of radio emission, as a star formation diagnostic in normal galaxies, will predominantly trace galaxies with the highest SFRs, especially towards higher redshifts where normal galaxies with low SFRs become radio faint (Lacki & Thompson, 2010).

However, large-scale radio observations, such as the National Radio Astronomy Observatory (NRAO) Very Large Array (VLA) Sky Survey (NVSS; Condon et al. 1998), and the Faint Images of the Radio Sky at Twenty-cm (FIRST; Becker et al. 1995), have

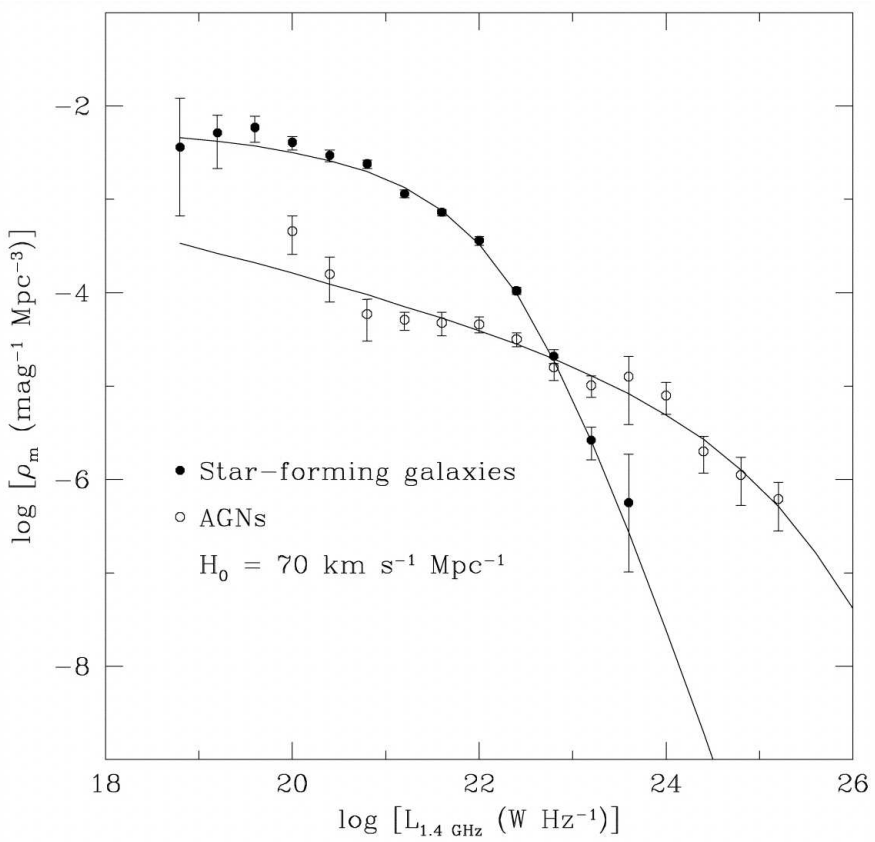

Figure 1.12: Luminosity functions of radio sources powered by AGN (open circles) and star formation (closed circles). Figure taken from Condon et al. (2002).

revealed a detailed view of the total radio emission across a significant amount of the sky, down to flux densities of a few mJy. Due to the low radio luminosities associated with star formation, such radio surveys have shown that the majority of the overall detected radio emission actually comes from populations of more luminous AGN (e.g. Sadler et al. 2002; Jarvis & Rawlings 2004; Simpson et al. 2006; Seymour et al. 2008; Kellermann et al. 2008; Padovani et al. 2009, 2011). This radio emission is also believed to be formed via synchrotron radiation generated through either accelerated charged particles within the relativistic jets associated with 'radio-loud' AGN (e.g. Rees 1971; Blandford & Rees 1974; Sambruna et al. 2004, 2006), or through a radio-emitting core in 'radio-quiet' AGN (e.g. Mauch & Sadler 2007; Jiang et al. 2010; Ishibashi & Courvoisier 2011; Ballo et al. 2012).

The radio luminosities of normal star forming galaxies have been shown to range between $10^{18} \lesssim L \lesssim 10^{23}$ W Hz^{-1} at 1.4GHz (Condon, 1992), and it is above this range

that radio-loud AGN are expected to dominate the radio continuum. This is confirmed by comparisons of the 1.4GHz radio luminosity functions of AGN and normal star forming galaxies from Condon et al. (2002), shown in Figure 1.12. This reveals, as expected, that towards lower radio luminosities emission from star formation dominates the radio continuum, with AGN becoming increasingly dominant above $\sim 10^{23}$W Hz^{-1}. However, with the next generation of low-frequency, deep radio surveys reaching many orders of magnitude deeper than the current deepest radio surveys; e.g. the Low-Frequency Array (LOFAR; van Haarlem et al. 2013), the South African MeerKAT (Jonas, 2009) and the Australian SKA Precursor (ASKAP; Johnston et al. 2008), AGN will no longer make up the dominant source of radio emission which will instead be dominated by star forming galaxies (e.g. Seymour et al. 2008; Padovani et al. 2009). Although it is proposed that radio-quiet AGN will still make significant contribution (e.g. Jarvis & Rawlings 2004; Simpson et al. 2006; Smolčić et al. 2009), these studies will allow for the detection of low-luminosity star forming galaxies via radio emission out to the highest redshifts (Jarvis et al, in prep).

1.7 Far-Infrared Investigations: SFR-Density

Initial studies of the relationship between SFR and infrared emission from galaxies focused on shorter wavelengths using the *Infrared Astronomical Satellite* (IRAS; Neugebauer et al. 1984) and more recently the *Spitzer Space Observatory* (Rieke et al., 2004). *IRAS* surveyed the vast majority of the sky between $12 - 100$ μm, providing a large census of dusty galaxies in the local Universe. Using these data, Goto (2005) investigated the optical properties of 4248 infrared-selected galaxies by positionally matching data from the *IRAS* with optical data from the SDSS. Using a volume limited sample at $z \leq 0.06$ and applying a 5th-nearest neighbour density estimate (described in Chapter 2), a trend was found such that galaxies with the highest infrared luminosities reside in relatively low-density local environments, suggesting that star-forming galaxies favour underdense regions, in agreement with previous studies at other wavelengths. The environmental densities of *IRAS*-detected luminous infrared galaxies

(LIRGs; $10^{11} \leq L_{FIR} < 10^{12}\,\mathrm{L}_{\odot}$) at $0.03 \leq z < 0.17$ were also studied by Hwang et al. (2010). They found that the fraction of LIRGs was strongly dependent on both the morphology and the distance to the nearest neighbour galaxy. They conclude that the evolution of the SFR-density relation from high to low redshifts is consistent with the idea that galaxy-galaxy interactions and merging play a critical role in triggering star formation in LIRGs, in agreement with the discussion in Section 1.5.

Additionally, Tekola et al. (2012) examined the relationship between star formation and the environments of LIRGs selected from *IRAS* and compared these with other types of high- and low- redshift galaxies out to $z \sim 1$. They identified a luminosity ($L_{IR} \sim 10^{11} h^{-2}\,\mathrm{L}_{\odot}$) at which infrared selected galaxies preferentially resided in higher density environments, compared to 'normal' galaxies. Above this luminosity the average density increases, whereas below this luminosity, infrared-selected galaxies reside in environments of equal density, similar to the general population. They conclude, therefore, that infrared activity for non-LIRGs is not dependent on density and that the SFR-density relationship for these galaxies is similar to that of blue galaxies at $z \sim 1$. At higher redshifts, Feruglio et al. (2010) used 24μm observations from *Spitzer* to investigate the environmental effects on star formation in LIRGs and ULIRGs in the Cosmic Evolution Survey (COSMOS; Scoville et al. 2007) at $0.3 < z < 1.2$. They found the fraction of these galaxies to decrease with density out to $z \sim 1$, but that the relationship flattens out with increasing redshift.

Due to the wavelength coverage of IRAS ($12 - 100\mu$m), the majority of galaxies detected by these studies were found by Bregman et al. (1998) to be spirals and starbursts in the local universe ($z < 0.1$). This restriction resulted in the IRAS providing little information about the cooler dust, which traces the bulk of the dust mass (e.g. Dunne et al., 2011) in other galaxy populations, especially early-type morphologies. In comparison, *Spitzer* can probe longer wavelengths ($24 - 160\mu$m) and therefore is less susceptible to this bias, although galaxies with the coldest dust temperatures would still be missed (Eales et al. 2010; Symeonidis et al. 2011, 2013). Considering that cold dust is present across all types of galaxies and is a major contributor to infrared luminosity (Willmer et al., 2009), and closely traces the total dust mass, it is crucial that

we are able to select galaxies at longer wavelengths.

Since the launch of the *Herschel Space Observatory* (Pilbratt et al., 2010) on the 14th of May 2009, it has been possible to select galaxies at these longer wavelengths. A number of studies have begun to investigate how star formation in a galaxy, traced by far-infrared emission at $\geq 250\mu$m, is linked to the environment in which each galaxy resides. Dariush et al. (2011) used far-infrared data from the *Herschel* Astrophysical Terahertz Large Area Survey (H-ATLAS; Eales et al. 2010) Science Demonstration Phase (SDP) to examine the ultraviolet and optical properties and environments of low redshift galaxies ($0.02 \leq z \leq 0.2$) from the Sloan Digital Sky Survey (SDSS; Abazajian et al. 2009) and Galaxy And Mass Assembly survey (GAMA; Driver et al. 2011; Hill et al. 2011; Baldry et al. 2010). They found H-ATLAS detects predominantly blue/star-forming galaxies with a minor contribution from red galaxies (comprising of highly obscured and passive systems). Using the 5th-nearest neighbour technique as an estimate of the environmental density, they found that the fraction of H-ATLAS detected galaxies is much higher ($\sim$ 70 per cent) in low-density environments compared to high-density environments where the fraction was found to be $\sim$ 30 per cent. However, their detection rate of red and blue galaxies appeared to be similar for both high- and low-density environments, indicating that it is the colour of a galaxy, rather than the density of its local environment, that determines whether it is detectable by H-ATLAS.

A consistent result was also found by Rowlands et al. (2012), who find that H-ATLAS detected early-type galaxies tend to have bluer (NUV-r) colours, higher sSFRs and younger stellar populations than galaxies with early-type morphologies. They compare 354 spiral and 30 early-type galaxy morphologies at low redshift ($z < 0.18$), finding no significant difference between the environmental densities of these populations. However, it is possible that they are not sampling a large enough range of environments with such small population samples.

Coppin et al. (2011) also used far-infrared data from H-ATLAS to examine the centres of 66 optically selected galaxy clusters at $z \sim 0.25$ to search for statistical evidence of obscured star formation in the cluster population. Using Voronoi tessellations

(described in Chapter 2) to locate cluster members, they found an excess in the surface density of far-infrared sources within $\sim$ 1.2Mpc of the centre of these clusters. They conclude that the far-infrared emission is associated with dust-obscured star formation in cluster galaxies, translating to a rate of $\sim 7\,\mathrm{M}_{\odot}\,\mathrm{yr}^{-1}$. This SFR, maintained over the 3 Gyr since $z = 0.25$, would contribute enough mass to construct a typical $S0$ type bulge that would match the observed increase in bulge dominated galaxies in cores of clusters over the same timescale.

The effects of environment on the far-infrared properties of galaxies are also discussed by Davies et al. (2010), who use data from the *Herschel* Virgo Cluster Survey (HeViCS; Davies et al. 2012), finding that relatively few far-infrared sources are associated with confirmed Virgo cluster members. Furthermore, studies by Cortese et al. (2010a,b) present *Herschel* observations of the perturbed galaxy NGC 4438 in the Virgo cluster and identify regions of extra-planar dust up to $\sim 4-5$ kpc away from the galaxy disk. This dust is found to closely follow the distribution of stripped atomic and molecular hydrogen, supporting the idea that gas and dust are perturbed in a similar way within the cluster environment.

In contrast to these results, Geach et al. (2011a), using 24μm observations from *Spitzer*, investigated large-scale filamentary structure surrounding rich clusters out to $z \sim 0.55$, and found that the SFRs of individual galaxy members within a cluster are not significantly different to identically selected field galaxies. Although pockets of enhanced star formation were observed, they suggest that this is the result of some 'pre-processing' effect where satellite groups have star formation triggered via gravitational tidal interactions during cluster infall. However, they state that there is no environmental mechanism acting to enhance the star formation within individual galaxies.

It is evident that the majority of these previous studies have either used density measures that do not detect differences on the smallest environmental scales (i.e. Nth-nearest neighbour or aperture gridding) and/or they have focused entirely on narrow and local redshifts ($z \lesssim 0.2$). There is therefore an opportunity to improve upon these previous studies by combining an environmental measure that can detect differences in

density on the smallest scales, while harnessing large-scale survey data out to intermediate redshifts. This marks the main motivation of this thesis where I have used data from H-ATLAS to investigate the environmental dependence of far-infrared emission (and hence star formation) using a technique based on Voronoi tessellations. Unlike the Nth-nearest neighbour technique, Voronoi tessellations calculate the environmental density of galaxies based upon the precise gridding of each environment. This is such that the gridded cells associated with Voronoi tessellations contain only space closer to that object than any other, and thus form a multitude of different shapes depending on the distribution of galaxies. This is different to the Nth-nearest neighbour technique that always assumes a set radius, and thus a circular area, to define its cells. This comparison is investigated further in the next chapter.

1.8 In This Thesis

I present and examine the relationship between the environmental densities of galaxies and their associated properties, such as SFR and dust temperature. In Chapter 2, I discuss common methods of environmental density measurements and outline a new method involving Voronoi tessellations that I then use throughout this thesis. In Chapter 3, I use my density method to compare the relationship between environment and SFR out to $z \sim 0.5$ between a 250μm selected sample from the science demonstration phase of the H-ATLAS, against a large optically selected sample combining the SDSS and GAMA surveys. I then apply my method to synthetic light cones generated from semi-analytic models to compare results. In Chapter 4, I expand my analysis of the SFR-Density relation, incorporating the entire Phase-One field of the H-ATLAS and incorporate galaxy dust temperatures and compare these with environment. In Chapter 5, I investigate the relationship between radio emission and density out to $z \sim 2$ by applying my environmental measure to near-infrared data from the VISTA Infrared Deep Extragalactic Observations (VIDEO) survey in conjunction with radio observations from the VLA. In Chapter 6, I conclude and summarise this thesis and outline the potential future work that may be conducted as new data becomes available.

2

Voronoi Tessellations as a Measure of Environmental Density

As detailed in Chapter 1, numerous studies of galaxy properties such as morphology (e.g. Dressler 1980; Postman & Geller 1984; Dressler et al. 1997; Domínguez et al. 2001; Goto et al. 2003; Lee et al. 2010), mass (e.g. Kauffmann et al. 2004; Li et al. 2006; Deng et al. 2011; Ideue et al. 2012), SFR (e.g. Kauffmann et al. 2004; Elbaz et al. 2007; Welikala et al. 2008; Patel et al. 2009) and colour (e.g. Poggianti et al. 2006; Ball et al. 2008; O'Mill et al. 2008; Bamford et al. 2009), have yielded several distinct correlations with environmental density. Understanding the astrophysical processes that drive these trends is a crucial problem in modern cosmology. Successfully unifying the different correlations will greatly enhance our understanding of galaxy evolution leading to the creation of more detailed evolutionary models. Therefore the accuracy

of the techniques used to measure galaxy environments is of great importance and are a vital tool in the quest to understand our universe.

One of the main focuses of this work has involved the creation of a structured algorithm that has the ability to accurately determine the environmental density of a galaxy, on an individual galaxy basis, normalised across any designated redshift range. In this chapter I describe previous methods of environmental characterisation before introducing a new method for measuring the environmental densities of galaxies using a mathematical grouping technique called Voronoi tessellations. I describe how the algorithm works before using sample catalogues to examine the output of the technique against a more well established local density measure.

2.1 Environmental Characterisations

2.1.1 Cluster-Finding Algorithms

There are a number of approaches towards the characterisation of galaxy environments found within the literature. Clusters of galaxies are the largest known virialized structure in the universe, and analysis of such structure plays an important role in the understanding of the evolutionary processes that have shaped our universe. Obtaining detailed catalogues of galaxy clusters has enhanced the understanding of large-scale evolution from the initial collapse of dark matter haloes to the formation of galaxies and their interactions with their local environment. Therefore, in initial studies of galaxy redshift surveys, the environmental properties of galaxies were determined based on their association with large-scale structure. This was such that by attributing a galaxy to a particular group or cluster based upon its position relative to its neighbouring galaxies provided a quantitative estimate of overdensity in the field. Many environmental studies of the low redshift universe have applied this 'cluster-finding' approach via a number of distinct techniques (e.g. Tully 1987; Maia et al. 1989; Garcia 1993; Ramella et al. 1997, 1999; Espino-Briones et al. 2007; Tempel et al. 2012).

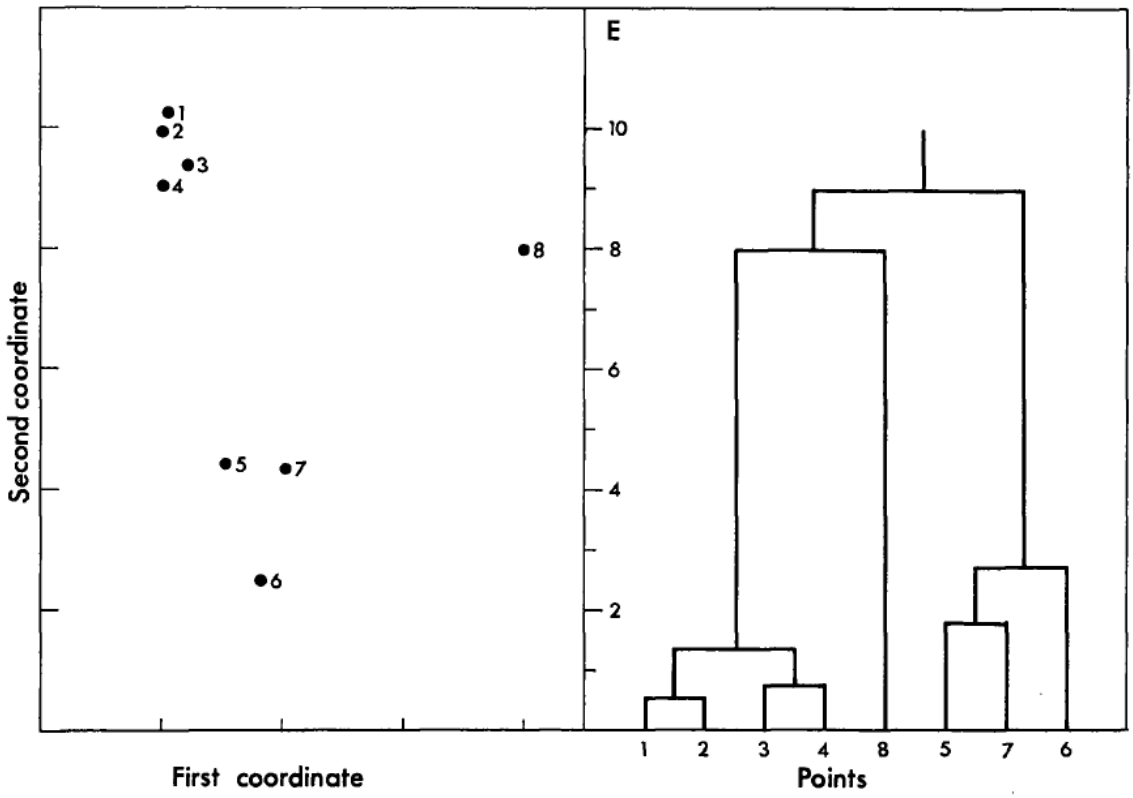

Figure 2.1: *Left*: Two-dimensional distribution of points (galaxies) distributed according to position. *Right*: A Dendrogram showing the merging of these points to form hierarchy, starting from single points joining to form clusters. The value E defines the criterion according to which the merging takes place. Image taken from Materne (1978).

The Hierarchical technique:

The Hierarchical technique (Materne 1978; Tully 1980) assigns group/cluster identification by first selecting galaxies with similar group/cluster velocity dispersions in order to distinguish them from background sources, mapping their two-dimensional positions (RA & Dec.) in the field. Utilising the hierarchical structure formation model of the universe, the algorithm determines which galaxies would merge through gravitational interaction earlier than others if allowed to freely evolve with time based upon their initial separations. Galaxies that merge sooner are deemed to be more strongly associated with each other (i.e clustered) than objects that merge later. Figure 2.1, taken from Materne (1978), illustrates an example of this method with the left-hand plot showing a two-dimensional representation of objects positioned and numbered accordingly. The

right-hand side of the figure illustrates the process of merging and hierarchy (a plot known as a 'Dendrogram') and shows, in terms of a unit-less parameter representative of the chronology of merging (E), the sequence in which the objects will merge. The Dendrogram shows that objects 1 and 2, due to their relative proximity, will merge first followed by the merging of 3 and 4. The resultant group produced by these two merging events will also merge at a later time at $E \sim 1.5$. This is followed by the merging of objects 5, 6 and 7 which eventually merge into one group around $E \sim 3$. Object 8 does not merge with any of the other groups in the field until much later ($E \sim 8$) suggesting that it is not as well associated with any group of objects compared to the rest of the field. The resultant ordering of E values associated with object mergers can be determined by either the physical proximity of objects in the field, leading to closer objects merging sooner, or the ordering is selected based upon reducing the dispersion in distance and velocity at each merger to a minimum [see Materne (1978) for further discussion]. As all objects in the Dendrogram will eventually merge, a particular value of E is therefore defined to represent the limit between which objects can be considered members of a group and which are 'field' galaxies unassociated with the group. This E_0 value is a free parameter that lies within the range $3.5 < E < 8$ in Figure 2.1. Therefore object 8 in Figure 2.1 may be considered a 'field' galaxy whereas the rest of the objects are considered cluster members with objects 1, 2, 3 and 4 being demonstrably more clustered than 5, 6 and 7. This sequence is reflected by the positions of these objects in the left-hand two-dimensional plot.

The Percolation technique:

The more popular Percolation technique (Huchra & Geller 1982), which is commonly referred to as the 'friends-of-friends' method (hereafter FOF) again uses the physical proximity of objects to establish their environmental structure while incorporating a more direct measure of position. The basic FOF algorithm cycles through each field object (i) searching for all companion objects (j) that lie within a specific projected 'linking-length' (l) which is defined as

$$l = b \cdot \bar{n}^{-1/3} \quad , \tag{2.1}$$

where $\bar{n}$ is the mean galaxy number density of the field and b is a unit-less parameter representing the mean galaxy separation in the field, usually given the value $b = 0.2$ (Frenk et al. 1988; More et al. 2011). All neighbouring galaxies found to satisfy the linking-length criterion are added to a new 'friends' group (k) that includes i and all j companions. The search is then extended to each j galaxy in this group, again searching for any associated counterparts which are further added to k. This process is continued until no further companions are located and the cluster boundary is reached. The final k catalogue contains all objects that are defined as one group and are considered associated with each other. If the number of objects in k falls below a minimum value (N_{min}) then the group is removed from the final structure catalogue. N_{min} is widely assigned the value of 3 (Botzler et al., 2004) and therefore only galaxy pairs are excluded from the final group structure catalogue. If no j companions are found at all within l then i is considered an isolated 'field' object and also removed from the final group catalogue.

However at higher redshifts the FOF technique is somewhat complicated by the fact that the galaxies in the vicinity of clusters possess strong distortions in redshift due to peculiar motion and small-scale galaxy dynamics within each group (Trasarti-Battistoni, 1998). In addition, selection effects due to imposed magnitude limits on the observations also make detections more difficult at higher redshifts. Therefore, the number density of galaxies ($\bar{n}$) at distance (d) above a given magnitude limit (m_{lim}) increases with apparent magnitude and decreases with increasing distance, shown by Botzler et al. (2004) to be

$$\bar{n}(d, m_{lim}) = \int_{-\infty}^{M_{lim}(d)} \Phi(M) dM \quad , \tag{2.2}$$

where $\Phi(M)$ is the Schechter luminosity function. In order to counteract this number density decrease with redshift, the projected separation linking-length (l) is replaced by projected and radial separation limits D_{max} and V_{max} such that

$$D_{max} = D_0 \cdot R \tag{2.3}$$

and

$$V_{max} = V_0 \cdot R \quad , \tag{2.4}$$

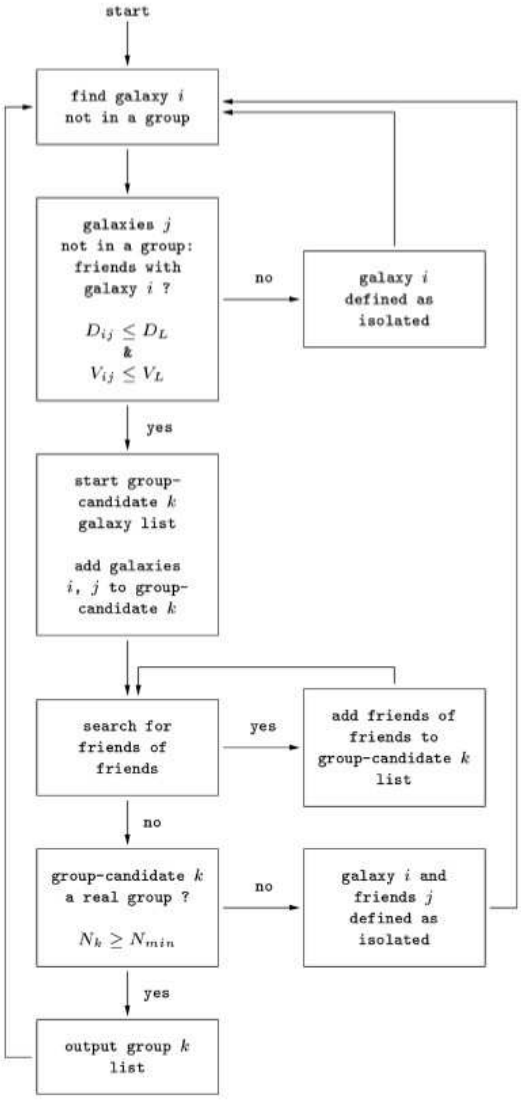

FIGURE 2.2: Modified flow diagram of Huchra & Geller (1982) illustrating the processes undertaken by the FOF algorithm. Image taken from Botzler et al. (2004).

where D_0 and V_0 represent the limits at some arbitrary velocity, R is a selection function that represents the reduction in galaxy number density as a function of radial distance, usually expressed in terms of the luminosity function. A galaxy can only be considered a companion if its separation in both projected and radial space are within these limits. Figure 2.2, taken from Botzler et al. (2004), shows a flow diagram illustrating the processes of the FOF algorithm.

Voronoi tessellations as a cluster finder:

There are several disadvantages associated with both the Hierarchical and FOF cluster-finding methods. Both techniques require the use of pre-fixed parameters (D_{max}, V_{max}, E_0 etc.) in order to function successfully. This generates the need for calibration of these parameters in order to fine-tune the method output into producing the most accurate result. This is an inefficient process, especially as the calibration may involve the usage of mock catalogues drawn from N-body simulations, opening up the possibility of systematic differences across different applications of the same technique (Nolthenius & White 1987; Marinoni et al. 2002). The FOF technique also suffers from insensitivity towards small-scale density differences due to the fixed radius search window deployed to locate associated neighbours. Any structural differences within this boundary will be lost due to this lack of resolution. Therefore additional prior knowledge of the data set is required, again reducing the efficiency of the technique. In addition, both cluster-finding algorithms are time consuming processes, with the FOF method cycling through each galaxy in the data set in a linear fashion before moving through each companion in the same process.

Subsequently another method of cluster detection has been introduced that uses aspects of the well established FOF algorithm with additional input from a mathematical grouping technique called 'Voronoi tessellations' (VT). This method of cluster identification determines the environmental characteristics of galaxies on a much more localised and independent level, reducing the impact of small-scale insensitivity found with the standard cluster-finding methods above. First introduced by Icke & van de Weygaert (1987) and van de Weygaert & Icke (1989) initially as a method for modelling the large-scale structure of the universe, the technique was later adapted into a cluster-finding tool in a number of studies (e.g. Ebeling & Wiedenmann 1993; Kim et al. 2000, 2002; Ramella et al. 2001; Marinoni et al. 2002; van Breukelen et al. 2006a,b; van Breukelen & Clewley 2009; Geach et al. 2011b; Soares-Santos et al. 2011). The technique works by treating each galaxy within the sample as a single point source (or nucleus) on a two-dimensional plane around which a convex polygon is constructed, otherwise known as a 'Voronoi cell'. Each Voronoi cell encloses all co-ordinate space

that lies closer to that cell's nucleus than any other, the area of each cell is therefore a good representation of the local environment of each nucleus - the smaller the cell the greater the density. The construction of the Voronoi cell involves a process of triangulation known as *Delaunay Triangulation* (Okabe et al., 1992) which defines the exact boundaries of each Voronoi cell in the field. The technique begins by selecting a primary nucleus in the field (N_1), around which it will create the first Voronoi cell (V_1). A series of '*Delaunay triangles*' (defined as a triangle whose vertices are represented by different nuclei and whose circumscribing circle contains no other nuclei) are then applied with one vertex of each triangle fixed to N_1. The centre of each circumscribing circle (which does not have to lie within its Delaunay triangle) marks a different vertex of V_1 which are then joined together to complete the Voronoi cell. The method then moves to the next nucleus in the field (N_2) and the process is repeated until all objects in the field are enclosed within a Voronoi cell. An example of Delaunay triangles and Voronoi cells is illustrated in Figure 2.3, taken from Icke & van de Weygaert (1987).

Potential cluster candidates can then be identified through an analysis of the probability that their Voronoi cell density (a reciprocal of the cell area) would be found in a randomly distributed field. Kiang (1966) showed that for a random (Poissonian) distribution of points, the differential distribution of Voronoi cell areas is well represented by

$$dp(\tilde{a}) = \frac{4^4}{\Gamma(4)}\tilde{a}^3 \exp^{-4\tilde{a}}\, d\tilde{a} \quad , \tag{2.5}$$

where $\tilde{a} \equiv a\langle a \rangle$ is the dimensionless Voronoi cell area in units of the average cell area: $\langle a \rangle = \frac{1}{N}\sum_{i=1}^{N} a_i$, the total number of cells is given by N and $\Gamma(x)$ is the Gamma function. Following Ebeling & Wiedenmann (1993), the integration of equation 2.5 gives the cumulative distribution function for the cell area $\tilde{a}$:

$$P(\tilde{a}) = \int_0^{\tilde{a}} dp = 1 - \exp^{-4\tilde{a}}\left(\frac{32\tilde{a}^2}{3} + 8\tilde{a}^2 + 4\tilde{a} + 1\right) \quad , \tag{2.6}$$

the reciprocal of which gives the density of each Voronoi cell

$$P(\tilde{f}) = \exp^{-4/\tilde{f}}\left(\frac{32}{3\tilde{f}^3} + \frac{8}{\tilde{f}^2} + \frac{4}{\tilde{f}} + 1\right) \quad , \tag{2.7}$$

where $\tilde{f}$ is a dimensionless Voronoi cell density given as the inverse of the cell area in units of mean cell density $\tilde{f} = f/\langle f \rangle = \langle a \rangle / a$.

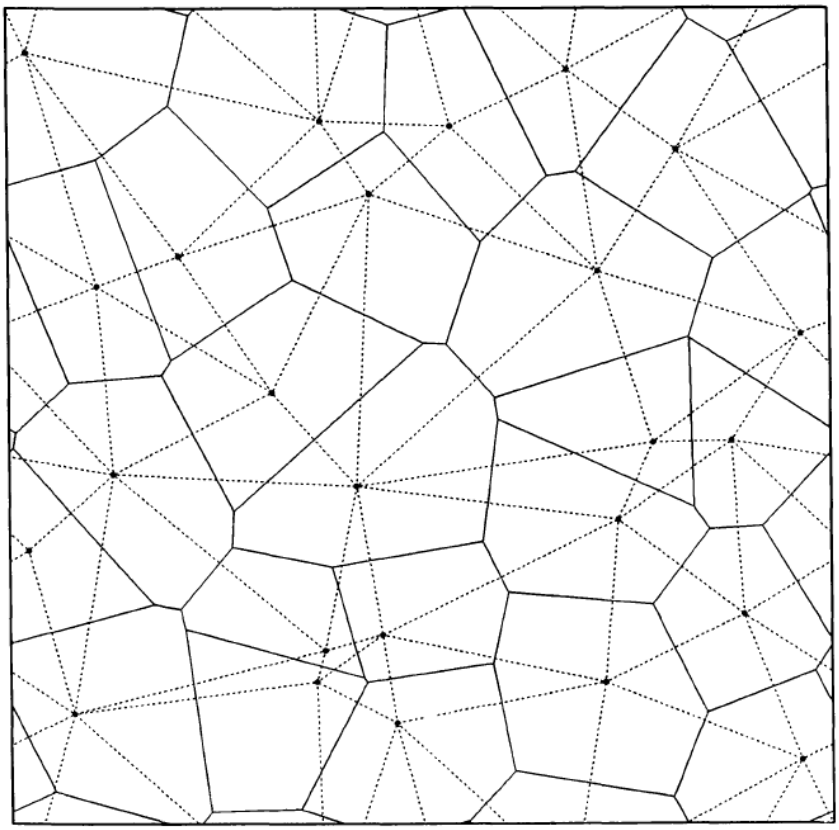

Figure 2.3: An illustration of how the Voronoi cells are constructed. The dashed lines show the Delaunay triangulation joining each nucleus (solid points) together. The solid lines represent the boundary of the Voronoi cells, segregating the triangulation lines. The smaller the Voronoi cell the denser its environment. Image taken from Icke & van de Weygaert (1987).

Galaxies residing in overdense regions (i.e. cluster candidates) can then be identified as any galaxy with a Voronoi cell density ($\tilde{f}$) larger than the some limit ($\tilde{f}_{min}$) above the background density of the field. This background density is estimated in a number of studies (e.g. Ramella et al. 2001; van Breukelen et al. 2006a,b; van Breukelen & Clewley 2009; Geach et al. 2011b) and by again following the method of Ebeling & Wiedenmann (1993), fitting the cumulative distribution function of Kiang (1966) (equation 2.6) to the empirical cumulative distribution of the real data in a region of low density not affected by structures (defined as $\tilde{f} \leq 0.8$). This fit provides an estimate of the background density from which any overdensity can be scaled. Galaxies considered to be in overdense environments ($\tilde{f} > \tilde{f}_{min}$) are selected and added to a separate catalogue where spatially adjoining cells are grouped together, until no further

companions above the density limit are found. If this new group consists of more members than a specific lower limit (n_{lim}) it is considered a real cluster.

This n_{lim} parameter is calculated by assigning a lower limit on the expected number of groups that will be found in the field due to background fluctuations ($N_{\rm exp}$), derived by Ebeling & Wiedenmann (1993) as

$$N_{fluct}(\tilde{f}_{min}, n_{gal}) = n_{bg} N_{fluct}(\tilde{f}_{min}, 0) \exp^{-b(\tilde{f}_{min}) n_{gal}} \quad , \tag{2.8}$$

where n_{gal} is the number of galaxies above the background density level that may belong to a group; N is the number of detected groups or clusters; and n_{bg} is the number of background galaxies expected in the field equal to $A/\langle a \rangle$, where A is the total area of the field. $N_{fluct}(\tilde{f}_{min}, 0)$ is the total number of overdense groups with no extra galaxies above the background density and is shown along with $b(\tilde{f}_{min})$ by Ebeling & Wiedenmann (1993) to obey the following numerical relations:

$$N_{fluct}(\tilde{f}_{min}, 0) = 0.047 \tilde{f}_{min} - 0.04 \tag{2.9}$$

and

$$b(\tilde{f}_{min}) = 0.62 \tilde{f}_{min} - 0.45 \quad . \tag{2.10}$$

They show that by integrating equation 2.8 between n_{lim} and ∞ gives the expected number of galaxy groups ($N_{\rm exp}$) caused by background fluctuations with $n_{gal} < n_{lim}$ is given by

$$N_{\rm exp}(\tilde{f}_{min}, n_{gal} > n_{lim}) = n_{bg} \frac{N_{fluct}(\tilde{f}_{min}, 0)}{b(\tilde{f}_{min})} \exp^{-b(\tilde{f}_{min}) n_{lim}} \quad . \tag{2.11}$$

Therefore the limiting number of galaxies that defines whether a group is accepted can be expressed as

$$n_{lim} = \frac{-1}{b(\tilde{f}_{min})} ln \left[\frac{b(\tilde{f}_{min}) N_{\rm exp}}{N_{fluct}(\tilde{f}_{min}, 0) n_{bg}} \right] \quad . \tag{2.12}$$

The usage of VT as a cluster-finding algorithm has a number of advantages over other cluster-finding techniques. Principally, the use of Voronoi cells in defining the environment of a galaxy increases the sensitivity of the technique on small scales, compared to the standard FOF method, as individual galaxy environments are probed. Therefore the VT is an unbiased approach in environmental characterisation that does

not rely upon a specific search radius or linking length to define the boundary of a cluster. The technique is therefore not restricted to finding overdensities associated with fully virialized clusters and can be applied to locate finer structure within an overdensity. The only limitation of the VT, in comparison to aperture methods, involves the loss of resolution surrounding the outermost edge of a galaxy sample. As explained in Section 2.2.1, at this boundary the triangulation fails to construct new cells and environmental detail may be lost, although any bias associated with this can be accounted for.

2.1.2 Local Density Estimators

One of the main drawbacks of using cluster-finding algorithms in galaxy environmental characterisation is that only a relatively small fraction of galaxies from a particular sample are likely to be associated with groups or clusters. This is due to the aforementioned ways in which these methods characterise groups (through a linking-length or limit on how many galaxy members define a cluster), thus small groups of galaxies with only one or two neighbours are often omitted from the data-set by these measures. Therefore in recent years the preference in extra-galactic environmental studies has been to acquire localised environmental information via direct measures of environmental density. This therefore removes the necessity to detect multiple objects within pre-set radii, as required with cluster-finding methods. Focusing on the local or even individual environments of galaxies within a field allows for improved accuracy with more detailed higher-resolution environmental studies.

Nth-Nearest Neighbour:

The analysis of galaxy environmental density has predominantly relied on a form of density measure that estimates the local density of galaxies using the projected Nth-nearest neighbour metric (Σ_N) which measures the environmental density in terms of the number of galaxies within a circular region defined by the radius to the Nth-nearest galaxy, measured in galaxies per Mpc^2. The popularity of this technique is evident by

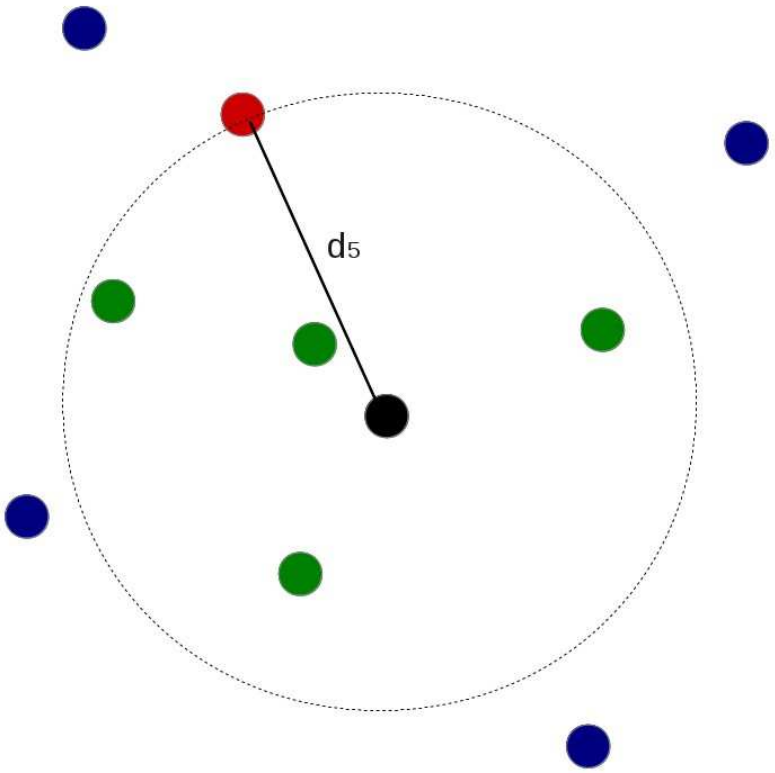

FIGURE 2.4: Example of the nearest neighbour technique where the density of the primary object (*black*) is established by finding its 5th-nearest neighbour (*red*) and measuring its projected separation (d_5). Objects outside of this radius (*blue*) are not considered associated with the primary object in this method.

the number of studies in which it is used to obtain localised density information (e.g. Dressler 1980; Dressler et al. 1997; Hashimoto et al. 1998; Domínguez et al. 2001; Lewis et al. 2002; Gómez et al. 2003; Goto et al. 2003; Miller et al. 2003; Balogh et al. 2004; Cooper et al. 2005; Ball et al. 2008; O'Mill et al. 2008; Bamford et al. 2009; Silverman et al. 2009a; Cucciati et al. 2010; Lee et al. 2010; Hernández-Fernández et al. 2012; Wijesinghe et al. 2012).

The nearest neighbour (NN) approach defines the environmental density of an object as a surface density in relation to other neighbouring galaxies that are within an appropriate velocity interval, representative of the velocity dispersion of the group or cluster within which the galaxy resides. The NN metric is therefore given by

$$\Sigma_N = \frac{N}{\pi d_N^2} \quad , \tag{2.13}$$

where d_N is the projected separation to the Nth-nearest object defined as

$$d_N = [2D_{c,1}D_{c,2}(1 - cos\theta)]^{1/2} \ , \tag{2.14}$$

where $D_{c,1}$ and $D_{c,2}$ are the co-moving distances (Mpc) to both the primary and Nth nearest objects from the observer and θ is the angular separation. The specific value of N can be set to any value, usually between the range $2 - 10$, however a limiting factor is the richness of structure within the field. If N is set to a higher value than the average richness of groups/clusters that make up the overdensities within the field, then the technique may erroneously include objects from surrounding underdense regions or even neighbouring overdensities, thus making the incorrect association that these objects form the same structure. This would lead to a flattening of the returned density distribution, resulting in the inability to detect small scale differences in density and ultimately the loss of detailed structure from the field, as described in Cooper et al. (2005). Figure 2.4 illustrates an example of the technique where N is set to 5.

This reliance on a user-defined grouping parameter (N) is reminiscent of the limitations of the cluster finding methods previously mentioned, the selection of which could significantly change the resolution of the technique and hence the output of the density profile. For example, even if $N = 1$, and thus the density is measured with respect to the very nearest neighbour, the area defined for the primary object will still be limited to a circular area. Thus a fundamental limit to the resolution on the smallest of scales remains. Therefore a technique of density measurement is required that can calculate an environmental density of the primary object on these smallest of scales without losing this resolution. From the methodology of the Voronoi tessellations cluster-finding algorithm (Chapter 2.1.1) it is evident that one does not need to necessarily categorise each galaxy into a group or cluster, but can instead simply measure the surface density of that galaxy directly from the properties of its Voronoi cell. This direct density measure forms the basis of the work in this chapter, as I establish a structured algorithm that can accurately determine the environmental density of a galaxy using Voronoi tessellations, normalised across any designated redshift range.

2.2 Voronoi Tessellation Density Measure

This environmental density algorithm was created for the analysis described throughout this thesis, where I have compared numerous catalogues in order to establish if there is any significant relation between their densities. In the following sections of this chapter I outline the processes undertaken within this algorithm, where necessary I use appropriate data sets for illustrative purposes.

2.2.1 Redshift Sampling

The Voronoi tessellation density measure (hereafter VT algorithm) requires that the galaxies onto which it will apply Delaunay triangulation reside in a two-dimensional plane. Therefore in order to obtain the most accurate density measurement for each galaxy in a three-dimensional field, each redshift must first be determined. This is to avoid any projection effects that may otherwise contaminate the density calculation, such as background galaxies being erroneously associated with foreground objects.

For the following description of the VT algorithm I use precise redshift data obtained from a simulated catalogue generated via a large N-body simulation, the *Millennium Simulation* (Springel et al., 2005a). This data set consists of $\sim 130,000$ simulated galaxies across a redshift range of $0 < z \leq 0.5$ and is described in detail in Chapter 3.3 of this work where it is used extensively. With precise redshift values known for each object the field can be divided into appropriate redshift slices onto which the VT algorithm can then be applied. This ensures that only objects that reside within the same redshift slice can be associated with each other environmentally (i.e. have any influence on each others density values). The size of each slice is limited by the fact that, if too wide, the very projection effects I am trying to resolve may come back into effect and if too small, a region that is in fact overdense in terms of the rest of the field may go undetected by the VT algorithm as it may be spread across multiple slices. For example, the typical velocity dispersion in a gravitationally bound cluster of galaxies is within the region of a few hundred kilometres per second (e.g. Haynes et al. 1984;

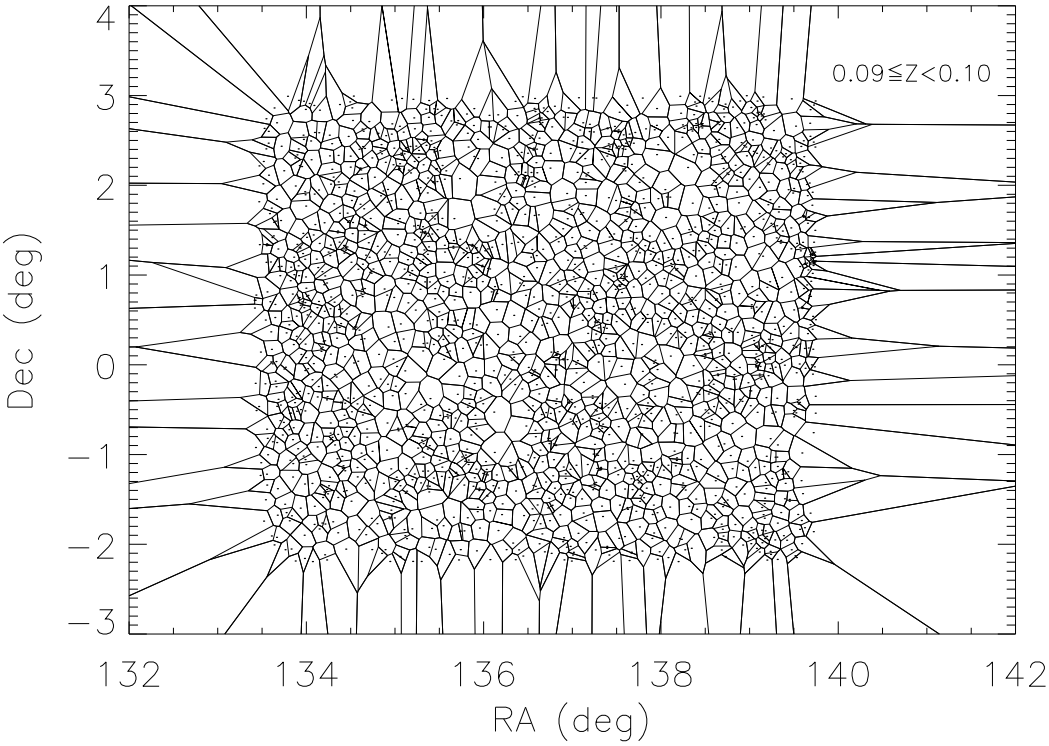

Figure 2.5: An example of one VT plot produced by the VT algorithm, showing a subset of objects placed within the redshift slice $0.09 \leq z < 0.10$. The VT cells illustrate where the densest regions lie. As the algorithm requires more than one object within a specific region to accurately construct a cell boundary, the lack of neighbours around the edge of the image results in overly large cell areas. These outer cells are removed from the rest of the analysis.

Martini et al. 2007; Miley & De Breuck 2008), from

$$\Delta z = \frac{\Delta v(1+z)}{c} \ , \tag{2.15}$$

this equates to a spread in redshift of $\Delta z \sim 10^{-3}$ at $z \sim 1$. Using precise redshifts from the *Millennium Simulation*, to accurately determine the densities of the individual objects that make up this cluster, the redshift slicing must be wider than this redshift spread. For each object within each redshift slice, its Voronoi cell area (x_i) is calculated. Taking an inverse of this area gives a value for the environmental density (ρ_i) for that object:

$$\rho_i = \frac{1}{x_i} \ . \tag{2.16}$$

Figure 2.5 shows an example of one such VT slice (containing a small subset of

the data for illustrative purposes) and it is immediately clear that objects towards the outside of the field have overly large Voronoi cell areas. This 'edge effect' is the result of the VT algorithm not finding any objects outside of this boundary and consequently being unable to triangulate in these areas. In order to prevent this edge effect altering the mean density result, a cut is made around the outside of the field to remove the outermost objects (and their overly large cell areas) from the data set. To determine the position of this cut it is necessary to investigate how far the edge effect penetrates into the field. This is achieved by first applying the VT algorithm to the entire field after which the RA and Dec. positions of each object are plotted separately against a value that represents the normalised mean area, the significance (S), which accounts for the peak in the number density and changes in uniformity across the field. Cuts are then applied in both RA and Dec. parameters reducing the size of the field until all large values of S (i.e. those with significantly larger cell areas than the field mean) are removed from the data set. This is repeated for each new data set onto which the algorithm will be applied.

2.2.2 Density Normalisation

With a value for the environmental density (x_i) calculated for each object in the field it is possible to examine the 3D density distribution across the entire redshift range. Due to the combination of the flux-density limit of the observations along with the evolution of the luminosity function, the field will likely show a peak in the number of detections at a particular redshift which will correspond to the peak in the density distribution. This peak in the detection rate would naturally lead to an increase in the mean density being returned by the VT algorithm due to the bias associated with having more objects in the sample. Therefore two Voronoi cells from two different redshift slices cannot be accurately compared in terms of their environment. If these two slices have different numbers of detections within them, the cell sizes returned by the VT algorithm will be biased towards the denser population. This is such that a redshift slice with a larger number of detections will be considered to have a larger mean density than a slice with fewer objects. In order to counteract this bias it is necessary to

normalise the Voronoi cell areas across the entire redshift range to produce a normalised environmental density for each object.

This is achieved by first summing all the Voronoi cell areas (x_i) within one redshift slice and then dividing by the number of detections in that slice (N) to give the mean Voronoi cell size of the slice ($\bar{x}_{slice}$). Calculating the standard deviation (σ) of the slice given by

$$\sigma = \sqrt{\frac{\sum(x_i - \bar{x}_{slice})^2}{N}} \ , \tag{2.17}$$

where x_i is in each case the individual Voronoi cell area of each object calculated by the VT algorithm. This is repeated for every redshift slice throughout the entire field. With the VT algorithm I can now list each object in the field in terms of not only its relation to the mean cell area of its slice ($\bar{x}_{slice}$), but also in terms of the standard deviation (σ), where a larger σ represents a more 'non-uniform' distribution of objects and a smaller σ represents a more evenly spread 'uniform' distribution. By taking the difference between the size of each Voronoi cell (x_i) and its associated overall slice mean ($\bar{x}_{slice}$) and then dividing by the standard deviation (σ) of that slice, I can represent every object in the field as a fraction of σ given by

$$S_i = \frac{\bar{x}_{slice} - x_i}{\sigma} \ , \tag{2.18}$$

where S_i is the normalised environmental density such that $S_i > 0$ signifies an overdensity in terms of the entire redshift range, while $S_i < 0$ represents an underdensity.

However, while this normalisation takes differences in the number density between redshift slices into account, this parameter does not account for differences in uniformity between slices. This is such that an 'underdense' region in one slice (i.e. where $S_i < 0$) may actually be more dense than an 'overdensity' in another slice (i.e. where $S_i > 0$). For example; consider a clustered galaxy (A) with an individual VT cell density value (d_A) within a redshift slice (1), where the mean density of the slice is ($\bar{d}_1$). Now assume a second galaxy (B) with an individual density (d_B) in a different redshift slice (2) where the field is fairly uniform in density with a mean ($\bar{d}_2$). Galaxies A and B will have normalised environmental density values (S_A) and (S_B) as calculated from equation 2.18 above. Assume A resides in a clustered region within its slice, whereas

B does not (thus $S_A > d_A$ and $S_B \sim d_B$). The initial density normalisation (equation 2.18) will conclude that $S_A > S_B$ (i.e. A is more overdense than B). However, if for example $d_A = d_B$ due to the uniform field being particularly densely populated, it is not correct to simply state that A is more overdense than B based only on the initial normalisation density values.

Therefore an addition is required to the normalisation that will take this effect into account by comparing the individual densities of each galaxy, not to the mean density of the slice it resides in ($\bar{x}_{slice}$), but to the mean density of a virtually constructed, randomly distributed field ($\bar{x}_R$) of matching number density. The algorithm creates this separate 'random' field by applying random RA and Dec. values to each object within the original field region, in each redshift slice. This ensures that the random field contains the same number of objects per redshift slice as that of the real field in order to maintain comparison accuracy between densities. Once this random field is created the algorithm again applies the Voronoi tessellations to the field calculating values for the mean cell area $\bar{x}_R$ and standard deviation σ_R of each random redshift slice. Substituting these random field values back into equation 2.19 such that

$$S_c = \frac{\bar{x}_R - x_i}{\sigma_R} \ , \tag{2.19}$$

where x_i remains the measured VT cell area for each object from the real field, this gives the normalised density value in comparison to a random distribution (S_c) for each object. This S_c value parametrises how the real field normalised environmental density value (S_i) compares to a completely random distribution, in terms of the standard deviation σ_R of that random distribution, and thus accounts for differences in uniformity of the field between slices. Therefore, this final normalisation allows for the direct comparison of two objects from separate redshift slices that may have different population densities and different levels of uniformity.

2.3 Nearest-Neighbour Density Comparison

Using Voronoi tessellations to probe galactic environments on individual galaxy scales is a new approach to the study of galaxy density. It is therefore important to test this VT

algorithm against the more well established Nth-nearest neighbour density measure, described in Chapter 2.1.2. This comparison is necessary to establish whether there are any significant differences between the results obtained from both techniques, both in terms of how overall correlations in density are affected as well as a comparison of the techniques ability to probe detailed structure.

For this comparison the 5th-nearest neighbour metric ($N = 5$) is selected in line with the majority of recent studies that have used the NN technique to examine local galaxy density (e.g. O'Mill et al. 2008; Cucciati et al. 2010; Wijesinghe et al. 2012; Hernández-Fernández et al. 2012). A NN algorithm is created that follows exactly the same processes as the VT algorithm as described in Chapter 2.2, with the NN algorithm being applied to each redshift slice, once more normalising the field to account for differences in number density and uniformity across the redshift range. The only difference between the methods comes as a result of the fact that, unlike a VT cell, the Σ_N parameter represents larger densities with larger values and thus, to reflect this, the sign of equation 2.19 is reversed such that positive values of S_c once more represent a normalised overdensity

$$S_c = \frac{x_i - \bar{x}_{slice}}{\sigma} \quad . \tag{2.20}$$

As with the VT algorithm, the NN is also liable to suffer from edge effects. If the primary object is situated near to the edge of the field such that its 5th-nearest neighbour, or objects closer than this 5th-nearest neighbour are located outside of the observed field, the NN method will overlook these objects incorrectly calculating Σ_5 via neighbouring galaxies from within the field. This would lead to an underestimation of the density of the primary object. Consequently the same boundary cuts applied within the VT density calculation are maintained both to prevent such edge effects and to maintain comparison accuracy between the two methods.

Both the Voronoi tessellation and Nth-nearest neighbour techniques were applied independently to the sample field, with both algorithms being applied to each redshift slice of width $\Delta z = 0.01$. Following normalisation of the field to account for differences in number density and uniformity across the redshift range, each algorithm produced normalised comparison densities (S_c) for each object. Figure 2.6 shows the resultant

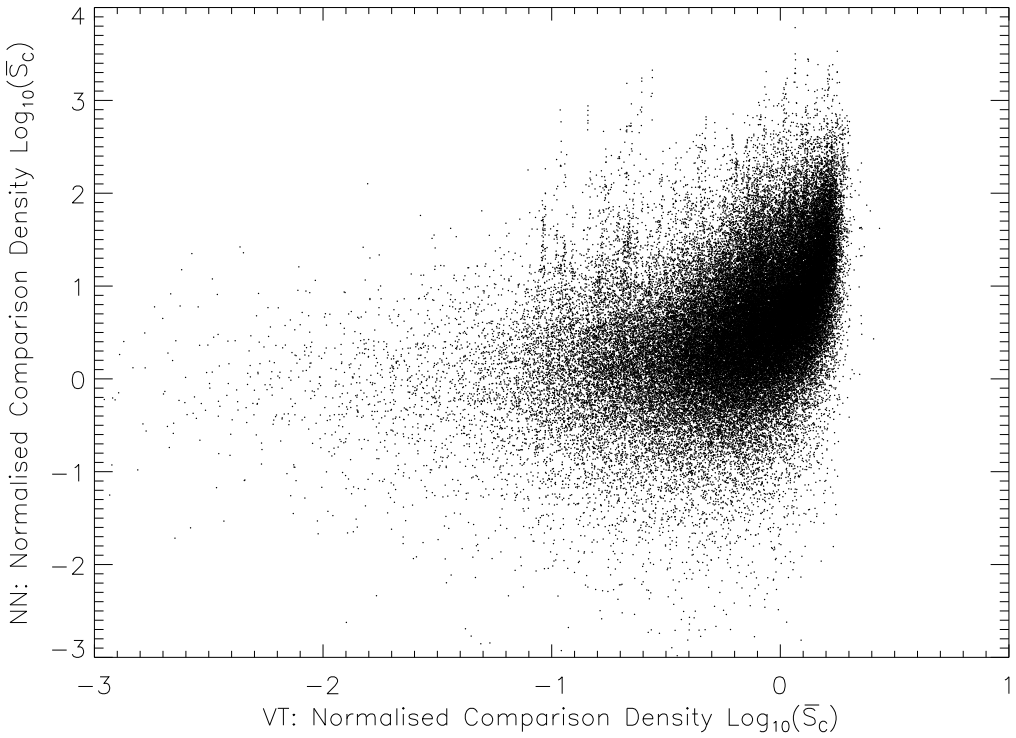

FIGURE 2.6: Plot of the relationship between the normalised densities returned by the VT and NN techniques based on precise redshift values. The Spearman's Rank Correlation Coefficient (r_s) between both density distributions returns a value of $r_s = 0.749$ at a $> 5\sigma$ level, indicating a good correlation.

relationship between these S_c values from both techniques. Calculating the Spearman's Rank Correlation Coefficient (r_s) between both density distributions returned a value of $r_s = 0.749$ at $> 5\sigma$ significance indicating a good correlation, although it is clear from the plot that the overall spread in data is much greater for the output of the NN method in comparison to the VT.

2.3.1 Monte-Carlo Realisations

Due to spectroscopic inefficiencies and observational constraints associated with large-scale surveys, precise redshift information is rarely known for the majority of objects within any given observation, thus the three-dimensional distribution of galaxies is difficult to measure precisely. Therefore, for the VT algorithm to be applicable to real observations and to conduct a more realistic technique comparison, it was necessary

to adjust the VT algorithm in order to incorporate the redshift errors associated with real observations, in particular to enable the use of photometric redshifts. For this to be achieved, the VT algorithm was modified to utilise the full redshift probability distribution function (z-PDF) of each galaxy in order to establish as accurately as possible the galaxy's position relative to all other galaxies in three-dimensional space. The shape of a galaxy's z-PDF is dependent on whether its redshift has been measured spectroscopically or estimated photometrically. The fundamental difference being that photometrically estimated redshifts have uncertainties of the order of $\sigma \sim 0.1$, whereas spectroscopically measured galaxies have much smaller errors ($\sigma \sim 0.001$) and narrower z-PDFs. The full z-PDF of each photometrically determined galaxy can be derived from

$$P(x) = \frac{1}{\sigma\sqrt{2\pi}} \exp\left[-\frac{1}{2\sigma^2}(z-\mu)^2\right] \quad , \tag{2.21}$$

where σ is the calculated Gaussian photometric redshift uncertainty, z is each step through the redshift range (e.g. z=0.01 from Chapter 2.2.1) and μ is the 'peak' probability of the redshift, the best-fit value returned by the photometric redshift estimator. Substituting the relevant values for each galaxy into equation 2.21 produces the complete z-PDF for that galaxy, although it is important to note that this does not allow for catastrophic outliers. Different galaxies will also inevitably have different peak photometric redshifts and 1σ errors associated with them, producing a wide variety of z-PDFs that are unlikely to be purely Gaussian, although the effect is likely to be small. As the exact value of a spectroscopic redshift is more precisely known, it has a much smaller error associated with its z-PDF than the average photometric redshift error, and as such, provides a much more reliable redshift. As a consequence of this, where available, spectroscopic redshifts were used by the VT algorithm in preference of any photometric redshift for all the work in this thesis.

The VT algorithm then works to produce an array of redshifts that map (based on the size and shape of the z-PDF) the galaxy's overall statistical redshift distribution. To obtain this redshift array I used 'Monte-Carlo (MC) Realisations' to randomly sample each z-PDF a designated number of times. With each sample the object was placed within a virtual cube in terms of its RA, Dec. and MC-sampled redshift, as used by

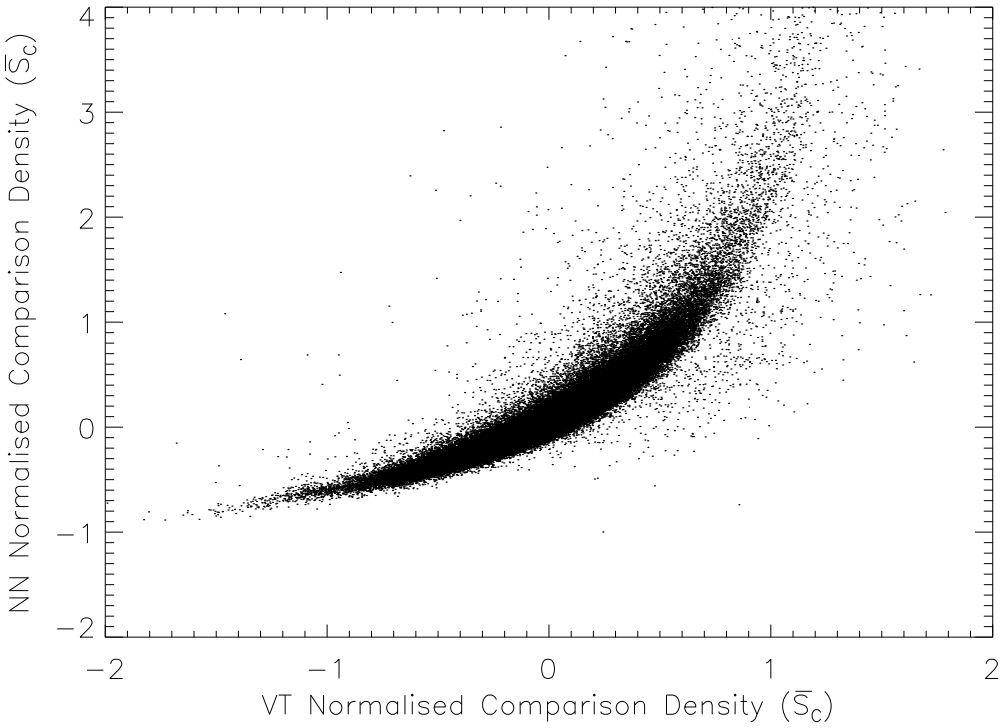

Figure 2.7: Plot of the relationship between the normalised densities returned by the VT and NN techniques from 1000 Monte-Carlo samples of the z-PDF. The Spearman's Rank Correlation Coefficient (r_s) between both density distributions returns a value of $r_s = 0.960$ at a $> 5\sigma$ level, indicating a strong correlation.

van Breukelen & Clewley (2009). The shape of the z-PDF has a significant effect on the position of the object within its MC cubes between different samples. A sharp narrow peak results in the object being placed at a similar redshift in the majority of the MC realisations, a wider z-PDF results in a more even spread of redshifts. The number of times the z-PDF is sampled is a compromise between computation-time and the minimum sampling accuracy that is deemed necessary. Due to the statistical nature of probability distribution functions, a larger number of samples were required to achieve sampling out to the edges of the distribution. Consequently, the more times a z-PDF were sampled the more accurate the overall density calculation became, while taking longer to process computationally. This value could be adjusted for each application of the algorithm, however throughout this work, in order to attain a highly accurate sampling of the photometric redshift as possible, I sampled each z-PDF 1000 times

generating 1000 MC cubes for each galaxy in the field. The algorithm then grouped together each MC cube in terms of which z-PDF sample it came from; stacking together all of the cubes generated by the first z-PDF sample, the second sample, third sample etc., producing 1000 3D MC realisations of the entire field.

Each individual galaxy appears once in each MC cube. Applying the same redshift sampling, as described in Section 2.2.1, to each of these cubes, again grouped the galaxies into $\Delta z \sim 0.01$ slices. Depending on the shape of its z-PDF, each galaxy would appear in different redshift slices within each 3D cube, with a higher frequency around its 'peak' redshift value. Again, for each object in each MC cube its Voronoi cell area (x_i) were calculated, the mean of which ($\bar{x_i}$) gave the overall mean area calculated for that object across all of the MC realisations. Repeating the density normalisation from Chapter 2.2.2, across all 1000 MC realisations allowed for a mean environmental density value ($\bar{S}_c$) to be calculated for each object.

Using this value I could then re-apply the comparison between the Voronoi tessellation and 5th-nearest neighbour techniques to asses whether the incorporation of the full z-PDF had any impact on the comparison. Figure 2.7 shows the resultant relationship between the $\bar{S}_c$ output values from both techniques. It is clear that there is a tighter correlation between both VT and NN density outputs, with a Spearman Rank of $rs = 0.960$ at a $> 5\sigma$ level, indicating a strong (although non-linear) correlation. By utilising the full z-PDF of each galaxy and MC sampling this 1000 times, the redshift position of each galaxy is allowed to drift in relation to other galaxies between different samples. Therefore, any extreme over- or under-densities are reduced in comparison to when precise redshifts are used, hence scatter on the density output decreases. This sampling also has an impact on the correlation between the two techniques as each galaxy's S_c value is, in essence, a measure of its mean cell area across the redshift slice in which it resides. With increased sampling, the mean of this value ($\bar{S}_c$) will approach 0, thus the distributions become progressively more normalised with increasing samples and hence, after 1000 samples, the correlation improves. It is clear that the NN method has a greater dynamic range in the densest environments where the VT method has a limited range. Conversely, the VT method appears more suited to

distinguishing between less dense environments where the comparative range of the NN method is small. Further investigation of the pros and cons of different density measures is beyond the scope of this thesis, however such work has been conducted by Muldrew et al. (2012) who find that the NN technique is very poorly correlated with the respective dark-matter-halo mass, although the NN technique is able to describe the internal densities of high-mass haloes.

Figure 2.8 shows the normalised comparison densities ($\bar{S}_c$) returned by each technique, plotted according to RA and Dec. positions and coloured according to density. For clarity, the VT and NN algorithms are applied to an alternative data set, taken from Chapter 3, that incorporates a larger area yet same number of objects and redshift range as the previously mentioned data. Once more, further details of this data set are not necessary for this comparison and the data is described in detail in Chapter 3, where it is used extensively. Both plots clearly show that each density measure has successfully reproduced the same general density structure across the field, with the most extreme over- and under-densities being located by both methods. However, there are some slight difference between the methods indicating that the intensity of the local density in specific regions differs between each method. The NN density distribution in Figure 2.8 (*Bottom*), in this case selecting the 5th-nearest neighbour, contains larger regions of peak overdensities with less defined regions of intermediate density in comparison with the structure distribution from the VT method (*Top*). This is such that, at this value of N, the NN technique appears to suffer from a reduced resolution around the edges of the most dense regions. As previously discussed, by using an Nth-nearest neighbour to establish a density within a circle (defined by its radius to that neighbour), the true edge of the density profile may be lost. As the VT method calculates density on individual galaxy scales, it does not suffer from this problem. In effect, the VT acts as a nearest (1st) neighbour density measure and subsequently has N times the resolution of the NN method, providing greater density detail on small scales. It is therefore clear that the initial value selected for N will determine the accuracy of the NN technique in various environments. Where the value of N remains below the number of associated satellites, the measured density will increase with increasing values

of N. Subsequently, in the comparison with the VT method, the peak overdensities returned from the 5th-nearest neighbour would be reduced if, for example, only the 3rd-nearest neighbour were used. With a larger value of N, the NN method will lose resolution and become more susceptible to the projected separations between distinct overdense regions, influencing the density result.

To examine this further, I repeated the NN analysis using the 2nd- and then 1st-nearest neighbours to calculate the density of the field. The colour-density plots from these analyses are displayed in Figure 2.9. With a reduced neighbour selection, the 2nd-nearest neighbour (*Top*) shows that the same maximum over- and under-densities are found, however there is a clear loss of dynamic range within the density distribution. The 1st-nearest neighbour (*Bottom*) shows an even greater loss of detail, with the dynamic range reducing even further. Considering that the structure distribution returned by the NN method is closely represented by the VT method when $N = 5$, in addition to the fact that the majority of previous galaxy environment studies have adopted the NN method with this N value (e.g. O'Mill et al. 2008; Cucciati et al. 2010; Wijesinghe et al. 2012; Hernández-Fernández et al. 2012), I selected $N = 5$ as the standard with which to compare the VT method throughout this thesis. Further, from Section 2.2, it is evident that with the VT method one does not need to necessarily categorise each galaxy into a group or cluster, but can instead simply measure the surface density of that galaxy directly from the properties of its Voronoi cell. Consequently the VT method is fully adaptable to changes in uniformity of the field and calculates densities on individual galaxy scales.

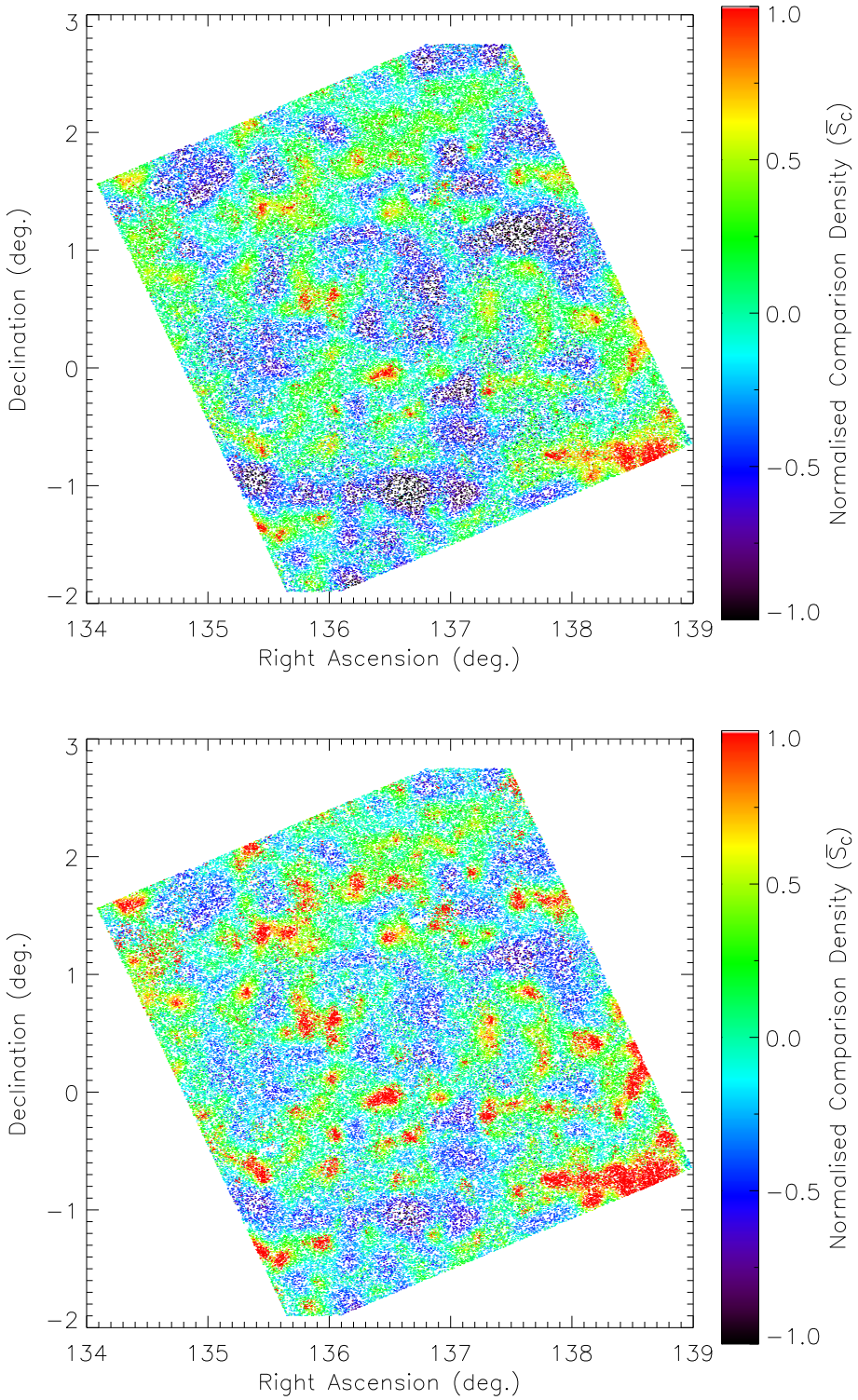

FIGURE 2.8: *Top*: Colour co-ordinated density plot of the VT method output showing the field with all redshift slices compiled to show the whole density distribution, where red and orange colours represent the most overdense regions (positive $\bar{S}_c$ values) and blue and purple represents the most underdense regions (negative $\bar{S}_c$ values). *Bottom*: 5th-nearest neighbour output colour co-ordinated density plot of the field. The plot confirms that the VT and NN methods reproduce the same density structure across the field. Both plots are based on 1000 MC samples of the full z-PDF.

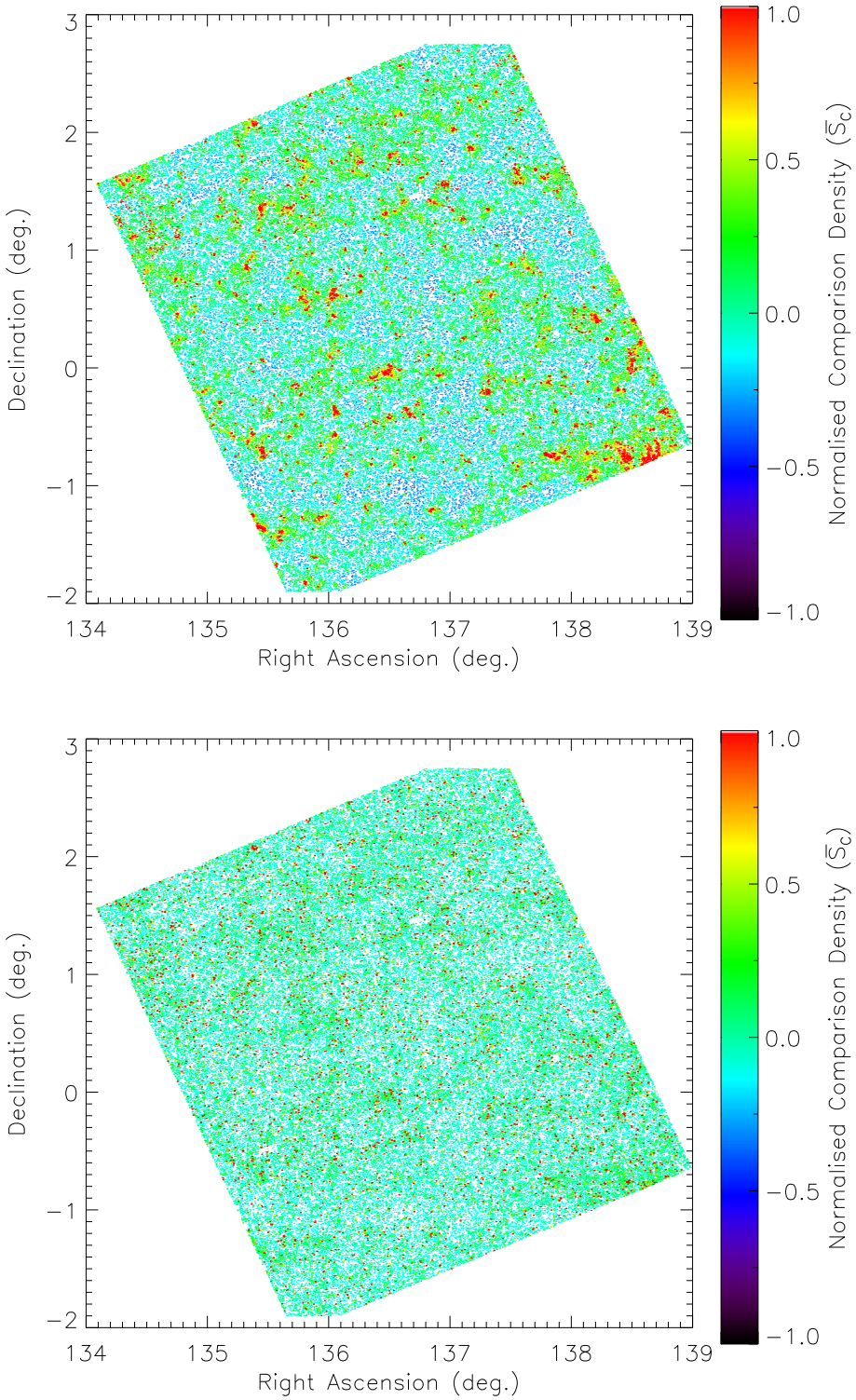

Figure 2.9: *Top*: Colour co-ordinated density plot from the 2nd-nearest neighbour method. Again, red colours represent the most overdense regions (positive $\bar{S}_c$ values) and blue and purple represents the most underdense regions (negative $\bar{S}_c$ values). *Bottom*: The colour-density output from the 1st-nearest neighbour method. These plots, along with Figure 2.8, confirm that the resolution of the NN method is dependent on the value of N.

2.3.2 Comparison of Halo Mass From Millennium Data

Due to the observed mass-density relation associated with clusters of galaxies, as discussed in Chapter 1, there is an expected positive correlation between the environmental density of a galaxy population and the masses of its constituent galaxies (e.g. Kauffmann et al. 2004; Li et al. 2006; Deng et al. 2011; Ideue et al. 2012). Therefore another important test of the accuracy of the VT and NN algorithms is to examine how well they reproduce this correlation in comparison with each other. For this comparison to be undertaken, a value for the virial background halo mass (M_{vir}) of each galaxy is obtained from the Millennium sample data set.

Figure 2.10 shows all objects from the simulated catalogue, with the normalised density parameter $\bar{S}_c$, from both the VT (*top*) and NN (*bottom*) methods, plotted against the M_{vir} values. In both plots the expected correlation between mass and density, such that higher mass galaxies are found in the highest density regions, is identified via the application of the Spearman test producing values of $r_s = 0.273$ and $r_s = 0.254$ at a $> 5\sigma$ level for the VT and NN methods respectively. There is a much higher level of scatter visible in the density measure of the NN technique, highlighting the aforementioned low-resolution of the technique when dealing with the densest structure. In comparison, the VT method produces a more tightly correlated distribution that shows little scatter associated with the density measure.

This result further supports the usage of the Voronoi tessellations as a reliable alternative to the more commonly used Nth-nearest neighbour technique in determining environmental density. In the following chapters, I employ the VT algorithm as my primary tool for investigating environmental densities in a number of data sets.

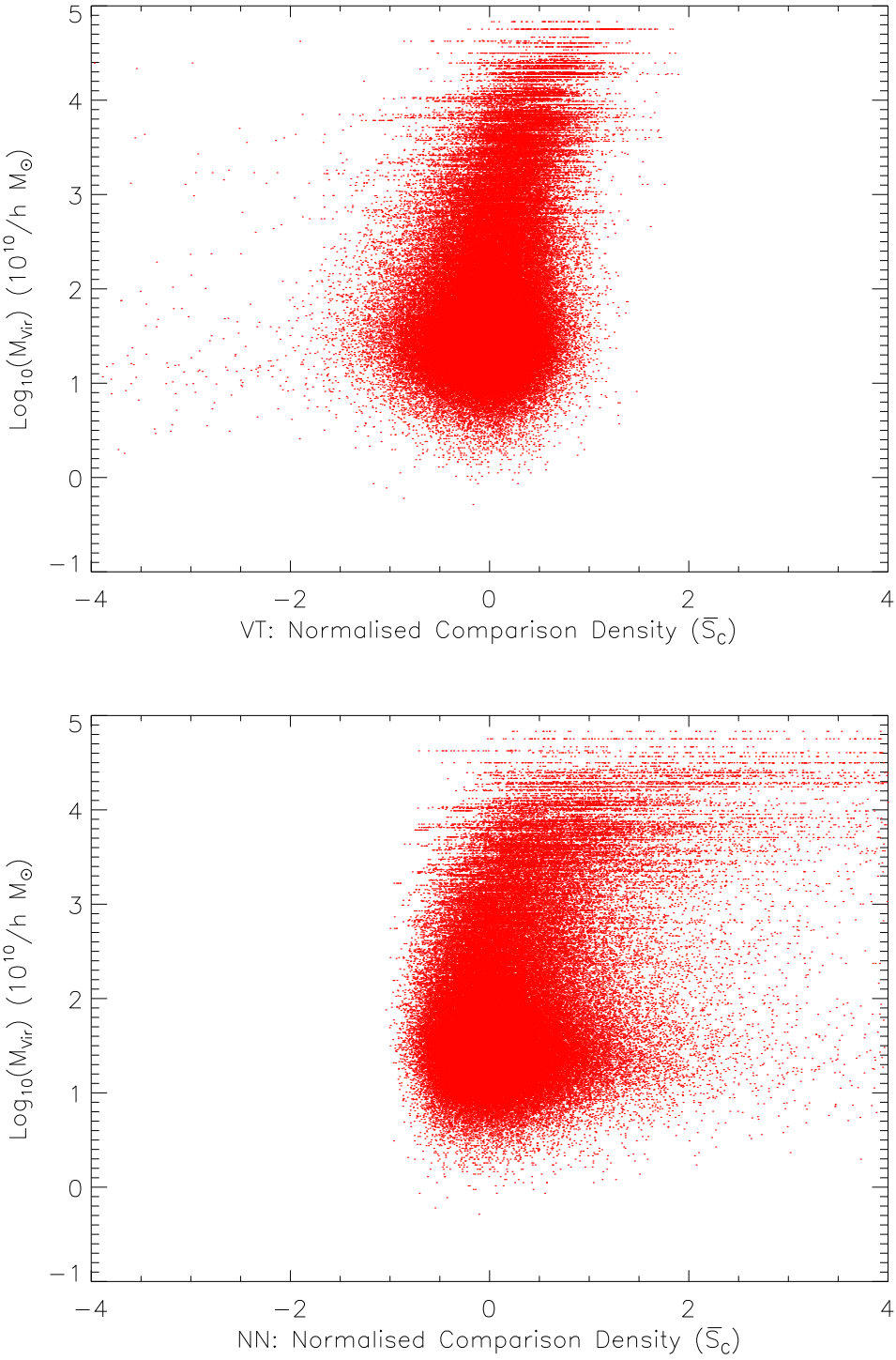

Figure 2.10: The normalised density ($\bar{S}_c$) against virial mass of the dark-matter halo (M_{vir}) of each galaxy in the simulated field. *Top*: The output returned by the VT technique with little scatter showing the expected mass-density correlation in the galaxy population with a Spearman test returning the correlation coefficient of $r_s = 0.273$ at a $> 5\sigma$ level. *Bottom*: The output from the NN technique across the same field, again showing the mass-density correlation with a Spearman test returning $r_s = 0.254$ at a $> 5\sigma$ level. There is a much greater level of scatter in the density measure associated with the lower resolution of the NN technique in comparison to VT.

3

Environmental Density of Far-Infrared Bright Galaxies at z $\leq$ 0.5

The work described within this chapter is an expansion of that presented in Burton et al. (2013). Here I describe my application of the Voronoi tessellation environmental density algorithm, introduced in Chapter 2, to investigate the SFR-density relationship discussed in Chapter 1 out to $z \sim 0.5$. With the addition of synthetic light cones, generated from semi-analytic models, I also investigate whether the same correlations between star formation and environmental density are found. I then use these results to establish which processes may or may not be the primary mechanism driving the observed environmental trends.

3.1 The H-ATLAS SDP Field

3.1.1 Far-Infrared Data

For this analysis I use far-infrared data from the science demonstration phase of H-ATLAS (Rigby et al. 2011). H-ATLAS provides data across a wavelength range of 100-500 μm using the Photo-detector Array Camera and Spectrometer (PACS; Poglitsch et al. 2010) at 100 and 160 μm; and the Spectral and Photometric Imaging REceiver (SPIRE; Griffin et al. 2010) at 250, 350 and 500μm. The H-ATLAS observations consist of two scans in parallel mode reaching 5σ point source sensitivities of 132, 126, 32, 36 and 45 mJy in the 100, 160, 250, 350, and 500μm channels, respectively, with beam sizes of approximately 9, 13, 18, 25 and 35 arcsec in the same five bands. The SPIRE and PACS map-making procedures are described by Pascale et al. (2011) and Ibar et al. (2010) respectively, while the catalogues are described by Rigby et al. (2011). Smith et al. (2011) used a likelihood ratio method to associate optical counterparts with the H-ATLAS galaxies down to a limiting magnitude of $r = 22.4$ within a 10 arcsec radius. This resulted in optical counterparts for $2,423$ objects from the H-ATLAS 250μm catalogue, each with a reliability $R \geq 0.8$ which ensures that not only the contamination rate is low but also that only one $r-$band source dominates the far-infrared emission. While the entire H-ATLAS survey aims to compile a catalogue of $\sim 10^5$ extra-galactic far-infrared sources out to z $\sim$ 3, the SDP field covers $\sim$ 3 per cent of this, over an area of $\sim$ 4.0 deg $\times$ 3.6 deg centred on ($09^{\rm h}05^{\rm m}$, $+0°30'$).

3.1.2 Optical and Near-Infrared Data

I use spectroscopic redshifts from both the SDSS and the GAMA survey Data Release One (DR1). Spectroscopic redshifts are provided for magnitude limits of $r < 19.4$, $K < 17.6$ and $z < 18.2$ in the GAMA 9hr (G09) field which includes the H-ATLAS SDP. This is combined with photometric redshifts derived from the combination of optical (*ugriz*) SDSS and near-infrared (*YJHK*) UKIDSS-LAS imaging data as detailed in Smith et al. (2011). This complete optical–near-infrared catalogue, containing photometric and

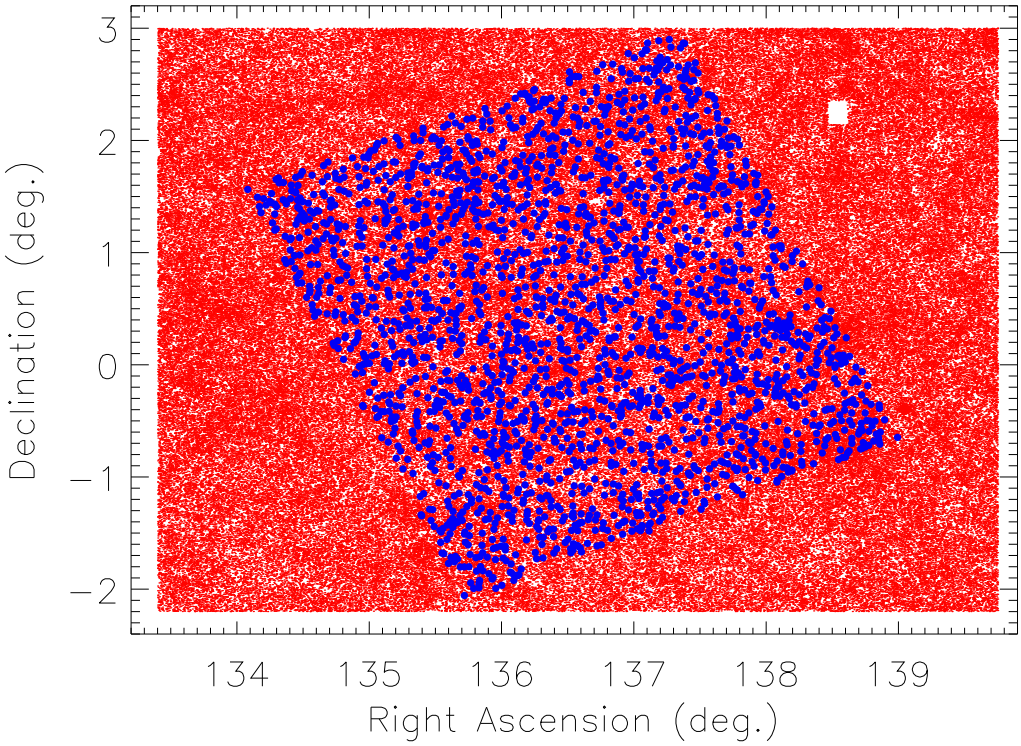

Figure 3.1: The Optical-9hr field using data from the SDSS and UKIDSS/LAS, with point like sources filtered out resulting in a sample of 323, 969 objects (*red*). Also shown are the 2, 423 objects with reliable counterparts from the H-ATLAS SDP field (*blue*).

spectroscopic redshifts (hereafter named the Optical-9hr catalogue), totals 909,985 objects from which I remove all sources with $r > 21.5$ due to the fact that at fainter magnitudes the signal-to-noise ratio increases to an extent where errors associated with the photometry become large. This results in the photometric redshift errors increasing to a level where the measured redshifts of these objects can no longer can be treated as reliable. In addition, I remove objects classified as point-like in the SDSS imaging (i.e. with a point spread function $\mathrm{PSF}_r > 0.5$). This reduced the Optical-9hr catalogue to 323, 969 objects, of which 8, 875 had spectroscopic redshifts across the range $0 < z < 1.2$. Despite spectroscopic redshifts being more accurate, photometric redshift estimation is by far the most efficient technique considering the large number of objects in the imaging data. As a consequence of this the fact that the majority of objects had photometric redshifts without a spectroscopic redshift value is

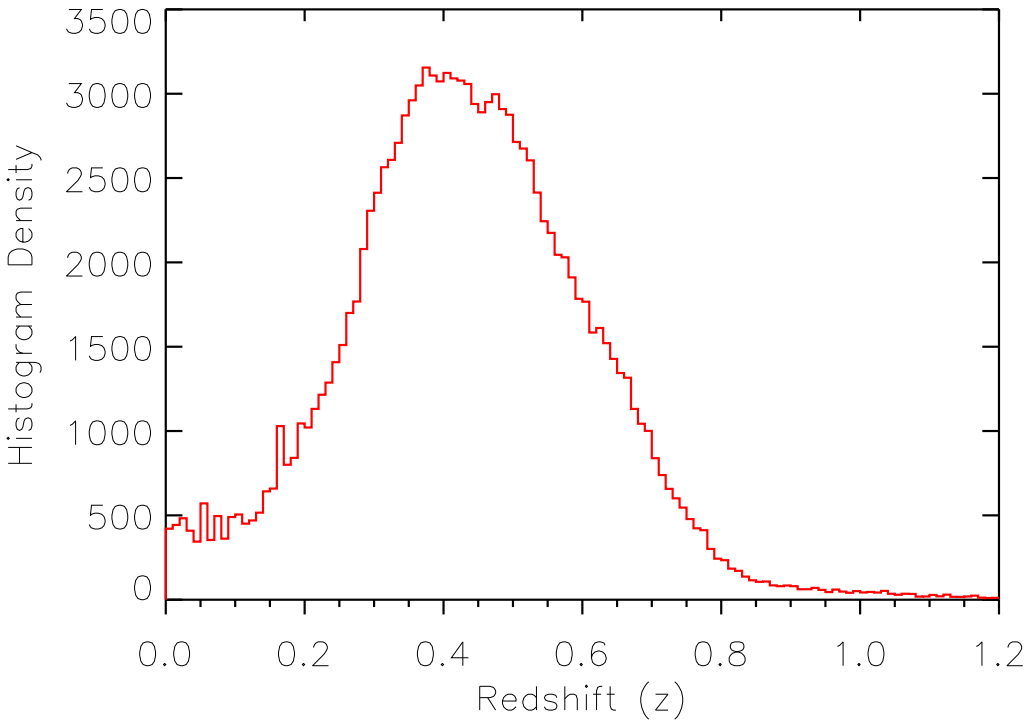

Figure 3.2: The redshift distribution of all 129,518 objects in the Optical-9hr field. There is clearly a majority in the number of detected objects residing at z ∼ 0.40, due to the evolution of the luminosity function and flux limit of the observations.

not unexpected. Figure 3.1 shows the H-ATLAS SDP field and the Optical-9hr fields in relation to each other.

3.2 Density Analysis of the SDP Field

3.2.1 Application of the VT Algorithm

The typical velocity dispersion between gravitationally bound group/cluster galaxies is within the region of a few hundred kilometres per second, as shown by equation 2.15 in Chapter 2.2.1, equating to a spread in redshift of $\Delta z \sim 10^{-3}$ at $z = 1$. Therefore for this analysis, I adopted a redshift slice of width $\Delta z = 0.01$, easily incorporating associated galaxy environments and resulting in 120 slices across each of the 1000 3D MC realisations up to $z = 1.2$. However, for density analyses based on observed data, the impact of photometric errors should also be considered. If these errors are larger

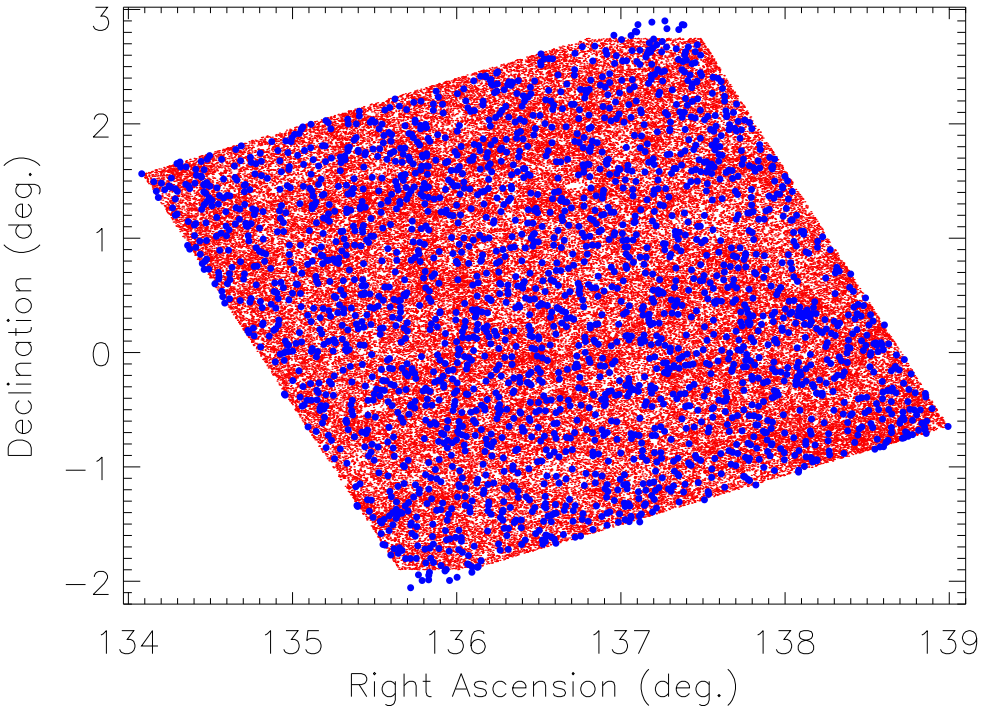

Figure 3.3: The remaining Optical field (*red*) after the necessary cuts have been applied to the initial data. The Herschel-SDP objects (*blue*) mark the extent of the new field. Note: The horizontal cuts applied to the highest and lowest declination Optical objects that are missing from the field. This marks the boundary applied to avoid VT edge-effects.

than the expected spread in redshift, calculated above, the density distribution may be flattened. Therefore it may be necessary to increase the redshift slice used. In response to this, I investigate the effect of larger redshift slices on the resultant density calculation in the appendices of this thesis.

As expected, due to the evolution of the luminosity function and flux-density limit of the observations, a peak in the number density of the Optical-9hr field was found to reside at $z \sim 0.40$ (as shown in Figure 3.2). This was resolved via the VT algorithms normalisation procedure described in Chapter 2. In addition, testing for the VT edge-effect discussed in Chapter 2.2.2 (i.e without applying boundary limits) revealed, unsurprisingly, a sharp increase in mean area of the cells towards the outside of the field and that this edge-effect penetrated the field by approximately ± 0.30 deg in both RA and Dec. Remaining objects within this region did not contribute further to the

density calculation.

To ensure that the accuracy of the comparison between the two fields was maintained, it was necessary to include only Optical-9hr objects that reside within the boundary of the Herschel-SDP field. This ensures that the all objects included in the density measure are from across the same region and thus have been observed by both SDSS and H-ATLAS. This is so that when comparing between the two fields (Section 3.2.2) I was not counting any Optical-9hr objects that would otherwise be detected in the Herschel-SDP catalogue if it were not for the boundary limits of the Herschel-SDP region. Figure 3.3 shows the remaining Optical-9hr objects. After these region cuts are applied, the final Optical-9hr catalogue was reduced to 129,518 objects.

3.2.2 Far-Infrared and Control Samples

As described in Section 3.1.1, Smith et al. (2011) calculate the probability that an optical source is in fact a reliable counterpart to a 250μm selected source from the H-ATLAS survey. Applying a *likelihood ratio* technique, a reliability parameter (R) is established, where objects with $R \geq 0.8$ are considered to be true matches. This reliability parameter cut returned $2,423$ *Herschel* detections with matching Optical-9hr counterparts. By cross-matching these sources directly with the remaining Optical-9hr sources via their mutual SDSS identification numbers, I find that there are $2,265$ Optical-9hr sources that have far-infrared detections. These cross-matched far-infrared sources are hereafter named 'FIR' while simultaneously removing them from the Optical-9hr catalogue reducing this sample to $127,250$ objects (hereafter renamed 'Optical').

In order to accurately compare how $\bar{S}_c$ values differ between the FIR and Optical catalogues it is necessary to ensure that I am comparing like with like, such that the objects selected for comparison should be considered to be from the same population. By selecting a matched sample of galaxies based on their colour, r-band magnitude and redshift distributions ($g-r$, $r-i$, m_r and z) I can ensure that these properties have no influence on any differences in environmental density found between the two catalogues. This was achieved by gridding the field in four dimensions in order to incorporate all $g-r$, $r-i$, m_r and z parameter space, selecting matched objects as only those which

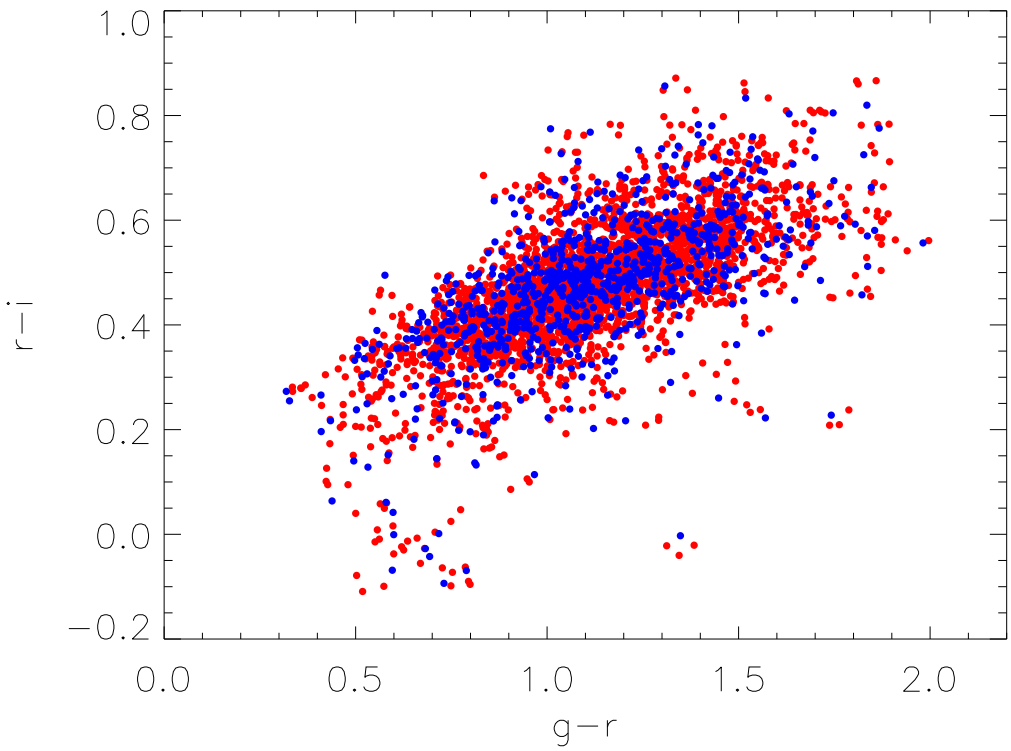

Figure 3.4: $g-r$ versus $r-i$ colour distribution for the 'matched' catalogues Optical (*red*) and Herschel (*blue*) numbering 2,706 and 902 sources respectively.

share an associated grid space in all four planes. The choice of $g-r$ and $r-i$ colours were selected as I limited the Optical catalogue in the r-band apparent magnitude. As explained in Section 3.1.2 and as shown in Taylor et al. (2011), colours provide a reasonable method of matching sources in terms of their stellar mass over the redshift range under investigation here, although I also investigate this further in Section 3.2.6. The grid elements applied to the total $g-r$ and $r-i$ colour distributions incorporate 0.1 and 0.06 magnitudes respectively in colour space. This difference reflects the larger range of the total $g-r$ colour distribution. Simultaneously, the z and m_r ranges have grid elements incorporating 0.02 in redshift and 0.38 in $r-$band magnitude.

All Optical sources that shared an associated grid space with a FIR detection in all four planes were initially grouped as potential matches to those FIR objects. Then, within each grid space, a multiple of the potential matches (totalling three times the FIR sources in that grid space) were selected as matched objects. Selecting

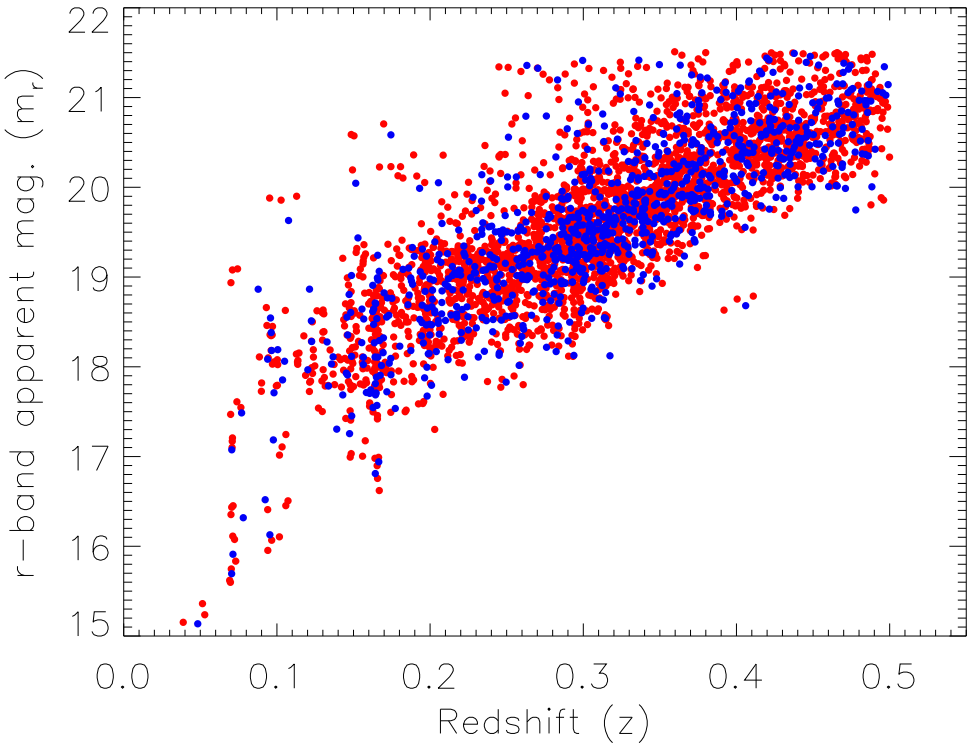

Figure 3.5: Redshift versus r-band apparent magnitude (m_r) for the 'matched' Optical (*red*) and Herschel (*blue*) catalogues. Only the redshift range of $0 < z \leq 0.5$ and m_r range of $15 < m_r < 21.5$ was included in the sampling; the completeness of these catalogues reduced significantly outside of these ranges.

Optical matches equal to a multiple of the FIR sources in each grid allows for a more robust comparison without sacrificing any similarities between their distributions. Any additional Optical or FIR sources that were not matched were discarded. The FIR sample contains considerably fewer objects than the Optical sample ($2,265$ against $127,250$), therefore a large proportion of the Optical sample will not have an associated FIR object and thus will be lost from the final cross-match. This reduces the sample size to $2,706$ and 902 for the Optical and FIR samples respectively. In addition, the number-density of galaxies reduces with increasing redshift to such an extent as to affect our sampling. Therefore we apply a maximum peak redshift limit onto the samples of $z \leq 0.5$. This maximum redshift does not influence the $\bar{S}_c$ values of the remaining sample due to the fact that each $\bar{S}_c$ value already incorporates the high redshift galaxies via the full z-PDF sampling achieved within the algorithm. Figures 3.4 & 3.5 show the

colour, redshift and magnitude distributions for these two matched samples.

3.2.3 Comparison of the FIR and Optical Galaxies

The Optical catalogue is labelled as '*op*' in figures and tables for clarity and is three times the size of the FIR sample, labelled as '*FIR*'. For each population I measured the distribution for the environmental density ($(\bar{S}_c)_{op}$ and $(\bar{S}_c)_{FIR}$) along with distributions for redshift (z_{op} and z_{FIR}), colour $[(g-r)_{op}, (r-i)_{op}$ and $(g-r)_{FIR}, (r-i)_{FIR}]$ and r-band apparent magnitude ($m_{r(op)}$ and $m_{r(FIR)}$). A statistical test was required to determine whether the null hypothesis (that two separate data-sets are consistent with being sampled from the same underlying distribution) can be rejected within a designated level of significance. I have used one- and two-dimensional Kolmogorov-Smirnoff tests (KS-tests) to check that my matched samples are indeed drawn from the same underlying distribution in terms of their colour, magnitude and redshift distributions.

Beginning with one-dimensional KS-tests applied to the redshift distributions (z_{op} versus z_{FIR}), returned a KS probability of 0.999. I then applied the KS-test to the colour distributions $[(g-r)_{op}$ versus $(g-r)_{FIR}]$ and $[(r-i)_{op}$ versus $(r-i)_{FIR}]$ returning probabilities of 0.974 and 0.395 respectively. Finally, applying a KS-test to the r-band magnitude distributions ($m_{r(op)}$ versus $m_{r(FIR)}$) returned a probability of 0.719. These values are large and show that the null hypothesis cannot be rejected based on any reasonable statistical significance level (taking $2\sigma \sim 5\%$ as the minimum requirement to reject the null hypothesis). All of these tests demonstrate that the 'Optical' control sample is drawn from the same underlying distribution as the FIR sample. I then applied the one-dimensional KS-test to the environmental density measurements for the Optical and FIR samples ($\bar{S}_c$), which returned a probability of just 4.22×10^{-4}, rejecting the null hypothesis of them being drawn from the same underlying distribution at the 3.5σ level. Therefore I found a significant difference in the distribution of the galaxy environmental density between far-infrared selected galaxies and a control sample with no detectable far-infrared emission. To test this result further, I applied a two-dimensional KS-test to various parameters in colour, magnitude and redshift space for both Optical and FIR populations. Once more the probabilities returned by the

KS-test were large enough to confirm that the null hypothesis could not be rejected for these distributions, and these values are also presented in Table 3.1.

However, the two-dimensional KS-tests comparing the colour, r-band magnitude and redshift distributions to the normalised environmental density distributions of my FIR and Optical samples, returned low probabilities indicating a significant difference. For the $[(g-r, \bar{S}_c)_{op}$ versus $(g-r, \bar{S}_c)_{FIR}]$ distributions KS-tests returned a probability of 0.005; for $[(r-i, \bar{S}_c)_{op}$ versus $(r-i, \bar{S}_c)_{FIR}]$ a KS probability of 0.005; for $[(m_r, \bar{S}_c)_{op}$ versus $(m_r, \bar{S}_c)_{FIR}]$ a KS probability of 0.006; and for $[(z, \bar{S}_c)_{op}$ versus $(z, \bar{S}_c)_{FIR}]$ a KS probability of 0.010. This confirmed that, again, the environmental density distributions $(\bar{S}_c)$ are significantly different and that the null hypothesis can be rejected to at least the 2.6σ level. Again these statistical results are presented in Table 3.1.

The extent of this difference is illustrated in Figure 3.6 where I show normalized histograms of the two environmental density distributions. It is clear that the Optical population (*red*), with the mean of its distribution at $\bar{S}_c = (12.70 \pm 0.95) \times 10^{-2}$ (denoted by the red dashed line), is more overdense (has larger values of $\bar{S}_c$) than the FIR population (*blue*), with the mean of its distribution at $\bar{S}_c = (3.46 \pm 1.49) \times 10^{-2}$ (denoted by the blue dashed line). Using the Mann-Whitney U (MWU) test I also test for differences between the median values of the distributions. For the Optical and FIR populations the test returns a probability of 5×10^{-6}, indicating that the two populations have significantly different median values at the 4.5σ level.

3.2.4 Redshift Binning

Clearly in any flux-density limited sample there is a bias in the sense that the higher-redshift sources are more luminous than those at lower redshift. Therefore, to further examine the difference between the Optical and FIR environmental density distributions I split the two populations into two redshift slices of $0 < z \leq 0.25$ and $0.25 < z \leq 0.5$ and repeat the density comparison.

The lowest of the two bins ($0 \leq z < 0.25$) contained 680 objects from the Optical population with 227 objects from the FIR population. Applying a KS-test to the density measurements within this bin (Table 3.2) returned a probability value of 0.028

Table 3.1: Two sample and two-dimensional KS- and MWU-test results over the full SFR and redshift range ($0 < z \leq 0.5$). Where *op* represents Optical (2,706 objects) and *FIR* represents FIR (902 objects). The two density distributions are different at the 3.5σ level from KS-tests, with the means of the distributions different at the 4.5σ level from MWU tests.

Distributions Compared			KS Probability	MWU Probability
$z_{(op)}$	versus	$z_{(FIR)}$	0.999	0.403
$(g-r)_{op}$	versus	$(g-r)_{FIR}$	0.974	0.374
$(r-i)_{op}$	versus	$(r-i)_{FIR}$	0.395	0.239
$m_{r(op)}$	versus	$m_{r(FIR)}$	0.719	0.290
$(\bar{S}_c)_{op}$	versus	$(\bar{S}_c)_{FIR}$	4.22×10^{-4}	5.25×10^{-6}
$(g-r, r-i)_{op}$	versus	$(g-r, r-i)_{FIR}$	0.224	-
$(g-r, z)_{op}$	versus	$(g-r, z)_{FIR}$	0.956	-
$(r-i, z)_{op}$	versus	$(r-i, z)_{FIR}$	0.468	-
$(m_r, z)_{op}$	versus	$(m_r, z)_{FIR}$	0.755	-
$(g-r, m_r)_{op}$	versus	$(g-r, m_r)_{FIR}$	0.839	-
$(r-i, m_r)_{op}$	versus	$(r-i, m_r)_{FIR}$	0.339	-
$(g-r, \bar{S}_c)_{op}$	versus	$(g-r, \bar{S}_c)_{FIR}$	0.005	-
$(r-i, \bar{S}_c)_{op}$	versus	$(r-i, \bar{S}_c)_{FIR}$	0.005	-
$(m_r, \bar{S}_c)_{op}$	versus	$(m_r, \bar{S}_c)_{FIR}$	0.006	-
$(z, \bar{S}_c)_{op}$	versus	$(z, \bar{S}_c)_{FIR}$	0.010	-

Table 3.2: KS-test and MWU-test results for the comparison of both the Optical and FIR populations $\bar{S}_c$ distributions within individual redshift slices shown in Figure 3.7. From KS results the density distributions are different between the 2.2σ-3.3σ level. The number of objects from each population are given:

Redshift Slice	Optical	FIR	KS Probability	MWU Probability
$0 \leq z < 0.25$	680	227	0.028	0.028
$0.25 \leq z < 0.50$	2,026	675	7.46×10^{-4}	3.42×10^{-5}

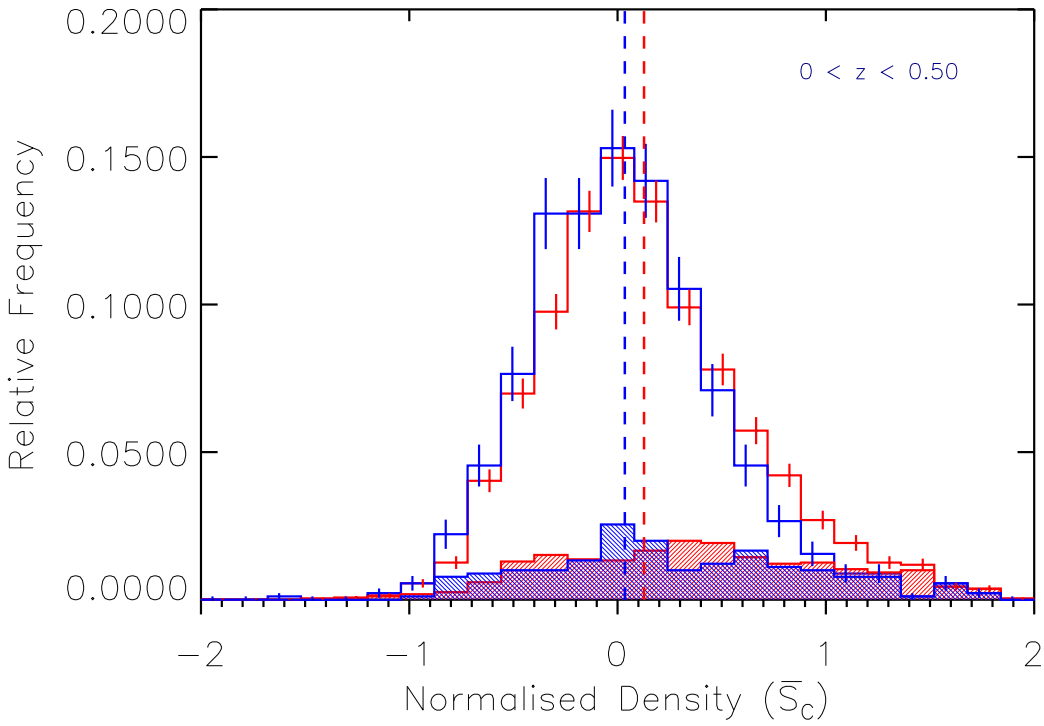

Figure 3.6: A normalised histogram showing how the distributions of environmental density ($\bar{S}_c$) of the total Optical (*red*) and FIR (*blue*) populations (2706 and 902 objects respectively) compare, with shaded histograms representing the number of spectroscopic redshifts in each sample. Error-bars depict the error associated with each bin, where $\bar{S}_c > 0$ signifies and over-density and $\bar{S}_c < 0$ signifies an under-density in terms of the entire redshift range ($0 \leq z < 0.5$). The FIR data is shifted generally to lower $\bar{S}_c$ values, with the mean of its distribution at $(3.46 \pm 1.49) \times 10^{-2}$ (*blue dashed line*), this is contrasted against the mean of the Optical distribution at $(12.70 \pm 0.95) \times 10^{-2}$ (*red dashed line*).

thus, as with the full redshift range, the null hypothesis could be rejected and the two populations can be considered significantly different in terms of their overall density distributions at the 2.2σ level. Applying a MWU test returned a probability of 0.028 indicating that the two distributions have significantly different mean values and that the null hypothesis can be rejected at the 2.2σ level. Visual inspection of the two distributions within this slice (Figure 3.7 - *Top*) confirm a separation between the distributions with the FIR population favouring lower densities, however there are larger uncertainties on some of the bins, due to the smaller number of objects being compared than across the full redshift range, that may hinder the MWU comparison. This low number density issue will be remedied by the vastly increased number of

objects that will be available in the full H-ATLAS survey area.

The higher redshift bin ($0.25 \leq z < 0.5$) contains overall a much larger proportion of the objects with 2026 objects from the Optical population and 675 objects from the FIR population. Once more I apply KS- and MWU-tests to the distributions returning a KS probability value of 7.46×10^{-4} which indicates the two populations are significantly different at the 3.3σ level and a MWU probability value of 3.42×10^{-5} which indicates that the mean values of two distributions within this redshift bin are significantly different at the 4.1σ level. The histogram of this redshift bin (Figure 3.7 - *Bottom*) shows once more that the separation between the distributions with the FIR population favouring lower densities. With a larger number of objects available in each distribution the normalised errors are smaller than the lower redshift case indicating a clear difference.

These results show that, as with the full redshift range, objects in both redshift bins are significantly different in terms of both their overall distribution and their mean values. However, it is evident that these statistical differences are higher in the higher-redshift bin and that this bin contains a larger number of objects in both samples. I investigate the impact of this difference in number density with increasing redshift by matching the number of galaxies in the higher and lower bins and repeating the sample comparisons. First, by increasing the redshift boundary between the higher and lower bins (from $z = 0.25$ to $z = 0.32$) to achieve approximate matching in sample sizes above and below this redshift. Second, by reducing the number of objects within the higher redshift bin to match exactly with the lower bin samples. In both cases the same trends are found and my results remain the same.

With fewer objects in the lower redshift bin, the signal-to-noise will be lower at these redshifts, affecting the comparison. Furthermore, at higher redshifts, objects with lower IR luminosities are excluded by the flux-density limit of the H-ATLAS survey, leading to a bias towards the detection of the highest luminosity objects and thus objects with the higher levels of star formation. This bias is compounded by the fact that these observations cover a greater volume of sky at higher redshifts increasing the likelihood of detecting the most far-infrared luminous galaxies. This results in

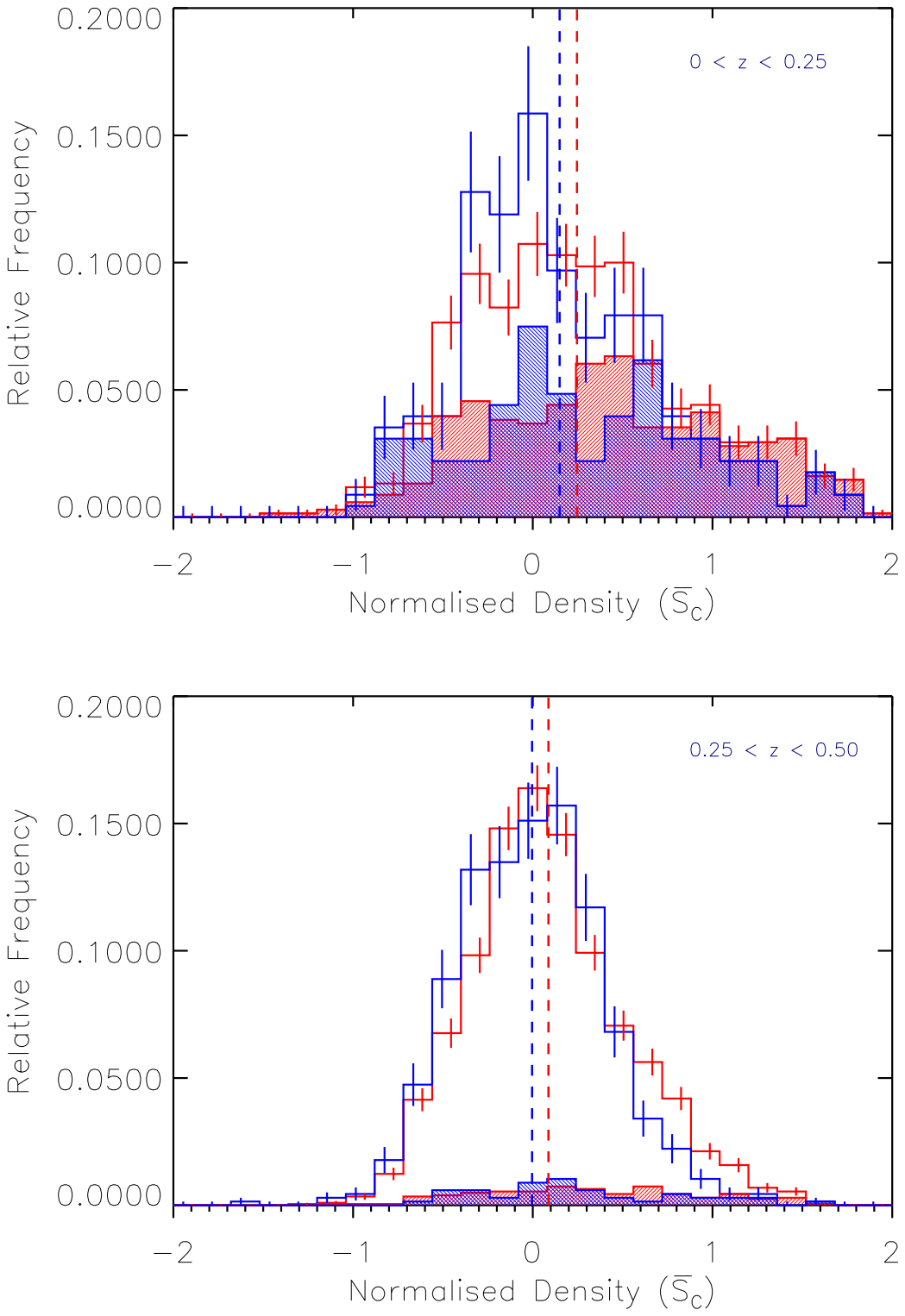

Figure 3.7: Normalized histograms that show the full matched sample binned in Redshift $0 \leq z < 0.25$ and $0.25 \leq z < 0.50$ (*Top* and *Bottom*) respectively, showing a continued separation between the $\bar{S}_c$ distributions increasing with redshift from 2.2σ to 3.3σ significance. Again, shaded histograms represent the number of spectroscopic redshifts in each sample.

the far-infrared detected population within the lower redshift bin being predominantly occupied by galaxies with low star formation rates. Thus, the environmental density distribution of the less luminous far-infrared galaxies may actually be similar to the Optical population. In contrast the higher redshift bins contain a much higher proportion of galaxies with higher levels of star formation and therefore exhibit a stronger correlation with density. The consequence of this bias is that the statistical differences found between the total Optical and FIR distributions (shown in Table 3.1) may be being diluted by galaxies with low star formation rates at low redshift. In order to examine the full impact of these objects, in Section 3.2.5, I apply SFR bins to the FIR catalogue and repeat the above analysis.

3.2.5 Star Formation Rate vs Environmental Density

The SED's of galaxies observed in the near-IR, UV and optical wavelengths are dominated by galactic starlight emission, whereas the far-infrared SED is dominated by the thermal dust emission of the ISM. The star formation rate of a galaxy (in solar masses per year) can be estimated using the relation given in Kennicutt (1998) as proportional to the total IR luminosity (L_{FIR}) over 8-1000μm, assuming a Salpeter initial mass function between $0.1 - 100\,\mathrm{M}_\odot$ (Salpeter, 1955), such that:

$$SFR(\,\mathrm{M}_\odot \mathrm{yr}^{-1}) = 4.5 \times 10^{-44} \cdot L_{\mathrm{FIR}}(\mathrm{ergs} \cdot \mathrm{s}^{-1}) \; . \tag{3.1}$$

The thermal emission of far-infrared galaxies can be represented by a modified black body emission spectrum, modified to account for the complex mix of dust grains at different temperatures within the ISM. Using the modified black body spectrum from Blain et al. (2003):

$$f_\nu = \varepsilon_\nu B_\nu = \frac{2h\nu^{3+\beta}}{c^2} \frac{1}{\exp(\frac{h\nu}{KT}) - 1} \; , \tag{3.2}$$

where h is the Planck constant, k is the Boltzmann constant, ν is the rest-frame frequency of the galaxy, B_ν is the Planck function, and ε_ν is a frequency-dependent emissivity function $\varepsilon \propto \nu^\beta$. The emissivity index, β modifies the Planck function by assuming that the dust emissivity varies as a power law with frequency, ν^β, where β can be between 1-2 as described in Hildebrand (1983), depending on the frequency of

the observations. I fix the dust emissivity index to $\beta = 1.5$ with dust temperature (T) equal to 26K as found by Dye et al. (2010) and Jarvis et al. (2010), and integrate the modified blackbody over the wavelength range $8 - 1000\mu$m to obtain the far-infrared luminosity. This gives the proportional change between the rest- and observed-frame SED such that:

$$L_{FIR} = A_\nu \cdot \int_{\nu_{min}}^{\nu_{max}} \frac{\nu^{3+\beta}}{\exp(\frac{h\nu}{KT}) - 1}\, d\nu \ , \tag{3.3}$$

where A_ν is now the normalisation constant between the rest and observed frames and ν_{max} and ν_{min} mark the upper and lower frequency boundaries of the total integrated far-infrared luminosity (8-1000μm). Combining equations 3.1 and 3.3 gives a SFR (in $M_\odot$ yr^{-1}) for each galaxy (see Figure 3.8).

As a check of my L_{FIR} values, I compared the galaxies in my sample to the subset of objects with far-infrared luminosities determined from the full energy balance models of da Cunha et al. (2008) by Smith et al. (2012a). I found that my L_{FIR} values were slightly underestimated, and a correction factor of 1.25 was needed to produce a 1:1 correlation. This suggests that, as I am assuming a fixed dust temperature of 26K, my estimate misses $\sim$ 25 per cent of the total dust luminosity, and hence the SFRs are underestimated in my calculation. I therefore applied this correction factor to my L_{FIR} values to account for this difference in my resultant SFRs. I note that this correction makes very little difference to my overall results on the relative environmental densities between different bins in SFR.

It is also worth noting that the high SFRs estimated from the far-infrared emission may be overestimates of the true SFR. It is known that far-infrared is a tracer of star formation in an idealised case, where young stars dominate the radiation field and dust opacity is high (Kennicutt et al. 2009). Multi-temperature dust distributions and emission from dust heated by older ISM stars (da Cunha et al. 2008; Smith et al. 2012a) are not be expected to be consistent with equation 3.1, and this also plays a part in my correction factor of 1.25. This must also be balanced against the fact that any unobscured component of star formation would not be detected in the far-infrared. Thus, although far-infrared emission is highly correlated with SFR I note that the absolute values of SFR should be used with caution.

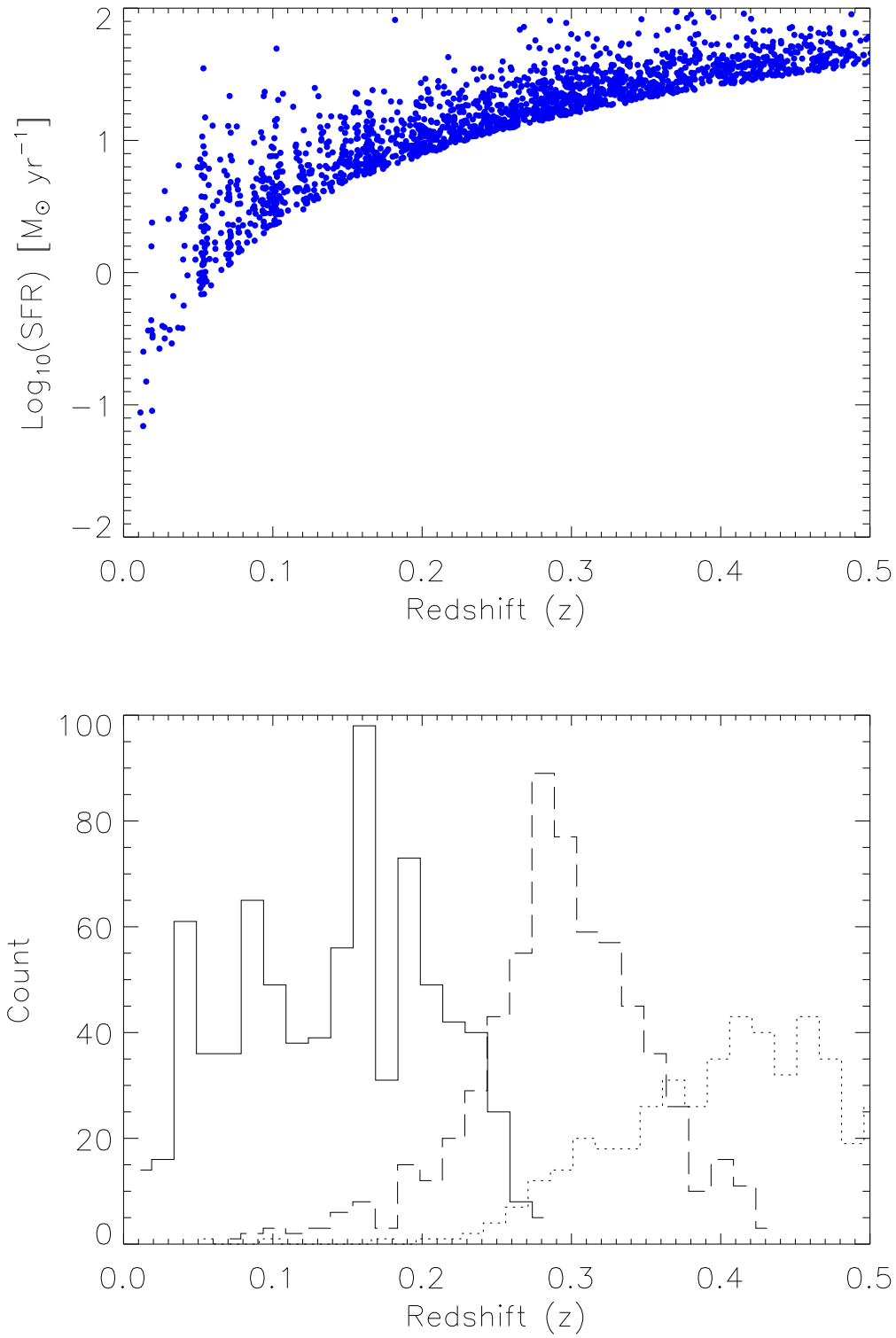

Figure 3.8: *Top*: The calculated SFR ($\mathrm{M_{\odot}yr^{-1}}$) against redshift for the total FIR catalogue. The plot covers the redshift range relevant for this analysis ($0 < z \leq 0.5$). *Bottom*: Plot of the three SFR bins from the FIR catalogue versus redshift. The $0 <$ SFR $< 15\,\mathrm{M_{\odot}yr^{-1}}$ bin (Solid line) containing 781 objects, the $15 <$ SFR $\leq 30\,\mathrm{M_{\odot}yr^{-1}}$ bin (Dashed line) containing 631 objects and the $SFR > 30\,\mathrm{M_{\odot}yr^{-1}}$ bin (Dotted line) containing 423 objects $z \leq 0.5$.

I bin the FIR objects in terms of their SFR in bins of 0−15, 15−30 and $> 30\,\mathrm{M}_{\odot}\,\mathrm{yr}^{-1}$ in order to compare the impact of different SFR on my initial results. Again matching the control sample to the individual binned SFR samples I perform KS-tests and MWU-tests on all combinations. Beginning with the lowest SFR bin ($0 <$ SFR ≤ 15 $\mathrm{M}_{\odot}\mathrm{yr}^{-1}$) this reduces the total FIR population to 781 objects, as is expected from the SFR-z relation shown in Figure 3.8. As a consequence of this reduced total FIR population, when cross-matching with the total Optical population in terms of colour, r-band magnitude and redshift distributions (as in Section 3.2.2), the number of matched objects will also be reduced. In this SFR bin I find the number of cross-matched Optical objects to equal 414 (down from 2,706 in the full SFR sample) and the number of cross-matched FIR objects to equal 138 (down from 902 in the full SFR sample). The parameters of this cross-match were adjusted slightly from the full SFR bin cross-match to account for changes to the boundaries of the selection criteria ($g - r$, $r - i$, m_r and z) brought on by applying SFR binning. Within this SFR bin the redshift distribution of these objects are primarily low redshift objects and as such the redshift range in the cross-match is limited to between $0.05 \leq z \leq 0.30$ and the m_r limited to $15 < m_r < 20$, all other parameters remained identical to the full SFR cross-match. I apply the KS- and MWU-test analysis as described in Chapter 3.2.3. The results continue to show a significant difference between the binned Optical and FIR density distributions at the 2.6σ level, as shown along with all following statistical results from this section, in Table 3.3. This is also true of a visual inspection of the distributions plotted in Figure 3.9 with mean values of $\bar{S}_c$ from the binned Optical and FIR distributions equalling 0.24 ± 0.03 (*red dashed line*) and 0.12 ± 0.05 (*blue dashed line*) respectively and MWU test results confirming these values are again significantly different at the 2.6σ level.

The second SFR bin ($15 <$ SFR $\leq 30\,\mathrm{M}_{\odot}\mathrm{yr}^{-1}$) contains 631 objects from the total FIR population. Cross-matching this with the total Optical catalogue yields 1104 cross-matched Optical objects and 368 cross-matched FIR objects. Further adjustments are made to account for the increased redshift range of the data (see Figure 3.8) $0.05 < z \leq 0.50$ and an increased r-band magnitude limit to $15 < m_r \leq 21$. Repeating the statistical analysis produces KS- and MWU-test results that confirm that the two

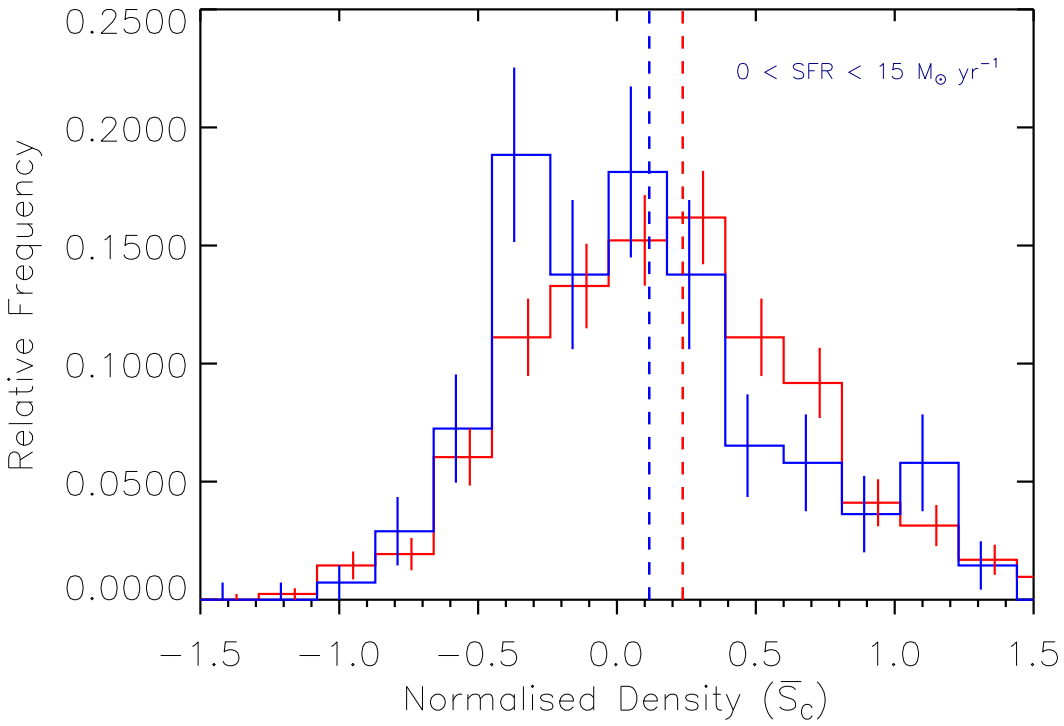

Figure 3.9: A histogram showing the normalised density distributions of the Optical (*red*) and FIR (*blue*) samples with SFRs from 0 to 15 $M_\odot$ yr^{-1} (containing 414 and 138 objects respectively). Vertical dashed lines show the location of the mean value of each distribution coloured accordingly. KS- and MWU-tests confirm the distributions are significantly different at the 2.6σ level, with the Optical population favouring over-dense regions, in agreement with Figure 3.6.

cross-matched populations do have significantly different density distributions at the 2.7σ level. Both binned Optical and FIR density distributions are plotted together in Figure 3.10. The mean of the $\bar{S}_c$ distributions, with Optical $= 0.11 \pm 0.01$ (*red dashed line*) and FIR $= -1.41 \times 10^{-4} \pm 0.02$ (*blue dashed line*) respectively, are confirmed by MWU tests to be significantly different at the 3.8σ level.

Finally, the highest SFR bin ($SFR > 30\,M_\odot yr^{-1}$) contains 423 objects from the total FIR population. Cross-matching with the total Optical population yields 879 cross-matched Optical objects and 293 cross-matched FIR objects. To account for the higher redshifts in this bin the cross-match parameters were again adjusted to account for this with the m_r limit increased further to $15 < m_r < 21.5$, again all other parameters remaining the same. KS-test results from the direct comparison between

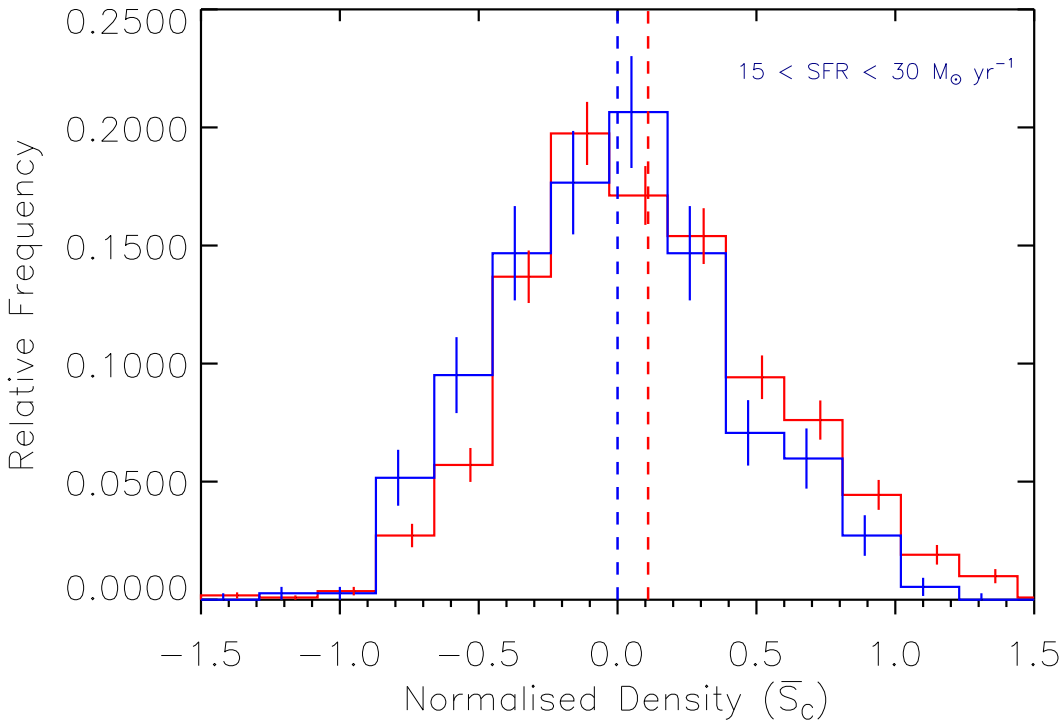

Figure 3.10: A histogram showing the normalised density distributions of the Optical (*red*) and FIR (*blue*) samples from 15 to 30 $M_{\odot}yr^{-1}$ (containing 1,104 and 368 objects respectively). Vertical dashed lines show the location of the mean value of each distribution. KS- and MWU-tests confirm agreement with Figure 3.6 and are significantly different between the 2.7σ - 3.8σ level, with an increased distance between the mean of the distributions compared to lower SFR limits.

the total density distributions confirm that they are still significantly different at the 3.3σ level. Plotting both binned Optical and FIR density distributions together in Figure 3.11 with the mean of the $\bar{S}_c$ distributions, equal to (13.56 ± 1.43) x 10^{-2} (*red dashed line*) and $(-4.45 \pm 20.9) \times 10^{-3}$ (*blue dashed line*) respectively, are again shown to be significantly different by MWU test at the 4.8σ level.

The results from all of these tests are shown in Table 3.3. This shows that the SFR derived from the far-infrared emission of galaxies is strongly linked to the environmental density of the galaxy. Selecting only those galaxies with the highest SFR results in an ever more pronounced difference between the normalised density distributions of the Optical and FIR populations. I was not able to increase the SFR binning to higher limits due to the limiting number of objects found with SFR higher than $\sim 30\,M_{\odot}yr^{-1}$

Table 3.3: Two sample KS- and MWU-test results for each SFR bin, collectively over the full redshift range ($0 < z \leq 0.5$) where *op* represents the Optical and *FIR* represents the FIR populations. (A): SFR of 0 to 15 $M_\odot\,yr^{-1}$ contains 414 cross-matched Optical objects and 138 cross-matched FIR objects. (B): SFR of 15 to 30 $M_\odot\,yr^{-1}$ bin contains 1,104 cross-matched Optical objects and 368 cross-matched FIR objects. (C): Minimum SFR of 30 $M_\odot\,yr^{-1}$ bin containing 879 cross-matched Optical objects and 293 cross-matched FIR objects:

Distributions Compared			KS Prob. (A)	MWU Prob. (A)	KS Prob. (B)	MWU Prob. (B)	KS Prob. (C)	MWU Prob. (C)
$z_{(op)}$	versus	$z_{(FIR)}$	0.999	0.484	0.911	0.359	0.324	0.372
$(g-r)_{op}$	versus	$(g-r)_{FIR}$	0.834	0.357	0.964	0.420	0.997	0.420
$(r-i)_{op}$	versus	$(r-i)_{FIR}$	0.054	0.057	0.998	0.453	0.999	0.474
$m_{r(op)}$	versus	$m_{r(FIR)}$	0.994	0.410	0.994	0.368	0.630	0.310
$(\bar{S}_c)_{op}$	versus	$(\bar{S}_c)_{FIR}$	9.06×10^{-3}	8.73×10^{-3}	5.64×10^{-3}	1.59×10^{-4}	9.50×10^{-4}	1.132×10^{-6}

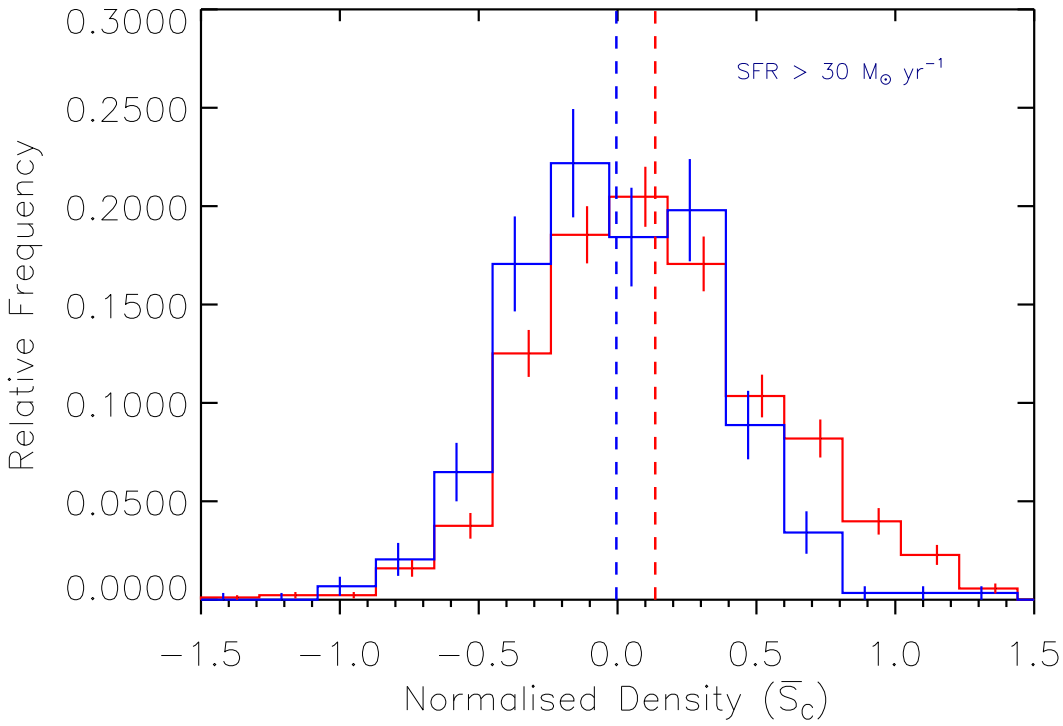

Figure 3.11: A histogram showing the normalised density distributions of the Optical (*red*) and FIR (*blue*) distributions with SFRs $> 30\,\mathrm{M_{\odot}yr^{-1}}$ (containing 879 and 293 objects respectively). Vertical dashed lines show the location of the mean value of each distribution coloured accordingly. Again, from KS- and MWU-test results, the two distributions are significantly different between the 3.3σ - 4.8σ level with an increase in their mean separation compared to lower SFR limits.

within the redshift range of the analysis ($z \leq 0.5$) as illustrated in Figure 3.8.

3.2.6 Dust Reddening Effects

In this analysis I have only used the most sensitive optical bands to define my optical and far-infrared selected samples, due to the wealth of such data over the survey region used. However, it is expected that the galaxies which are detected in H-ATLAS will be subject to dust reddening effects, as it is known that they must have significant amounts of dust in them to be detected in the first place. This could cause the Optical and FIR galaxies to be mismatched in terms of their intrinsic stellar colours and their stellar masses. To investigate this I include the $K-$band data from the UKIRT Infrared Sky Survey (Lawrence et al., 2007), which is available for many (but not all) of the sources.

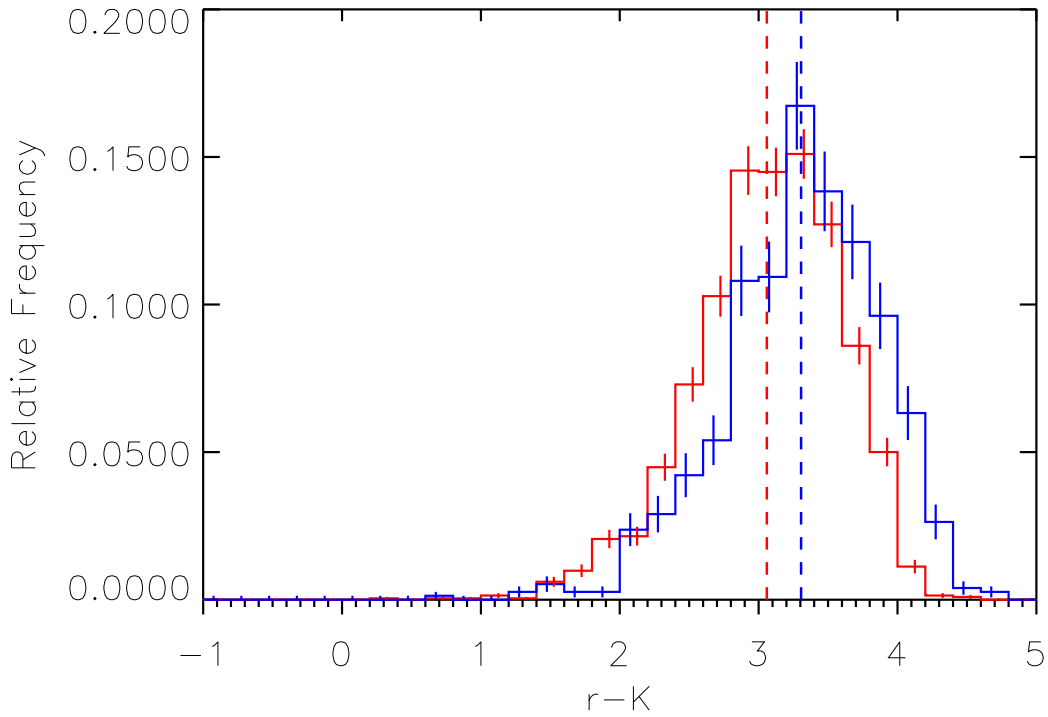

Figure 3.12: Histograms of the $r - K$ colours for the Optical (red) and FIR (blue) samples showing that they have significantly different distributions at a $> 5\sigma$ level with the FIR galaxies lying redward of the Optical galaxies.

I do not use this initially as the number of galaxies with a $K-$band identification is much less than the number which are identified in the g, r and i bands. In Figure 3.12 I show a histogram of the $r - K$ colours of the matched sample of Optical (*red*) and FIR (*blue*) galaxies, where, due to the smaller number of K-band detections, the size of each sample is reduced to $2,139$ and 759 objects respectively. This shows that there is indeed a significant difference in the $r - K$ distributions between the Optical and FIR galaxies at a $> 5\sigma$ level, suggesting that dust reddening may well be biasing my results. However, accounting for this reddening would act only to strengthen my conclusions. This is due to the fact that, as the FIR sources are more highly reddened, I am more likely to underestimate their r-band magnitudes and subsequently their masses. Given that it is known that more massive galaxies generally trace denser environments (e.g. Kauffmann et al. 2004; Baldry et al. 2006; Li et al. 2006), correcting for this would lead to a larger difference between the Optical and FIR samples.

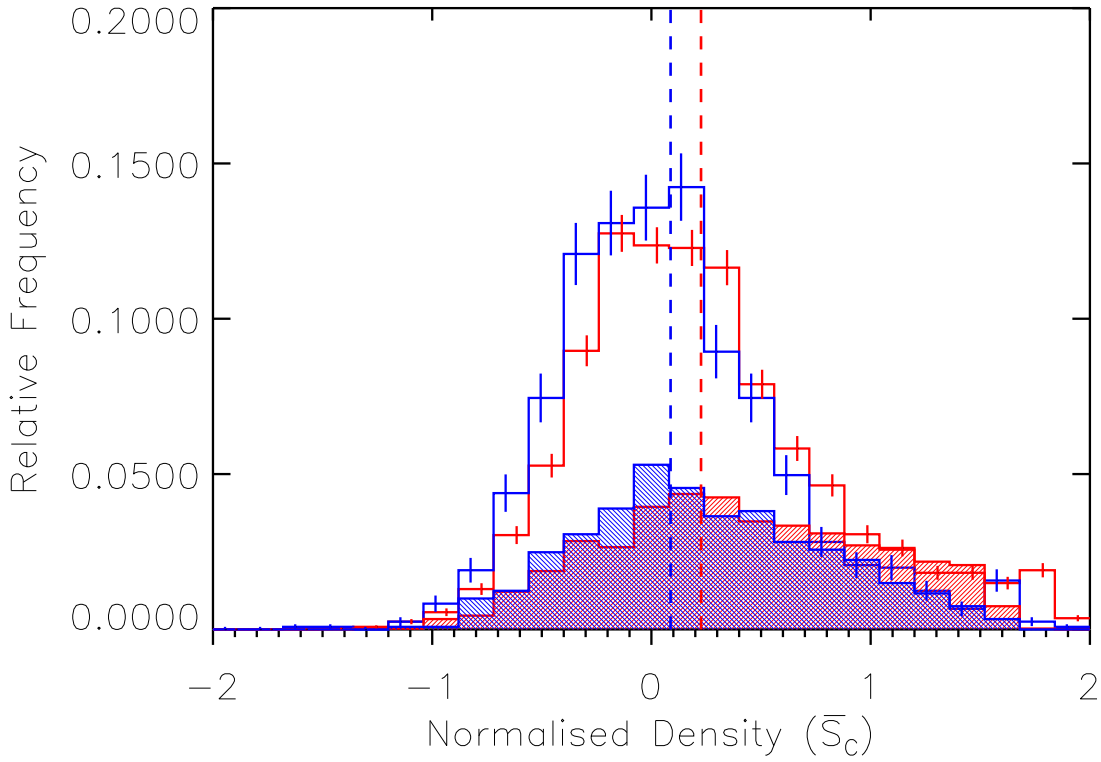

Figure 3.13: Normalised histograms of the environmental density ($\bar{S}_c$) of both Optical (*red*) and FIR (*blue*) populations, cross-matched in $r-K$, m_K and z parameter space. KS- and MWU-tests indicate a significant difference at the $> 5\sigma$ level. The FIR data is shifted generally to lower $\bar{S}_c$ values, with the mean of its distribution at 0.09 ± 0.02 (*blue dashed line*), contrasted against the mean of the Optical distribution at 0.23 ± 0.01 (*red dashed line*).

To test the robustness of this result I repeat the density analysis with Optical and FIR samples cross-matched in terms of $r-K$, m_K and z parameter space. As this new cross-matching takes into consideration only three dimensions, the resultant number of objects considered matched in all three of these parameters is larger than in the initial four-dimensional cross-matching, with 3,624 Optical and 1,208 FIR objects. Applying KS- and MWU-tests to the data still returned a significant difference between the environmental density distributions at the $> 5\sigma$ level, with the FIR population once more favouring underdense regions compared to the Optical sample with mean values of 0.09 ± 0.02 and 0.23 ± 0.01 respectively. Table 3.4 gives the results of the statistical comparison and the density distributions are plotted in Figure 3.13. I do not extend on this analysis here as new data from the VISTA VIKING Survey (e.g. Findlay et al.,

Table 3.4: Two sample and two-dimensional KS- and MWU-test results over the full SFR and redshift range ($0 < z \leq 0.5$). Where *op* represents Optical (3,624 objects) and *FIR* represents FIR (1,208 objects) matched in terms of their $K-$band magnitude, $r-K$ colour and redshift distribution.

Distributions Compared			KS Prob.	MWU Prob.
z_{op}	versus	z_{FIR}	0.996	0.489
$(r-K)_{op}$	versus	$(r-K)_{FIR}$	0.626	0.485
$m_{K(op)}$	versus	$m_{K(FIR)}$	0.136	0.137
$(\bar{S}_c)_{op}$	versus	$(\bar{S}_c)_{FIR}$	$< 10^{-9}$	$< 10^{-10}$
$(r-K,z)_{op}$	versus	$(r-K,z)_{FIR}$	0.493	-
$(m_K,z)_{op}$	versus	$(m_K,z)_{FIR}$	0.177	-
$(r-K,m_K)_{op}$	versus	$(r-K,m_K)_{FIR}$	0.313	-
$(r-K,\bar{S}_c)_{op}$	versus	$(r-K,\bar{S}_c)_{FIR}$	$< 10^{-5}$	-
$(m_K,\bar{S}_c)_{op}$	versus	$(m_K,\bar{S}_c)_{FIR}$	$< 10^{-7}$	-
$(z,\bar{S}_c)_{op}$	versus	$(z,\bar{S}_c)_{FIR}$	$< 10^{-5}$	-

2012) over the full H-ATLAS fields will mean that the analysis presented here could be carried out with a $K-$band selected sample in the near future.

3.2.7 Nearest Neighbour Results

I repeat the full statistical analysis using the Nth-nearest neighbour technique described in Chapter 2.3. I apply the NN algorithm to the field, calculating normalised density values for each galaxy across the same redshift range ($0 < z \leq 0.5$), again cross-matching the two catalogues via the reliability parameter and applying cross-matching in $g-r$, $r-i$, z and m_r parameter space. Applying the same KS and MWU statistical comparisons from Section 3.2.3 between my cross-matched FIR and Optical data sets, I find good agreement with the VT method such that the two NN defined normalised density distributions ($\bar{S}_c$) are significantly different, with a KS-test probability of 8.72 x 10^{-5} indicating a significant difference at the 3.9σ level. As with the VT method, all other parameter comparisons show no significant difference as displayed in Table 3.5.

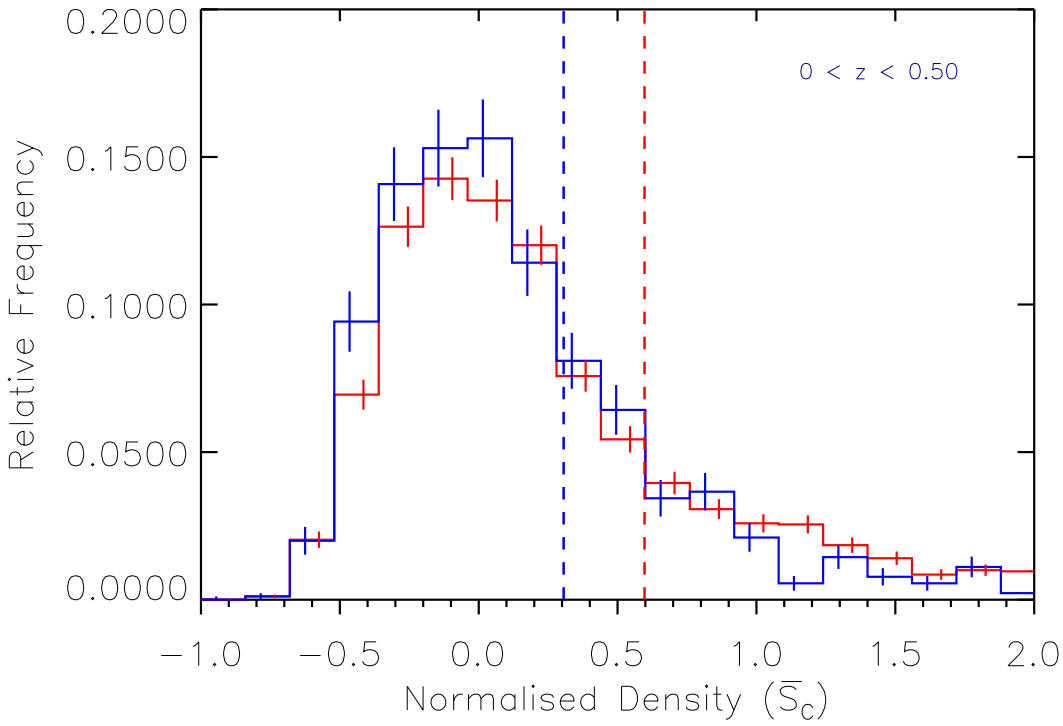

Figure 3.14: A normalised histogram of both environmental density ($\bar{S}_c$) distributions from the total Optical (*red*) and FIR (*blue*) populations after the application of the 5th-nearest neighbour technique (2, 706 and 902 objects respectively). The FIR data is shifted generally to lower $\bar{S}_c$ values, with the mean of its distribution at 0.31 ± 0.04 (*blue dashed line*) contrasted against the mean of the Optical distribution at 0.60 ± 0.05 (*red dashed line*). Comparison of the median values are found at 0.05 and 0.13 for the FIR and Optical catalogues respectively, consistent with the mean values.

In further agreement with the results established using the VT method, the mean values of the two density distributions revealed that the cross-matched FIR catalogue contained objects with lower environmental densities than the Optical catalogue, with mean values of 0.31 ± 0.04 and 0.60 ± 0.05 respectively. MWU tests revealed a significant difference between these mean values at the 4.6σ level. Figure 3.14 shows the normalised histograms of the two density distributions illustrating this difference. As these distributions are more skewed about $\bar{S}_c = 0$, it is useful in this case to instead compare the median values of these populations. These are found at 0.05 and 0.13 for the FIR and Optical catalogues respectively, consistent with their mean values.

Table 3.5: Two sample and two-dimensional KS- and MWU-test results from the application of the 5th-nearest neighbour technique to the SDSS and Herschel-SDP data from Section 3.2. Where *op* represents Optical (2,706 objects) and *FIR* represents FIR (902 objects).

Distributions Compared			KS Probability	MWU Probability
$z_{(op)}$	versus	$z_{(FIR)}$	0.999	0.403
$(g-r)_{op}$	versus	$(g-r)_{FIR}$	0.974	0.374
$(r-i)_{op}$	versus	$(r-i)_{FIR}$	0.395	0.239
$m_{r(op)}$	versus	$m_{r(FIR)}$	0.719	0.290
$(\bar{S}_c)_{op}$	versus	$(\bar{S}_c)_{FIR}$	$< 10^{-4}$	$< 10^{-5}$
$(g-r, r-i)_{op}$	versus	$(g-r, r-i)_{FIR}$	0.223	-
$(g-r, z)_{op}$	versus	$(g-r, z)_{FIR}$	0.956	-
$(r-i, z)_{op}$	versus	$(r-i, z)_{FIR}$	0.468	-
$(m_r, z)_{op}$	versus	$(m_r, z)_{FIR}$	0.755	-
$(g-r, m_r)_{op}$	versus	$(g-r, m_r)_{FIR}$	0.839	-
$(r-i, m_r)_{op}$	versus	$(r-i, m_r)_{FIR}$	0.339	-
$(g-r, \bar{S}_c)_{op}$	versus	$(g-r, \bar{S}_c)_{FIR}$	0.003	-
$(r-i, \bar{S}_c)_{op}$	versus	$(r-i, \bar{S}_c)_{FIR}$	0.003	-
$(m_r, \bar{S}_c)_{op}$	versus	$(m_r, \bar{S}_c)_{FIR}$	0.003	-
$(z, \bar{S}_c)_{op}$	versus	$(z, \bar{S}_c)_{FIR}$	0.004	-

3.3 Comparison With Semi-Analytic Models

The ΛCDM model of the universe has provided a solid foundation towards understanding the evolution of structure in the universe, where the initial density fluctuations in the CMB, coupled with rapid expansion of the early universe, results in hierarchical growth of structure. An important tool in the testing and refinement of such models, as well as evaluating the impact of dark-matter and dark-energy, is the ability to compare accurate observations with theoretical calculations.

As the hierarchical build up of structure in the universe is a definitively non-linear

process, these theoretical calculations can be represented as a simulation of a dynamical system of free 'particles' placed under the influence of pre-defined physical forces, known as an *N-body* simulation. As the dominant mass component in the universe (dark-matter) is suspected to consists of some elementary particle that only interacts gravitationally with the baryonic content of the universe, the free 'particles' in the *N-body* simulation can be considered representative of the dark-matter fluid. The *Millennium Simulation* (Springel et al., 2005b) maps the evolution of dark matter haloes from the early universe ($z = 127$) through to the present day. This is achieved via a large cosmological N-body simulation of the dark matter 'fluid' consisting of 2160^3 particles, each of mass $8.6 \times 10^8 h^{-1}\,\mathrm{M}_\odot$ within a co-moving box of $500h^{-1}$ Mpc in size. The simulation adopts the standard ΛCDM cosmological model with $\Omega_m = 0.25$, $\Omega_b = 0.045$, $h = 0.73$ and $\Omega_\Lambda = 0.75$ where $H_0 = 100\ h$ kms^{-1} Mpc^{-1}. Under this cosmology the dark-matter particle fluid was allowed to evolve from $z = 127$ to $z = 0$, a time-frame that was divided into 64 snapshots or 'time-slices'. Post-processing software was then used to identify all resolved dark-matter haloes and sub-haloes before linking these slices together with neighbouring outputs to produce a detailed formation 'tree' for each object (Springel et al., 2005b).

The detailed formation trees produced by the simulation can then be used as a foundation for various semi-analytic models (SAM's) that provide a description of the evolution of the mass and number density of dark-matter haloes. These SAM's are used to predict the evolution of galaxy properties such as stellar mass, luminosity, SFR, size, rotation velocity, morphology, gas content, metallicity, as well as scaling relations linking these properties. By adjusting the various astrophysical parameters that affect the baryonic component of the dark-matter halo within the SAM, the simulation output can then be compared to real observations (e.g. Croton et al. 2006; Bower et al. 2006; De Lucia & Blaizot 2007; Guo et al. 2011; Henriques et al. 2012). Any differences between the simulated output and observations suggests that one or more of the variable parameters is incorrect. Conversely, closely matched simulation outputs with real observations may indicate a SAM that is more representative of real astrophysical parameters. In recent years there have been several attempts at formulating a SAM

that represents a more accurate reproduction of real observations via application to the *Millennium Simulation* (e.g. Springel et al. 2005b; Croton et al. 2006; Bower et al. 2006; De Lucia & Blaizot 2007; Kitzbichler & White 2007; Guo et al. 2011). Each study makes refinements to the parameters of SAM's used in previous studies with the intent of improving the simulated-to-real comparison.

Here I use the semi-analytic models (SAMs) of Henriques et al. (2012), who construct 24 pencil-beam synthetic light-cones for square areas (1.4 deg $\times$ 1.4 deg) out to high redshift. These light-cones are based on the SAM of Guo et al. (2011) which itself is built upon previous SAMs, such as Croton et al. (2006), to take into account a full range of astrophysical processes; reionisation, cooling, disk size, star formation, supernova feedback, satellites, gas stripping, mergers, bulge formation, black hole growth, feedback from AGN, metal enrichment, dust extinction, stellar mass and the luminosity function. Each pencil-beam light-cone is constructed to account for the fact that each side of the co-moving Millennium Simulation box is equal to $500h^{-1}$Mpc which is smaller than the co-moving distance of an object at $z \sim 2$. Therefore periodic replication of the simulation can lead to multiples of the same object being included due to discontinuities in large scale structure at the boundaries between replications (Kitzbichler & White, 2007). *Pencil-beam* light-cones allow for the simulation to be sampled without including multiple images of the same object and thus represent the SAM's in a way that mimics real observations (for further discussion see Henriques et al. 2012).

3.3.1 SAM Analysis

Here I apply my environmental density measurement to the mock catalogues of Henriques et al. (2012) in order to establish whether the same relationship between environmental density and SFR is found. My results from Section 3.2 have shown there is a statistically significant difference between the density distributions of galaxies with and without obscured star formation (as traced by far-infrared emission), this is such that galaxies with obscured star formation favour under-dense regions, while galaxies without star-formation favour over-dense regions.

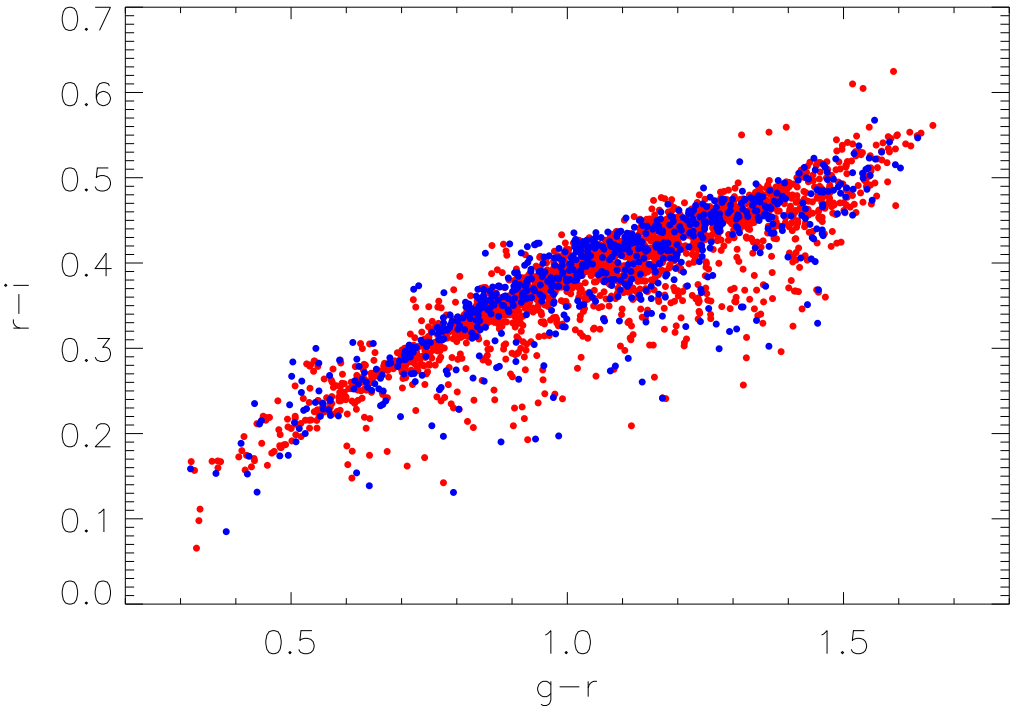

Figure 3.15: Plot of the $g - r$ versus $r - i$ colour distribution. The post-matched 2,184 Optical-Sim (*red*) objects overlaid by the pre-matched 728 FIR-Sim catalogue (*blue*).

I use all 24 Henriques et al. (2012) mock catalogues with additional data taken from the mock catalogue of Guo et al. (2011). The data is selected to span the same redshift range as my observed data ($0 < z \leq 0.5$), however these catalogues do not initially contain any errors on their redshifts. Therefore in order to achieve similar redshift sampling as within my environmental density measurement in Section 2.2, it was necessary to apply a redshift error to each object based on matching the r-band magnitude (m_r) and photometric redshift (z) values from the observed data catalogue. This therefore establishes a likely value for the redshift error based on these parameters. This is achieved by cross-matching each simulated Henriques & Guo object (hereafter Sim) to the total Optical-9hr catalogue, locating all matches in r-band magnitude (m_r) and best-fit photometric redshift (z). For each match, the photometric error from the Optical-9hr catalogue is applied as the redshift error to the Sim object. Where a spectroscopic redshift is located, a standard error for a spectroscopic redshift (0.001) is applied, as in the initial analysis (Section 2.2). In addition, as with the observed

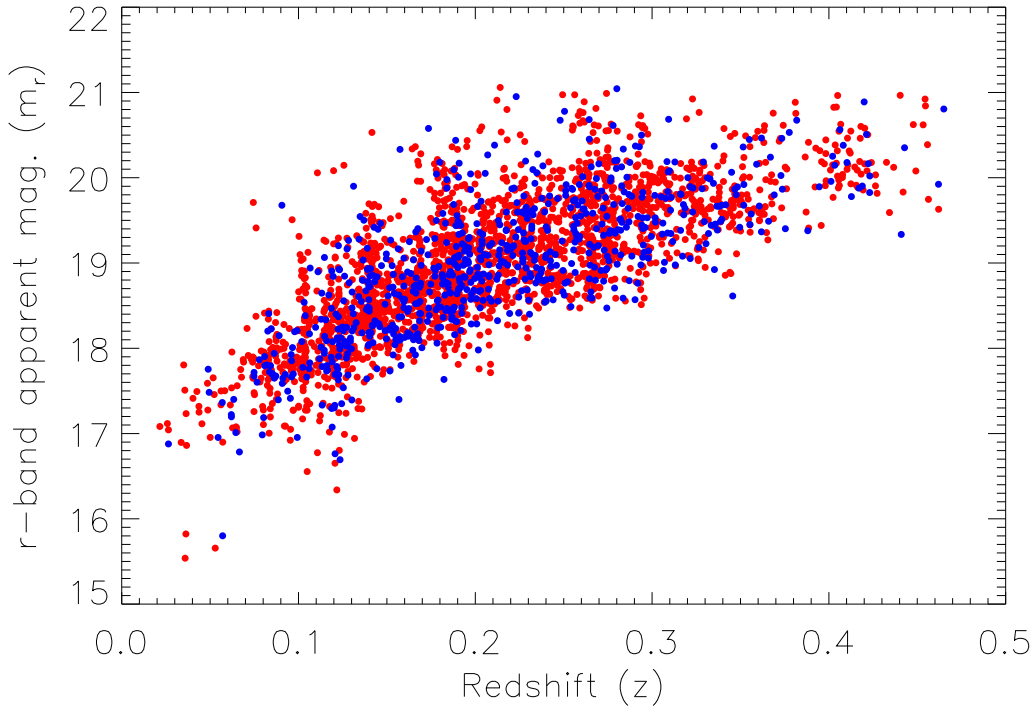

FIGURE 3.16: Plot of the redshift versus r-band magnitude (m_r) distribution. The post-matched 2,184 Optical-Sim (*red*) objects overlaid by the pre-matched 728 FIR-Sim catalogue (*blue*).

data in Section 3.1.2, an apparent r-band magnitude cut was implemented removing all fainter magnitudes than 21.5. The resultant number of objects across the Sim catalogue totals 260,303 objects. Applying the environmental density measure returns normalised environmental density values in comparison to a random field ($\bar{S}_c$) for each object, as with the observed data in Section 2.2.2. However, due to the smaller field size ($-0°.7 < \mathrm{RA} < 0°.7$ and $-0°.7 < \mathrm{Dec} < 0°.7$) the edge-effect cuts imposed during the analysis have a greater impact on the number of sources cut from my Sim catalogue, further reducing the catalogue to 112,125 objects.

Next it was necessary to determine which galaxies in the simulated catalogue would have far-infrared emission, and thus be detectable by the H-ATLAS survey. This was achieved by calculating the 250μm flux for each object from the given SFR and redshift values given by the SAM. This was the direct reverse of the calculation in Chapter

3.2.5 where I calculate the SFR assuming a temperature and emissivity index, from the 250μm flux of each FIR galaxy. At this point 19,616 objects are found not to have SFR information from the SAM output and these are removed from the analysis. The 5σ 250μm flux limit of the H-ATLAS observations (33.5 mJy), taken from Rigby et al. (2011), provides an exact cut-off point for which a galaxy could be considered detectable in the survey. From here the Sim catalogue could be split into IR and non-infrared detected objects, equivalent to my FIR and Optical catalogues in my observed data. Objects with a 250 μm flux density greater than 33.5 mJy are therefore considered detectable by H-ATLAS, hereafter called FIR-Sim (1,919 objects), and those with a 250 μm flux density less than 33.5 mJy are not considered detectable by H-ATLAS and hereafter named Optical-Sim (110,206 objects).

As with my observed data, a like-for-like cross-matching process is applied. I find 2,184 objects from the Optical-Sim population, matched with 728 objects from the FIR-Sim population. Both of these cross-matched samples represent approximately the same percentage of their parent populations as found with my observed cross-matched samples. This was such that the cross-matched Optical and Optical-Sim samples represent $\sim$ 2 and $\sim$ 1 per cent of their parent populations respectively, with the FIR and FIR-Sim samples representing $\sim$ 40 and $\sim$ 35 per cent respectively. The distributions are shown in figures 3.15 and 3.16 illustrating the extent of the populations after the cross-matching.

3.3.2 SAM Statistical Testing

I perform the same statistical analysis, as with the observed data, i.e. applying two sample and two-dimensional KS-tests as well as MWU-tests to the two cross-matched populations. The results of these tests are given in Table 3.6, and show that the null hypothesis can be rejected to at least the 4σ level for the normalised environmental density ($\bar{S}_c$) of the Optical-Sim and FIR-Sim populations, in agreement with my observed data in Section 3.2.3. All other parameter comparisons cannot be considered significantly different at any reliable statistical level.

Table 3.6: Two sample and two-dimensional KS- and MWU-test results over full redshift range ($0 < z \leq 0.5$) where x represents Optical-Sim (2,184 objects) and y represents FIR-Sim (728 objects).

Distributions Compared			KS Prob.	MWU Prob.
z_{op}	versus	z_{FIR}	0.658	0.318
$(g-r)_{op}$	versus	$(g-r)_{FIR}$	0.990	0.452
$(r-i)_{op}$	versus	$(r-i)_{FIR}$	0.198	0.172
$m_{r(op)}$	versus	$m_{r(FIR)}$	0.237	0.125
$(\bar{S}_c)_{op}$	versus	$(\bar{S}_c)_{FIR}$	$< 10^{-4}$	$< 10^{-5}$
$(g-r, r-i)_{op}$	versus	$(g-r, r-i)_{FIR}$	0.131	-
$(g-r, z)_{op}$	versus	$(g-r, z)_{FIR}$	0.751	-
$(r-i, z)_{op}$	versus	$(r-i, z)_{FIR}$	0.278	-
$(m_r, z)_{op}$	versus	$(m_r, z)_{FIR}$	0.081	-
$(g-r, m_r)_{op}$	versus	$(g-r, m_r)_{FIR}$	0.343	-
$(r-i, m_r)_{op}$	versus	$(r-i, m_r)_{FIR}$	0.090	-
$(g-r, \bar{S}_c)_{op}$	versus	$(g-r, \bar{S}_c)_{FIR}$	$< 10^{-3}$	-
$(r-i, \bar{S}_c)_{op}$	versus	$(r-i, \bar{S}_c)_{FIR}$	$< 10^{-3}$	-
$(m_r, \bar{S}_c)_{op}$	versus	$(m_r, \bar{S}_c)_{FIR}$	0.002	-
$(z, \bar{S}_c)_{op}$	versus	$(z, \bar{S}_c)_{FIR}$	0.001	-

The two density distributions are shown in Figure 3.17. As expected, it is the FIR-Sim population (*blue*), with the mean of its distribution at $\bar{S}_c = (-4.84 \pm 1.54) \times 10^{-2}$ (*blue dashed line*), that is biased towards underdense regions, while the Optical-Sim population (*red*), with the mean of its distribution at $\bar{S}_c = (2.59 \pm 1.72) \times 10^{-2}$ (*red dashed line*), shows a bias towards overdense regions. It is worth noting that if I do not include simulated photometric errors and treat the SAM redshift values as precise, the resultant $\bar{S}_c$ distributions exhibit a much larger spread in values. Inclusion of photometric errors evidently reduces this spread by essentially 'washing out' the density structure I am trying to recover. However, when precise redshifts values are used, I

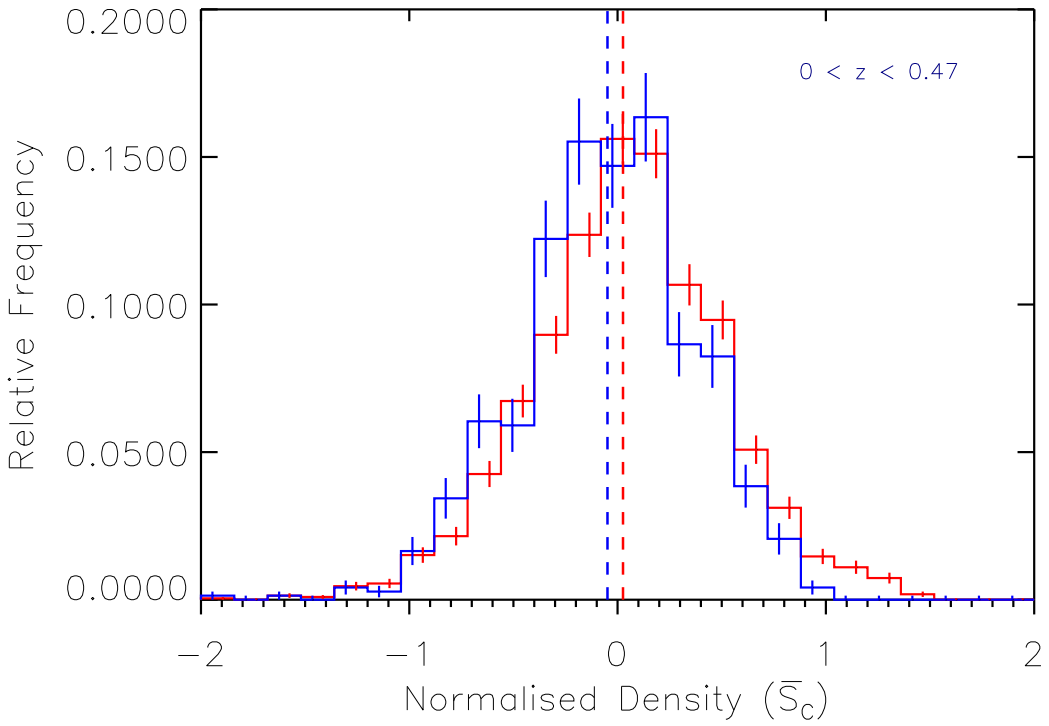

Figure 3.17: A normalised histogram of both environmental density ($\bar{S}_c$) distributions from the total Optical-Sim (*red*) and FIR-Sim (*blue*) populations with 2,184 and 728 objects respectively.

find the same correlations are found between the Optical-Sim and FIR-Sim populations, despite the increased spread, with both populations exhibiting a significant difference. As described in Section 3.2.1, this flattening of the density structure may be due to the associated photometric redshift errors being larger than the redshift binning applied. This is investigated in the appendices, where I repeat the density analysis using wider redshift binning.

To further examine the difference found between the Optical-Sim and FIR-Sim populations I once more split the two populations into redshift bins, repeating the analysis from Section 3.2.3. Figure 3.18 shows the redshift distributions of both the FIR (dashed line) and FIR-Sim (solid line) data. It is immediately clear that the FIR-Sim population is primarily weighted towards lower redshifts with a mean value of $(1.82 \pm 0.02) \times 10^{-1}$. Its number density falls off beyond $z \sim 0.25$ reaching a maximum redshift of $z = 0.47$, short of the full redshift range of the FIR sample. In

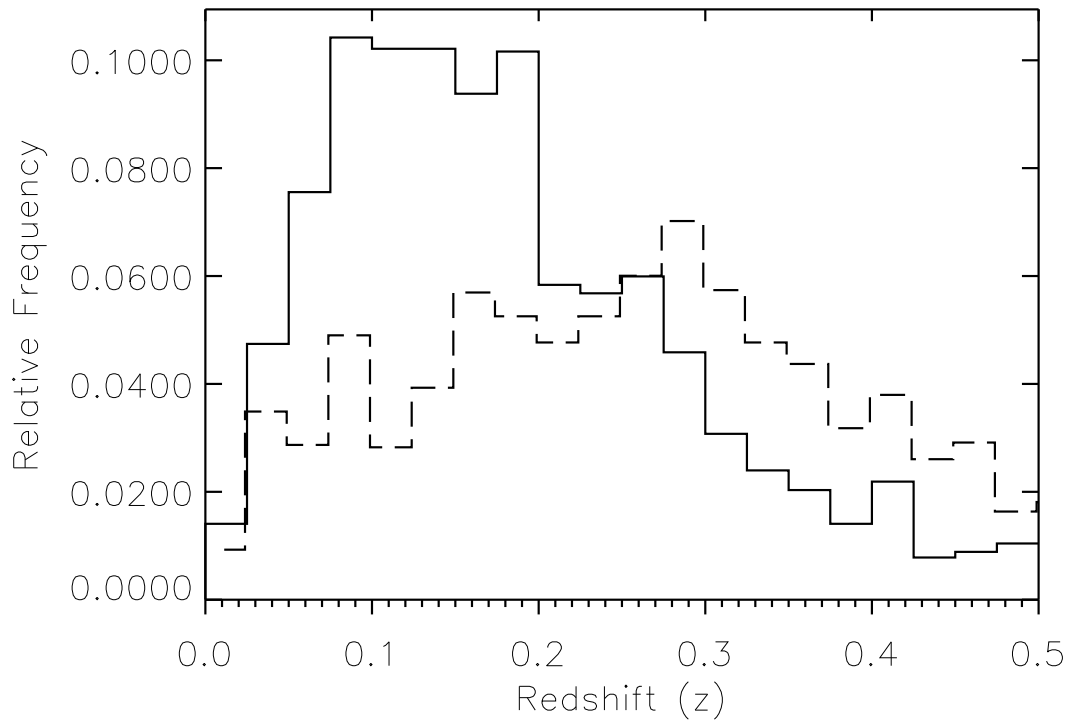

FIGURE 3.18: *Solid line*: The total FIR-Sim redshift distribution showing a clear weighting towards lower redshifts. *Dashed line*: The total FIR redshift distribution showing a more uniform redshift distribution.

comparison, the FIR population retains an approximately consistent number density across its entire redshift range with a mean value of $(3.30 \pm 0.04) \times 10^{-1}$. Therefore it was necessary to adjust the redshift binning from that applied to the FIR data in Section 3.2.3 to account for this difference. Reducing the boundary between my higher and lower redshift bins from $z = 0.25$ to $z = 0.22$, I bin the Optical-Sim and FIR-Sim populations, re-plotting histograms to represent the data within these redshift bins and reapplying KS-tests and MWU-tests to the data. The redshift bins are plotted as normalised histograms in Figure 3.19 and the KS- and MWU-test results from this redshift binning are given in Table 3.7.

Within the lower redshift bin ($0 < z \leq 0.22$) the statistical results show that with a KS probability of 0.020 and MWU probability of 0.003, the two populations are significantly different and that the null hypothesis can be rejected to at least the 2.4σ level. In agreement with my observational results it is the FIR-Sim population which

Table 3.7: KS-test and MWU-test results for both the Optical-Sim and FIR-Sim populations for $\bar{S}_c$ distributions within the individual redshift slices shown in Figure 3.19. The null hypothesis is rejected at the 2.4σ-2.9σ level for both distributions in the lower redshift bin from KS- and MWU-tests. The null hypothesis is rejected at the 3.4σ-3.9σ level in the higher redshift bin:

Redshift Slice	Optical	IR	KS Prob.	MWU Prob.
$0 \leq z < 0.22$	1,273	418	0.020	0.003
$0.22 \leq z < 0.47$	911	310	$< 10^{-3}$	$< 10^{-4}$

is found to occupy less dense regions with mean $\bar{S}_c$ values of $(2.38 \pm 2.70) \times 10^{-2}$ and $(-3.25 \pm 2.05) \times 10^{-2}$ for the Optical-Sim (*red*) and FIR-Sim (*blue*) populations respectively. Within the higher redshift bin ($0.22 < z \leq 0.47$), despite the drop-off in the number of Optical-Sim and FIR-Sim objects in comparison to my observed data, statistical tests returned a KS probability of 6.33×10^{-3} and a MWU probability of 9.63×10^{-5} indicating that the null hypothesis is rejected to at least the 3.4σ level. Again it is the FIR-Sim population occupying more underdense regions with mean $\bar{S}_c$ values of $(2.88 \pm 1.50) \times 10^{-2}$ and $(-6.99 \pm 2.33) \times 10^{-2}$ for the Optical-Sim (*red*) and FIR-Sim (*blue*) populations respectively. These statistical tests confirm that the same SFR-density trend with redshift is found as with my observational data analysis in Section 3.2.3. This trend is found despite the observed differences between the redshift distributions of both observed and simulated FIR data sets (Figure 3.18).

3.3.3 Applying SFR Limits to SAM

As noted in Section 3.2.5 my calculation of the SFR from far-infrared luminosity is subject to a range of assumptions that may, or may not, be valid. Furthermore, the parameters used within the SAM to calculate SFR may also not accurately incorporate all of the physical processes that govern SFR. Detailed analysis of these effects are beyond the scope of this thesis, therefore I adopt a conservative approach and consider that the results from the observations and the SAMs are in qualitative agreement.

Here I repeat the same SFR binning analysis from Section 3.2.5 to the SAMs. The

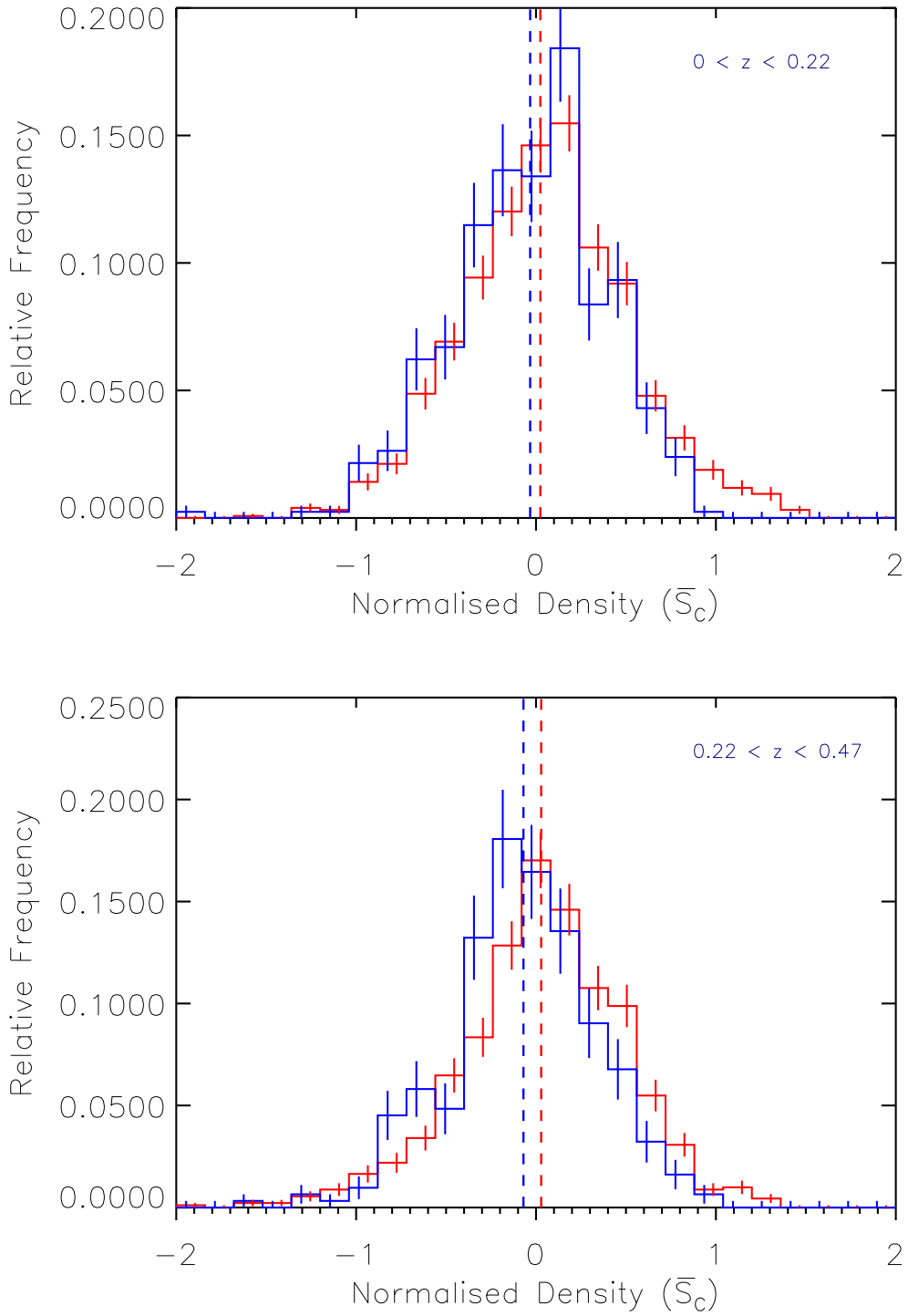

FIGURE 3.19: Normalised histograms showing how the distribution of environmental density ($\bar{S}_c$) of the colour matched Optical-Sim (*red*) and FIR-Sim (*blue*) populations change with redshift for the redshift bins $0 < z \leq 0.22$ (*top*) and $0.22 < z \leq 0.47$ (*bottom*).

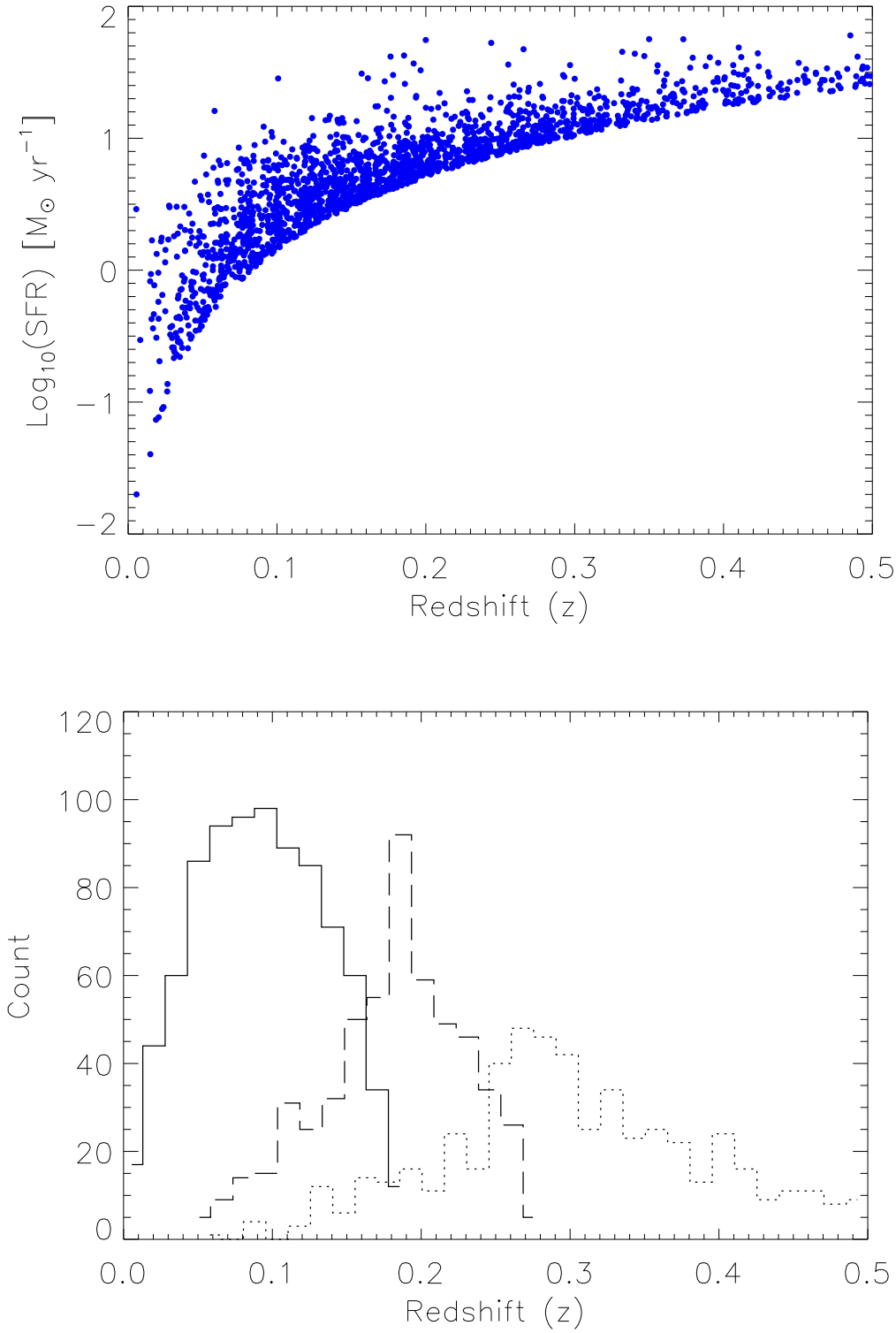

Figure 3.20: *Top*: SFR ($M_\odot\,yr^{-1}$) versus redshift for the total FIR-Sim catalogue. This shows that above 10 $M_\odot\,yr^{-1}$ the number of objects reduces significantly. *Bottom*: Plot of the three SFR bins from the FIR-Sim catalogue versus redshift. The $0 < SFR < 5\,M_\odot\,yr^{-1}$ bin (Solid line) containing 846 objects, the $5 < SFR \leq 10\,M_\odot\,yr^{-1}$ bin (Dashed line) containing 547 objects and the $SFR > 10\,M_\odot\,yr^{-1}$ bin (Dotted line) containing 526 objects.

reduction in the number of FIR-Sim objects between the low and high redshift bins is illustrated in Figure 3.20. This shows how the number density of the FIR-Sim population falls off beyond $z \sim 0.25$, in comparison with the observed data in Figure 3.8. It is evident that the FIR-Sim population has a higher fraction of sources at higher redshifts than the FIR population. Due to the majority of the FIR-Sim population residing below $z \sim 0.25$ it is necessary to adjust the SFR binning parameters, from those applied to the FIR population, to narrower SFR ranges in order to achieve three comparative samples of this population. I therefore bin the FIR-Sim objects in terms of their SFR in bins of $0-5$, $5-10$ and $>10\,\mathrm{M}_{\odot}\,\mathrm{yr}^{-1}$. All statistical results for the following SFR binning are displayed in Table 3.8.

Beginning with an initial bin of $0-5\,\mathrm{M}_{\odot}\mathrm{yr}^{-1}$ which contains 846 of the 1,919 FIR-Sim objects, cross-matching this reduced catalogue to the Optical-Sim catalogue, as in Chapters 3.2.2 and 3.3.1, yields a reduced number of Optical-Sim objects down from 2,184 to 729 and a significantly reduced number of FIR-Sim objects down from 728 to just 243. Applying KS- and MWU-tests to the two populations I find no significant difference between the density distributions of the two populations within this SFR bin. The two density distributions are shown in Figure 3.21, with a KS probability of 0.450 and a MWU probability of 0.098 failing to indicate a significant difference at any reasonable confidence limit. The mean of the FIR-Sim density distribution is situated at $\bar{S}_c = (-1.47 \pm 2.78) \times 10^{-2}$ and the mean of the Optical-Sim density distribution at $\bar{S}_c = (-3.85 \pm 45.5) \times 10^{-3}$, indicating generally less dense values of FIR-Sim although not significantly.

The second bin of $5-10\,\mathrm{M}_{\odot}\mathrm{yr}^{-1}$ contains 547 FIR-Sim objects, cross-matching this with the Optical-Sim catalogue yields 984 Optical-Sim objects and 328 FIR-Sim objects. Applying KS- and MWU-tests returned probability values indicating a significant difference between the two density distributions, with a KS and MWU probabilities of 0.001 implying a significant difference at the 3.3σ level. The two density distributions are displayed in Figure 3.22. The mean of the FIR-Sim density distribution is $\bar{S}_c = (-5.97 \pm 2.21) \times 10^{-2}$ and the mean of the Optical-Sim density distribution at $\bar{S}_c = (2.83 \pm 1.48) \times 10^{-2}$, indicating an increased separation at these higher SFRs,

Table 3.8: Two sample KS and MWU-test results where *op* represents Optical-Sim and *FIR* represents FIR-Sim. (A): SFR of 0 to 5 $M_\odot\,yr^{-1}$ containing Optical-Sim 729 objects and 243 FIR-Sim objects. (B): SFR of 5 to 10 $M_\odot\,yr^{-1}$ containing 984 Optical-Sim objects and 328 FIR-Sim objects. (C): SFR of > 10 $M_\odot\,yr^{-1}$ containing 669 Optical-Sim objects and 223 FIR-Sim objects:

Distributions Compared			KS Prob. (A)	MWU Prob. (A)	KS Prob. (B)	MWU Prob. (B)	KS Prob. (C)	MWU Prob. (C)
z_{op}	versus	z_{FIR}	0.175	0.201	0.310	0.277	0.344	0.443
$(g-r)_{op}$	versus	$(g-r)_{FIR}$	0.947	0.328	0.965	0.423	0.770	0.322
$(r-i)_{op}$	versus	$(r-i)_{FIR}$	0.125	0.090	0.057	0.080	0.958	0.360
$m_{r(op)}$	versus	$m_{r(FIR)}$	0.065	0.134	0.909	0.301	0.216	0.089
$(\bar{S}_c)_{op}$	versus	$(\bar{S}_c)_{FIR}$	0.450	0.098	0.001	0.001	0.004	$< 10^{-3}$

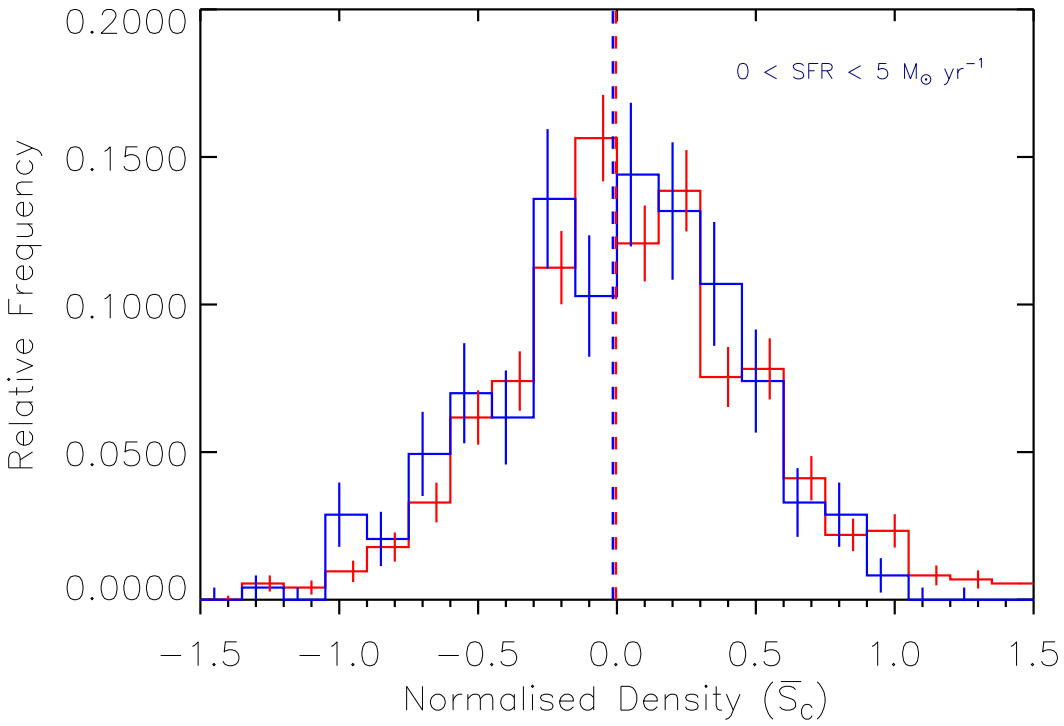

Figure 3.21: Normalised histograms of both environmental density ($\bar{S}_c$) distributions from the Optical-Sim (*red*) and FIR-Sim (*blue*) populations across 0 to 5 $M_{\odot}yr^{-1}$ SFR bin containing 729 and 243 objects respectively. The mean values of the two distribution (*red-* and *blue-dashed* lines) are also shown.

with the FIR-Sim density distribution favouring underdense regions.

Further increasing my SFR bin to include all objects with $SFR > 10\,M_{\odot}yr^{-1}$ contains 526 FIR-Sim objects, cross-matching this with the Optical-Sim catalogue yields 669 Optical-Sim objects and 223 FIR-Sim objects. The statistical tests once more returned probability values indicating a significant difference between the two density distributions. With KS and MWU probabilities returned of 0.004 and 4.19×10^{-4} respectively, indicating a significant differences between the density distributions to at least the 3.0σ level. The distributions are displayed in Figure 3.23 with the mean of the FIR-Sim distribution at $\bar{S}_c = (-4.09 \pm 2.85) \times 10^{-2}$ and the mean of the Optical-Sim distribution at $\bar{S}_c = (6.88 \pm 1.75) \times 10^{-2}$.

For SFR bins of $5 - 10$ and $> 10\,M_{\odot}\,yr^{-1}$, I find that with higher levels of star

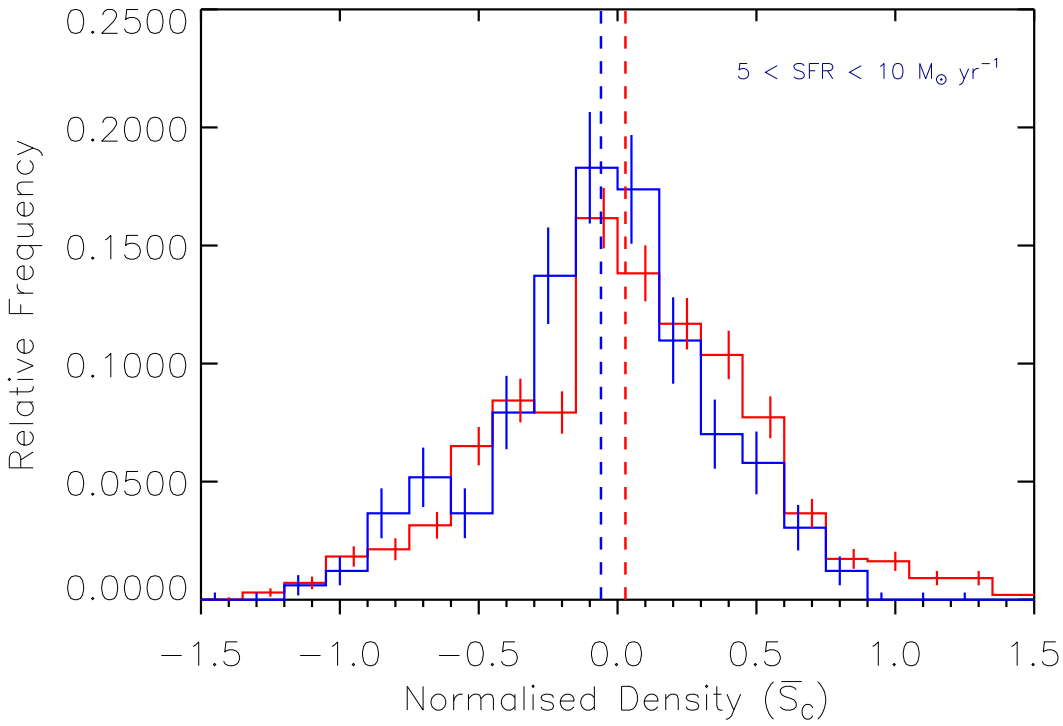

Figure 3.22: Normalised histograms of both environmental density ($\bar{S}_c$) distributions from the Optical-Sim (*red*) and FIR-Sim (*blue*) populations across 5 to 10 $M_{\odot}yr^{-1}$ SFR bin containing 984 and 328 objects respectively. The mean values of the two distribution (*red-* and *blue-dashed* lines) are also shown.

formation the statistical difference between the two populations from KS- and MWU-tests increases, as shown in Table 3.8 and in agreement with my results in Section 3.2.5. However, in the lowest SFR bin ($0-5\,M_{\odot}\,yr^{-1}$) there is no significant difference found. This is likely due to the fact that there is a smaller SFR range in the simulated data, leading to a smaller number of objects within this lower bin compared to the observed data. Figure 3.20 shows how, at higher SFRs, the number density of objects reduces to such an extent that it makes further analysis unfeasible. Thus, it was not possible to introduce bins at higher SFRs than $10\,M_{\odot}yr^{-1}$ to the analysis. Despite this, some key conclusions can be made with regards to the Optical-Sim/ FIR-Sim comparison based on the three SFR bins. For galaxies with SFRs higher than 5 $M_{\odot}yr^{-1}$, there is a statistically significant difference between both $\bar{S}_c$ distributions of the Optical-Sim and FIR-Sim populations. This statistical difference becomes more pronounced in the bins

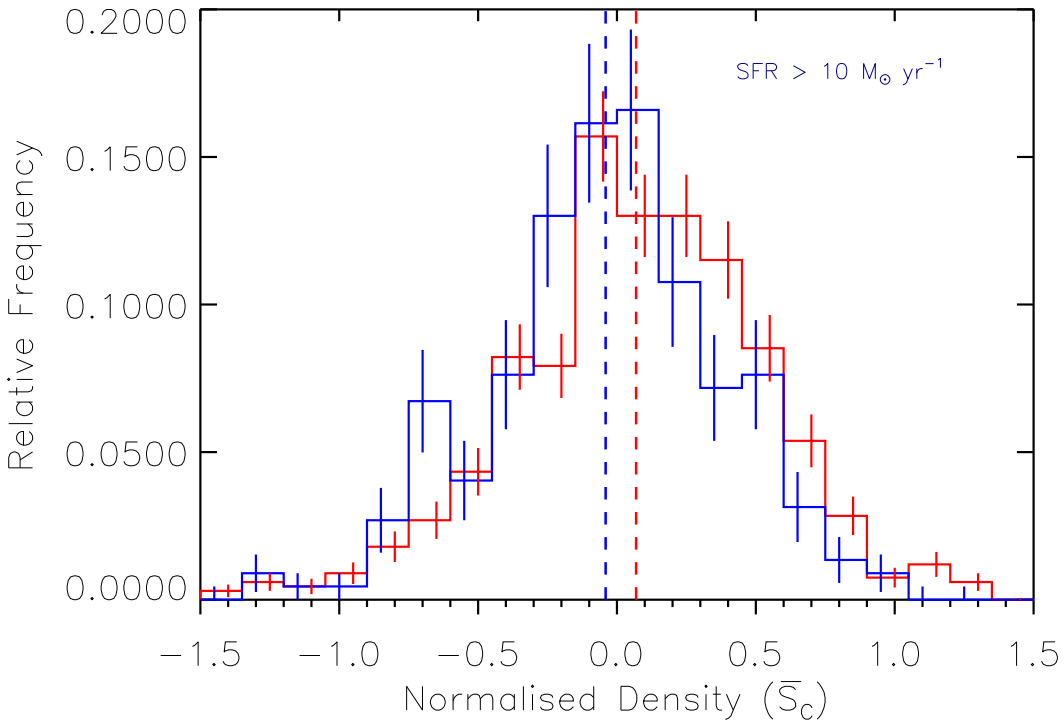

Figure 3.23: Normalised histograms of both environmental density ($\bar{S}_c$) distributions from the Optical-Sim (*red*) and FIR-Sim (*blue*) populations across $< 10\,\mathrm{M_\odot yr^{-1}}$ SFR bin containing 669 and 223 objects respectively. The mean values of the two distribution (*red-* and *blue-dashed* lines) are also shown.

of higher SFR and this is a result of the removal of objects with lower SFRs from the comparison. This ranges from there being no statistical difference found between the $\bar{S}_c$ distributions when SFRs are less than 5 $\mathrm{M_\odot yr^{-1}}$, to finding a significant difference at the 3σ level in the highest SFR bin.

3.3.4 Nearest Neighbour SAM Results

I again apply the full statistical analysis to the SAM data using the Nth-nearest neighbour technique established in Chapter 2.3. Following the same processes from Sections 3.3.1 and 3.3.2 I apply the algorithm, changed to incorporate the NN method, to the total Sim catalogue, again dividing the output according to the H-ATLAS flux limit (33.5 mJy) and cross-matching in $g-r$, $r-i$, z and m_r parameter space. This, once again, provided two catalogues representative of optical and far-infrared (Optical-Sim

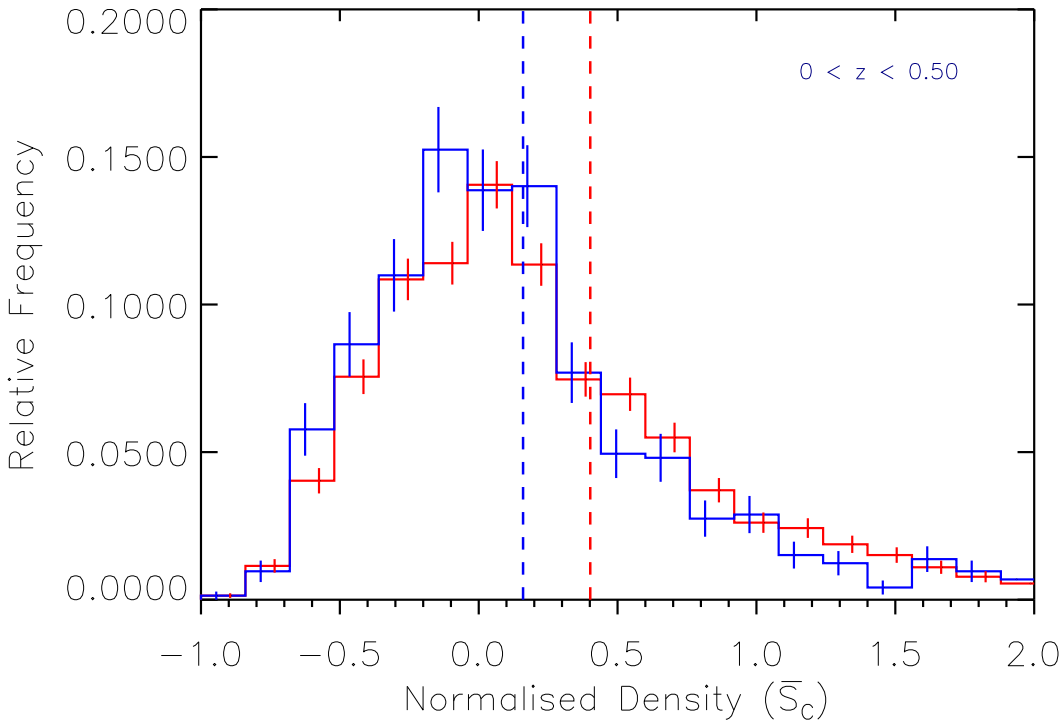

Figure 3.24: A normalised histogram of both environmental density ($\bar{S}_c$) distributions from the total Optical-Sim (*red*) and FIR-Sim (*blue*) populations after the application of the 5th-nearest neighbour technique (2,184 and 728 objects respectively). The FIR data is shifted generally to lower $\bar{S}_c$ values, with the mean of its distribution at $(1.60 \pm 0.21) \times 10^{-1}$ (*blue dashed line*) contrasted against the mean of the Optical distribution at $(4.02 \pm 0.24) \times 10^{-1}$ (*red dashed line*).

and FIR-Sim) that can be accurately compared to analyse differences in density.

I find that these results match those of Section 3.3.2, with KS- and MWU-test results finding a significant difference between the normalised densities of the Optical-Sim and FIR-Sim populations only. With a KS- and MWU-tests returning probabilities of 1.08×10^{-5} and 3.87×10^{-6} respectively indicating a significant difference at $> 4\sigma$ in both cases. All statistical results are displayed in Table 3.9. The mean values of each distribution lie at $(4.02 \pm 0.24) \times 10^{-1}$ for the Optical-Sim and $(1.60 \pm 0.21) \times 10^{-1}$ for the FIR-Sim indicating that the Optical-Sim population occupies generally more overdense regions in agreement with my study using VT. Figure 3.24 shows a histogram of the two density distributions illustrating a clear difference between these two density distributions.

Table 3.9: Two sample and two-dimensional KS- and MWU-test results from the application of the 5th-nearest neighbour technique to my semi-analytic model analysis Optical-Sim and FIR-Sim populations. Where *op* represents Optical-Sim (2,184 objects) and *FIR* represents FIR-Sim (728 objects).

Distributions Compared			KS Probability	MWU Probability
z_{op}	versus	z_{FIR}	0.658	0.318
$(g-r)_{op}$	versus	$(g-r)_{FIR}$	0.990	0.452
$(r-i)_{op}$	versus	$(r-i)_{FIR}$	0.198	0.172
$m_{r(op)}$	versus	$m_{r(FIR)}$	0.237	0.125
$(\bar{S}_c)_{op}$	versus	$(\bar{S}_c)_{FIR}$	$< 10^{-4}$	$< 10^{-5}$
$(g-r, r-i)_{op}$	versus	$(g-r, r-i)_{FIR}$	0.131	-
$(g-r, z)_{op}$	versus	$(g-r, z)_{FIR}$	0.751	-
$(r-i, z)_{op}$	versus	$(r-i, z)_{FIR}$	0.278	-
$(m_r, z)_{op}$	versus	$(m_r, z)_{FIR}$	0.081	-
$(g-r, m_r)_{op}$	versus	$(g-r, m_r)_{FIR}$	0.343	-
$(r-i, m_r)_{op}$	versus	$(r-i, m_r)_{FIR}$	0.090	-
$(g-r, \bar{S}_c)_{op}$	versus	$(g-r, \bar{S}_c)_{FIR}$	$< 10^{-3}$	-
$(r-i, \bar{S}_c)_{op}$	versus	$(r-i, \bar{S}_c)_{FIR}$	$< 10^{-3}$	-
$(m_r, \bar{S}_c)_{op}$	versus	$(m_r, \bar{S}_c)_{FIR}$	0.001	-
$(z, \bar{S}_c)_{op}$	versus	$(z, \bar{S}_c)_{FIR}$	$< 10^{-3}$	-

3.4 Discussion

The increased statistical separation between the Optical and FIR density distributions, found with both increasing redshift and increasing SFR, provides a clue to the role of environment in the evolution of galaxies over the redshift range ($0 < z \leq 0.5$). I have found a clear segregation in the galaxy environmental density between far–infrared-detected sources and those galaxies that are matched in terms of optical colour, magnitude and redshift but devoid of detectable far-infrared emission. Moreover, I find that this segregation becomes more pronounced at brighter far-infrared luminosity (or

SFR) or at higher redshift. Unfortunately the data precludes me from distinguishing between an evolutionary effect and one associated with the level of star formation activity.

It is important to note that the reliability criterion ($R \geq 0.8$), that I employ from Smith et al. (2011) to select optical counterparts to the FIR data, could cause a bias in my results. This potential bias is such that in denser regions, with an increased number of potential optical counterparts to a FIR object, the reliability parameter for that FIR object, as defined in Smith et al. (2012a), would reduce. In other words, in denser regions it potentially becomes more difficult to reliably associate the FIR detection with a unique optical source. Therefore the FIR object may be excluded leaving only the FIR detections in relatively low-density environments. I tested this possible bias by making a more inclusive cut to the FIR sample based on the minimum likelihood-ratio (LR; see Smith et al. 2011 for further details) rather than the reliability criterion (R). The FIR sample was therefore increased to include these previously missing sources. Upon repeating the analysis I found that I still obtained similarly significant differences between the FIR and Optical samples.

The results presented in this chapter support previous studies that also suggest the presence of star formation in a galaxy is negatively correlated with the density of its environment (e.g. Dressler 1980; Postman & Geller 1984; Dressler et al. 1997; Domínguez et al. 2001; Goto et al. 2003; Kauffmann et al. 2004; O'Mill et al. 2008; Lee et al. 2010). My analysis has shown that this correlation holds on individual galaxy scales, and thus the processes responsible for this correlation must have influence at this level as well as on larger scales. In addition, the use of far-infrared observations mean my results are not affected by uncertainties associated with extinction. However, the exact mechanism responsible for the observed reduction of SFR with increase in density remains uncertain. Recent studies by Deng et al. (2011) and Wijesinghe et al. (2012) suggest that there is no trend with environment when restricting the SFR-density comparison to purely star forming objects. They conclude that the observed SFR-density correlation is due to the increasing fraction of passive galaxies across the total galaxy sample since $z \sim 1$. Deng et al. (2011) go further and suggest that the

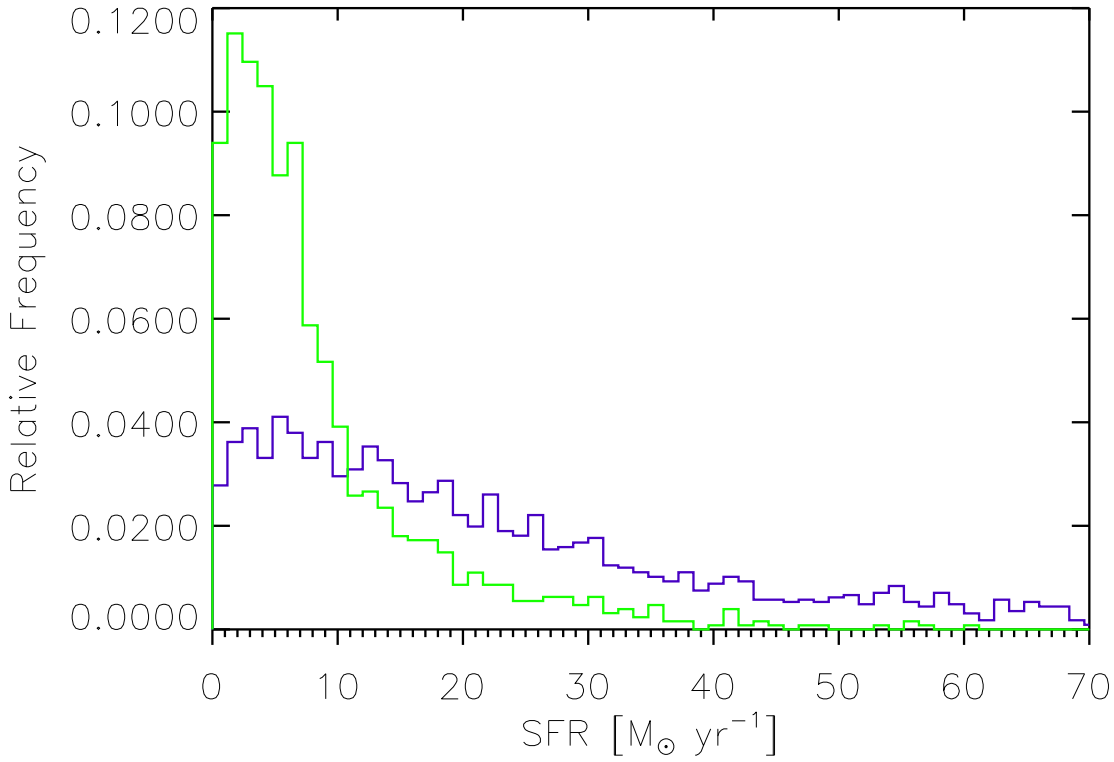

Figure 3.25: *Green line:* The total FIR-Sim SFR distribution showing a clear weighting towards lower redshifts. *Blue line:* The total FIR SFR distribution showing a more uniform redshift distribution.

SFR-density relation is strongly colour dependent, with blue galaxies exhibiting a very weak correlation between environment and SFR. In contrast, they find red galaxies to exhibit a strong correlation between environmental density and SFR attributing this to the increasing presence of red late-type morphologies.

As this analysis has focused on the direct comparison of star formation properties with the individual environmental densities of each object, I have shown that there is a clear difference between the star-forming and passive population in my colour-matched samples in agreement with earlier work by Gómez et al. (2003) and Welikala et al. (2008). Furthermore, I have carried out the same analysis on Semi-Analytic Models (SAMs) where I obtain a similar result, i.e. the environmental density distributions from the total simulated Optical-Sim and FIR-Sim populations were found to be significantly different at the 3σ level. Qualitative agreement is also found when I bin in terms

of both redshift and SFR. This SFR-density trend with redshift is found despite the observed discrepancies between the redshift distributions of both observed and simulated FIR data sets (Figure 3.18). As I determine the FIR-Sim population by selecting objects based on their 250μm flux, which is itself calculated from the individual SFR derived from the SAM of Guo et al. (2011), I can investigate this population difference by investigating the origin of these SFR values. It is possible that the parameters used within the SAM to calculate these SFR are not accurately representing the physical processes that govern star formation in the universe. Figure 3.25 shows a histogram of the SFRs of both total FIR (*blue line*) and FIR-Sim (*green line*) populations. What is instantly noticeable is that the SFR of the FIR-Sim population are predominantly dominated by low SFR objects ($< 10\,\mathrm{M_{\odot}yr^{-1}}$) in contrast to the FIR population which is more evenly distributed with fewer galaxies with low SFRs and more galaxies with high SFRs than the FIR-Sim population. There may be several potential explanations for these observed differences, such as either an underestimation of the amount of FIR-Sim emission at higher redshifts or the prediction of a brighter population of star forming galaxies at lower redshifts than is actually observed.

In order to investigate this further I examine the semi-analytic model of Guo et al. (2011) - and by extension its progenitor from Croton et al. (2006) - to determine what are the key assumptions that lead to the difference in environmental density between star-forming galaxies and their more quiescent counterparts.

AGN Radiative Feedback:

The SAM invokes AGN feedback effects to suppress cooling flows during the hierarchical build up of structure. This includes both the radio (accretion driven) and quasar (merger driven) modes of black hole growth. However, Guo et al. (2011) state that they do not explicitly account for radiative feedback from their AGN (optical/ultraviolet and X-ray emission from AGN ionising and heating their surrounding IGM leading to the suppression of cooling flows and the quenching of future star formation), despite acknowledging that there is substantial evidence for such processes. Instead they assume that this radiative feedback is closely associated with starbursts in merging

galaxies and as such can be partially represented in the SAM by an enhanced feedback efficiency associated with star formation and supernova feedback (Croton et al., 2006). However, in the real universe, despite a fraction of this ionising radiation coming from star formation related feedback, a significant contribution will be from radiative AGN feedback, especially at lower redshifts ($z \lesssim 2$) where the number density of star forming galaxies decreases (e.g. Mo et al. 2010; van de Voort et al. 2011; Kimm et al. 2012). By not accounting for this radiative feedback in their SAM, gas cooling flows in low-mass galaxies will not be suppressed at lower redshifts and thus will continue to form stars to later times than observed. This may lead to the observed weighting at lower redshifts in the FIR-Sim population as illustrated in Figure 3.18.

Major/Minor Merger Definition:

The SAM treatment of mergers may also be a factor in the noted discrepancies between simulated and observed FIR distributions. As detailed in Chapter 1, these violent interactions between two galaxies can be divided into two sub-categories (major or minor) which are dependent on the mass ratios of the merging galaxies themselves. A major merger will destroy the disks of the interacting progenitors leading to a change in structure towards a spheroidal morphology. This will include an initial significant starburst event, followed by a reduction in the overall SFR in that galaxy towards lower redshift. In contrast, the larger galaxy within a minor merger will accrete the cold gas and stellar component of the smaller galaxy with a less significant starburst event and no overall loss of SFR or morphology change (e.g. Barnes & Hernquist 1991; Heller & Shlosman 1994; Mihos & Hernquist 1996; Athanassoula 2003; Mo et al. 2010; Lee et al. 2012). Guo et al. (2011) define their major merger interactions as where the baryonic mass of both galaxies differ by less than a factor of 3. A larger mass difference than this constitutes a minor merger in their SAM. This mass difference between the progenitors of the merger is taken from Springel et al. (2001) who imply that this value is assumed without consideration to its potential evolutionary impact. The use of this mass ratio limit in the SAM therefore appears quite arbitrary. If this value is in fact too low, then it is possible that galaxies are being treated as minor

mergers within the SAM where in reality they should be undergoing a major type merger event. Consequently they will not undergo the SFR quenching at later times as would be expected observationally. This could lead to continued star formation in areas undergoing interactions and post-interaction (feedback) effects, at lower redshifts than are actually observed.

Warm Dust Component:

Figure 3.18 shows that at higher redshifts there is a turn-over in the relationship between the FIR and FIR-Sim populations in terms of their relative number densities. Beyond $z \sim 0.2$ the number density of galaxies in the FIR-Sim population drops-off in comparison with the FIR population, in contrast to the distributions at lower redshifts. This drop-off may be related to the assumptions made within the SAMs already discussed. However, it is also worth considering another possibility that those galaxies with high SFRs determined from the FIR luminosities may actually have their SFRs overestimated. It is known that far-infrared is a tracer of star formation in an idealised case, where young stars dominate the radiation field and dust opacity is high. However the scenario is often intrinsically more complex as the FIR thermal emission can be split into two components; the 'warm' dust component from the absorption of UV emission of young stars being thermally emitted in the far-infrared; and the 'cold' dust component which results from longer wavelength emission from old stars and the ISM, being absorbed and re-emitted in the far-infrared (Kennicutt, 1998). In blue late-type star forming galaxies, both of these dust components are dominated by young stars. However in early-type more passive galaxies, the spectrum of stellar emission decreases in the blue and dust heating becomes dominated by their older stellar populations. It is this contribution towards the far-infrared emission by the older stellar populations within these red galaxies that may lead to an overestimation of the SFR in the overall population. As a consequence, the 250μm far-infrared observations by H-ATLAS may include emission from dust heated by these older stellar populations and subsequently overestimate the SFR.

Recent work by Smith et al. (2012a) shows that the 250μm detected galaxies in H-ATLAS may contain larger dust masses then previously thought. As it is the cold dust component that dominates the total dust mass within a galaxy, a larger total dust mass would lead to a greater influence of the cold dust component in the largest galaxies, therefore resulting in a higher proportion of the observed far-infrared emission (and hence the calculated SFR). A change in the dust mass would have the most significant impact in terms of the 250μm measured flux on galaxies with the highest levels of star formation, which are predominantly found towards high redshifts. Consequently the separation in number density between the FIR and FIR-Sim populations at high redshifts could well be reduced by this effect. In terms of my observational results from Section 3.2, I do not expect this discrepancy to affect my overall statistical results as the effect of increasing the dust mass would be small.

Cooling & Gas Stripping:

There are some assumptions within the SAM associated with the treatment of cooling and gas stripping of satellite galaxies that may explain the observed discrepancy. In the SAM, stripping effects, such as ram pressure and tidal stripping are only effective within the virial radius of the central galaxy. Therefore in the SAM, a satellite beyond this radius is not considered associated with the central galaxy. This would result in an overall reduction in the number of satellite galaxies compared to if the stripping methods had influence to larger radii. This assumption may lead to a slower and continued hierarchical build up of structure into later times than would be observed. The SAM also prevents ram pressure stripping from having any impact on the cold gas content of galaxies. Guo et al. (2011) acknowledge that this is unrealistic as it would lead to passive S0 galaxies retaining significant gas and dust which should otherwise have been removed. Even with this prescription, my results still qualitatively agree with the SAM, which leads me to conclude that ram-pressure stripping is probably not the key physical mechanism which causes the difference in environmental density between far-IR detected and non-detected galaxies.

4

Environment and Temperature Relations in the Far-Infrared

In this chapter, I expand upon my analysis of the environmental dependence of star formation, discussed in Chapter 3, by introducing much larger optical and far-infrared samples that span three fields. By using an increased number of galaxies I am able to further demonstrate the effectiveness of my Voronoi tessellation density algorithm, while obtaining better statistics on more varied properties of the galaxy sample. I investigate, with the addition of isothermal dust temperatures for the far-infrared population, the relationship between dust temperature and environment.

4.1 The H-ATLAS Phase-One Fields

4.1.1 Far-Infrared Data

For this analysis I used 250μm far-infrared observations from the full 'Phase-One' data set of the H-ATLAS (Eales et al., 2010). The specific details and observational characteristics of the H-ATLAS have already been detailed in Chapter 3.1.1 where the smaller science demonstration phase (SDP) was introduced and used throughout. The 250μm far-infrared data obtained from Phase-One span a much larger area of sky than the SDP; which covered just $\sim 4.0 \times 3.6$ deg^2 between $134.0 < RA < 139.0$ and $3.0 < Dec < 1.7$ (Figure 3.1) and contained only $2,423$ galaxies with reliable optical counterparts (as defined in Chapter 3.1.1 to have a reliability $R \geq 0.8$ from Smith et al. 2011). The Phase-One data however encompasses three separate fields, chosen to correspond with spectroscopic observations from GAMA 9hr, 12hr and 15hr fields that each extend $\sim 12.0 \times 3.0$ deg^2 in size, as outlined below in Section 4.1.2.

The 9hr H-ATLAS Phase-One field (hereafter *Herschel*-9P1) included the entire SDP field, extending between $128.0 < RA < 142.0$ and $2.8 < Dec < -1.8$. Using the same likelihood ratio (LR) method from Smith et al. (2011) that was applied to the SDP in Chapter 3, there are $7,813$ objects from the *Herschel*-9P1 250μm catalogue with optical counterparts down to a limiting magnitude of $m_r = 22.4$ with a reliability $R \geq 0.8$. The 12hr H-ATLAS Phase-One field (hereafter *Herschel*-12P1) extended between $172.5 < RA < 186.5$ and $1.8 < Dec < -2.6$. Again applying the LR method there are $7,919$ objects from the *Herschel*-12P1 250μm catalogue with optical counterparts. Finally, the 15hr H-ATLAS Phase-One field (hereafter *Herschel*-15P1) extended between $210.5 < RA < 224.5$ and $2.8 < Dec < -1.9$. With $6,732$ objects from the *Herschel*-12P1 250μm catalogue with the same limiting magnitude and reliability cuts once more applied. The *Herschel*-9P1, 12P1 and 15P1 fields are displayed as the blue data points in the three fields in Figure 4.1.

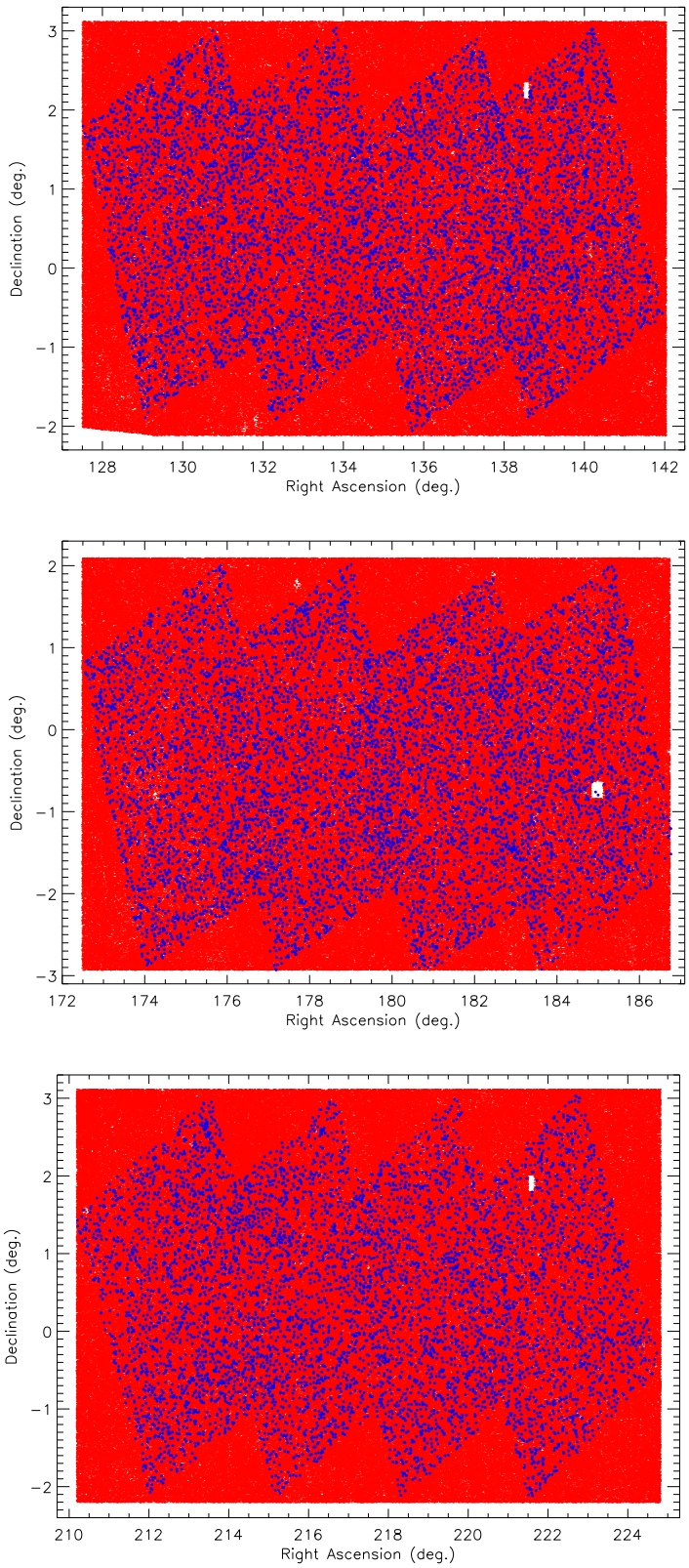

Figure 4.1: The H-ATLAS Phase-One fields *Top*: The Optical-9P1 data (*red*) numbering 751,651, whereas the overlying *Herschel*-9P1 data points (*blue*) number 7,813. *Middle*: The Optical-12P1 data (*red*) number 723,477 and the *Herschel*-12P1 data points (*blue*) number 7,919. *Bottom*: The Optical-15P1 data (*red*) number 785,536, whereas the *Herschel*-15P1 data points (*blue*) number 6,732.

4.1.2 Optical and Near-Infrared Data

For the 9hr Phase-One optical field I used the same spectroscopic and photometric data detailed in Section 3.1.2, expanded to encompass the entire *Herschel*-9P1 catalogue. This data again consisted of spectroscopic redshifts from both the SDSS and GAMA data release one (DR1) surveys combined with photometric redshifts derived from the combination of SDSS and UKIDSS-LAS imaging data. This initial optical catalogue (hereafter named Optical-9P1) consisted of $2,793,356$ objects before I removed all sources with r-band apparent magnitudes ($m_r > 21.5$) and $\mathrm{PSF}_r > 0.5$ in-line with the same treatment of the data in Section 3.1.2. This reduced the Optical-9P1 catalogue to $751,651$ objects of which $53,581$ had spectroscopic redshifts between $0 < z \leq 1.2$. This catalogue is displayed as the red data points at the top of Figure 4.1.

The 12hr Phase-One optical field (hereafter named Optical-12P1) also consisted of SDSS and GAMA-DR1 spectroscopy in conjunction with photometry from the SDSS and UKIDSS-LAS. The initial Optical-12P1 catalogue contained $2,311,647$ objects enclosing the entire *Herschel*-12P1 field. After $m_r > 21.5$ and PSF> 0.5 cuts were applied this reduced the catalogue to $723,477$ objects of which $60,725$ had spectroscopic redshifts between $0 < z \leq 1.2$. The Optical-12P1 catalogue is displayed as the red data points at the centre of Figure 4.1.

Finally, the 15hr Phase-One optical field (hereafter named Optical-15P1) included sources enclosing all of the *Herschel*-15P1 field. This catalogue initially consisted of $3,122,282$ objects reduced to to $785,536$ with $m_r > 21.5$ and PSF> 0.5 cuts applied across the redshift range $0 < z \leq 1.2$ with $53,200$ spectroscopic redshifts. The Optical-15P1 catalogue is displayed as red data points at the bottom of Figure 4.1.

4.2 Density Analysis: Individual Phase-One Fields

In order to further investigate the relationship between the far-infrared properties of galaxies and their environmental densities, in an expansion of the work in Chapter 3, I applied my analysis to each of the three H-ATLAS Phase-One fields (9P1, 12P1 & 15P1) individually. The methodology of Chapter 3 is followed and the analysis of the

9P1 field is initially detailed before outlining the 12P1 and 15P1 results.

4.2.1 Application of the VT Algorithm

For the analysis of environmental density within the Optical-9P1 catalogue, I applied the same parameters within my VT algorithm that are described in Chapter 3. This is such that the same redshift slicing was applied across the complete redshift range of the data ($\Delta z = 0.01$) resulting in 120 redshift slices across each of the 1000 3D MC realisations. This was in addition to the same edge-effect cuts of ± 0.30 deg being applied in both RA and Dec, to once more account for the outer VT cells excessive cell sizes interfering with the density calculation. Objects residing outside of this region were again removed from the remainder of the analysis. Furthermore, a peak in the number density of the optical catalogue was again found to reside at $z \sim 0.40$ (as shown in Figure 4.2). However, this distinct peak in number density did not affect the final environmental density measures again due to the normalization procedure within my VT algorithm (as described in Section 2.2.2).

Finally, in order to ensure the comparison between the Optical-9P1 and *Herschel*-9P1 catalogues were accurate, the Optical-9P1 catalogue was restricted to include only those objects that lie within the *Herschel*-9P1 region as maintained for the previous analysis of the SDP field in Chapter 3. With these region cuts applied the final reduced Optical-9P1 field consisted of $513,750$ objects. Figure 4.3 shows the density distribution within the Optical-9P1 field.

4.2.2 Far-Infrared and Control Samples

As introduced above, following the same methodology as described in Section 3.2.2, I applied the reliability cut of $R \geq 0.8$, as derived from the LR technique of Smith et al. (2011), to maintain only the *Herschel*-9P1 objects with reliable optical counterparts, finding $7,813$ objects. After the regions cuts to the sample have been applied to account for the VT edge-effect and size of the sample area, this is reduced to $7,272$ objects with matching *Herschel*-9P1 detections. This catalogue is hereafter named

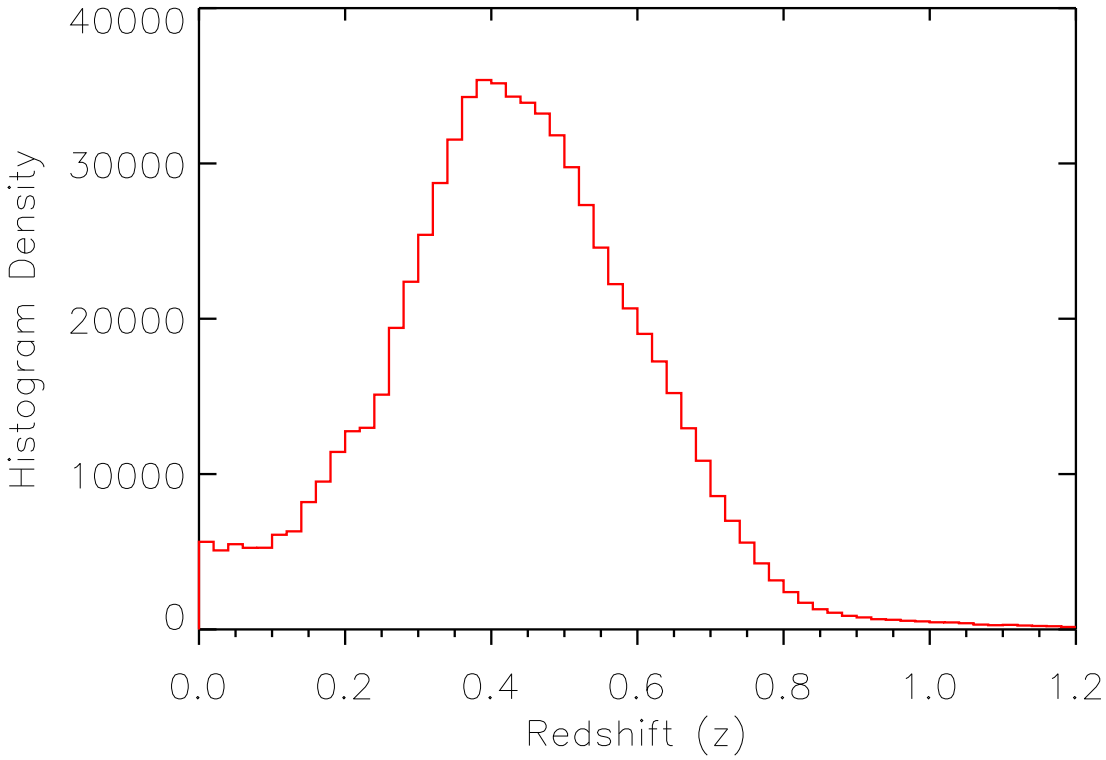

Figure 4.2: The redshift distribution of all 751,651 objects in the Optical-9P1 field. There is clearly a majority in the number of detected objects residing at z $\sim$ 0.40, due to the evolution of the luminosity function and flux limit of the observations.

'FIR-9P1' and these optical counterpart sources were removed from the Optical-9P1 catalogue reducing it to 506,478 galaxies.

It was also again necessary to match the Optical and FIR samples so that they have indistinguishable distributions in various observed parameters in order to achieve an appropriate like with like comparison. This is such that objects selected for comparison should be considered to be as similar as possible so that any differences in environmental density cannot be attributed to other inherent differences than the presence of FIR emission. This was again achieved by cross-matching both catalogues in terms of their colour, r-band magnitude and redshift distributions ($g-r$, $r-i$, m_r and z). The same four-dimensional gridding was applied to both populations, as detailed in Section 3.2.2, selecting objects from both catalogues that are matched only in these parameter spaces with additional Optical-9P1 and FIR-9P1 sources removed from the

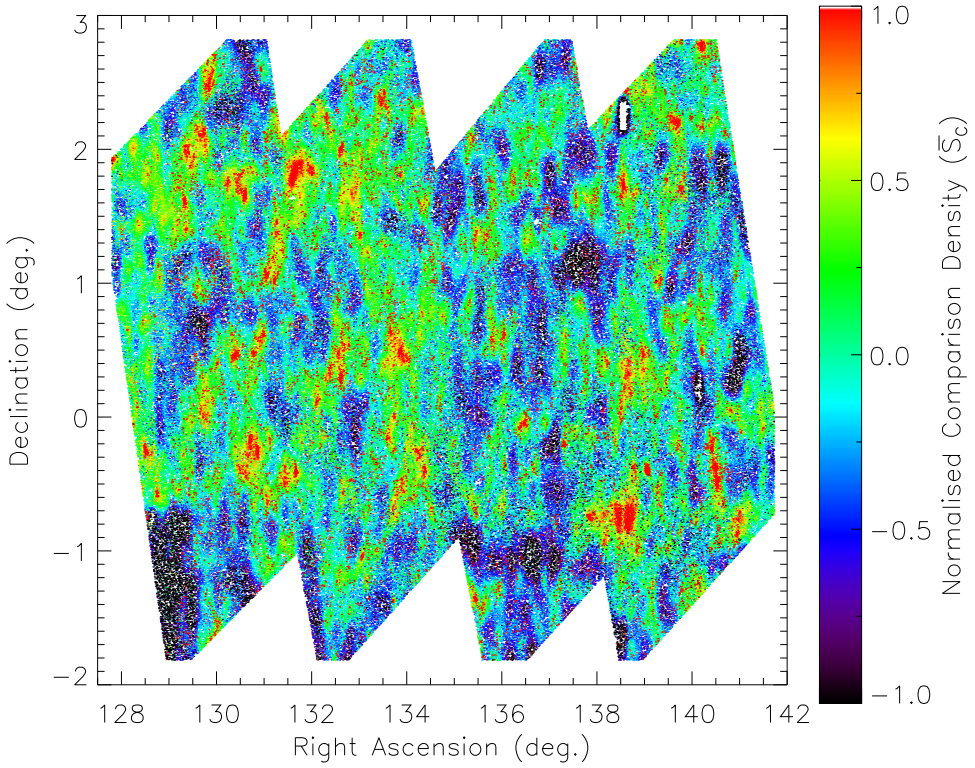

Figure 4.3: All 513,750 Optical-9P1 objects with all redshift slices compiled to show the whole density distribution. Red and orange colours represent the most overdense regions (positive $\bar{S}_c$ values) and blue and purple represent underdense regions (negative $\bar{S}_c$ values) with the range of the normalized density limited to $-1 \leq \bar{S}_c \leq 1$ for clarity.

analysis. Once more, due to the number of FIR-9P1 objects being far fewer than the Optical-9P1 catalogue (7,272 against 506,478) and due to the way the parameter space cross-matching selects associated data, the resultant cross-matched samples consisted of 8,133 and 2,711 objects for the Optical-9P1 and FIR-9P1 samples respectively. In addition, again due to the number of high redshift galaxies reducing to such an extent as to affect the sampling, these matched samples are both limited to a maximum redshift of $z \leq 0.5$. As with the SDP analysis in Chapter 3, this insertion of a maximum redshift limit does not influence the density result due to the fact that each $\bar{S}_c$ value incorporates the influence of higher redshift objects via the full z-PDF analysis within my VT algorithm. Figures 4.4 and 4.5 show the colour, r-band magnitude and redshift matched distributions of the Optical-9P1 and FIR-9P1 matched samples.

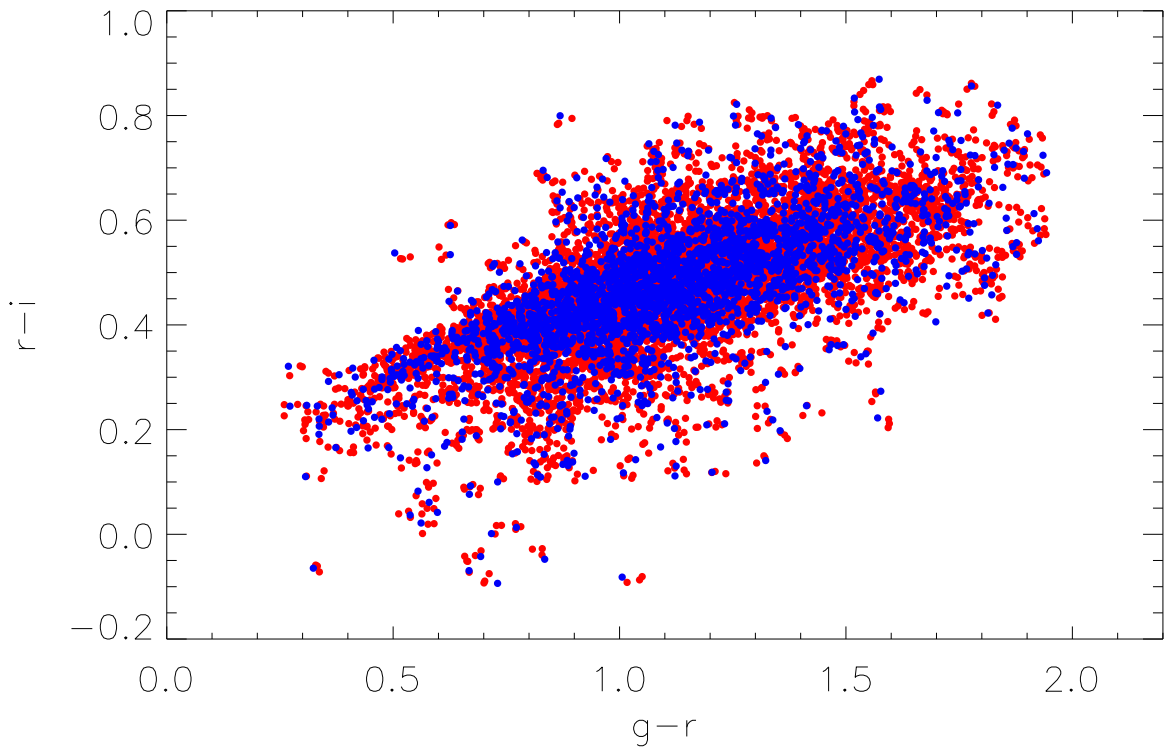

FIGURE 4.4: $g-r$ versus $r-i$ colour distribution for the 'matched' samples of Optical-9P1 (*red*) and FIR-9P1 (*blue*) numbering 8,133 and 2,711 sources respectively.

4.2.3 Comparison Between FIR and Optical Galaxies

With the successful creation of the Optical and FIR samples cross-matched in colour, redshift and r-band apparent magnitude, I could then statistically compare the two samples. I once again applied one- and two-dimensional KS- and MWU-tests to the data, with the aim or establishing if the same trends between SFR and density are found for these larger data samples, in continuation of the analysis conducted in Chapter 3. Following the notation in Section 3.2.3 the Optical-9P1 matched sample is labelled as '*op*' and the FIR-9P1 matched sample is labelled 'FIR' in all tables for clarity.

I initially applied the KS- and MWU-tests in order to confirm that the matched samples are indeed drawn from the same underlying distribution in terms of their colours, magnitudes and redshift distributions and that the various combinations are consistent with each other. The probability values returned by these tests demonstrate that this is the case, with values large enough so that the null hypotheses could not be rejected for

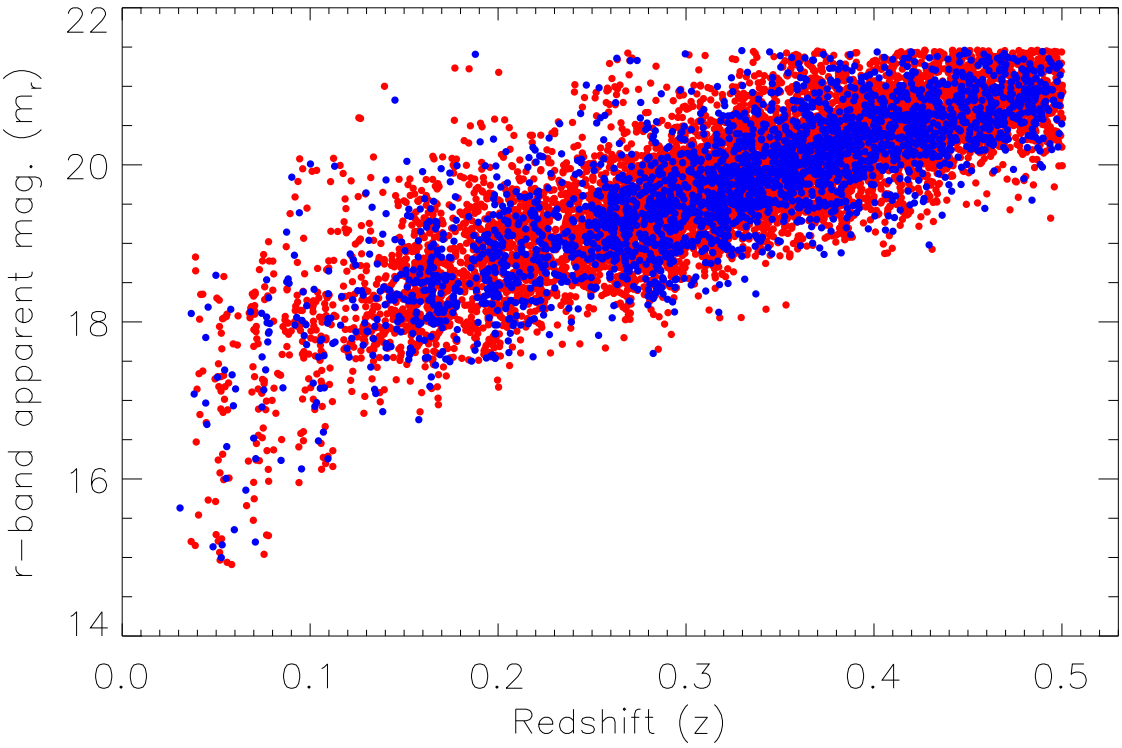

Figure 4.5: Redshift versus r-band apparent magnitude (m_r) for the 'matched' Optical-9P1 (*red*) and FIR-9P1 (*blue*) samples. Only the redshift range of $0 < z \leq 0.5$ and m_r range of $15 < m_r < 21.5$ were included in the sampling as the completeness of the sample reduced significantly outside of these ranges.

combinations of these distributions. Thus confirming a successful cross-matching with respect to these parameters for both the Optical-9P1 and FIR-9P1 samples. These results are presented in Table 4.1. The application of the one-dimensional KS-test to the environmental density distributions of both matched samples ($\bar{S}_{op}$ versus $\bar{S}_{FIR}$) returned a probability of 1.18×10^{-4} indicating a significant difference, i.e. the null hypothesis is rejected at the 3.9σ level. Figure 4.6 shows the normalised histograms of the two density distributions. Applying a MWU-test revealed that there is a significant difference between their mean values, with a probability of 2.33×10^{-6} revealing the null hypothesis can be rejected at the 4.9σ level. Examining the mean $\bar{S}_c$ values reveals that the Optical-9P1 densities favour overdense regions compared to the FIR-9P1 densities, with mean $\bar{S}_c$ values of $(18.31 \pm 0.62) \times 10^{-2}$ and $(12.48 \pm 1.09) \times 10^{-2}$ respectively. To test this result further the $\bar{S}_c$ values were then compared with combinations of colour,

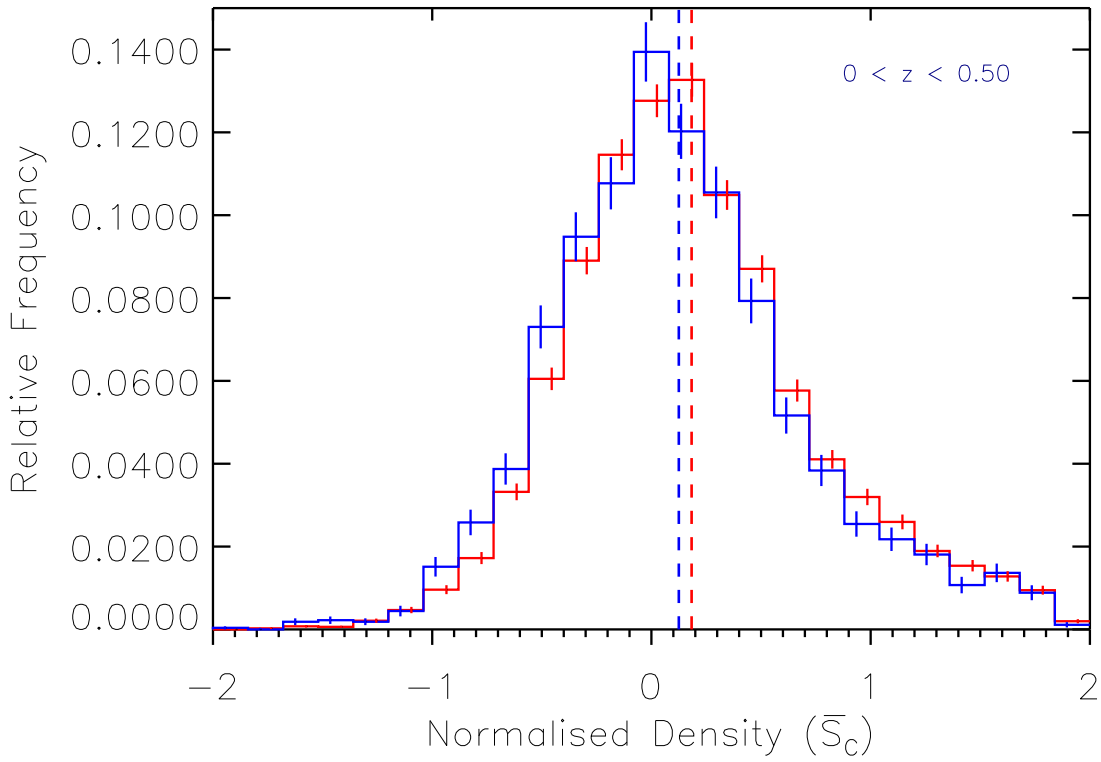

FIGURE 4.6: Normalized histograms showing how the distributions of environmental density ($\bar{S}_c$) for the total colour, r-band magnitude and redshift matched Optical-9P1 (*red*) and FIR-9P1 (*blue*) samples compare. The histograms show error-bars depicting normalized errors associated with each bin, where $\bar{S}_c > 0$ signifies an overdensity and $\bar{S}_c < 0$ signifies an underdensity in terms of the entire matched redshift range $0 < z \leq 0.5$. The FIR-9P1 data is shifted to generally lower densities with its distribution mean given by the *blue* dashed-line at $(12.48 \pm 1.09) \times 10^{-2}$. The Optical-9P1 distribution is shifted towards higher densities with the mean of its distribution given by the *red* dashed-line at $(18.31 \pm 0.62) \times 10^{-2}$.

redshift and m_r distributions using two-dimensional KS-tests. These values confirmed significant differences are maintained between the density distributions in all cases. All statistical results are presented in Table 4.1.

From the SDP analysis in Chapter 3 we know that with any flux-density limited survey there will be a bias associated with the highest-redshift sources being preferentially be more luminous (and hence have higher SFR's) than lower redshift sources. As a consequence of this bias one would expect to identify a larger separation between the density distributions of FIR and non-FIR sources towards higher redshifts, as was

Table 4.1: Two sample and two-dimensional KS- and MWU-test results over the full redshift range ($0 < z \leq 0.5$). Where *op* represents Optical-9P1 ($8,133$ objects) and *FIR* represents FIR-9P1 ($2,711$ objects). The two density distributions are different at the 3.9σ level from KS-tests, with the means of the distributions different at the 4.9σ level from MWU-tests.

Distributions Compared			KS Probability	MWU Probability
$z_{(op)}$	versus	$z_{(FIR)}$	0.892	0.298
$(g-r)_{op}$	versus	$(g-r)_{FIR}$	0.999	0.446
$(r-i)_{op}$	versus	$(r-i)_{FIR}$	0.987	0.415
$m_{r(op)}$	versus	$m_{r(FIR)}$	0.320	0.087
$(\bar{S}_c)_{op}$	versus	$(\bar{S}_c)_{FIR}$	1.18×10^{-4}	2.33×10^{-6}
$(g-r, r-i)_{op}$	versus	$(g-r, r-i)_{FIR}$	0.965	-
$(g-r, z)_{op}$	versus	$(g-r, z)_{FIR}$	0.921	-
$(r-i, z)_{op}$	versus	$(r-i, z)_{FIR}$	0.858	-
$(m_r, z)_{op}$	versus	$(m_r, z)_{FIR}$	0.191	-
$(g-r, m_r)_{op}$	versus	$(g-r, m_r)_{FIR}$	0.500	-
$(r-i, m_r)_{op}$	versus	$(r-i, m_r)_{FIR}$	0.490	-
$(g-r, \bar{S}_c)_{op}$	versus	$(g-r, \bar{S}_c)_{FIR}$	2.80×10^{-4}	-
$(r-i, \bar{S}_c)_{op}$	versus	$(r-i, \bar{S}_c)_{FIR}$	1.06×10^{-3}	-
$(m_r, \bar{S}_c)_{op}$	versus	$(m_r, \bar{S}_c)_{FIR}$	3.13×10^{-5}	-
$(z, \bar{S}_c)_{op}$	versus	$(z, \bar{S}_c)_{FIR}$	6.66×10^{-5}	-

Table 4.2: KS-test and MWU-test results for the comparison of both the Optical-9P1 and FIR-9P1 matched samples $\bar{S}_c$ distributions within each redshift slice shown in figure 4.7. The number of objects from each population are also given:

Redshift Slice	Optical	FIR	KS Probability	MWU Probability
$0 \leq z < 0.25$	1,867	604	0.110	0.198
$0.25 \leq z < 0.50$	6,262	2,107	3.10×10^{-8}	$< 10^{-10}$

found in analysis of the smaller SDP field. Therefore I once more divided the redshift distributions of both matched Optical-9P1 and FIR-9P1 samples to investigate whether the same increase in separation with increasing redshift could be identified in the Phase-One 9hr field. The resultant lower redshift bin covered $0 \leq z < 0.25$ and contained $1,867$ Optical-9P1 and 604 FIR-9P1 objects, the higher redshift bin covered $0.25 \leq z < 0.5$ and contained $6,262$ Optical-9P1 and $2,107$ FIR-9P1 objects. The normalized density distributions of both matched populations within each redshift bin are displayed in Figure 4.7. Applying statistical tests to each redshift bin revealed the same trends found for the SDP analysis. From KS-tests, the lower redshift bin returned no significant difference between the Optical-9P1 and FIR-9P1 $\bar{S}_c$ samples, with a probability of 0.110. Applying a MWU-test to this bin also indicated no significant difference with a probability of 0.20. However, the higher redshift bin returned a highly significant difference at the 5.8σ level with a probability of 3.10×10^{-8} and applying MWU-tests to this bin also revealed a $> 6\sigma$ difference between the means of the $\bar{S}_c$ distributions. These statistical results are presented in Table 4.2.

These trends are in agreement with those found in the analysis of the SDP field in Chapter 3. With galaxies exhibiting brighter FIR luminosities (and hence higher SFR's), predominantly found at higher redshifts, showing a stronger anti-correlation with density than lower FIR luminous galaxies, at lower redshifts. As with the SDP analysis, these trends are influenced by low signal-to-noise ratios and smaller number densities in the lower redshift bin influencing the result. This is in addition to the lowest star forming galaxies flattening the density distribution and affecting the comparison as demonstrated in Section 3.2.5.

4.2.4 Dust Reddening Effects

In Section 3.2.6 I investigated the influence of dust reddening on my overall result in terms of the potential mismatching in colours and stellar masses between my Optical and FIR samples in the SDP field. It was therefore necessary to investigate reddening influences on the larger Phase-One sample to establish how my main statistical results are affected.

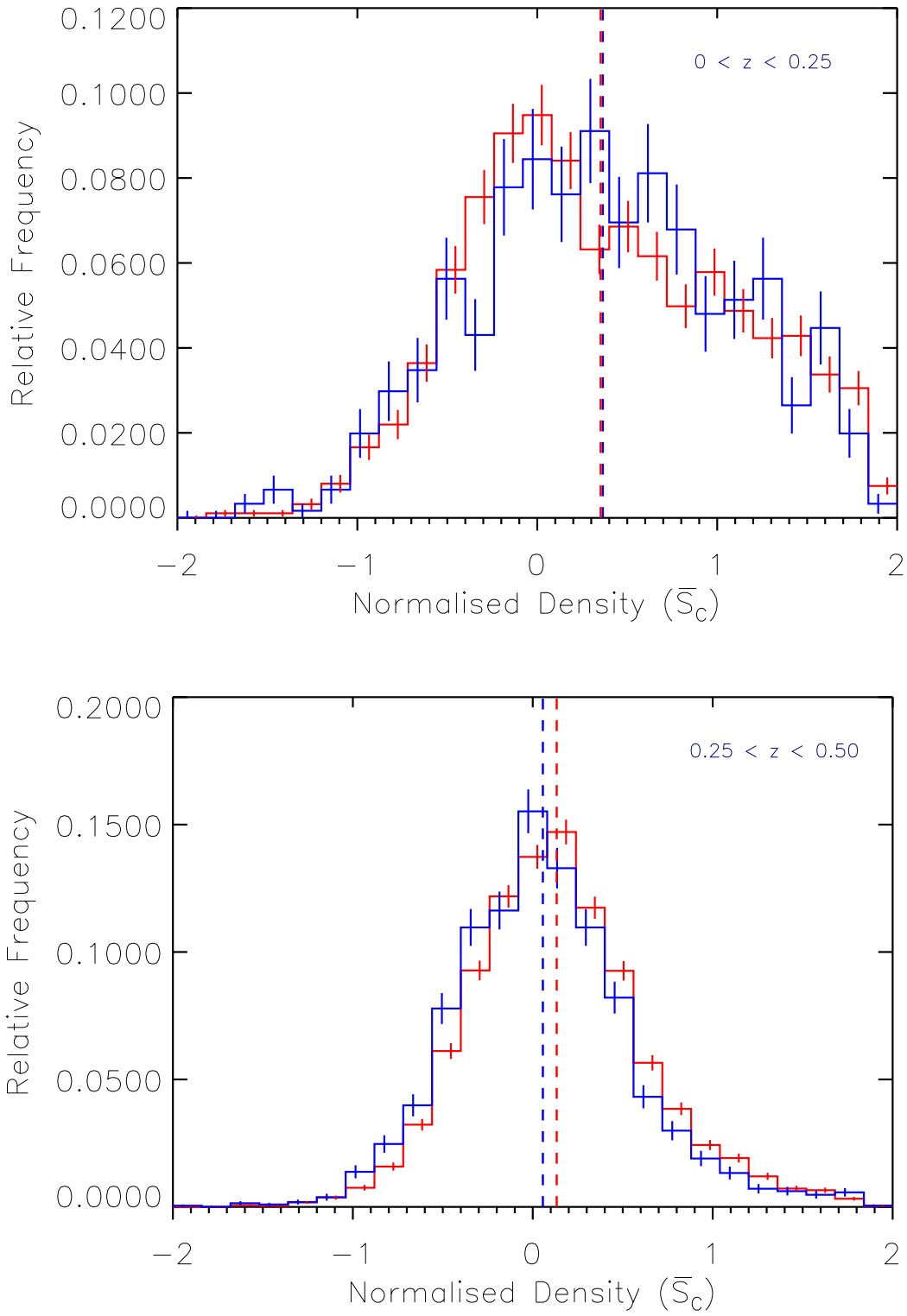

Figure 4.7: Normalized histograms that show the full matched Optical-9P1 (*red*) and FIR-9P1 (*blue*) samples binned in redshift *Top*: ($0 \leq z < 0.25$) No significant differences are found between the two samples. *Bottom*: ($0.25 \leq z < 0.50$) Both samples are significantly different at the 5.7σ level from KS-tests.

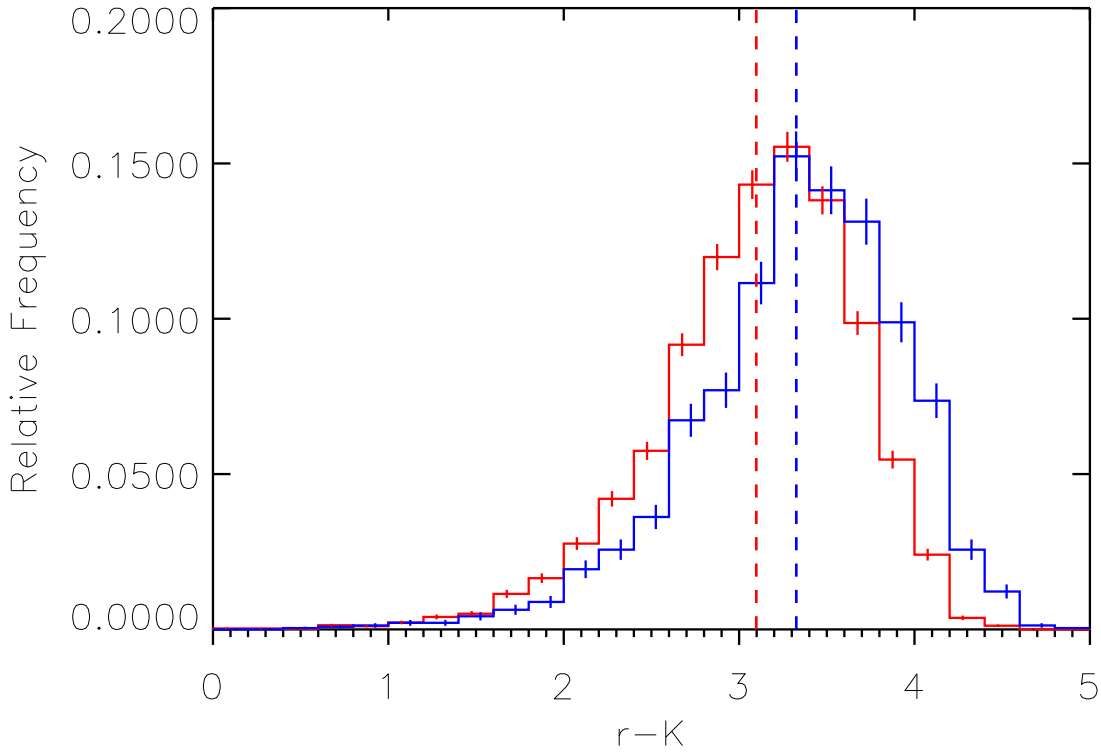

FIGURE 4.8: Normalized histograms of the $r-K$ colours of the $g-r$, $r-i$, z and m_r matched Optical-9P1 (*red*) and FIR-9P1 (*blue*) samples reduced in size due to the lack of m_K data to 6,733 and 2,377 objects respectively. They have significantly different colour distributions at the $> 6\sigma$ level.

Following my analysis of the SDP field, I again introduce K-band (m_K) data from the UKIRT Infrared Sky Survey (Lawrence et al. 2007). Figure 4.8 shows the $r-K$ distributions of the matched Optical-9P1 and FIR-9P1 samples (reduced in size due to the lack of m_K data to 6,733 and 2,377 respectively) and there is a clear difference between the two populations. This is confirmed by KS-tests returning a significant difference at the $> 6\sigma$ level establishing that dust reddening is found within the FIR-9P1 sample in agreement with the reddening analysis conducted on the SDP field in Section 3.2.6. Once more, as reddening leads to an underestimation of the masses in the FIR-9P1 sample, reducing the reddening would lead to an increase in the mass estimates for these galaxies. As more massive galaxies are known to favour overdense regions, this increase in mass would lead to an increase in the separation between FIR and Optical sources, strengthening my results in Section 4.2.3.

Table 4.3: Two sample and two-dimensional KS- and MWU-test results where *op* represents Optical-9P1 (12,579 objects) and *FIR* represents FIR-9P1 (4,193 objects) matched in terms of their $K-$band magnitude, $r-K$ colour and redshift distribution.

Distributions Compared			KS Prob.	MWU Prob.
$z_{(op)}$	versus	$z_{(FIR)}$	0.999	0.463
$(r-K)_{op}$	versus	$(r-K)_{FIR}$	0.878	0.490
$m_{K(op)}$	versus	$m_{K(FIR)}$	0.304	0.175
$(\bar{S}_c)_{op}$	versus	$(\bar{S}_c)_{FIR}$	$< 10^{-23}$	$< 10^{-10}$
$(r-K,z)_{op}$	versus	$(r-K,z)_{FIR}$	0.812	-
$(m_K,z)_{op}$	versus	$(m_K,z)_{FIR}$	0.408	-
$(r-K,m_K)_{op}$	versus	$(r-K,m_K)_{FIR}$	0.302	-
$(r-K,\bar{S}_c)_{op}$	versus	$(r-K,\bar{S}_c)_{FIR}$	$< 10^{-15}$	-
$(m_K,\bar{S}_c)_{op}$	versus	$(m_K,\bar{S}_c)_{FIR}$	$< 10^{-15}$	-
$(z,\bar{S}_c)_{op}$	versus	$(z,\bar{S}_c)_{FIR}$	$< 10^{-15}$	-

Table 4.4: KS-test and MWU-test results for the comparison of the $\bar{S}_c$ distributions of both redshift binned Optical-9P1 and FIR-9P1 distributions, matched in m_K magnitude, $r-K$ colour and redshift. The number of objects from each population are also given:

Redshift Slice	Optical	FIR	KS Probability	MWU Probability
$0 \leq z < 0.25$	4,368	1,463	$< 10^{-6}$	$< 10^{-10}$
$0.25 \leq z < 0.50$	8,074	2,687	$< 10^{-24}$	$< 10^{-10}$

In continuation of the analysis preformed on the SDP field, I test the robustness of these results by removing the reddening effect and repeating the environmental density comparison. This is achieved by cross-matching both Optical-9P1 and FIR-9P1 samples in terms of their $r-K$ colour, m_K and redshift distributions. As m_K data was not available for the entire Optical-9P1 sample, the data taken through this new comparison represented a subset of the initial samples. Therefore the Optical-9P1 sample was reduced from 506,478 to 257,903 objects and the FIR-9P1 sample reduced

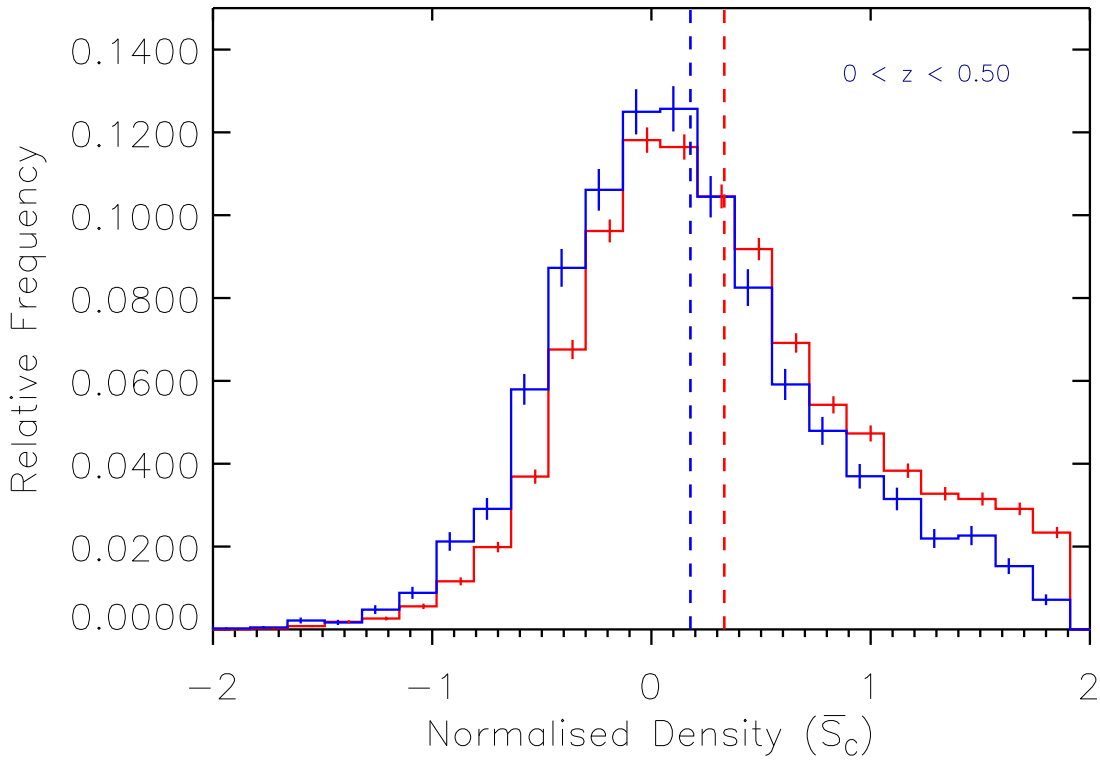

FIGURE 4.9: Normalized histograms showing how the distributions of environmental density ($\bar{S}_c$) for the total $r-K$, m_K and z matched Optical-9P1 (*red*) and FIR-9P1 (*blue*) samples compare across the matched redshift range $0 < z \leq 0.5$. The FIR-9P1 data is shifted to generally lower densities with its distribution mean given by the *blue* dashed-line at 0.180 $\pm$ 0.009. The Optical-9P1 distribution is shifted towards higher densities with the mean of its distribution given by the *red* dashed-line at 0.330 $\pm$ 0.006.

from 7,272 to 6,331 objects with detected m_K emission. The remaining sources were then compared using the same gridding technique described previously in Section 3.2.2, adjusted to find cross-matches across $r-K$, z and m_K parameter space only. The resultant cross-matched samples consisted of 12,579 Optical-9P1 and 4,193 FIR-9P1 objects. Applying KS- and MWU-tests to combinations of these parameters revealed, once more, a significant difference between the both $\bar{S}_c$ distributions, at the $> 6\sigma$ level from a probability of just 1.44×10^{-24}. These distributions are displayed in Figure 4.9 where it is clear that the FIR-9P1 data favour generally lower densities with its distribution mean at 0.180 ± 0.009. Conversely the Optical-9P1 distribution favours higher densities with its distribution mean at 0.330 ± 0.006. From MWU-tests these mean values are significantly different at the $> 6\sigma$ level. This significant

difference was maintained for all combinations involving the $\bar{S}_c$ parameters and Table 4.3 presents all of the statistical values returned from these tests. In addition, applying the same redshift binning as previously applied to these distributions, and repeating the statistical comparisons, shows that there is a much improved significant difference between the Optical-9P1 and FIR-9P1 density distributions in both bins, to at least the 5σ level in both bins. These values are presented in Table 4.4.

4.2.5 12hr and 15hr Phase-One Density Analysis

With the density analysis across the full 9P1 field complete, I could then repeat this full investigation across the total 12P1 and 15P1 fields to test whether the same correlations between density and FIR emission were found. I applied the VT algorithm to each field incorporating the same fundamental parameters concerning redshift limits, edge-effect cuts and FIR region matches as were applied to the Optical-9P1 field described in Section 4.2. The normalised environmental densities of the galaxies displayed within the Optical-12P1 and Optical-15P1 fields are illustrated in colour-density plots in Figure 4.10 where red and orange colours represent the most overdense regions (positive $\bar{S}_c$ values) and blue and purple represent underdense regions (negative $\bar{S}_c$ values). The visible voids in the fields, where no data points are found, represents where a foreground object has been removed to avoid interference with the density calculation.

Repeating the application of the reliability ($R \geq 0.8$) cut from Smith et al. (2011) to the *Herschel*-12P1 and *Herschel*-15P1 catalogues, and removing these optical counterparts from the Optical-12P1 and Optical-15P1 catalogues, returned $7,272$ FIR-12P1 and $6,128$ FIR-15P1 galaxies. Following the analysis of the 9P1 field, these were then cross-matched in $g-r$, $r-i$, z and m_r space against the Optical-12P1 and Optical-15P1 samples. This cross-matching returned $4,248$ Optical-12P1 and $1,416$ FIR-12P1 objects in addition to $5,925$ Optical-15P1 and $1,975$ FIR-15P1 objects respectively. These cross-matched samples were again statistically compared with one- and two-dimensional KS- and MWU-tests in order to establish whether the same trends between SFR and density were repeated across the 12P1 and 15P1 fields. I found high probability values between these matched distributions, such that the null hypothesis

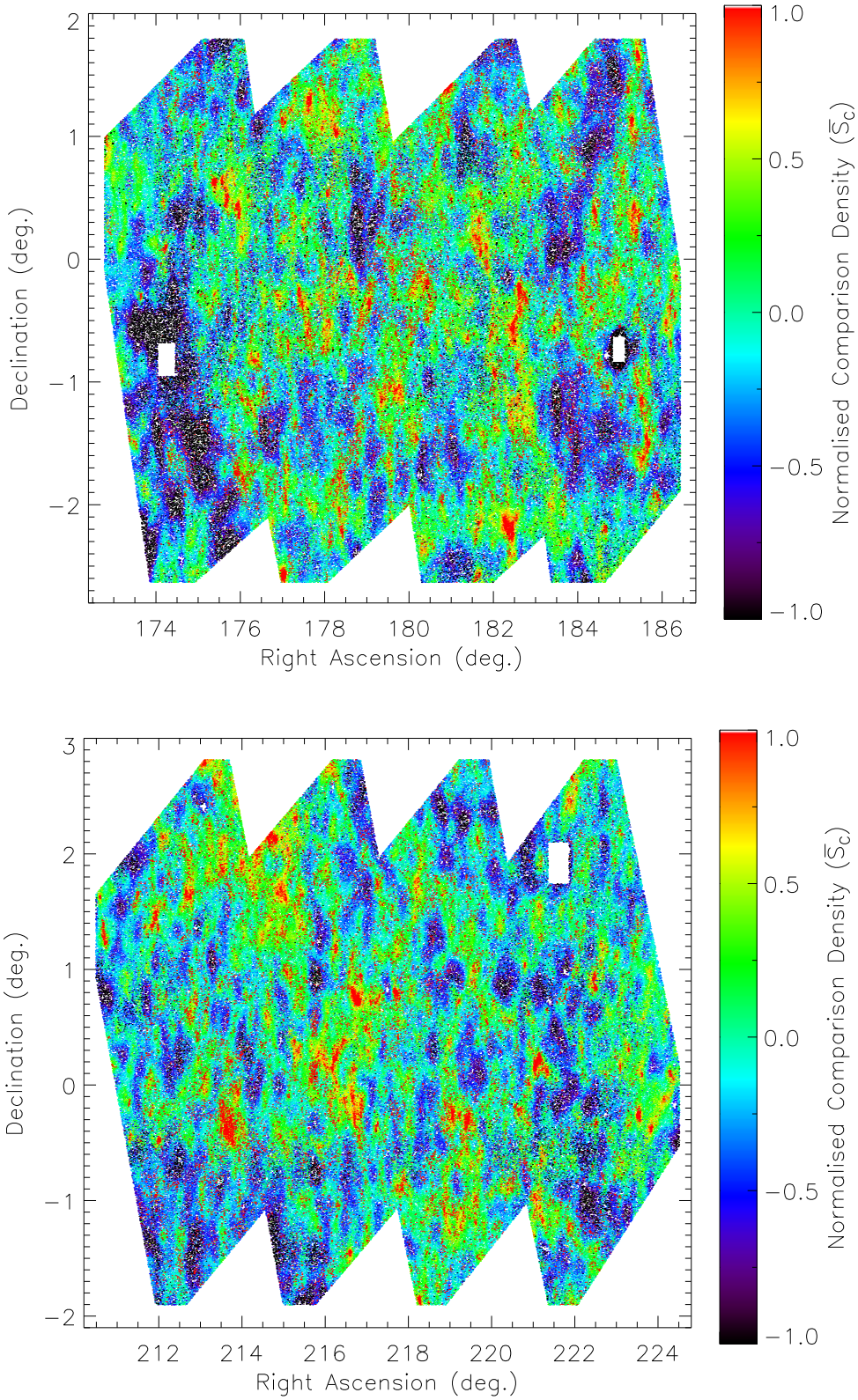

FIGURE 4.10: Colour co-ordinated plot of the total Optical-12P1 (*top*) and Optical-15P1 (*bottom*) catalogues with all redshift slices compiled to show the whole density distribution. Red and orange colours represent the most overdense regions (positive $\bar{S}_c$ values) and blue and purple represent underdense regions (negative $\bar{S}_c$ values) with the range of the normalized density limited to $-1 \leq \bar{S}_c \leq 1$ for clarity.

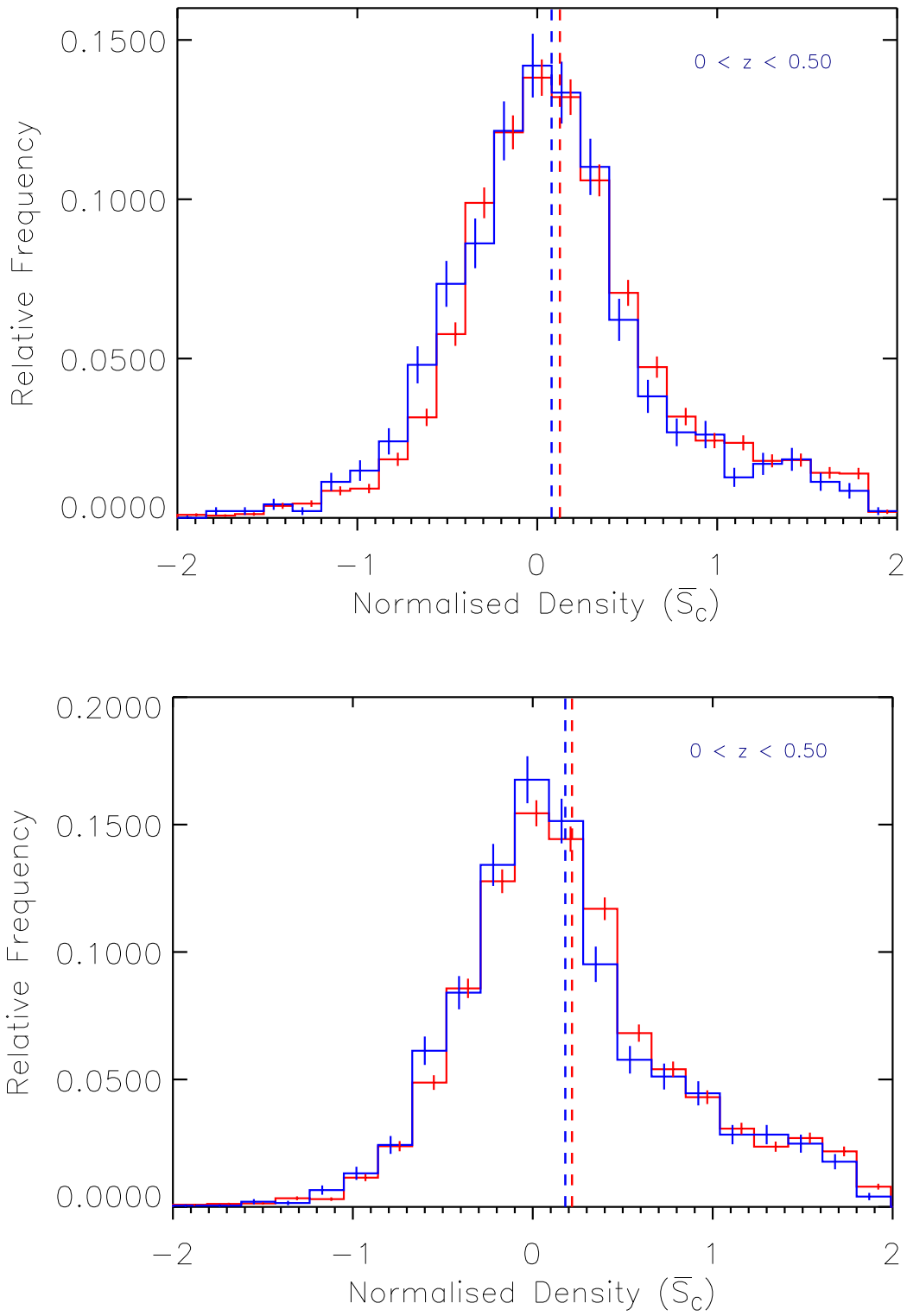

Figure 4.11: Normalized histograms showing the environmental density ($\bar{S}_c$) distributions for the total colour, r-band magnitude and redshift matched samples for the 12P1 (*Top*) and 15P1 (*Bottom*) samples. In both cases, the FIR samples (*blue*) are shifted to generally lower densities compared to the Optical samples (*red*).

TABLE 4.5: One- and two-dimensional KS- and MWU-test results over the full redshift range ($0 < z \leq 0.5$). Where *op* represents Optical-12P1 (4,248 objects) and *FIR* represents FIR-12P1 (1,416 objects). The two density distributions are different at the 3.0σ level from KS-tests, with the means of the distributions different at the 3.5σ level from MWU-tests.

Distributions Compared			KS Probability	MWU Probability
$z_{(op)}$	versus	$z_{(FIR)}$	0.999	0.474
$(g-r)_{op}$	versus	$(g-r)_{FIR}$	0.999	0.444
$(r-i)_{op}$	versus	$(r-i)_{FIR}$	0.996	0.490
$m_{r(op)}$	versus	$m_{r(FIR)}$	0.594	0.264
$(\bar{S}_c)_{op}$	versus	$(\bar{S}_c)_{FIR}$	3.77×10^{-3}	5.92×10^{-4}
$(g-r, r-i)_{op}$	versus	$(g-r, r-i)_{FIR}$	0.999	-
$(g-r, z)_{op}$	versus	$(g-r, z)_{FIR}$	0.991	-
$(r-i, z)_{op}$	versus	$(r-i, z)_{FIR}$	0.999	-
$(m_r, z)_{op}$	versus	$(m_r, z)_{FIR}$	0.491	-
$(g-r, m_r)_{op}$	versus	$(g-r, m_r)_{FIR}$	0.792	-
$(r-i, m_r)_{op}$	versus	$(r-i, m_r)_{FIR}$	0.570	-
$(g-r, \bar{S}_c)_{op}$	versus	$(g-r, \bar{S}_c)_{FIR}$	0.017	-
$(r-i, \bar{S}_c)_{op}$	versus	$(r-i, \bar{S}_c)_{FIR}$	0.030	-
$(m_r, \bar{S}_c)_{op}$	versus	$(m_r, \bar{S}_c)_{FIR}$	7.61×10^{-3}	-
$(z, \bar{S}_c)_{op}$	versus	$(z, \bar{S}_c)_{FIR}$	0.018	-

could not be rejected to any level of significance. This confirmed that these matched samples are consistent with having been drawn from the same underlying distribution in terms of their colour, redshift and magnitude distributions. Comparisons of the normalised density distributions ($\bar{S}_{op}$ versus $\bar{S}_{FIR}$) in both 12P1 and 15P1 fields return low probabilities, confirming significant differences between their density distributions at the 3.0σ and 2.9σ level respectively. All statistical results from these comparisons are presented in Tables 4.5 and 4.6 for the 12P1 and 15P1 fields. Figure 4.11 displays the normalised histograms of the density distributions of both 12P1 (*top*) and 15P1 (*bottom*) fields, indicating in both cases that the FIR samples favour underdense

Table 4.6: One- and two-dimensional KS- and MWU-test results over the full redshift range ($0 < z \leq 0.5$). Where *op* represents Optical-15P1 ($5,925$ objects) and *FIR* represents FIR-15P1 ($1,975$ objects). The two density distributions are different at the 2.9σ level from KS-tests, with the means of the distributions different at the 2.9σ level from MWU-tests.

Distributions Compared			KS Probability	MWU Probability
$z_{(op)}$	versus	$z_{(FIR)}$	0.994	0.381
$(g-r)_{op}$	versus	$(g-r)_{FIR}$	0.993	0.435
$(r-i)_{op}$	versus	$(r-i)_{FIR}$	0.998	0.407
$m_{r(op)}$	versus	$m_{r(FIR)}$	0.403	0.172
$(\bar{S}_c)_{op}$	versus	$(\bar{S}_c)_{FIR}$	5.14×10^{-3}	4.82×10^{-3}
$(g-r, r-i)_{op}$	versus	$(g-r, r-i)_{FIR}$	0.941	-
$(g-r, z)_{op}$	versus	$(g-r, z)_{FIR}$	0.974	-
$(r-i, z)_{op}$	versus	$(r-i, z)_{FIR}$	0.980	-
$(m_r, z)_{op}$	versus	$(m_r, z)_{FIR}$	0.349	-
$(g-r, m_r)_{op}$	versus	$(g-r, m_r)_{FIR}$	0.699	-
$(r-i, m_r)_{op}$	versus	$(r-i, m_r)_{FIR}$	0.595	-
$(g-r, \bar{S}_c)_{op}$	versus	$(g-r, \bar{S}_c)_{FIR}$	6.68×10^{-3}	-
$(r-i, \bar{S}_c)_{op}$	versus	$(r-i, \bar{S}_c)_{FIR}$	0.038	-
$(m_r, \bar{S}_c)_{op}$	versus	$(m_r, \bar{S}_c)_{FIR}$	0.027	-
$(z, \bar{S}_c)_{op}$	versus	$(z, \bar{S}_c)_{FIR}$	0.020	-

regions in agreement with the 9P1 field.

Following the analysis of the 9P1 field, I divided both the 12P1 and 15P1 fields into separate redshift bins and compare the distributions. The normalised density distributions of both samples in both bins are displayed as histograms in Figures 4.12 and 4.13 for the 12P1 and 15P1 fields respectively. In agreement with the 9P1 field, I find that a significant difference between the optical and FIR samples is only present in the higher redshift bin at the 3.0σ in the 12P1 field and 3.5σ in the 15P1 field. These statistical results, in addition to the number of objects for each sample found in each bin, are presented in Tables 4.7 and 4.8.

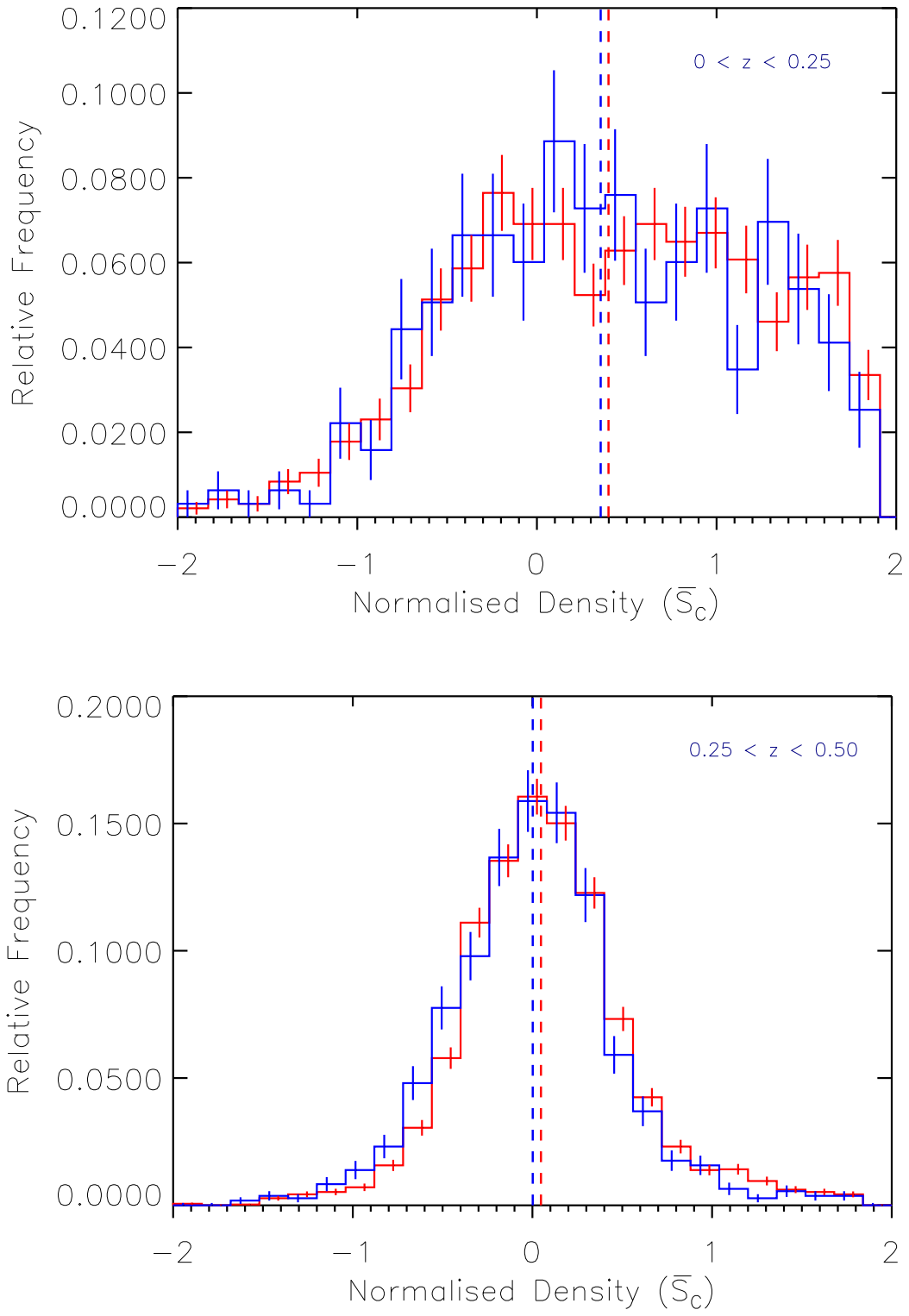

FIGURE 4.12: Normalized histograms showing the full matched Optical-12P1 (*red*) and FIR-12P1 (*blue*) samples binned in redshift *Top*: ($0 \leq z < 0.25$) No significant differences are found between the two samples. *Bottom*: ($0.25 \leq z < 0.50$) Both samples are significantly different at the 3.0σ level.

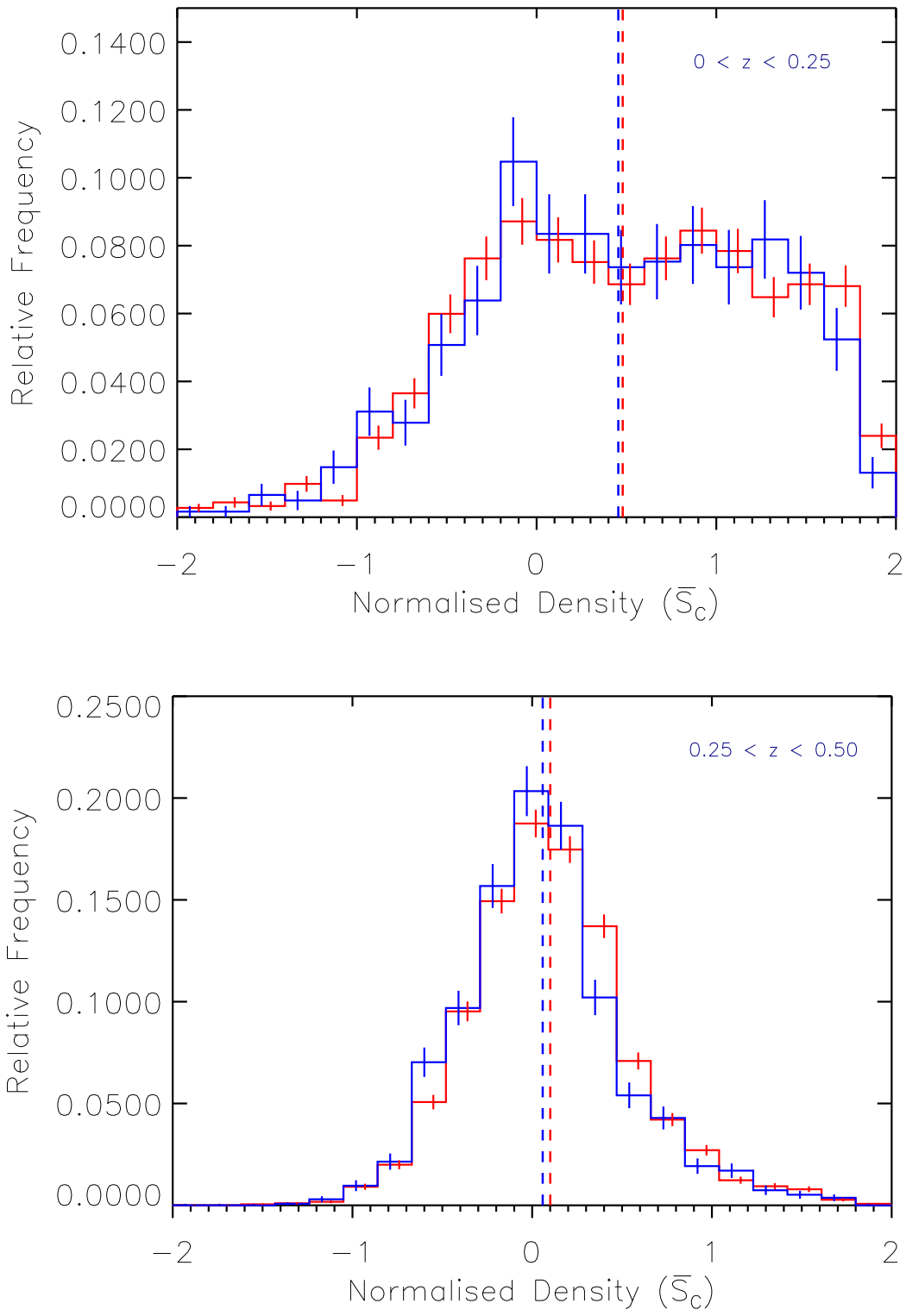

Figure 4.13: Normalized histograms that show the full matched Optical-15P1 (*red*) and FIR-15P1 (*blue*) samples binned in redshift *Top*: ($0 \leq z < 0.25$) No significant differences are found between the two samples. *Bottom*: ($0.25 \leq z < 0.50$) From KS- and MWU-tests both samples are significantly different between the 3.5σ and 3.6σ level.

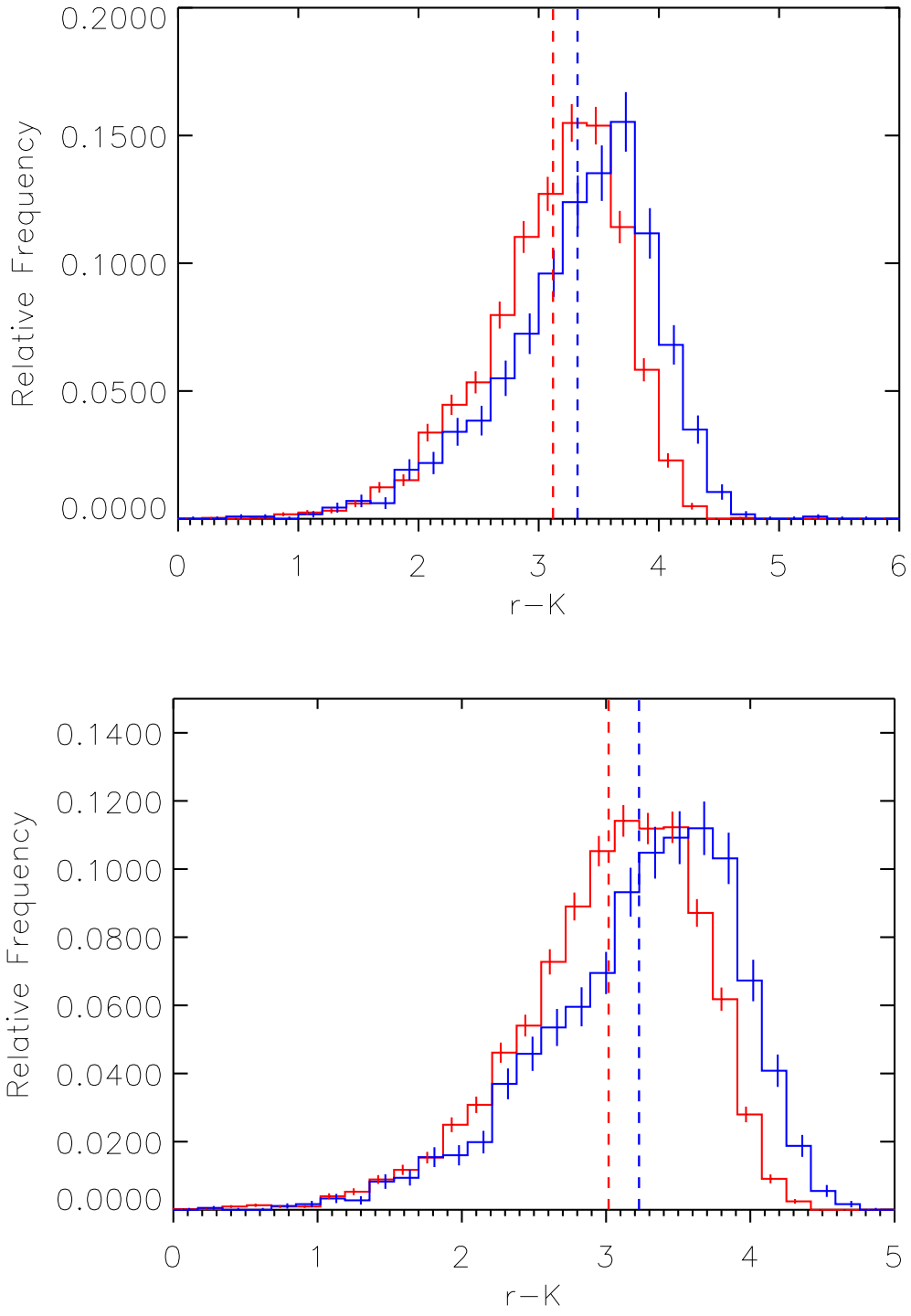

FIGURE 4.14: Normalized histograms of the $r-K$ colours of the $g-r$, $r-i$, z and m_r matched Optical (*red*) and FIR (*blue*) samples from the 12P1 (*Top*) and 15P1 (*Bottom*) fields. This shows both fields have significantly different colour distributions at the $> 6\sigma$ level. The brighter m_K magnitudes of the FIR-12P1 sample indicate the presence of dust reddening.

Table 4.7: KS-test and MWU-test results for the comparison of both the Optical-12P1 and FIR-12P1 matched sample $\bar{S}_c$ distributions within each redshift slice shown in figure 4.12. From KS results the density distributions are not significantly different in the lowest redshift bin, however in the higher redshift bin there is a significant difference at the 3.0σ level. The number of objects from each population are given:

Redshift Slice	Optical	FIR	KS Probability	MWU Probability
$0 \leq z < 0.25$	955	316	0.517	0.189
$0.25 \leq z < 0.50$	3,251	1,083	$< 10^{-3}$	$< 10^{-4}$

Table 4.8: KS-test and MWU-test results for the comparison of both the Optical-15P1 and FIR-15P1 matched samples $\bar{S}_c$ distributions within each redshift slice shown in figure 4.13. From KS results the density distributions are not significantly different in the lowest redshift bin, however in the higher redshift bin there is a significant difference at the 3.5σ level. The number of objects from each population are given:

Redshift Slice	Optical	FIR	KS Probability	MWU Probability
$0 \leq z < 0.25$	1,836	611	0.837	0.292
$0.25 \leq z < 0.50$	4,064	1,352	$< 10^{-4}$	$< 10^{-4}$

Repeating the dust reddening analysis from Section 4.2.4 on both the FIR-12P1 and FIR-15P1 samples returned the same trends and correlations found in the 9P1 field. Figure 4.14 displays the $r - K$ distributions of both Optical and FIR samples of the 12P1 and 15P1 samples (*top* and *bottom*) respectively, showing a clear difference between these distributions, with KS- and MWU-tests confirming that these differences were significant at the $> 6\sigma$ level for both fields. As these distributions were pre-matched in r-band magnitudes, the difference in $r - K$ colour must come from an underestimation of the m_r magnitudes (and hence galaxy masses) in the FIR-12P1 and FIR-15P1 samples. Therefore, in agreement with my analysis of the 9P1 field, reducing the dust reddening would lead to an increase in the separation between the cross-matched Optical and FIR samples for the 12P1 and 15P1 field displayed in Figures 4.11 and 4.11, strengthening my overall result.

In continuation of the test of robustness carried out in Section 3.2.6, I cross-matched

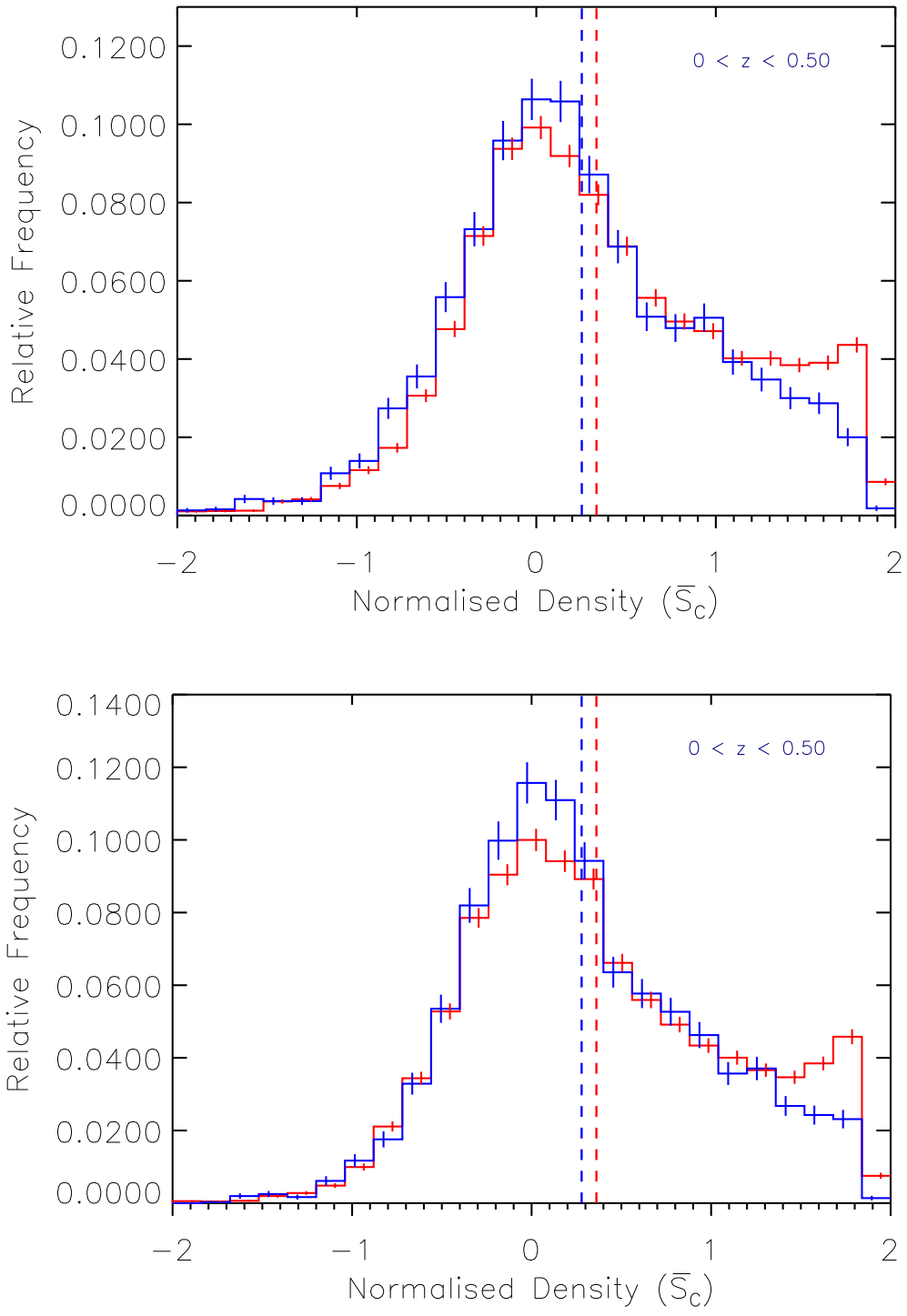

FIGURE 4.15: Normalized histograms showing the distributions of environmental density ($\bar{S}_c$) for the total $r-K$, m_K and z matched Optical (*red*) and FIR (*blue*) samples for the 12P1 (*top*) and 15P1 (*bottom*) fields. The FIR data are shifted to lower densities with KS-tests finding a significant differences at the $> 6\sigma$ level (*top*) and 5.9σ level (*bottom*).

Table 4.9: One- and two-dimensional KS- and MWU-test results where *op* represents Optical-12P1 (11,394 objects) and *FIR* represents FIR-12P1 (3,798 objects) matched in terms of their $K-$band magnitude, $r-K$ colour and redshift distributions. The two density distributions are different at the $> 6\sigma$ level from KS-tests, with the medians of the distributions different at the $> 6\sigma$ level from MWU-tests.

Distributions Compared			KS Prob.	MWU Prob.
$z_{(op)}$	versus	$z_{(FIR)}$	0.993	0.463
$(r-K)_{op}$	versus	$(r-K)_{FIR}$	0.999	0.468
$m_{K(op)}$	versus	$m_{K(FIR)}$	0.517	0.195
$(\bar{S}_c)_{op}$	versus	$(\bar{S}_c)_{FIR}$	$< 10^{-9}$	$< 10^{-10}$
$(r-K,z)_{op}$	versus	$(r-K,z)_{FIR}$	0.969	-
$(m_K,z)_{op}$	versus	$(m_K,z)_{FIR}$	0.396	-
$(r-K,m_K)_{op}$	versus	$(r-K,m_K)_{FIR}$	0.681	-
$(r-K,\bar{S}_c)_{op}$	versus	$(r-K,\bar{S}_c)_{FIR}$	$< 10^{-6}$	-
$(m_K,\bar{S}_c)_{op}$	versus	$(m_K,\bar{S}_c)_{FIR}$	$< 10^{-8}$	-
$(z,\bar{S}_c)_{op}$	versus	$(z,\bar{S}_c)_{FIR}$	$< 10^{-7}$	-

the Optical and FIR samples of the 12P1 and 15P1 fields in terms of their $r-K$, z and m_K distributions. Due to the lack of m_K data available this reduced the initial Optical-12P1 and FIR-12P1 samples to 204,218 and 5,876 objects with the resultant cross-matched samples numbering 11,394 and 3,798 objects respectively. The initial Optical-15P1 and FIR-15P1 samples were reduced to 237,708 and 5,487 objects before the cross-match, with 10,761 and 3,587 objects after the cross-matching respectively. These distributions are displayed in Figure 4.15 where it is clear that the FIR data favour generally lower densities in both fields. Applying KS- and MWU-tests to combinations of these parameters revealed significant differences between the $\bar{S}_c$ distributions at the $> 6\sigma$ level in the 12P1 field and at the 5.9σ level in the 15P1 field. These values are presented in Tables 4.9 and 4.10. Once more, applying the same redshift binning as previously applied to these distributions, and repeating the statistical comparisons, shows that there is a much improved significant difference between the Optical and FIR

TABLE 4.10: One- and two-dimensional KS- and MWU-test results where *op* represents Optical-15P1 (10,761 objects) and *FIR* represents FIR-15P1 (3,587 objects) matched in terms of their $K-$band magnitude, $r-K$ colour and redshift distributions. The two density distributions are different at the 5.9σ level from KS-tests, with the medians of the distributions different at the 5.4σ level from MWU-tests.

Distributions Compared			KS Prob.	MWU Prob.
$z_{(op)}$	versus	$z_{(FIR)}$	0.999	0.486
$(r-K)_{op}$	versus	$(r-K)_{FIR}$	0.999	0.464
$m_{K(op)}$	versus	$m_{K(FIR)}$	0.678	0.230
$(\bar{S}_c)_{op}$	versus	$(\bar{S}_c)_{FIR}$	$< 10^{-7}$	$< 10^{-6}$
$(r-K,z)_{op}$	versus	$(r-K,z)_{FIR}$	0.983	-
$(m_K,z)_{op}$	versus	$(m_K,z)_{FIR}$	0.712	-
$(r-K,m_K)_{op}$	versus	$(r-K,m_K)_{FIR}$	0.647	-
$(r-K,\bar{S}_c)_{op}$	versus	$(r-K,\bar{S}_c)_{FIR}$	$< 10^{-5}$	-
$(m_K,\bar{S}_c)_{op}$	versus	$(m_K,\bar{S}_c)_{FIR}$	$< 10^{-6}$	-
$(z,\bar{S}_c)_{op}$	versus	$(z,\bar{S}_c)_{FIR}$	$< 10^{-5}$	-

TABLE 4.11: KS-test and MWU-test results for the comparison of both the $\bar{S}_c$ distributions within each redshift bin of both Optical-12P1 and FIR-12P1 fields, cross-matched in m_K, $r-K$ colour and redshift. The number of objects from each population are given:

Redshift Slice	Optical	FIR	KS Probability	MWU Probability
$0 \leq z < 0.25$	4,811	1,606	$< 10^{-9}$	$< 10^{-10}$
$0.25 \leq z < 0.50$	6,460	2,156	$< 10^{-5}$	$< 10^{-6}$

TABLE 4.12: KS-test and MWU-test results for the comparison of both the $\bar{S}_c$ distributions within each redshift bin of both Optical-15P1 and FIR-15P1 fields, cross-matched in m_K, $r-K$ colour and redshift. The number of objects from each population are given:

Redshift Slice	Optical	FIR	KS Probability	MWU Probability
$0 \leq z < 0.25$	4,815	1,613	$< 10^{-10}$	$< 10^{-10}$
$0.25 \leq z < 0.50$	5,796	1,923	$< 10^{-3}$	0.124

density distributions, for both the 12P1 and 15P1 fields, in both bins. These values are presented in Tables 4.11 and 4.12.

4.3 Density Analysis: Combined Phase-One Fields

The analysis presented so far in this chapter has shown that the established correlations between the FIR and Optical populations, in terms of their environmental trends with FIR emission, are consistent across each of the three Phase-One fields (9hr, 12hr & 15hr). To further expand upon this analysis and to improve the statistical comparison between the data, I combine the three fields and repeat the density analyses. With the three fields combined, the increase in the number of both the Optical and FIR populations will allow for the acquisition of better statistics in terms of my comparisons between the various properties of the galaxies.

4.3.1 Combining the Fields

With normalised environmental densities calculated for each object across the Optical-9P1, Optical-12P1 and Optical-15P1 fields, I could then combine this data to form my total combined post-VT algorithm density catalogue. This combined catalogue, hereafter named 'Optical-Full', incorporated all of the same fundamental parameters concerning redshift limits, edge-effect cuts and FIR region matches as were applied to the individual fields in Section 4.2, resulting in a catalogue that consisted of $1,570,693$ galaxies. Combining the individual *Herschel*-9hr, *Herschel*-12hr and *Herschel*-15hr fields and applying the reliability ($R \geq 0.8$) cut, as derived from the LR technique of (Smith et al., 2011), resulted in a combined FIR catalogue of $22,464$ objects with reliable optical counterparts. I then cross-matched these sources directly with the Optical-Full catalogue in terms of there mutual SDSS identification numbers, finding $20,672$ galaxies with both Optical and FIR emission. This sample is hereafter called 'FIR-Full' and were simultaneously removed from the Optical-Full catalogue, reducing its number to $1,550,017$ galaxies.

Following the same methodology of the individual field analyses, the Optical-Full

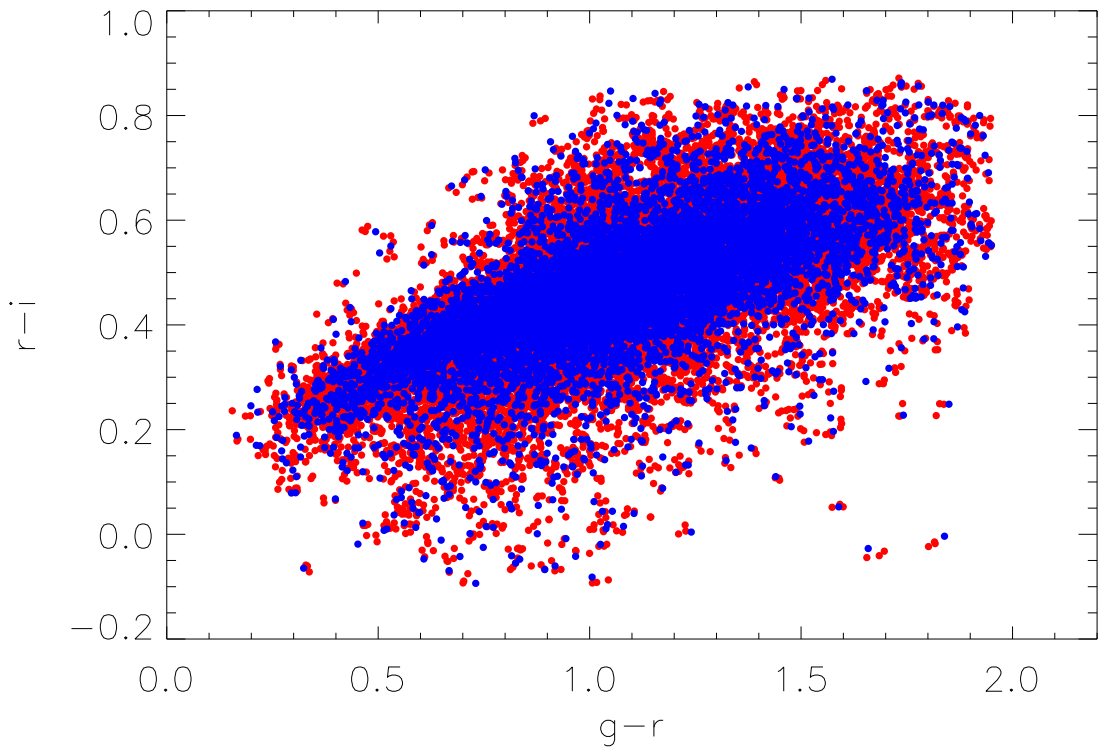

FIGURE 4.16: $g-r$ versus $r-i$ colour distribution for the 'matched' samples of Optical-Full (*red*) and FIR-Full (*blue*) numbering 28,302 and 9,434 sources respectively.

and FIR-Full samples were again cross-matched in terms of their colour, redshift and r-band magnitudes distributions ($g-r$, $r-i$, z & m_r) ensuring that they have equivalent distributions across these parameters, and that an appropriate like-for-like comparison can be achieved. Thus any differences found between their normalized environmental densities can not be attributed to other parameter differences other than the presence or absence of FIR emission. The same four-dimensional gridding was applied to both samples as detailed in Section 3.2.2, selecting matches from only those objects that share the appropriate grid spacing and with additional Optical-Full and FIR-Full galaxies being removed from the analysis. These cross-matched samples are displayed in Figures 4.16 and 4.17 displaying the resultant cross-matched Optical-Full sample (*red*) numbering 28,302 objects and the cross-matched FIR-Full sample (*blue*) numbering 9,434 objects. For consistency with the individual Phase-One field analysis, I applied the same maximum peak redshift limit into the cross-matching of $z \leq 0.5$.

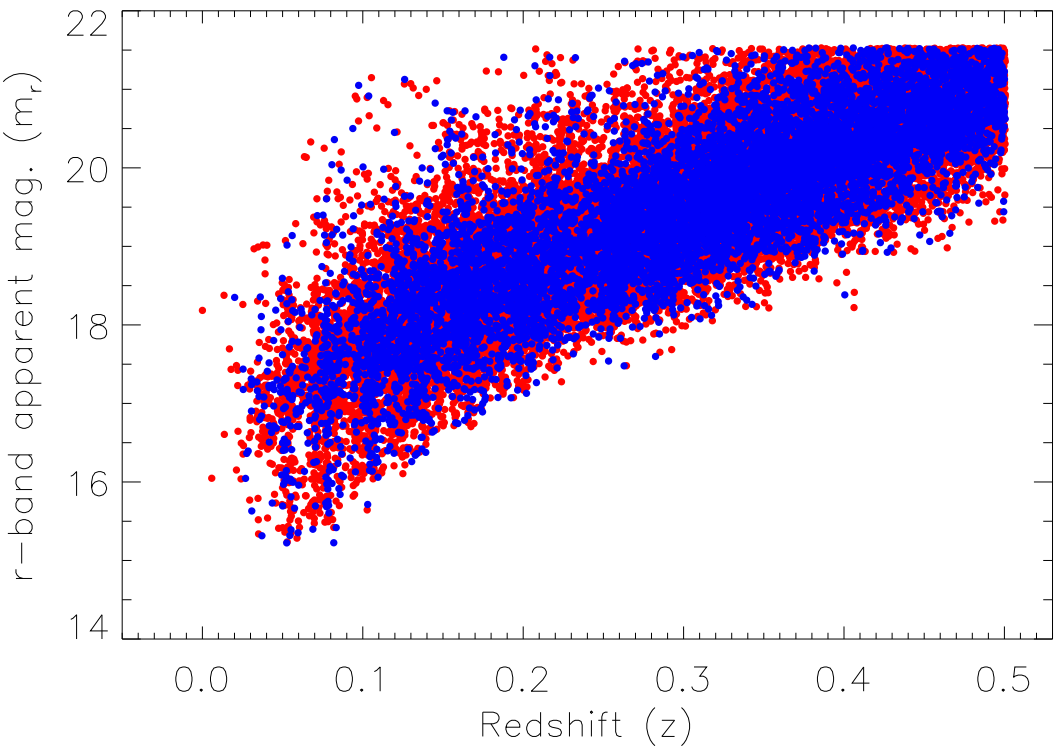

Figure 4.17: Redshift versus r-band apparent magnitude (m_r) for the 'matched' Optical-Full (*red*) and FIR-Full (*blue*) samples. Only the redshift range of $0 < z \leq 0.5$ and m_r range of $15 < m_r < 21.5$ were included in the sampling for consistency with the previous analysis.

Again, considering the full z-PDF analysis within my VT algorithm, each $\bar{S}_c$ value that remained within the allowed redshift range incorporated the influence of higher redshift objects without effecting the overall density calculation.

4.3.2 Comparison of the Combined FIR and Optical Galaxies

With two cross-matched samples representing the combined Optical and FIR populations from across the Phase-One field, I could then re-introduce the one- and two-dimensional KS and MWU statistical tests across these samples to again test the correlations between FIR emission and environmental density. Table 4.13 presents the resultant probabilities returned from these KS- and MWU tests across the various parameter distributions. The probability values returned for combinations of the colour,

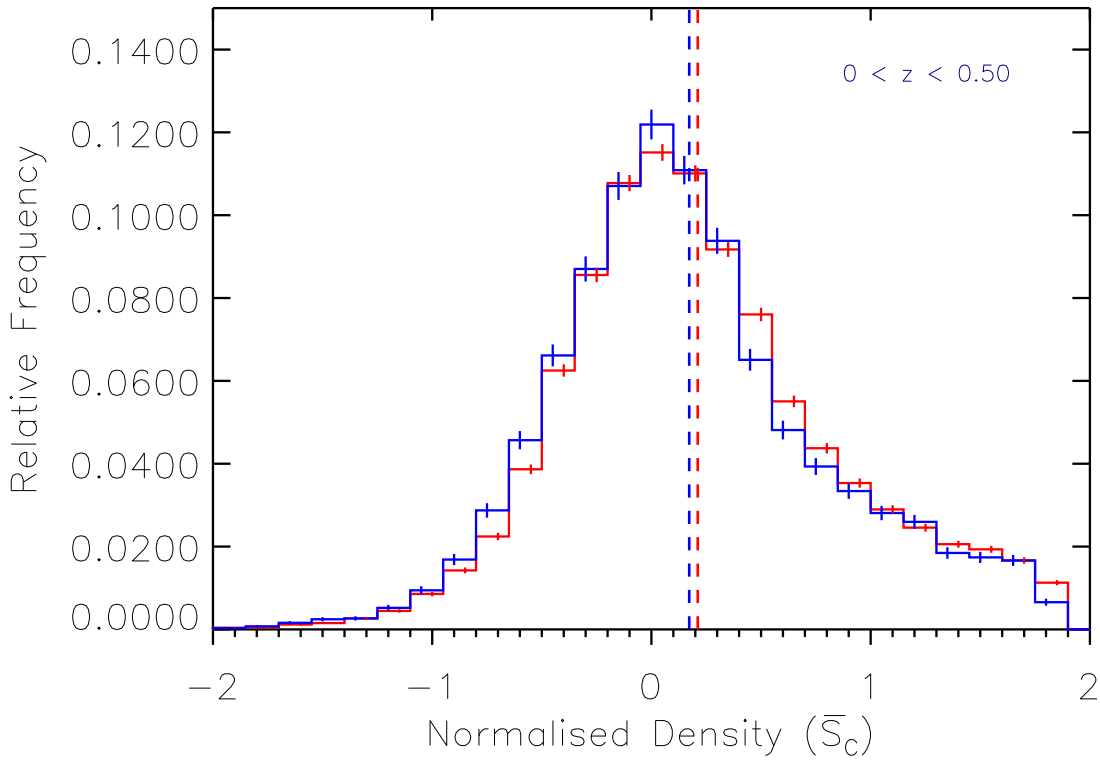

FIGURE 4.18: Normalized histograms showing how the distributions of environmental density ($\bar{S}_c$) for the total colour, r-band magnitude and redshift matched Optical-Full (*red*) and FIR-Full (*blue*) samples compare. The histograms show error-bars depicting normalized errors associated with each bin, where $\bar{S}_c > 0$ signifies an overdensity and $\bar{S}_c < 0$ signifies an underdensity in terms of the entire matched redshift range $0 < z \leq 0.5$. The FIR-Full data is shifted to generally lower densities with its distribution mean given by the *blue* dashed-line at 0.170 ± 0.006. The Optical-Full distribution is shifted towards higher densities with the mean of its distribution given by the *red* dashed-line at 0.210 ± 0.004.

redshift and r-band magnitudes distributions were large enough such that the null hypothesis could not be rejected. Thus confirming that these matched Optical-Full and FIR-Full samples were drawn from the same underlying distribution and that they were successfully cross-matched across this parameter space.

Application of the one-dimensional KS-test to the $\bar{S}_{op}$ and $\bar{S}_{FIR}$ distributions from these combined samples, returned a very low probability indicating a significant difference at the 5.4σ level, from a probability of 1.92×10^{-7}. A significant difference was also returned from comparisons between the density and other parameter distributions, as shown in Table 4.13 also at the $> 5\sigma$ level. Figure 4.18 shows how the normalized

histograms of the $\bar{S}_{op}$ (*red*) and $\bar{S}_{FIR}$ (*blue*) distributions compare. In agreement with my previous comparisons between Optical and FIR density distributions, it is the FIR-Full data that once more favours underdense regions with the mean of its density distribution at 0.170 ± 0.006 in comparison to the Optical-Full density distribution mean at 0.210 ± 0.004. MWU-tests applied to these mean values returned a highly significant difference at the $> 6\sigma$ level. Therefore, as expected due to the increase in the number of objects in the samples, the difference between these two density distributions is much more significant, in comparison with my individual Phase-One field analysis in Section 4.2.

From my analysis of both the SDP field in Chapter 3 in addition to the individual Phase-One fields in Section 4.2, it has been shown that there is a significant trend with redshift, such that towards higher redshifts the statistical difference between the Optical and FIR density distributions increases. With a much larger number of galaxies in the Optical-Full and FIR-Full samples available for comparison, due to the combination of the individual Phase-One fields, repeating the same binning analysis should reveal more accurate statistics from KS- and MWU-tests. Introducing the same redshift binning that was applied to the individual fields in Section 4.2.3 for consistency, revealed $9,422$ Optical-Full and $3,072$ FIR-Full objects in the lower redshift bin ($0 \leq z < 0.25$) and $18,857$ Optical-Full and $6,359$ FIR-Full objects in the higher redshift bin ($0.25 \leq z < 0.50$). Applying the KS and MWU statistical tests to the binned data revealed the same trends with redshift as were previously found in my individual Phase-One field analysis. In the lower redshift bin ($0 \leq z < 0.25$) no significant difference was found between the Optical-Full and FIR-Full $\bar{S}_c$ distributions from KS- or MWU tests, with probability values of 0.553 and 0.344 respectively. However, in the higher redshift bin ($0.25 \leq z < 0.5$) a highly significant difference was found with KS-tests returning a probability of 8.0×10^{-11} indicating that the null hypothesis could be rejected at the $> 6\sigma$ level in this bin. These statistical results are presented in Table 4.14.

Histograms of the normalised $\bar{S}_c$ distributions of the cross-matched Optical-Full and FIR-Full samples in both redshift bins are displayed in Figure 4.19. In the lowest redshift bin (*top*) there is clearly no significant separation between the two distributions,

TABLE 4.13: Two sample and two-dimensional KS- and MWU-test results over the full redshift range ($0 < z \leq 0.5$). Where *op* represents cross-matched Optical-Full (28,302 objects) and *FIR* represents cross-matched FIR-Full (9,434 objects). The two density distributions are different at the 5.4σ level from KS-tests, with the means of the distributions different at the $> 6\sigma$ level from MWU-tests.

Distributions Compared			KS Probability	MWU Probability
$z_{(op)}$	versus	$z_{(FIR)}$	0.707	0.234
$(g-r)_{op}$	versus	$(g-r)_{FIR}$	0.996	0.398
$(r-i)_{op}$	versus	$(r-i)_{FIR}$	0.920	0.313
$m_{r(op)}$	versus	$m_{r(FIR)}$	0.234	0.060
$(\bar{S}_c)_{op}$	versus	$(\bar{S}_c)_{FIR}$	1.92×10^{-7}	$< 10^{-10}$
$(g-r, r-i)_{op}$	versus	$(g-r, r-i)_{FIR}$	0.570	-
$(g-r, z)_{op}$	versus	$(g-r, z)_{FIR}$	0.700	-
$(r-i, z)_{op}$	versus	$(r-i, z)_{FIR}$	0.579	-
$(m_r, z)_{op}$	versus	$(m_r, z)_{FIR}$	0.328	-
$(g-r, m_r)_{op}$	versus	$(g-r, m_r)_{FIR}$	0.443	-
$(r-i, m_r)_{op}$	versus	$(r-i, m_r)_{FIR}$	0.225	-
$(g-r, \bar{S}_c)_{op}$	versus	$(g-r, \bar{S}_c)_{FIR}$	2.57×10^{-7}	-
$(r-i, \bar{S}_c)_{op}$	versus	$(r-i, \bar{S}_c)_{FIR}$	3.50×10^{-6}	-
$(m_r, \bar{S}_c)_{op}$	versus	$(m_r, \bar{S}_c)_{FIR}$	2.48×10^{-6}	-
$(z, \bar{S}_c)_{op}$	versus	$(z, \bar{S}_c)_{FIR}$	5.24×10^{-6}	-

TABLE 4.14: KS-test and MWU-test results for the comparison of both the Optical-Full and FIR-Full matched samples $\bar{S}_c$ distributions within each redshift slice shown in figure 4.19. The number of objects from each population are also given:

Redshift Slice	Optical	FIR	KS Probability	MWU Probability
$0 \leq z < 0.25$	9,422	3,072	0.553	0.344
$0.25 \leq z < 0.50$	18,857	6,359	$< 10^{-10}$	$< 10^{-10}$

as indicated by the KS and MWU results. However, the density distributions in the higher redshift bin (*bottom*) do show the clear separation as indicated by the KS and MWU values, with both distributions exhibiting small normalized errors associated with each bin and the the FIR-Full (*blue*) data clearly favouring underdense regions.

Therefore the same redshift trends, such that the separation between density distributions of the Optical and FIR samples increases with increasing redshift, were present across the combined Phase-One fields in agreement with the trends discovered across my SDP analysis in Chapter 3 and further across my individual Phase-One field analysis in Section 4.2. As expected, the statistical differences between the FIR and Optical populations are to a greater level of significance due to the larger number of objects being compared.

4.3.3 Dust Reddening Effects

The role of dust reddening within the H-ATLAS samples has already been demonstrated in both my analyses of the SDP field in Chapter 3 and in each of the individual Phase-One fields through Section 4.2. By combining these fields and thus increasing the number of galaxies in the Optical and FIR samples, one would not only expect the dust reddening effects to remain within the FIR population, but also that the the influence of this reddening to be more prominent.

I therefore repeated the dust reddening analysis, as applied to the individual Phase-One fields, re-introducing K-band data from the UKIRT Infrared Sky Survey and removing objects without K-band emission. This reduced the $g-r$, $r-i$, z and m_r cross-matched Optical-Full and FIR-Full samples to $23,603$ and $8,189$ objects respectively and their $r-K$ colour distributions are displayed in Figure 4.20. This plot shows that, as expected, there is a clear difference between the $r-K$ distributions of the Optical-Full and FIR-Full samples, with the FIR-Full sample exhibiting redder $r-K$ colours. As these two samples have already been cross-matched in terms of their r-band magnitudes, this difference is once more due to the m_K magnitudes being brighter in the FIR-Full sample. The galaxy masses within the FIR-Full sample are underestimated, in agreement with my analysis of the individual Phase-One fields in

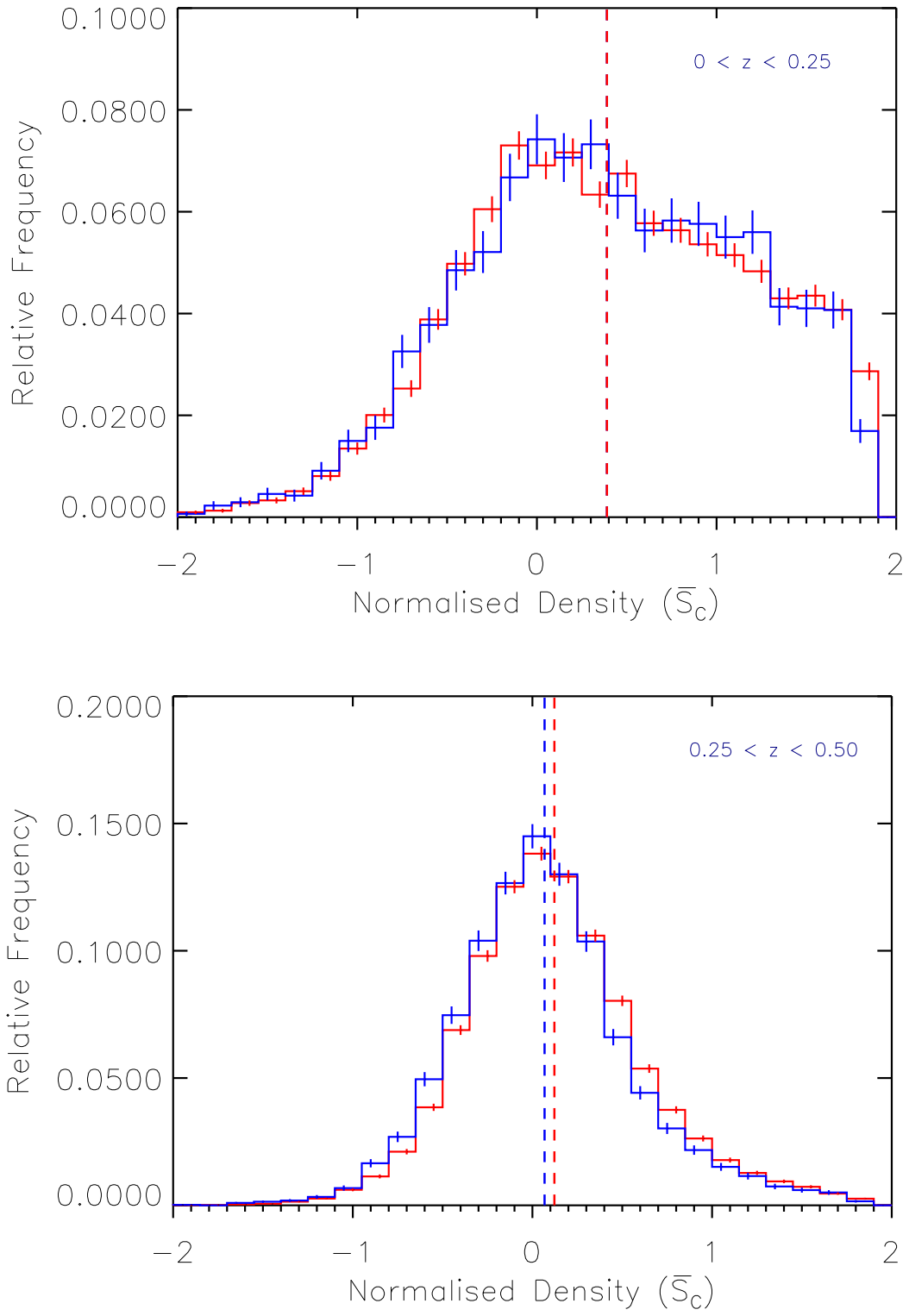

FIGURE 4.19: Normalized histograms that show the full matched Optical-Full (*red*) and FIR-Full (*blue*) samples binned in redshift *Top*: $(0 \leq z < 0.25)$ No significant differences are found between the two samples. *Bottom*: $(0.25 \leq z < 0.50)$ Both samples are significantly different at the $> 6\sigma$ level.

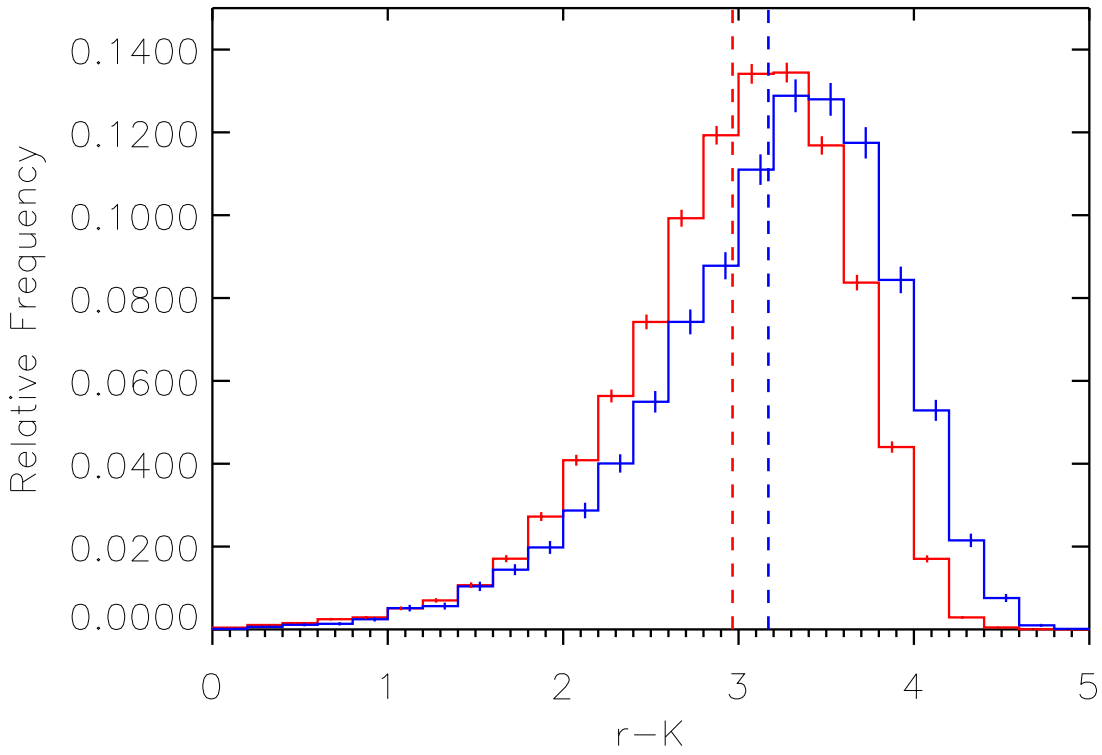

Figure 4.20: Normalized histograms of the $r-K$ colours of the $g-r$, $r-i$, z and m_r matched Optical-Full (*red*) and FIR-Full (*blue*) samples reduced in size due to the lack of m_K data to 23,603 and 8,189 objects respectively. They have significantly different colour distributions at the $> 6\sigma$ level.

Section 4.2. Application of KS- and MWU-tests confirm that the difference between the $r-K$ distributions was highly significant with the null hypothesis being rejected at the $> 6\sigma$ level. Therefore, as concluded previously, due to the known correlations between galaxy mass and density, reducing the reddening would reduce the overall estimated masses in the FIR-Full sample and consequently strengthen the measured correlation between density and FIR emission.

The robustness of these results were again tested by removing the reddening effect and repeating the environmental density comparison of the Optical-Full and FIR-Full samples. As with the individual Phase-One fields, I cross-matched the samples in terms of their $r-K$ colour, m_K and redshift distributions. However due to m_K data not being available for all objects within the initial Optical-Full and FIR-Full catalogues,

TABLE 4.15: Two sample and two-dimensional KS- and MWU-test results where *op* represents cross-matched Optical-Full (37,272 objects) and *FIR* represents FIR-Full (12,424 objects) matched in terms of their $K-$band magnitude, $r-K$ colour and redshift distributions.

Distributions Compared			KS Prob.	MWU Prob.
$z_{(op)}$	versus	$z_{(FIR)}$	0.818	0.489
$(r-K)_{op}$	versus	$(r-K)_{FIR}$	0.935	0.466
$m_{K(op)}$	versus	$m_{K(FIR)}$	0.061	0.058
$(\bar{S}_c)_{op}$	versus	$(\bar{S}_c)_{FIR}$	$< 10^{-40}$	$< 10^{-10}$
$(r-K,z)_{op}$	versus	$(r-K,z)_{FIR}$	0.437	-
$(m_K,z)_{op}$	versus	$(m_K,z)_{FIR}$	0.060	-
$(r-K,m_K)_{op}$	versus	$(r-K,m_K)_{FIR}$	0.093	-
$(r-K,\bar{S}_c)_{op}$	versus	$(r-K,\bar{S}_c)_{FIR}$	$< 10^{-29}$	-
$(m_K,\bar{S}_c)_{op}$	versus	$(m_K,\bar{S}_c)_{FIR}$	$< 10^{-26}$	-
$(z,\bar{S}_c)_{op}$	versus	$(z,\bar{S}_c)_{FIR}$	$< 10^{-28}$	-

TABLE 4.16: KS-test and MWU-test results for the comparison of both the $\bar{S}_c$ distributions within each redshift bin of both Optical-Full and FIR-Full fields, cross-matched in m_K, $r-K$ colour and redshift. The number of objects from each population are given:

Redshift Slice	Optical	FIR	KS Probability	MWU Probability
$0 \leq z < 0.25$	15,927	5,314	$< 10^{-16}$	$< 10^{-10}$
$0.25 \leq z < 0.50$	20,907	6,974	$< 10^{-44}$	$< 10^{-10}$

they were reduced to a subset of 699,829 and 17,694 objects respectively. Cross-matching these reduced samples across this parameter space, using the same gridding technique previously applied, returned 37,272 and 12,424 cross-matched Optical-Full and FIR-Full objects respectively. Applying KS- and MWU-tests to combinations of the cross-matched parameters revealed high probabilities and therefore no significant differences between them, thus confirming a successful cross-matching. These statistical values are presented in Table 4.15. Directly comparing the $\bar{S}_c$ distributions of the

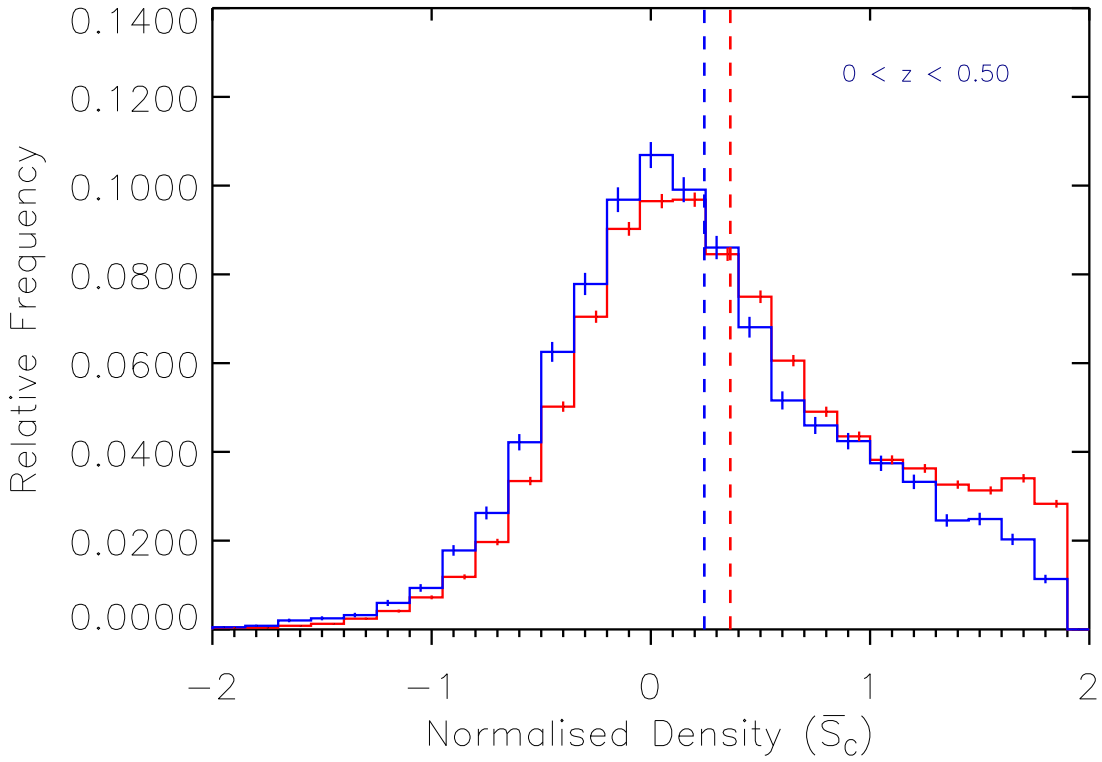

Figure 4.21: Normalized histograms showing how the distributions of environmental density ($\bar{S}_c$) for the total $r-K$, m_K and z matched Optical-Full (*red*) and FIR-Full (*blue*) samples compare across the matched redshift range $0 < z \leq 0.5$. The FIR-Full data is shifted to generally lower densities with its distribution mean given by the *blue* dashed-line at 0.240 ± 0.006. The Optical-Full distribution is shifted towards higher densities with the mean of its distribution given by the *red* dashed-line at 0.360 ± 0.004.

newly cross-matched Optical-Full and FIR-Full samples returned a KS probability of just 5.59×10^{-41}, indicating a highly significant difference at the $> 6\sigma$ level. These distributions are displayed in Figure 4.21 where it is clear that the FIR-Full sample favours underdense regions in comparison to the Optical-Full sample with density distribution mean values of 0.240 ± 0.006 and 0.360 ± 0.004 respectively. MWU-tests applied to these mean values confirm a significant difference at the $> 6\sigma$ level and these statistical values are presented in Table 4.15. Repeating the same redshift binning as previously applied to these distributions, and repeating the statistical comparisons, shows vastly improved significant differences between the Optical-Full and FIR-Full density distributions in both bins. These values are presented in Table 4.16.

4.4 Temperature Analysis of the Phase-One Fields

As discussed in Chapter 1, the increased wavelength sensitivity of the *Herschel Space Telescope* provides coverage of far-infrared emission out into the sub-millimetre regime. This probes much cooler dust temperatures than previously available from observations that focused on shorter, mid-infrared wavelengths such as IRAS and *Spitzer*. With shorter wavelength coverage from between 12 to 160μm, these mid-infrared observations were biased towards the warmer dust regions in galaxies which, due to the dust luminosity-temperature relation, trace galaxies with higher levels of star formation in the local universe (e.g. Bregman et al. 1998; Hwang et al. 2010; Feruglio et al. 2010). As such, these mid-infrared studies fail to detect galaxies with the coldest dust temperatures, which constitute the majority of the dust mass (e.g. Dunne et al. 2011), and therefore populations of cold dusty elliptical type morphologies and galaxies with low SFRs are excluded (Eales et al. 2010). For example, Devereux & Young (1990) showed that the ~ 90 per cent of galactic dust was missed by IRAS $60-100\mu$m mid-infrared observations. Therefore the the 250μm H-ATLAS observations used within this work are able to probe these coldest dust temperatures, which as a major contributor to infrared luminosity (Willmer et al., 2009), allows for a more robust picture of the relationships between dust temperature and environment.

An additional advantage of using 250μm data to probe the coldest dust temperatures is that, at this wavelength, AGN contamination should be reduced in the sample. This is due to the fact that the thermal infrared emission from the dusty tori of AGN peak in the mid-infrared of the observed-frame SED (e.g. Virdee et al. 2013; Del Moro et al. 2013) and as a result, fall shortward of the wavelength range of the H-ATLAS SPIRE instrument. Consequently, by using 250μm data my sample of far-infrared observations should predominantly include dust thermally heated by star-formation.

Therefore with the inclusion of isothermal dust temperatures associated with each H-ATLAS FIR source across all three fields of the total Phase-One catalogue (9hr, 12hr & 15hr), I am able to directly compare the environmental densities of the FIR sources with their respective temperature information so as to establish whether any significant

trends exist between them. Due to the greatly increased number of galaxies available in the Phase-One catalogue, in comparison with the SDP field, this temperature-density analysis provides insight into the relationships between hot and cold galaxies and their environments, in addition to furthering our understanding of the processes that drive FIR emission in these galaxies.

4.4.1 FIR Dust Temperature Calculation

The total H-ATLAS 250μm Phase-One catalogue contains isothermal dust temperatures for each source, calculated by Smith et al., (submitted) who assumed model far-infrared spectra with the form of an isothermal grey-body with an emissivity (β) = 1.89. Preferencing spectroscopic redshifts ahead of best-fit photometric redshifts, they determine a Chi-squared (χ^2) goodness-of-fit parameter on a grid of temperatures spaced at 0.2K using data at 100, 160, 250, 350 and 500μm. They then derive a PDF, as a function of temperature, for each galaxy, marginalised over the free parameters of effective temperature (T_{eff}) and total ($8 - 1000\mu$m) dust luminosity (L_{dust}). They then use this derived PDF to determine median-likelihood temperatures (i.e. the 50th percentile of the PDF) for each galaxy, with errors estimated according to the 16th and 84th percentiles of the temperature PDF. They use the resulting distributions of χ^2, summed across their sample, to determine that the global population mean temperature of galaxies in H-ATLAS is $\sim$ 23.2K. For further details of this temperature calculation, see Smith et al. (2013).

4.4.2 The 9hr Temperature-Density Analysis

Examining the full temperature distribution of the 7,272 objects in the FIR-9P1 catalogue (with optical counterparts with $R \geq 0.8$), I found the mean temperature of this distribution to be $\bar{T}_{50} = 23.4$K. I then divided this sample into two sub-samples based on whether the FIR temperature values resided above or below this mean value. This was such that where $T > \bar{T}_{50}$ (hereafter named Hot-9P1) these sources, numbering 3,490, have hotter isothermal dust temperatures than this mean temperature and

TABLE 4.17: One- and two-dimensional KS- and MWU-test results for the statistical comparison of the Optical-9P1 sample against the Hot-9P1 and Cold-9P1 samples individually, cross-matched in $g-r$, $r-i$, z and m_r space. The final row shows the relative comparison between the density distributions of these Hot-9P1 and Cold-9P1 samples, showing a difference at the 2.9σ level.

Distributions Compared			KS Probability	MWU Probability
$z_{(op)}$	versus	$z_{(hot)}$	0.814	0.357
$(g-r)_{op}$	versus	$(g-r)_{hot}$	0.999	0.483
$(r-i)_{op}$	versus	$(r-i)_{hot}$	0.992	0.398
$m_{r(op)}$	versus	$m_{r(hot)}$	0.344	0.156
$z_{(op)}$	versus	$z_{(cold)}$	0.989	0.358
$(g-r)_{op}$	versus	$(g-r)_{cold}$	0.999	0.436
$(r-i)_{op}$	versus	$(r-i)_{cold}$	0.999	0.493
$m_{r(op)}$	versus	$m_{r(cold)}$	0.161	0.054
$(\bar{S}_c)_{hot}$	versus	$(\bar{S}_c)_{cold}$	4.52×10^{-3}	8.79×10^{-3}

conversely where $T \leq \bar{T}_{50}$ (hereafter named Cold-9P1), these sources numbering $3,782$ have colder isothermal dust temperatures than the mean.

With the eventual aim of comparing the Hot-9P1 and Cold-9P1 FIR samples to examine any significant trends or differences, it was first necessary to cross-match the Hot-9P1 and Cold-9P1 samples individually with the $506,478$ objects of the Optical-9P1 sample in terms of colour, magnitude and redshift space ($g-r$, $r-i$, z and m_r) as achieved in Section 4.2.3. This cross-matching is necessary to counteract the selection bias associated with the coldest galaxies being detected at generally lower redshifts than hotter galaxies. This is due to the fact that galaxies with brighter FIR luminosities are associated with hotter dust temperatures (e.g. Dunne & Eales 2001; Chapman et al. 2003; Blain et al. 2003, 2004; Chapman et al. 2005; Kovács et al. 2006; Chanial et al. 2007; Yang et al. 2007; Chapin et al. 2009; Dye et al. 2009; Clements et al. 2010) and, in a flux-density limited survey, selection effects will prevent the coldest galaxies from being detected at the highest redshifts. By individually cross-matching the hot and

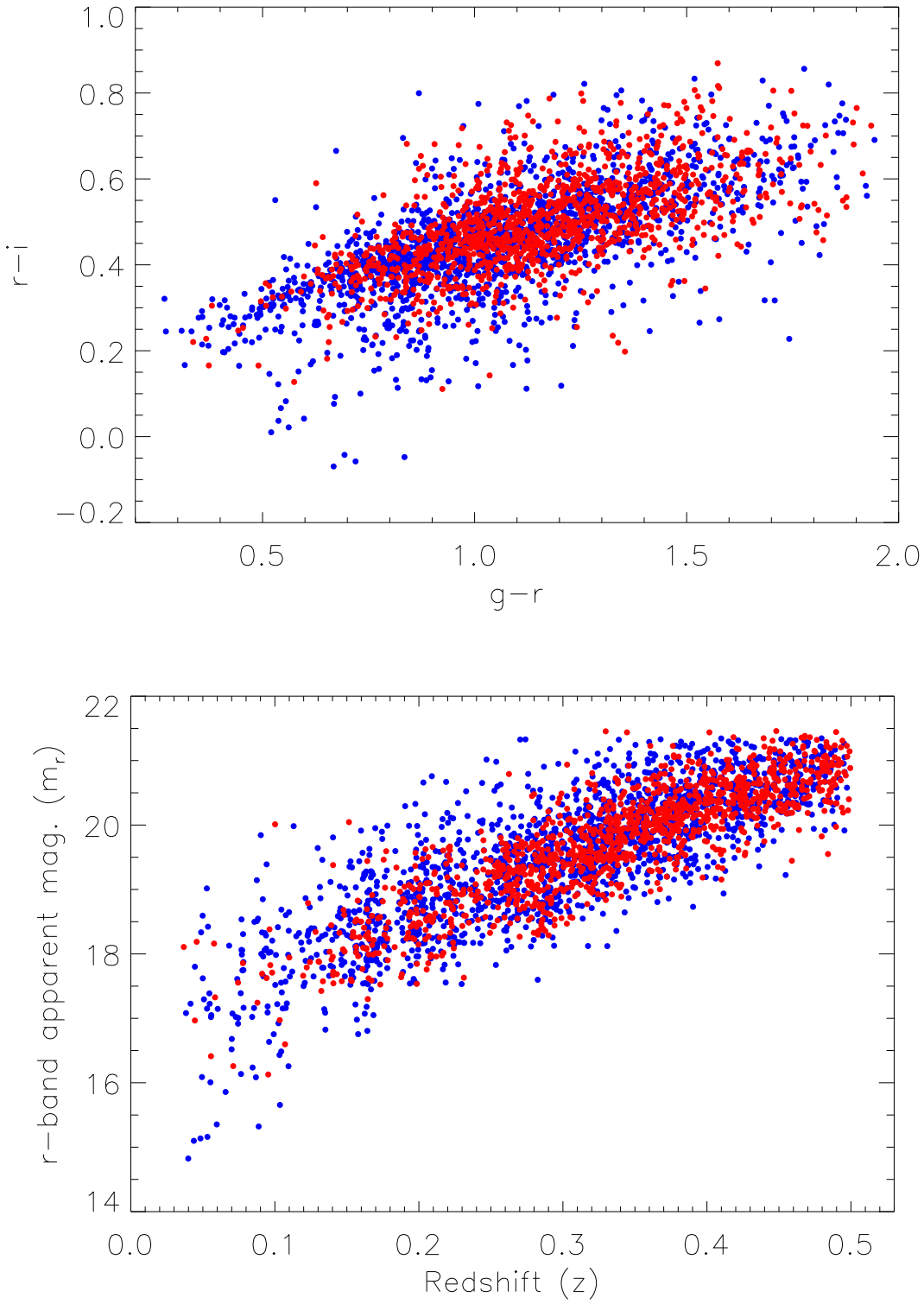

Figure 4.22: *Top*: Relative comparison of the $g-r$ versus $r-i$ distributions of the Hot-9P1 (*red*) and Cold-9P1 (*blue*) far-infrared sources numbering $1,266$ and $1,685$ respectively. *Bottom*: Redshift versus r-band apparent magnitude (m_r) for the same samples.

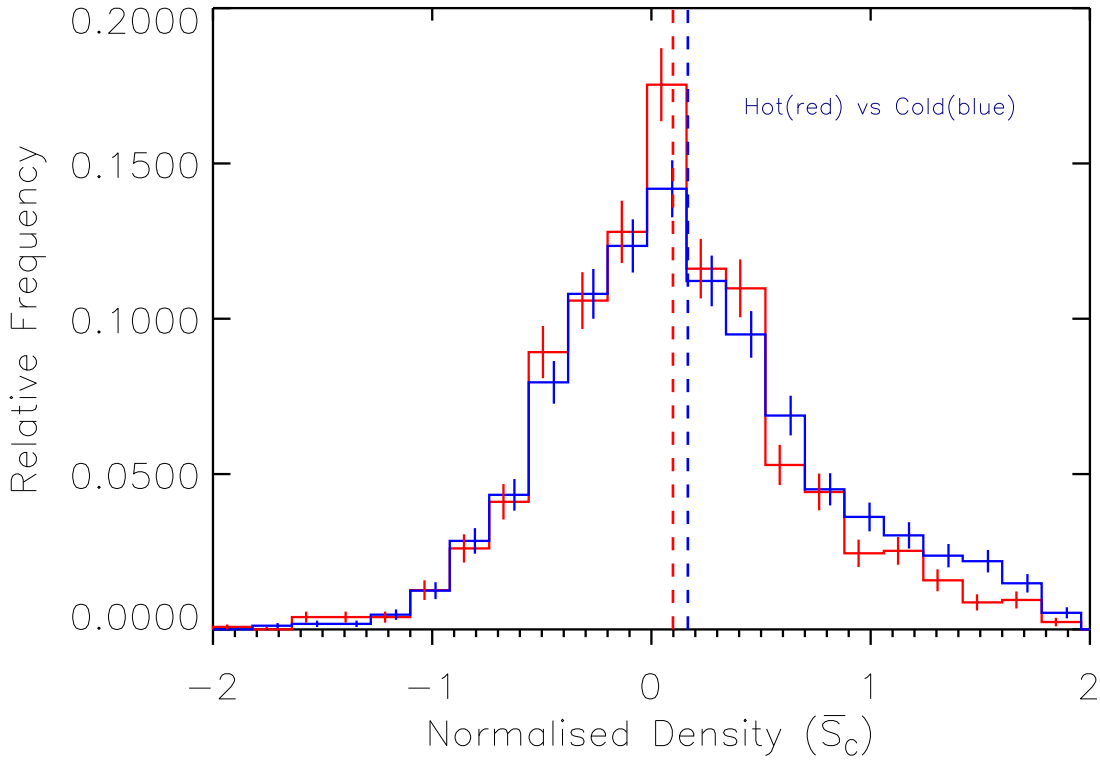

FIGURE 4.23: Normalized histograms showing how the distributions of environmental density ($\bar{S}_c$) of the matched Hot-9P1 (*red*) and Cold-9P1 (*blue*) samples compare. The Hot-9P1 data is shifted to generally lower densities with its distribution mean given by the *red* dashed-line at $(9.80 \pm 1.57) \times 10^{-2}$. The Cold-9P1 distribution is shifted towards higher densities with the mean of its distribution given by the *blue* dashed-line at $(16.60 \pm 1.48) \times 10^{-2}$. The distributions are different at the 2.9σ level from KS-tests.

cold samples to the optical field in $g-r$, $r-i$, z and m_r space, this selection bias can be removed from the resultant comparison.

Beginning with the 3,490 sources in the Hot-9P1 sample, these objects were cross-matched with the Optical-9P1 field locating 3,798 matched Optical sources and 1,266 FIR cross-matched across the parameter space. Furthermore, cross-matching the 3,782 Cold-9P1 sources with the Optical-9P1 field returned 5,055 matched Optical and 1,685 matched FIR cross-matched across the parameter space. KS- and MWU-tests were applied to their colour, magnitude and redshift distributions in order to confirm that the matched samples were indeed drawn from the same underlying distribution. The probability values returned by these tests were large enough so that the null hypotheses could not be rejected for these distributions, thus confirming a successful cross-matching of

the Hot-9P1 and Cold-9P1 samples individually with the full Optical-9P1 sample. All results from these KS- and MWU-tests are presented in Table 4.17 for the hot and cold samples respectively. The last row of the table gives the relative comparison between the density distributions of the cross-matched Hot-9P1 and Cold-9P1 samples. As these have both been cross-matched with the full Optical-9P1 sample in z, $g-r$, $r-i$ and m_r space, the only difference between them (other than their temperatures) should be their densities.

I could then directly compare the normalized environmental density distributions of both optically-matched $1,266$ Hot-9P1 and $1,685$ Cold-9P1 samples to test if any difference could be detected between them. Once more applying KS-tests to the data revealed a significant difference between the $\bar{S}_c$ values at the 2.9σ level with a probability of 4.52×10^{-3}. Figure 4.23 illustrates normalised histograms of these distributions showing that the Cold-9P1 sample (*blue*) generally favours overdense regions compared to the Hot-9P1 sample (*red*) with mean values of (9.80 ± 1.57) $\times 10^{-2}$ against (16.60 ± 1.48) $\times 10^{-2}$ respectively. MWU-tests applied to these mean values returned a significant difference at the 2.7σ level with a probability of 8.79×10^{-3}. The statistical results from KS- and MWU-tests between the $\bar{S}_{hot}$ and $\bar{S}_{cold}$ distributions are presented at the bottom of Table 4.17 and Figure 4.22 displays their $g-r$ versus $r-i$ colour-colour and m_r versus z plots.

Considering the trends between density and SFR; this significant difference between the hot and cold dust temperature populations, such that galaxies with colder isothermal dust temperatures are more prevalent in the densest regions, allows for the origin of FIR emission within dust obscured galaxies to be investigated. It is known from my SFR-density analysis in both the SDP field (Chapter 3) and this Phase-One 9hr data, that there is a well defined negative correlation between density and SFR. Consequently one would expect the highest density galaxies to have cooler dust temperatures due to the lack of bright young stars emitting high luminosity UV, thermally heating their dust. As many authors have shown (e.g. Ellis et al. 1997; Stanford et al. 1998; Balogh et al. 1999; Lee et al. 2010; Masters et al. 2010; Thomas et al. 2010; Whitaker et al. 2010; Rowlands et al. 2012; Snyder et al. 2012) galaxies with old stellar populations lie

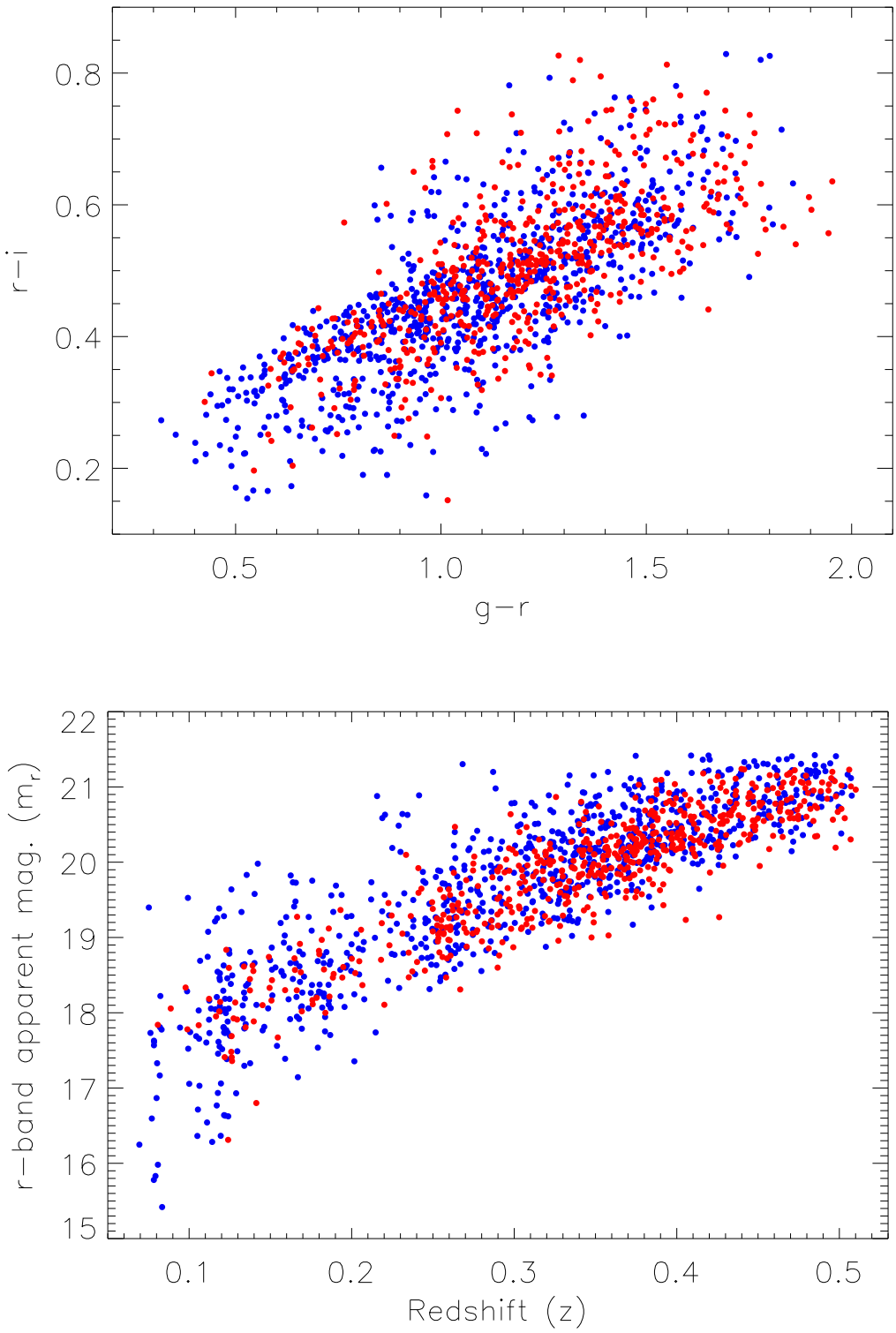

FIGURE 4.24: *Top*: Relative comparison of the $g-r$ versus $r-i$ distributions of the Hot-12P1 (*red*) and Cold-12P1 (*blue*) far-infrared sources numbering 581 and 826 respectively. *Bottom*: Redshift versus r-band apparent magnitude (m_r) for the same samples.

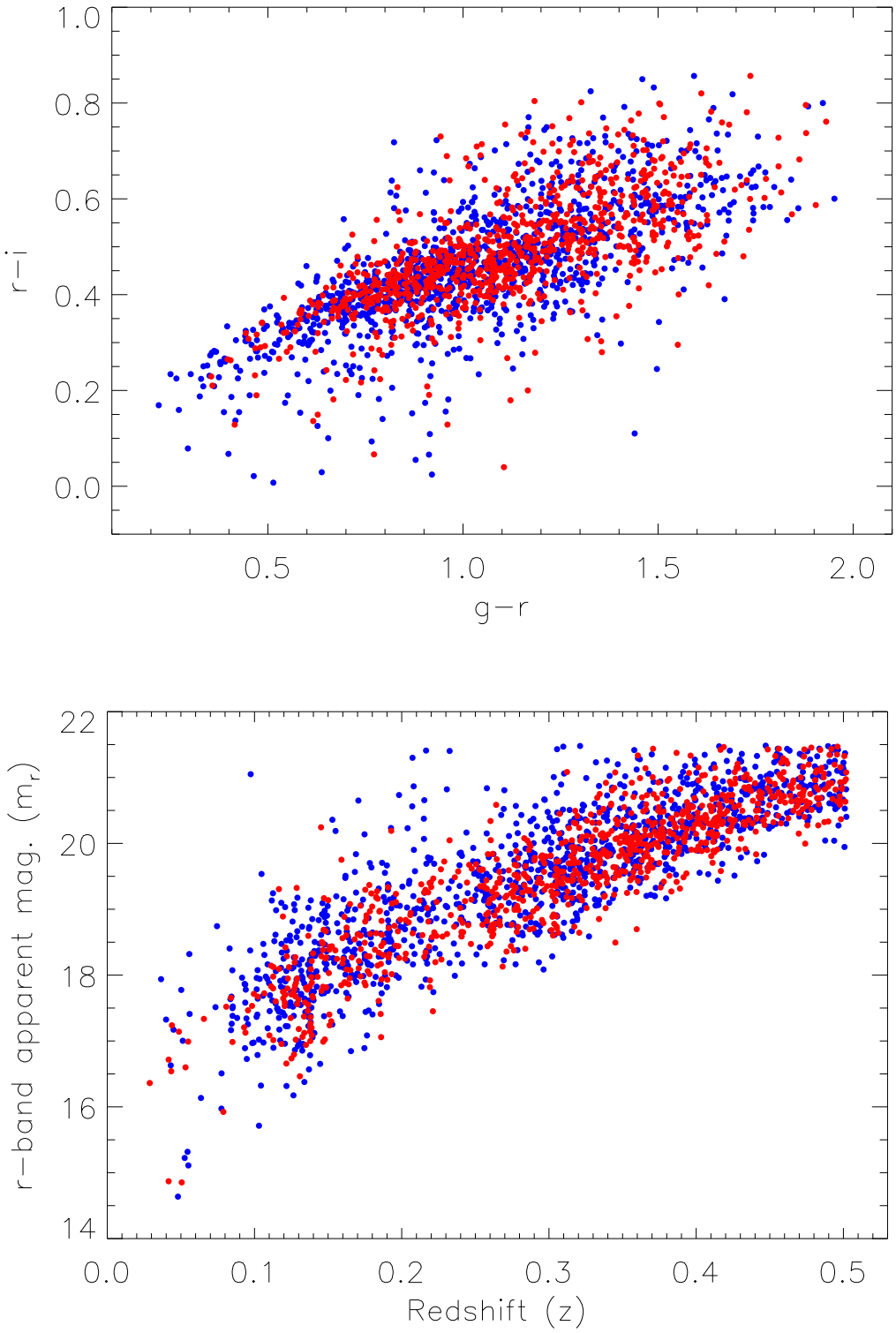

Figure 4.25: *Top*: Relative comparison of the $g-r$ versus $r-i$ distributions of the Hot-15P1 (*red*) and Cold-15P1 (*blue*) far-infrared sources numbering 891 and 1,172 respectively. *Bottom*: Redshift versus r-band apparent magnitude (m_r) for the same samples.

TABLE 4.18: One- and two-dimensional KS- and MWU-test results for the statistical comparison of the Optical-12P1 sample against the Hot-12P1 and Cold-12P1 samples individually, cross-matched in $g-r$, $r-i$, z and m_r space. The final row shows the relative comparison between the density distributions of these Hot-12P1 and Cold-12P1 samples, showing a difference at the 2.1σ level from KS-tests. The Optical versus Hot cross-match returned $1,743$ and 581 objects respectively, while the Optical versus Cold cross-match returned $2,478$ and 826 objects respectively.

Distributions Compared			KS Probability	MWU Probability
$z_{(op)}$	versus	$z_{(hot)}$	0.810	0.401
$(g-r)_{op}$	versus	$(g-r)_{hot}$	0.999	0.467
$(r-i)_{op}$	versus	$(r-i)_{hot}$	0.999	0.486
$m_{r(op)}$	versus	$m_{r(hot)}$	0.753	0.274
$z_{(op)}$	versus	$z_{(cold)}$	0.995	0.447
$(g-r)_{op}$	versus	$(g-r)_{cold}$	0.995	0.450
$(r-i)_{op}$	versus	$(r-i)_{cold}$	0.999	0.491
$m_{r(op)}$	versus	$m_{r(cold)}$	0.992	0.372
$(\bar{S}_c)_{hot}$	versus	$(\bar{S}_c)_{cold}$	0.038	0.345

within over dense regions, the FIR emission detected in these regions is therefore likely attributed to ISM heating from these older stars, in addition to other UV emitters such as active galactic nuclei (AGN) (e.g. Schmitt et al. 2006; da Cunha et al. 2008; Nardini et al. 2008; Bendo et al. 2010, 2012; Groves et al. 2012; Smith et al. 2012a; Smith et al. 2012b). Conversely, as it has been shown that with decreasing densities the rate of star formation increases (e.g. Chapter 3; Domínguez et al. 2001; Gómez et al. 2003; Goto et al. 2003; Balogh et al. 2004; Kauffmann et al. 2004; O'Mill et al. 2008; Wijesinghe et al. 2012; Burton et al. 2013), one would expect the dust temperatures of these galaxies to be higher as a product of absorption and re-emission of UV emission from bright young stars, in line with these results.

Table 4.19: One- and two-dimensional KS- and MWU-test results for the statistical comparison of the Optical-15P1 sample against the Hot-15P1 and Cold-15P1 samples individually, cross-matched in $g-r$, $r-i$, z and m_r space. The final row shows the relative comparison between the density distributions of these Hot-15P1 and Cold-15P1 samples, showing a difference at the 2.2σ level from KS-tests. The Optical versus Hot cross-match returned $2,673$ and 891 objects respectively, while the Optical versus Cold cross-match returned $3,516$ and $1,172$ objects respectively.

Distributions Compared			KS Probability	MWU Probability
$z_{(op)}$	versus	$z_{(hot)}$	0.993	0.380
$(g-r)_{op}$	versus	$(g-r)_{hot}$	0.999	0.453
$(r-i)_{op}$	versus	$(r-i)_{hot}$	0.999	0.431
$m_{r(op)}$	versus	$m_{r(hot)}$	0.820	0.287
$z_{(op)}$	versus	$z_{(cold)}$	0.999	0.426
$(g-r)_{op}$	versus	$(g-r)_{cold}$	0.996	0.446
$(r-i)_{op}$	versus	$(r-i)_{cold}$	0.985	0.432
$m_{r(op)}$	versus	$m_{r(cold)}$	0.789	0.249
$(\bar{S}_c)_{hot}$	versus	$(\bar{S}_c)_{cold}$	0.033	9.96×10^{-3}

4.4.3 12hr and 15hr Temperature-Density Analysis

I continued the temperature-density analysis across the 12P1 and 15P1 fields to investigate whether the same trends could be identified. I found the mean isothermal dust temperature of the initial FIR-12P1 and FIR-15P1 catalogues (with optical counterparts with $R \geq 0.8$) to be $\bar{T}_{50} = 23.24$K and $\bar{T}_{50} = 23.23$K respectively, and I subsequently divided these catalogues into hot and cold FIR sub-samples based on these mean temperatures. Once more, to counteract the selection effects discussed above, I repeated the cross-matching of these hot and cold FIR samples with there respective Optical samples in terms of their $g-r$, $r-i$, z and m_r parameter space, in order to produce a relative comparison. KS- and MWU-tests were again applied to these cross-matched samples and their results are presented in Tables 4.18 and 4.19. For both cross-matched 12P1 and 15P1 fields, the KS and MWU probabilities returned confirmed that their cross-matched distributions were consistent with being from the

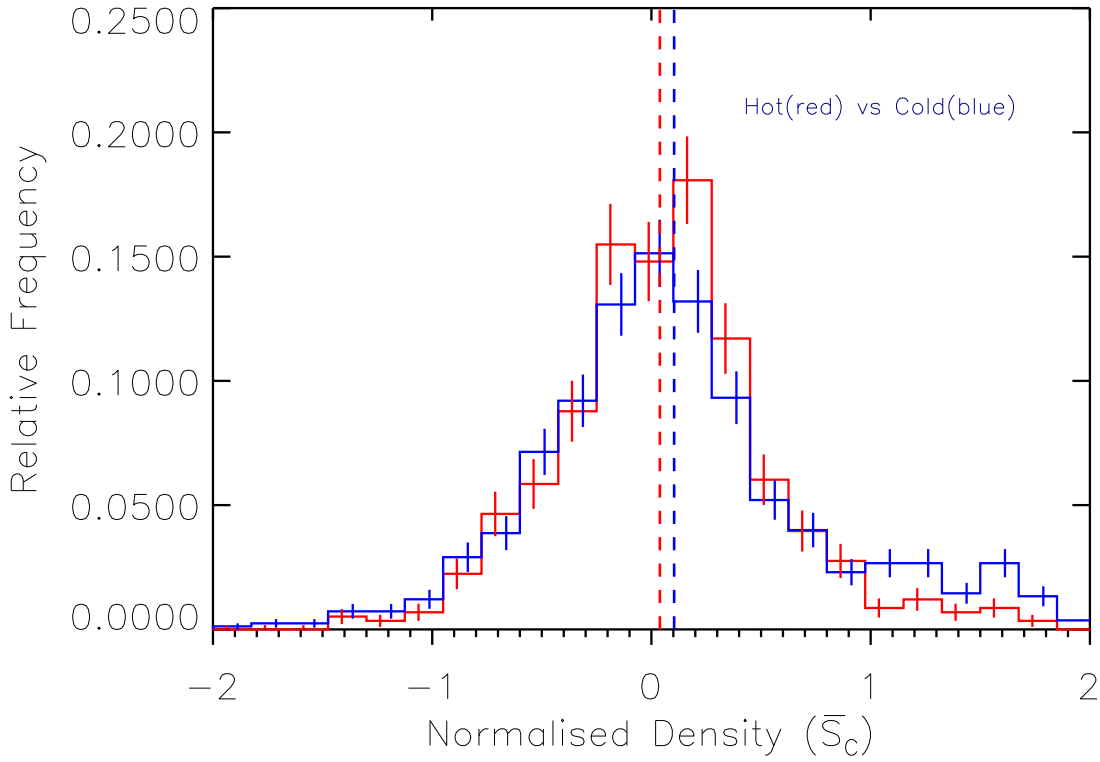

FIGURE 4.26: Normalized histograms of the environmental density ($\bar{S}_c$) distributions of the matched Hot-12P1 (*red*) and Cold-12P1 (*blue*) samples compare. The Hot-12P1 data is shifted to generally lower densities with its distribution mean given by the *red* dashed-line at $(3.82 \pm 2.97) \times 10^{-2}$. The Cold-12P1 distribution is shifted towards higher densities with the mean of its distribution given by the *blue* dashed-line at $(10.36 \pm 2.25) \times 10^{-2}$.

same underlying distribution. Comparisons of their normalised density distributions revealed that they were both different at the 2.1σ level and the 2.2σ level from KS-tests respectively and these normalised distributions are displayed in Figures 4.26 and 4.27, where the the Cold samples (*blue*) favour overdense regions in comparison to the Hot samples (*red*), in agreement with the 9P1 field.

For the 12P1 field, application of MWU-tests failed to find a significant difference between these mean values returning a probability of 0.345. This failure of the MWU-test to find a significant difference between these mean values, despite the standard errors on these means being small, may be due to the smaller number of colour, redshift and magnitude cross-matched objects located in this field in comparison to the 9P1 analysis. Considering that statistical tests favour larger samples, in the following

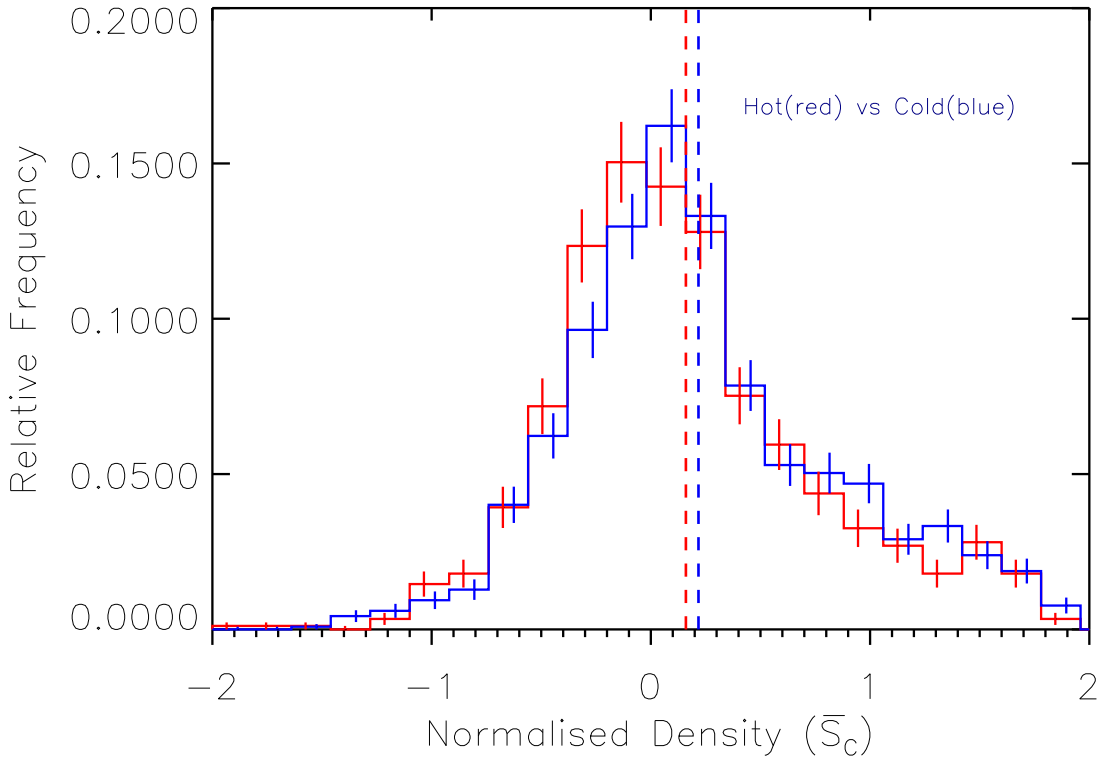

Figure 4.27: Normalized histograms showing how the distributions of environmental density ($\bar{S}_c$) of the matched Hot-15P1 (*red*) and Cold-15P1 (*blue*) samples compare. The Hot-15P1 data is shifted to generally lower densities with its distribution mean given by the *red* dashed-line at 0.160 ± 0.020. The Cold-15P1 distribution is shifted towards higher densities with the mean of its distribution given by the *blue* dashed-line at 0.220 ± 0.020.

section I use the combined Phase-One fields to provide a more robust comparison between density and temperature. By increasing the number of objects being compared this will improve the significance of numbers being returned and make my conclusions based on identified trends more accurate.

4.4.4 Combined Field Temperature-Density Analysis

Beginning with the full temperature distribution of the combined full FIR-full sample ($20,672$ objects), I found the mean isothermal dust temperature to be $\bar{T}_{50} = 23.3$K. I divided this sample into two sub-samples based on each galaxies dust temperature in relation to this mean value. Where $T > \bar{T}_{50}$ (numbering $9,857$ objects) hereafter named Hot-Full and where $T < \bar{T}_{50}$ (numbering $10,815$ objects) hereafter named Cold-Full.

TABLE 4.20: One- and two-dimensional KS- and MWU-test results for the statistical comparison of the Optical-Full sample against the Hot-Full and Cold-Full samples individually, cross-matched in $g-r$, $r-i$, z and m_r space. The final row shows the relative comparison between the density distributions of these Hot-Full and Cold-Full samples, showing a difference at the 3.9σ level from KS-tests. The Optical versus Hot cross-match returned $13,572$ and $4,524$ objects respectively, while the Optical versus Cold cross-match returned $17,199$ and $5,733$ objects respectively.

Distributions Compared			KS Probability	MWU Probability
$z_{(op)}$	versus	$z_{(hot)}$	0.793	0.246
$(g-r)_{op}$	versus	$(g-r)_{hot}$	0.999	0.439
$(r-i)_{op}$	versus	$(r-i)_{hot}$	0.844	0.331
$m_{r(op)}$	versus	$m_{r(hot)}$	0.354	0.092
$z_{(op)}$	versus	$z_{(cold)}$	0.902	0.317
$(g-r)_{op}$	versus	$(g-r)_{cold}$	0.997	0.402
$(r-i)_{op}$	versus	$(r-i)_{cold}$	0.953	0.366
$m_{r(op)}$	versus	$m_{r(cold)}$	0.269	0.065
$(\bar{S}_c)_{hot}$	versus	$(\bar{S}_c)_{cold}$	1.49×10^{-4}	5.48×10^{-4}

To remove the bias associated with the coldest galaxies being detected at generally lower redshifts (from selection effects favouring brighter FIR luminosities at higher redshifts), it was again necessary to cross-match these hot and cold sub-samples individually with the $1,550,017$ objects of the total Optical-Full catalogue in $g-r$, $r-i$, z and m_r parameter space. From the Hot-Full cross-match against the Optical-Full sample, there were $4,524$ and $13,572$ cross-matched objects located respectively. KS- and MWU-tests applied to the colour, r-band magnitude and redshift distributions of these cross-matched samples returned high probabilities such that the null hypothesis could not be rejected between these parameters. The cross-matching was therefore confirmed as successful across this parameter space. The Cold-Full cross-matching against the Optical-Full sample, located $5,733$ and $17,199$ cross-matched objects respectively and again, KS- and MWU-tests confirmed a successful cross-matching. All of these statistical values are presented in Table 4.20.

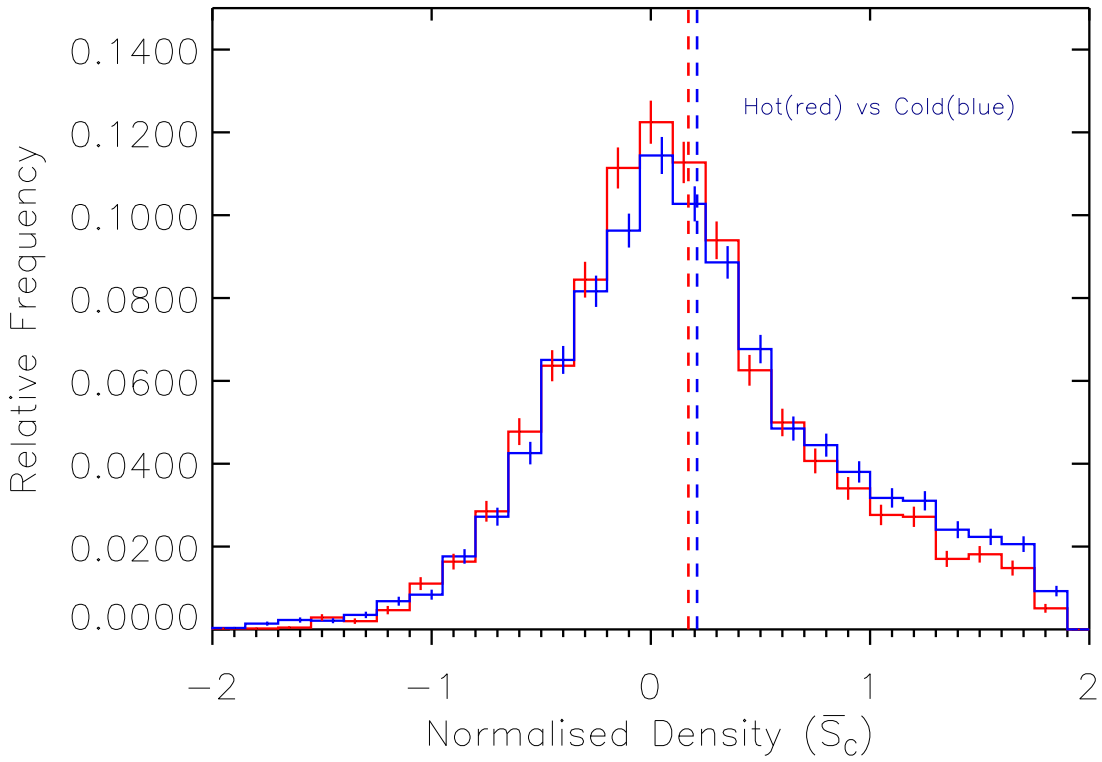

Figure 4.28: Normalized histograms showing how the distributions of environmental density ($\bar{S}_c$) for the matched Hot-Full (*red*) and Cold-Full (*blue*) samples compare. The Hot-Full data is shifted to generally lower densities with its distribution mean given by the *red* dashed-line at 0.170 ± 0.010. The Cold-Full distribution is shifted towards higher densities with the mean of its distribution given by the *blue* dashed-line at 0.210 ± 0.010.

Directly comparing the normalized environmental density distributions from the cross-matched Hot-Full and Cold-Full samples, numbering 4, 524 and 5, 733 objects respectively, I found KS-tests to return a low probability of 1.49×10^{-4} indicating that the null hypothesis could be rejected at the 3.9σ level. Histograms of these distributions are displayed in Figure 4.28 where a clear difference between the hot and cold distributions is visible such that, as expected, it is the cold sample that favours over-dense regions. This is confirmed by applying a MWU-test to the mean values of the two density distributions situated at 0.170 ± 0.010 and 0.210 ± 0.010 for the Hot-Full and Cold-Full samples respectively. The MWU-test returned a probability of 5.48×10^{-4} indicating that the means are significantly different at the 3.5σ level. The last row of the Table 4.20 presents these statistical results of the relative comparison.

TABLE 4.21: One- and two-dimensional KS- and MWU-test results for the statistical comparison of the Optical-Full sample against the Hot-Full and Cold-Full samples individually, cross-matched in $r-K$, z and m_K space. The final row shows the relative comparison between the density distributions of these Hot-Full and Cold-Full samples, showing a difference at the 4.7σ level from KS-tests. The Optical versus Hot cross-match returned 17,946 and 5,982 objects respectively, while the Optical versus Cold cross-match returned 20,880 and 6,960 objects respectively.

Distributions Compared			KS Probability	MWU Probability
$z_{(op)}$	versus	$z_{(hot)}$	0.694	0.479
$(r-K)_{op}$	versus	$(r-K)_{hot}$	0.972	0.444
$m_{K(op)}$	versus	$m_{K(hot)}$	0.148	0.081
$z_{(op)}$	versus	$z_{(cold)}$	0.612	0.472
$(r-K)_{op}$	versus	$(r-K)_{cold}$	0.993	0.430
$m_{K(op)}$	versus	$m_{K(cold)}$	0.391	0.177
$(\bar{S}_c)_{hot}$	versus	$(\bar{S}_c)_{cold}$	$< 10^{-5}$	$< 10^{-4}$

4.4.5 Dust Reddening Effects

To investigate what influence the dust reddening has on the relative comparison between the FIR-hot and FIR-cold sources, I repeated the dust reddening analysis for both of these samples across the combined Phase-One field. Beginning with the the 17,694 objects from the total FIR-Full sample with available m_K data, I divided this into hot and cold sub-samples based upon the mean temperature of this sample, found to be $\bar{T}_{50} = 23.51$K, returning 8,385 hot-FIR and 9,309 cold-FIR sources. Following the same method as described above, I cross-match each of these sub-samples individually against the 699,829 objects of the K-band selected Optical-Full sample in $r-K$, m_K and z parameter space. This cross-matching returned 17,946 matched Optical-hot, 5,982 matched FIR-hot objects and 20,880 matched Optical-cold and 6,960 matched FIR-cold objects. KS- and MWU-tests confirmed successful cross-matching between the colour, magnitude and redshift distributions, with high probabilities confirming the both Optical and FIR sample are consistent with being from the same underlying distribution. These values are presented at the top and middle of Table 4.21.

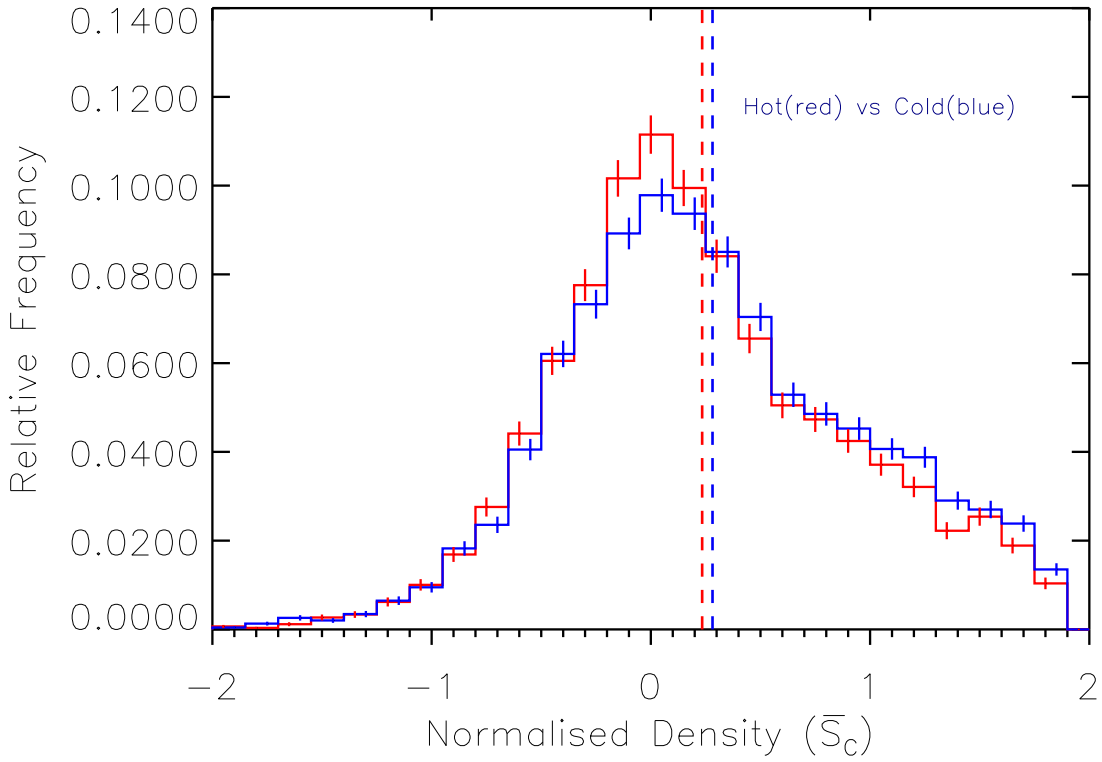

Figure 4.29: Normalized histograms showing the environmental density distributions ($\bar{S}_c$) for the $r-K$, m_K and z matched Hot-Full (*red*) and Cold-Full (*blue*) samples. The Hot-Full data is shifted to generally lower densities with its distribution mean given by the *red* dashed-line at 0.230 ± 0.010. The Cold-Full distribution is shifted towards higher densities with the mean of its distribution given by the *blue* dashed-line at 0.280 ± 0.010.

Finally, the relative comparison between these FIR-hot and FIR-cold samples returned a KS probability of 4.26 $\times 10^{-6}$ indicating a significant difference at the 4.7σ level, presented at the bottom of Table 4.21, with the FIR-cold objects favouring the most overdense regions in agreement with my earlier analysis. The normalised density distributions of these samples are displayed in Figure 4.29. Once more, with the inclusion of m_K data within the cross-matching, the reddening effect has been removed and the continued significance of the difference found between the hot and cold FIR samples confirms the robustness of my initial result.

4.5 Discussion

This analysis of the full H-ATLAS Phase-One field has shown that, once again, a significant difference is found between galaxies with and without FIR emission, such that galaxies with FIR emission favour underdense regions. This is in agreement with my analysis of the SDP field in Chapter 3 and follows the trends previously found between SFR and density by numerous authors (e.g. Dressler 1980; Postman & Geller 1984; Dressler et al. 1997; Domínguez et al. 2001; Goto et al. 2003; Kauffmann et al. 2004; O'Mill et al. 2008; Lee et al. 2010). The same trends with redshift are also present, such that the statistical separation between the FIR and Optical samples increases with increasing redshift. As described in Section 3.2.5, it is evident that this trend is in response to the flux-limit of the H-ATLAS survey detecting galaxies with higher far-infrared luminosities at high redshift (and thus higher SFRs). This is aided by the increased volume being sampled towards higher redshifts increasing the likelihood of detecting very highly luminous galaxies. This is again in addition to low signal-to-noise ratios and smaller number densities in the lower redshift bin, with the lowest star-forming galaxies acting to flatten the density distribution.

With the larger number of objects available within each of the three Phase-One fields (9P1, 12P1 & 15P1), these statistical trends are more robust than those returned from my analysis of the SDP field in Chapter 3, where the sample size was much smaller. As shown across each of these individual fields, the statistical separation between the Optical and FIR samples ranged between the $2.9\sigma - 3.9\sigma$ level, from KS-tests, for the full redshift distribution of each field. Therefore, while the significance of the separation between the Optical and FIR samples within each individual field was not necessarily greater than the SDP field, with larger sample numbers, these values are more robust and still provide significant confirmation of the presence of the SFR-density relationship out to $z \sim 0.5$. However, by combining these fields the largest number of objects within each sample was obtained and consequently the most robust analysis between the Optical and FIR samples could be achieved. Analysis of these combined samples returned an increased significance of the separation between the

Optical and FIR samples to the $> 5\sigma$ level.

With the inclusion of isothermal dust temperatures for each FIR galaxy, in addition to the large number of sources across the Phase-One fields, this has allowed for the relationship between temperature and environmental density to be probed to a good level significance on individual environmental scales. Over all three Phase-One fields, the same correlations between temperature and environmental density have been found, with galaxies exhibiting cooler dust temperatures generally favouring overdense regions. As with the correlations between SFR and density, combining the individual fields increases the sample number, further increasing the robustness of the statistical comparisons between my 'hot' and 'cold' samples. This is shown from the results of the KS-test comparisons between these samples increasing from between the $2.1\sigma - 2.9\sigma$ level up to the 3.9σ level when the fields are combined.

Therefore these correlations between dust temperature and the measured environmental density provide an insight into how the relationships between galactic properties may influence galaxy evolution. As detailed in Chapter 1, there are a number of well established correlations between a variety of galactic properties that have been confirmed observationally, building a detailed picture of galaxy formation throughout cosmic history. With my analysis of the relation between environmental density and its correlations with both SFR and temperature, my results confirm that there is indeed a significant relationship between these galaxy properties at $z < 0.5$. With the densest galaxies exhibiting the coldest dust temperatures and also the lowest SFRs, this suggests a population of galaxies with older stellar populations that have formed much earlier in their cosmic histories, in agreement with earlier studies of such a trend (e.g. Ellis et al. 1997; Stanford et al. 1998; Balogh et al. 1999; Lee et al. 2010; Masters et al. 2010; Thomas et al. 2010; Whitaker et al. 2010; Rowlands et al. 2012; Snyder et al. 2012). These correlations indicate that the far-infrared dust emission detected within these densest regions must have some other origin than the young O-B type stars emitting high luminosity UV, as found in the most underdense regions where dust temperatures are warmer. The far-infrared emission detected within the most overdense regions is therefore likely to be established from ISM heating by these older stellar

populations, in addition to some dust heating contribution from AGN (e.g. Schmitt et al. 2006; da Cunha et al. 2008; Nardini et al. 2008; Bendo et al. 2010, 2012; Groves et al. 2012; Smith et al. 2012a; Smith et al. 2012b).

5

Radio Emission and Environmental Density out to $z \sim 2$

As discussed in Chapter 1, radio emission generated via both thermal free-free and non-thermal synchrotron radiation can be used to trace ongoing star formation within normal galaxies at low radio luminosities. In addition, this radio emission can be used to trace AGN populations at higher radio luminosities. In this chapter, I apply my Voronoi tessellation algorithm to investigate the relationship between this radio emission and its associated environmental density, using a much narrower and deeper dataset than previously examined in this thesis, out to $z \sim 2$. I then divide my radio sample to investigate environmental dependence on both radio detected star formation and radio detected AGN.

5.1 Relations between AGN and Environment

From comparisons of the radio luminosity functions of radio detected star-forming galaxies and AGN, as shown in Figure 1.12 and discussed in Chapter 1, it is known that for $L \gtrsim 10^{23}$ W Hz^{-1}, AGN will dominate the vast majority of the radio emission. It has long been understood, under the standard model of AGN, that the mechanism responsible for driving these bright radio sources involves the accretion of gas onto a supermassive black hole (SMBH) at the galaxy's core (e.g. Lynden-Bell 1969; Hopkins & Hernquist 2006; Merloni & Heinz 2008; Levine et al. 2010). This accretion is believed to be triggered by galaxy interactions, such as gas-rich (wet) major mergers, removing angular momentum from the ISM of the merger remnant. After an initial starburst phase, AGN feedback processes will act to truncate the overall SFR in the host galaxy (e.g. Granato et al. 2004; Bower et al. 2006; Croton et al. 2006; Khalatyan et al. 2008; Teyssier et al. 2011; Bower et al. 2012).

Numerous studies have provided evidence in support of such a model, showing the radio detected AGN population to correlate with environment: Best et al. (2005) examined a sample of 1.4GHz radio selected AGN between $10^{23} - 10^{25}$ W Hz^{-1} out to $z < 0.3$, and found that the fraction of AGN are a strong function of stellar mass, such that AGN are found to be more common in high mass galaxies and thus the most overdense regions. The same trend was also found by Mauch & Sadler (2007) across a similar redshift range. In addition, Best et al. (2007) showed that for a sample of fixed stellar mass between $0.02 < z < 0.16$, radio galaxies are more likely to reside in the brightest groups and clusters than in less dense environments.

Hickox et al. (2009) compared the clustering of AGN detected in multiple wavebands including: 1.4GHz radio, X-ray and mid-infrared, between $0.25 < z < 0.8$. They find that the AGN populations detected in different wavebands do not overlap, and thus represent distinct populations of AGN. The galaxies detected in the radio waveband are very strongly clustered, to a greater degree than AGN detected in other wavebands, with X-ray and mid-infrared detected AGN showing weaker clustering respectively. They conclude that, as a galaxy's dark matter halo mass increases through hierarchical

build-up, at a critical mass between 10^{12} and $10^{13}\,\mathrm{M}_{\odot}$, an active 'quasar' stage is expected to occur, combined with rapid growth of the central black hole. Major mergers are proposed as a likely candidate for this event as this critical mass corresponds to the mass expected within small group environments where major mergers between galaxies with these masses are most common (Hopkins et al., 2008). Further investigations of AGN environments have shown that they commonly reside in dark matter haloes with masses $M_{halo} = 10^{12} - 10^{13}\,\mathrm{M}_{\odot}$ (e.g. Porciani et al. 2004; Hopkins et al. 2007; Bonoli et al. 2009; Mandelbaum et al. 2009; Pasquali et al. 2009; Bradshaw et al. 2011). After this phase, Hickox et al. (2009) conclude that the expected truncation of star formation shifts the accretion onto the AGN from a radiatively efficient mode (infrared and optically bright) to a radiatively inefficient mode (radio bright and optically faint). Thus an environmental effect triggers the AGN, in agreement with earlier studies.

The majority of local massive galaxies are known to contain a SMBH at their cores, despite not all massive galaxies being currently active. This is suggestive of the fact that these galaxies may have undergone an active phase at least once previously in their lifetimes, leading to the build-up in both stellar-mass (via starbursts) and SMBH mass (via accretion) which are known to be proportional (e.g. Kormendy & Gebhardt 2001; McLure & Dunlop 2002; Tremaine et al. 2002; Marconi & Hunt 2003; Bower et al. 2006; Vika et al. 2009). There is therefore a clear connection between AGN activity and SFR, and a number of studies have confirmed such a correlation, with comparisons between the evolution of the peak in global SFR density out to $z \sim 1 - 2$, against the measured peak in AGN activity found at the same redshift (e.g. Ueda et al. 2003; Richards et al. 2006; Hopkins et al. 2007; Ballo et al. 2012).

Silverman et al. (2009b) investigate the impact of environment on detected AGN activity out to $z < 1$ and find that AGN prefer environments equivalent to massive galaxies with high SFRs. Following this, Silverman et al. (2009c) show that the majority of AGN have higher SFRs than equivalent mass non-active galaxies out to $z < 1$ and show that the SFRs of AGN evolve with redshift similar to global galaxy populations, explaining the lower SFRs of AGN host galaxies at lower redshifts. In addition,

Bradshaw et al. (2011) examined the environments of radio-loud AGN at high redshifts ($1 < z < 1.5$) and find that they predominantly favour overdensities, with high powered radio AGN occupying slightly more evolved (most-clustered) cluster cores in similar environments as low-powered radio AGN in the local universe. This indicates a clear evolution in the radio AGN population, from high redshifts (where high and low radio luminosity detected AGN are shown to populate overdense regions), towards lower redshifts (where the lower radio luminosity AGN are shown to predominantly favour dense cluster regions, with the highest radio luminosity AGN existing in group or field environments).

It is evident therefore, that AGN properties and their hosts SFRs are inherently linked, while both are dependent on their environment. At higher redshifts it is believed that the most dense regions will contain enough gas to accrete onto the SMBH, driving the AGN while maintaining active star formation in their hosts (e.g. Hopkins & Hernquist 2006; Mullaney et al. 2012). However, feedback processes from the AGN are expected to disrupt the ISM, truncating the host galaxy star formation, while the SMBH continues to accrete the remaining gas (e.g. Granato et al. 2004; Bower et al. 2006; Croton et al. 2006; Khalatyan et al. 2008; Teyssier et al. 2011; Bower et al. 2012). With the reduction of available gas for accretion over time, the AGN will reduce in power as the accretion rate falls, thus leading to local AGN that reside in the densest environments exhibiting lower radio luminosities than those in less dense regions, as observed (e.g. Polletta et al. 2008; Shankar et al. 2009). Therefore, investigating the individual-galaxy-scale environmental dependence of radio emission from local to high redshifts can offer further insight into the origin of these correlations.

It is essential for estimations of radio source photometric redshifts, in addition to follow up spectroscopy, that optical and near-infrared imaging are available in order to establish accurate positions of each radio source. The Visible and Infrared Survey Telescope for Astronomy (VISTA; Emerson et al. 2004) Deep Extragalactic Observations (VIDEO; Jarvis et al. 2013) survey, is specifically designed to trace the evolution of galaxies and large scale structure as functions of epoch and environment to high redshifts ($z \sim 4$). By combining these observations with cross-matched radio data

from Very Large Array (VLA) radio observations (Bondi et al., 2003), with my environmental density algorithm, comparisons with individual-scale environments can be achieved.

5.2 The Radio and Near-Infrared Fields

5.2.1 Radio Data

The radio data used in this analysis were obtained by VLA observations at 1.4GHz, as part of the VIsible imaging Multi-Object Spectrograph (VIMOS) Deep Field Survey, undertaken by Bondi et al. (2003) over 56 hours across 9 days from November 1999 to January 2000. These observations cover over 1 deg^2 with nearly uniform noise over $\sim 17\mu$Jy and centred at $\alpha(\mathrm{J2000}) = 2^{\mathrm{h}}26^{\mathrm{m}}00^{\mathrm{s}}$ and $\delta(\mathrm{J2000}) = -4°30'00''$. The VLA B-configuration was used to maximise resolution giving a full width at half-maximum (FWHM) synthesised beam width of ~ 6 arcsec. The original catalogue produced by Bondi et al. (2003) identified 1054 radio sources, of which 19 were identified as multiple component sources, with a peak flux to local noise ratio of $\gtrsim 5\sigma$, with peak flux densities exceeding 60μJy. McAlpine et al. (2012), used a likelihood ratio (LR) method, similar to that of Smith et al. (2011), to associate reliable near-infrared counterparts with each radio object down to a limiting magnitude of $K \lesssim 22.6$ (total magnitude). From this sample, 908 radio galaxies were found to meet the criteria of having a reliable counterpart and these objects form my initial radio sample. The distribution of these radio objects are displayed as blue points in Figure 5.1.

5.2.2 Optical and Near-Infrared Data

Encompassing the entire 1 deg^2 field observed by the VLA, the VISTA-VIDEO survey has obtained photometry in the Z, Y, J, H, K_s bands to 5σ depths of 25.7, 24.6, 24.5, 24.0 and 23.5 magnitudes (2 arcsec diameter apertures) respectively. The complete VIDEO survey will cover $\sim$ 12 deg^2 in total, providing observations across a number of wide-field studies in high-Galactic-latitude fields, including three VISTA

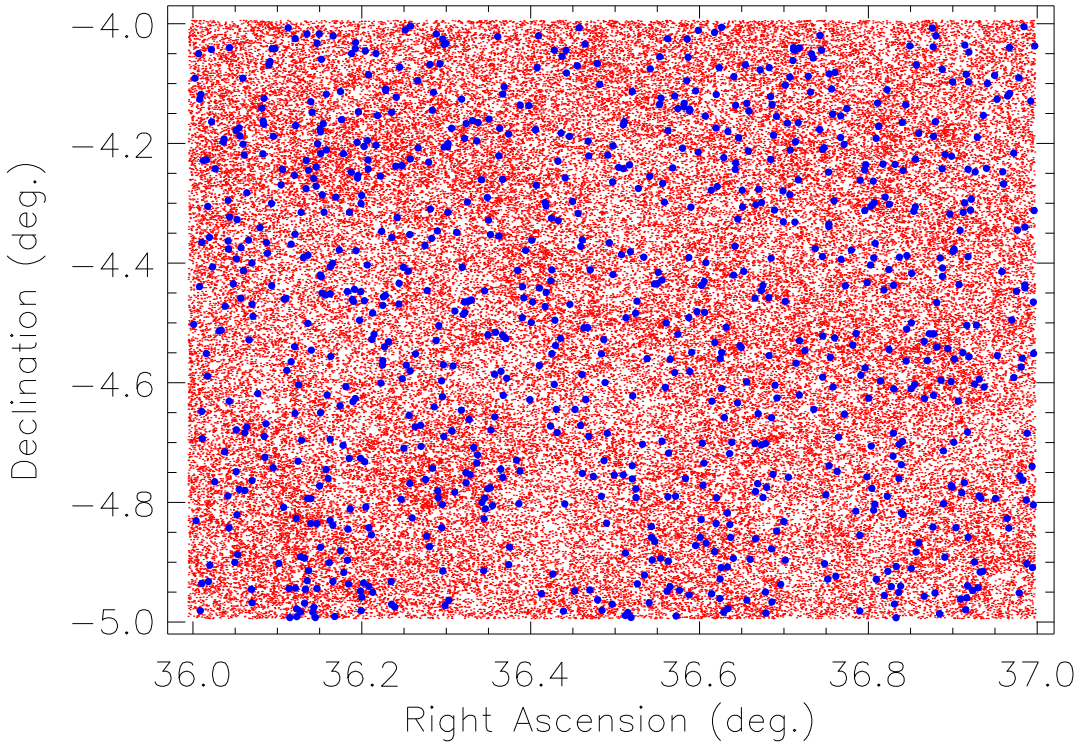

FIGURE 5.1: The 1 deg^2 VLA radio field, corresponding to the VIDEO-XMM3 field using near-infrared and optical photometry from the VIDEO and CFHTLS-D1 respectively consisting of 106,661 objects (*red*). The radio VLA field consists of 908 radio detected objects (*blue*).

tiles ($\sim$ 4.5 deg^2) in the *XMM-Newton* large-scale structure field. The near-infrared data used in this analysis has been obtained from the initial phase of VIDEO observations, observed between November 2009 and November 2011, over one of these tiles (VIDEO-XMM3) which covers the 1 deg^2 VLA radio field described above. This tile also includes observations by the Canada-France-Hawaii Telescope Legacy Survey Deep-1 field (CFHTLS-D1; Ilbert et al. 2006) which utilises the wide-field optical imaging camera MegaCAM (Boulade et al., 2003) on the 3.6m Canada-France-Hawaii telescope and provides additional photometry in the u, g, r, i & z optical bands. From these combined surveys, my initial sample contained 431,949 near-infrared selected objects which, after application of the 5σ K_s-band limit at $K_s < 23.5$ (defined in Jarvis et al. 2013), reduced this number to 106,661 objects across a complete redshift range of $0 < z < 6$ with a mean of $\bar{z} = 1.22$, however the number density drops off considerably

at $z \gtrsim 2.3$ as shown in Figure 5.3. My initial near-infrared/optical sample for which I apply my VT algorithm, is shown (*red*) against the VLA radio data (*blue*) in Figure 5.1.

5.3 Density Analysis of Radio Source Environments

In order to establish the environmental dependence of radio and non-radio detected sources, I once more apply my VT algorithm to this new dataset. The necessary adjustments and alterations to my previously described method are detailed below.

5.3.1 Star-Galaxy Separation

As with the samples used in Chapters 3 and 4, the initial 1 deg^2 field near-infrared/optical catalogue detailed above (numbering 106, 661 objects) did not initially consist purely of galaxies, but contained a proportion of stars contaminating the dataset. Therefore, in order to remove the stellar content from my analysis, I applied a star-galaxy separation, following the colour selection method of Baldry et al. (2010). They fit a quadratic function ($f_{locus}(x)$) to the stellar locus to separate galaxies from stars in the GAMA survey across a $g-i$ versus $J-K$ colour-colour diagram, first utilised by Ivezić et al. (2002) to test the success of the SDSS star-galaxy separation. They show that, when restricted to faint magnitudes, compact galaxies may be missed by a star-galaxy PSF$_r$ selection cut, as used in my SDSS/H-ATLAS analysis in Chapters 3 and 4. Therefore a colour based selection criterion is more suitable for higher redshift, fainter datasets.

The separation parameter defined by Baldry et al. (2010) is:

$$\Delta_{sg,jk} = J_{AB} - K_{AB} - f_{locus}(g-i) \ , \tag{5.1}$$

where Δ_{sg} is the $J-K$ separation from the locus, with the cut between galaxy and star defined as at $\Delta_{sg} > 0.20$. However, for application of the star-galaxy separation for VIDEO data, Jarvis et al. (2013) find a slight adjustment to the location of the locus along the $J-K$ axis is necessary to account for differences between the K-band filter in the UKIDSS and the K_s-band filter in VISTA. Consequently, the quadratic

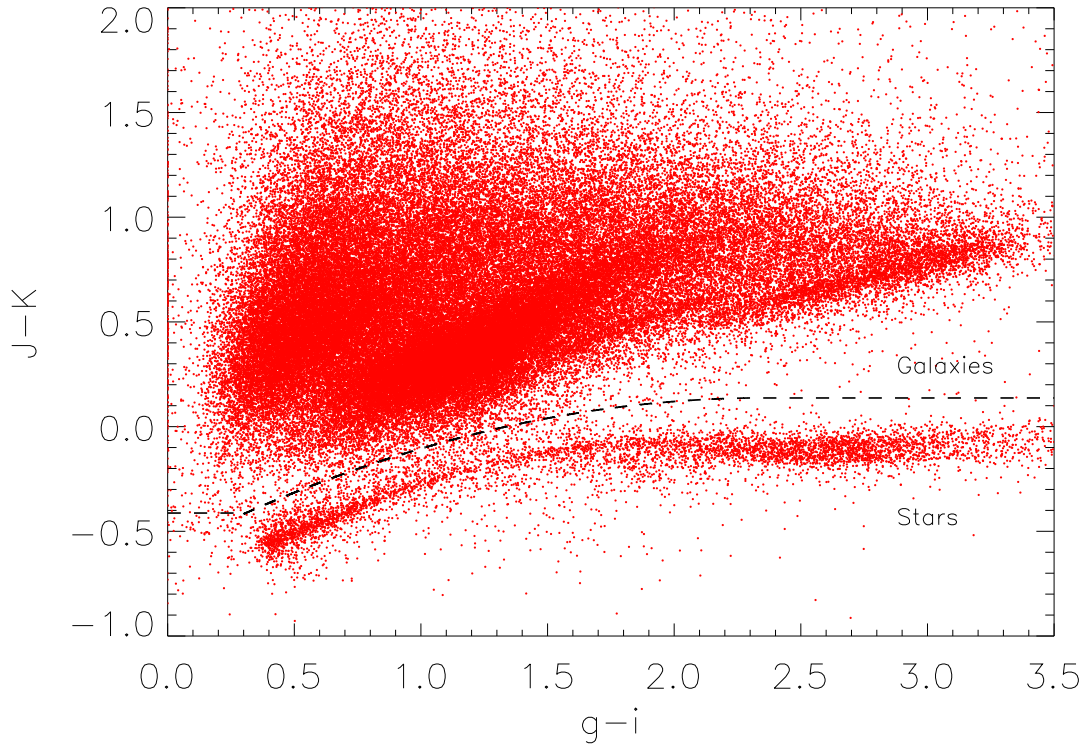

FIGURE 5.2: The fit to the stellar locus defines the star-galaxy separation, where $\Delta_{sg} > 0.20$ (*dashed line*), used to separate the stellar and galaxy content from my combined near-infrared/optical catalogue. All objects above this line are defined as galaxies, below are defined as stars and were removed from the analysis.

function fitted to the stellar locus is given by:

$$f_{locus}(x) = \begin{cases} -0.6127 & \text{for } x \leq 0.3 \\ -0.79 + 0.615x - 0.13x^2 & \text{for } 0.3 < x \leq 2.3 \\ -0.0632 & \text{for } x > 2.3 \end{cases}$$

where $x = g - i$ colour. I therefore incorporated these improved values for the positioning of my star-galaxy separation within my VT algorithm. Figure 5.2 shows my $g - i$ versus $J - K$ colour-colour plot. Objects with $\Delta_{sg} > 0.20$ were defined as galaxies and remained within my catalogue to be used in the density analysis, conversely objects below $\Delta_{sg} \leq 0.20$ were defined as stars and were removed from the analysis.

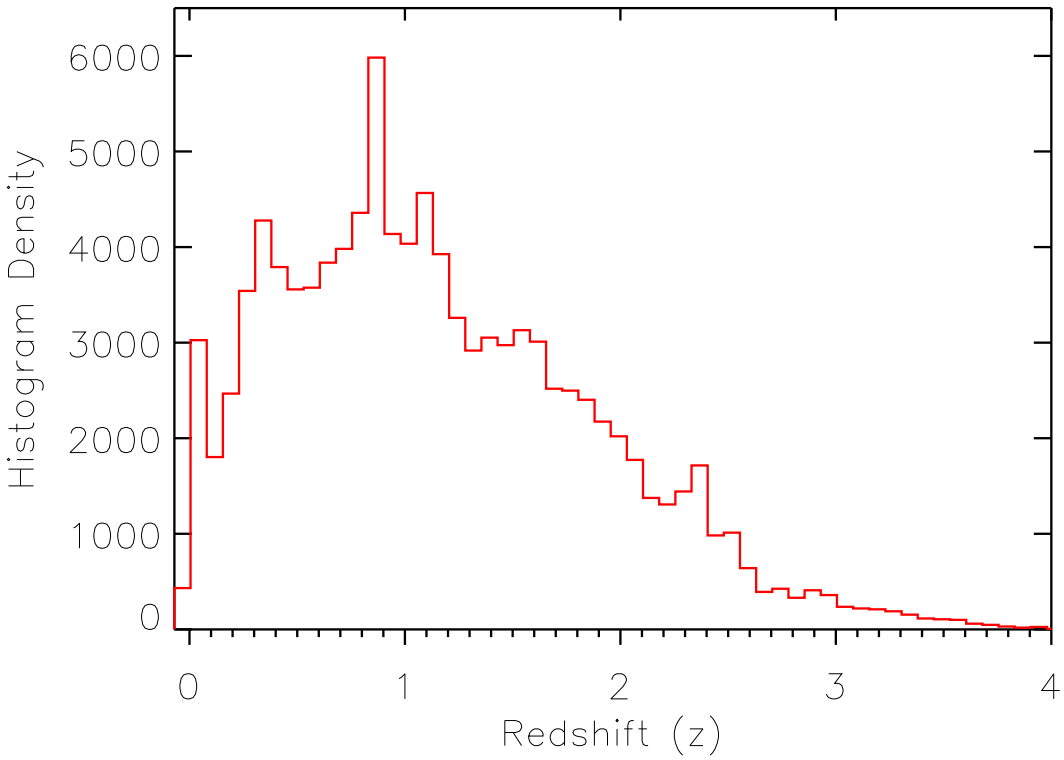

Figure 5.3: The redshift distribution of the total VIDEO field, showing the peak in the distribution to reside at $z \sim 1.22$ and that the number density drops-off considerably beyond $z \sim 2.5$.

5.3.2 Application of the VT Algorithm

The application of my VT algorithm maintained the same processes already described in earlier chapters, however there were some minor alterations considering the new dataset being examined, with a smaller area and larger depth to the field being observed in comparison to previous applications. With the greatly increased redshift range of the VIDEO field ($0 < z < 6$), an expanded redshift slicing of $\Delta z = 0.04$ was applied to each of the 1000 3D MC realisations, resulting in 150 redshift slices in total through the dataset. Unlike with my previous analyses, where I generated a z-PDF for each object, based upon a given peak photometric redshift and error, for this analysis the z-PDF's were created by Jarvis et al. (2013), using the publicly available photometric-redshift code 'Le Phare' (Arnouts et al. 1999; Ilbert et al. 2006), and applied directly within my code. The number density of objects beyond $z \sim 2.5$ fall dramatically and

therefore only objects with peak photometric redshifts $z \leq 3.0$ were initially included in the output of my algorithm. However, due to the full z-PDF sampling within my algorithm, objects with higher peak redshifts may still contribute to the overall density calculation if the width of their z-PDF reaches below this limit. Figure 5.3 shows the photometric redshift distribution of the VIDEO sample out to $z < 4$. This plot shows a clear peak in the distribution (at $z \sim 1.2$), consequently a normalisation procedure was again instigated within the code to account for differences in number density and uniformity across the separate redshift slices.

With the smaller and denser 1 deg^2 field, the VT edge effect will have influence across a greater proportion of the initial data. Thus, when excluding objects from around the edge of the field, in order to maintain density measurement accuracy, extra care was taken so as to remove as few objects as necessary. I therefore repeated the edge-effect test described in Section 2.2.1, finding that the minimum distance into the field from the edge must be 6 arcmin in order to avoid overly large cell sizes influencing the density measure. These outermost objects were subsequently removed from the density calculation during the application of the VT algorithm. After these star-galaxy separation, redshift and edge-effect cuts have been applied within my VT algorithm, the resultant dataset, with usable density information, numbered 62, 891 objects and a colour-density plot of this field is shown in Figure 5.4.

5.3.3 Radio and Control Samples

As introduced above, the complete 1 deg^2 field VLA radio sample was cross-matched with the VIDEO near-infrared/optical sample by McAlpine et al. (2012), who instigated a likelihood ratio technique, similar to that of Smith et al. (2011), which located associated near-infrared/optical counterparts to each radio source. They found 908 galaxies across the VIDEO dataset with radio counterparts, of which 578 remain when the outer edges are removed to account for the VT edge-effect. I removed these counterparts from the VIDEO catalogue to form my initial VLA radio sample (hereafter named Radio), with the remaining sources (61, 965) forming my near-infrared/optical sample (hereafter named NIR), which includes the removal of 347 extreme $g - i$ and

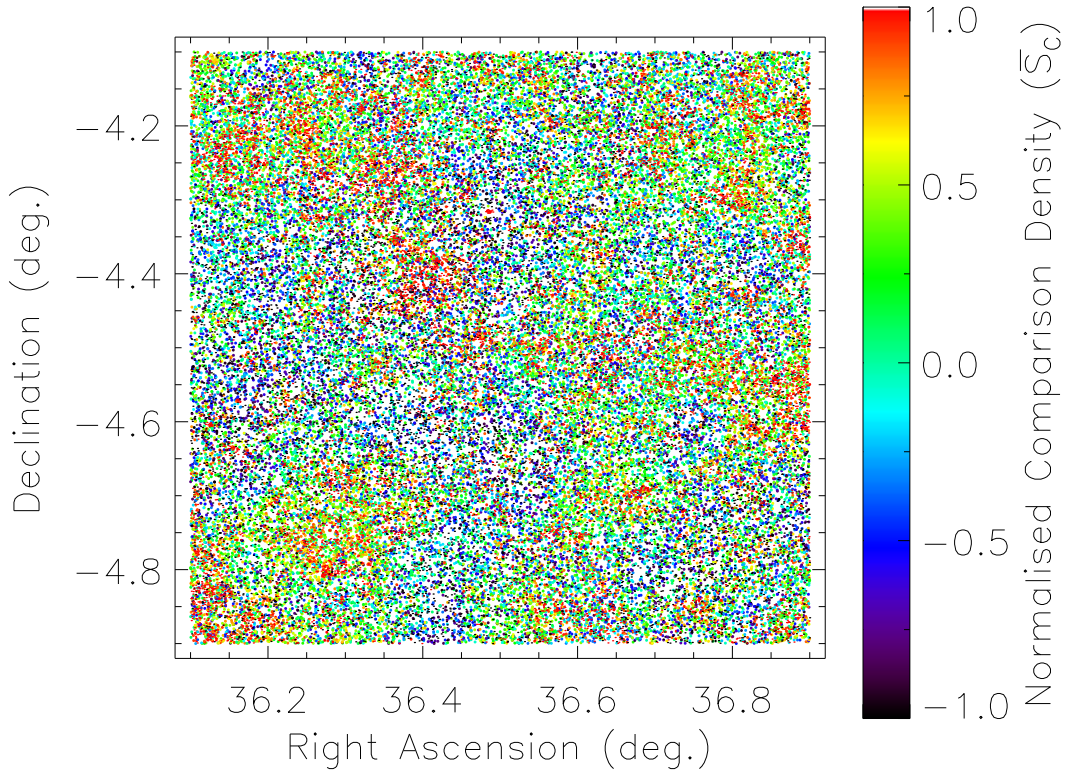

Figure 5.4: Colour coordinated plot of the 62,891 VIDEO objects with all redshift slices compiled to show the whole density distribution. The red and orange colours represent the most overdense regions (positive $\bar{S}$ values) and blue and purple represent the most underdense regions (negative $\bar{S}$ values).

$J-K$ colours from the sample.

In continuation of my method previously described in Chapters 3 and 4, it was necessary to cross-match these NIR and Radio samples in colour, redshift and magnitude space, in order to ensure an appropriate like with like comparison. Thus the same four-dimensional gridding procedure was applied across the $g-i$ and $J-K$ colour, K_S-band apparent magnitude (m_{K_s}) and redshift parameter space of each sample. This cross-matching located 230 matched Radio sources selected against 690 matched NIR objects (from within each grid spacing), these are displayed in Figure 5.5. As shown in Figure 5.3, with the sharp reduction in number density of the sample beyond $z \sim 2.5$, it was once more necessary to apply a redshift and magnitude limit to the cross-matched samples, as applied in my analyses of Chapters 3 and 4. Thus only the redshift range of $0 < z < 2.2$ and magnitude range of $m_K < 22$ were included, as the completeness of

these samples reduced significantly outside of these ranges. As previously stated, this redshift limit does not influence the $\bar{S}_c$ values of the remaining sample due to the fact that each $\bar{S}_c$ value already incorporates higher redshift galaxies through full z-PDF sampling.

5.3.4 Statistical Comparison of Radio and NIR Galaxies

With two cross-matched NIR and Radio samples obtained, I could once again apply KS- and MWU-tests to confirm that these matched samples are consistent with having been drawn from the same underlying distribution in terms of their colour, redshift and magnitude distributions. Table 5.1 presents the results of these statistical tests and confirms that the matched NIR and Radio samples are significantly different in terms of their normalised environmental density distributions at the 4σ level from KS tests and at the 3σ level from MWU tests. These density distributions are displayed in Figure 5.6 and it is clear that the Radio data (*blue*) are shifted generally to larger $\bar{S}_c$ values, with the mean of its distribution at (16.69 ± 6.37) x 10^{-2} (*blue dashed line*), and hence are shown to favour more overdense regions. This is in contrast to the mean of the NIR distribution which is situated at (-11.11 ± 7.84) x 10^{-2} (*red dashed line*) and thus is shown to generally favour underdense regions. It is therefore evident that galaxies traced by radio emission favour the most overdense regions in comparison with galaxies that are not observed in the radio across the entire redshift range of the matched samples. This correlation is in agreement with the numerous studies that have previously examined the environmental dependence of radio detected galaxies, as discussed in Section 5.1.

In continuation of my previous method, I binned the matched samples in terms of redshift in order to test what dependence this has on the observed radio-density correlation. As expected from my analysis in Chapters 3 and 4, with any flux-density limited sample, the highest redshift sample will show a bias towards the most luminous objects and thus the environmental relationship established across the entire redshift range will be amplified in this higher bin. With the increased total depth of my sample ($z \leq 2.2$), in comparison with my earlier analyses, this allowed me to probe

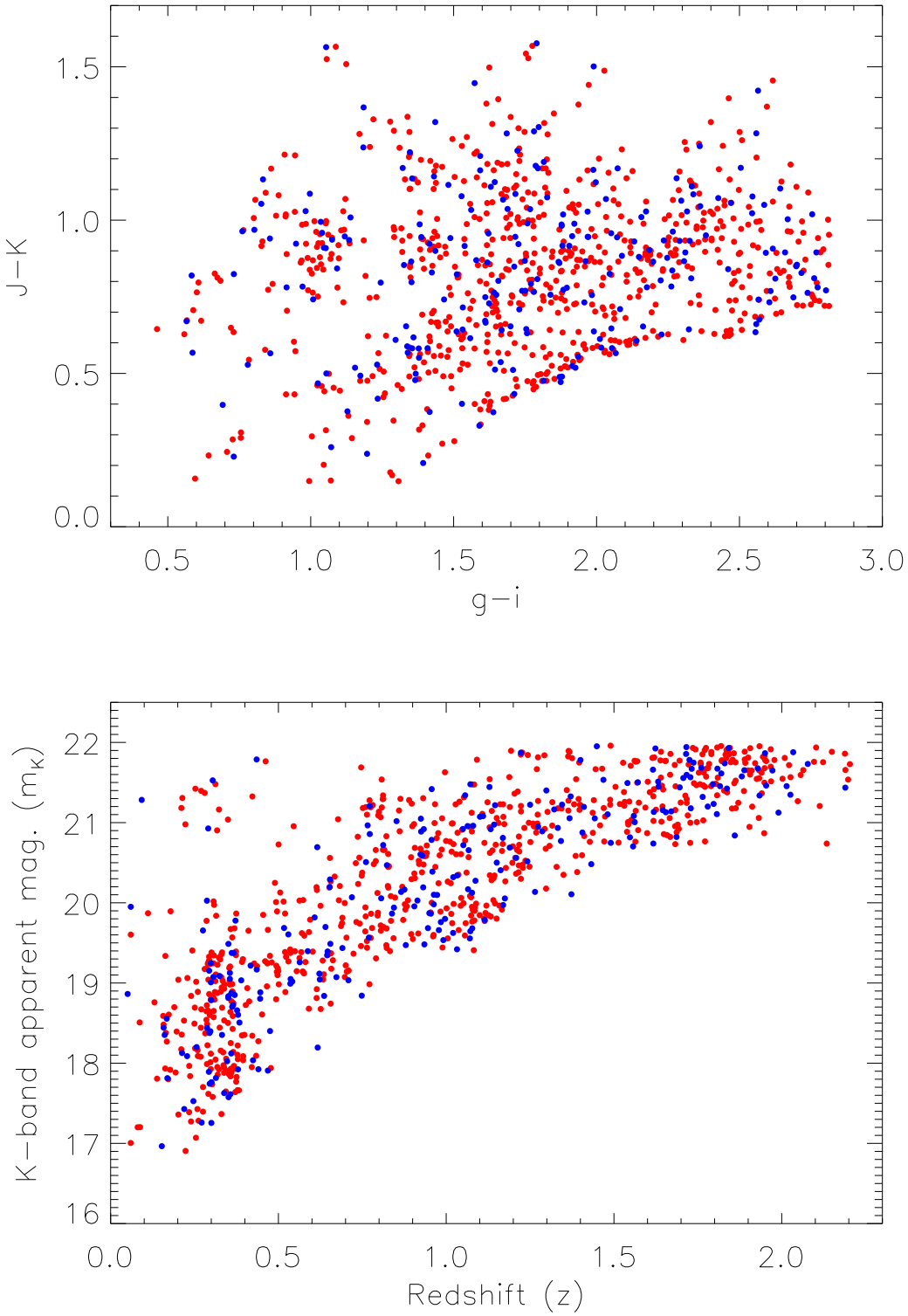

Figure 5.5: *Top*: The $g-i$ versus $J-K$ colour distribution for the matched sample of the NIR (*red*) and Radio (*blue*) sources, numbering 690 and 230 respectively. *Bottom*: The redshift versus K_S-band apparent magnitude for the same matched samples.

TABLE 5.1: Two sample and two-dimensional KS- and MWU-test results over the full redshift range ($0 < z < 2.2$) of the 690 NIR objects and 230 Radio objects. The two density distributions are different at the 4σ level from KS tests, with the means of the distributions different at the 3σ level from MWU tests.

Distributions Compared			KS Probability	MWU Probability
$z_{(NIR)}$	versus	$z_{(Radio)}$	0.870	0.406
$(g-i)_{NIR}$	versus	$(g-i)_{Radio}$	0.951	0.422
$(J-K)_{NIR}$	versus	$(J-K)_{Radio}$	0.816	0.270
$m_{K(NIR)}$	versus	$m_{K(Radio)}$	0.787	0.216
$(\bar{S}_c)_{NIR}$	versus	$(\bar{S}_c)_{Radio}$	6.81×10^{-5}	3.10×10^{-3}
$(g-i, J-K)_{NIR}$	versus	$(g-i, J-K)_{Radio}$	0.706	-
$(g-i, z)_{NIR}$	versus	$(g-i, z)_{Radio}$	0.756	-
$(J-K, z)_{NIR}$	versus	$(J-K, z)_{Radio}$	0.808	-
$(m_K, z)_{NIR}$	versus	$(m_K, z)_{Radio}$	0.734	-
$(g-i, m_K)_{NIR}$	versus	$(g-i, m_K)_{Radio}$	0.831	-
$(J-K, m_K)_{NIR}$	versus	$(J-K, m_K)_{Radio}$	0.507	-
$(g-i, \bar{S}_c)_{NIR}$	versus	$(g-i, \bar{S}_c)_{Radio}$	2.28×10^{-3}	-
$(J-K, \bar{S}_c)_{NIR}$	versus	$(J-K, \bar{S}_c)_{Radio}$	2.15×10^{-3}	-
$(m_K, \bar{S}_c)_{NIR}$	versus	$(m_K, \bar{S}_c)_{Radio}$	2.27×10^{-3}	-
$(z, \bar{S}_c)_{NIR}$	versus	$(z, \bar{S}_c)_{Radio}$	1.33×10^{-3}	-

TABLE 5.2: The KS-test and MWU-test results for both the NIR and Radio samples for $\bar{S}_c$ distributions within the individual redshift slices shown in figure 5.7. From KS results the density distributions are significantly different between the 2.1σ-3.4σ levels. The number of objects from each population are given:

Redshift Slice	NIR	Radio	KS Probability	MWU Probability
$0 \leq z < 1.10$	416	141	0.039	0.027
$1.10 \leq z < 2.20$	274	89	9.31×10^{-4}	0.017

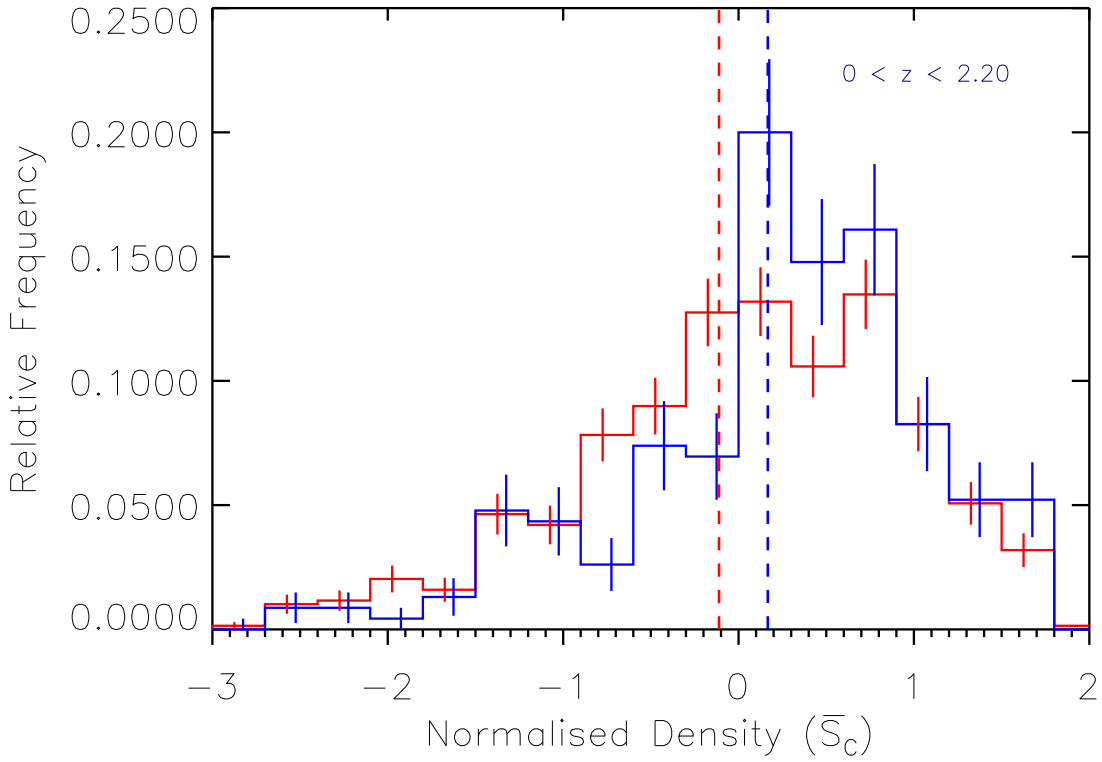

Figure 5.6: Normalised histogram of both environmental density ($\bar{S}_c$) distributions from the total NIR (*red*) and Radio (*blue*) populations (690 and 230 objects respectively), along with error-bars depicting the normalised error associated with each bin, where $\bar{S}_c > 0$ signifies an overdensity and $\bar{S}_c < 0$ signifies an underdensity in terms of the entire redshift range $0 \leq z < 2.2$. The Radio data is shifted generally to larger $\bar{S}_c$ values, with the mean of its distribution at (16.69 ± 6.37) x 10^{-2} (*blue dashed line*), this is contrasted against the mean of the NIR distribution at (-11.11 ± 7.84) x 10^{-2} (*red dashed line*). A KS-tests between these two distributions returned a probability value of 6.81×10^{-5} indicating that they are significantly different at the 4σ level, while a MWU test returned a probability of 3.10×10^{-3} indicating a significant difference between their mean values at the 3σ level.

the differences between environmental densities across a much larger range. Therefore, I split the data into two even redshift bins of $0 < z < 1.10$ (containing 416 NIR and 141 Radio sources) and $1.10 < z < 2.20$ (containing 274 NIR and 89 Radio sources) and reapplied my density analysis to each. The relatively small Radio sample across the total redshift range prevented me from applying a greater number of redshift bins, due to the resultant number density of the cross-matched samples being too small to accurately compare with KS and MWU tests.

Application of KS- and MWU-tests to the $0 < z < 1.10$ bin of my cross-matched

NIR and Radio samples returned a KS probability of 0.039, indicating a difference between the density distributions at the 2.1σ level, with a MWU probability of 0.027 indicating tentative evidence for a difference in their mean values at the 2.3σ level. Statistical comparisons of the higher redshift bin ($1.10 < z < 2.20$) returned differences at higher levels of significance, with KS-tests returning a probability of 9.31×10^{-4} and MWU-tests returning a probability of 0.017, indicating significant differences at the 3.4σ and 2.4σ levels respectively. These results are presented in Table 5.2 and the normalised density distributions of both redshift bins are displayed in Figure 5.7.

5.4 Comparisons of SF- and AGN-Radio Emission

In addition to examining the environmental dependence of the entire sample of radio sources against non-radio sources, which has shown a clearly significant difference, I have also investigated the environmental dependence of radio emission associated with contributions from both AGN and star-forming galaxies individually. Based upon comparisons of the radio luminosity functions in Figure 1.12 and discussed in Chapter 1, I have divided the radio sample at $L = 10^{23}$ W Hz^{-1} which is considered the transition between AGN and star formation dominated radio emission (Condon et al. 2002; Mauch & Sadler 2007). Above this luminosity, AGN are expected to dominate the radio population, while below it the radio emission is expected to be predominantly from star-forming galaxies. The radio luminosity–redshift plane for my sample, along with the division between AGN and star forming galaxies, is displayed in Figure 5.8.

5.4.1 Environments of AGN Radio Emission

After applying the radio luminosity cut to my total Radio sample of 578 objects, I found 403 galaxies with $L > 10^{23}$ W Hz^{-1} and these objects form my Radio-AGN sample with which I repeat the analysis. After cross-matching these objects in $g - i$, $J - K$, m_K and z parameter space with my NIR sample, the resultant cross-matched objects numbered 498 NIR and 166 Radio-AGN respectively across a redshift range of $0.3 < z < 2.2$. These cross-matched objects from both samples are displayed in

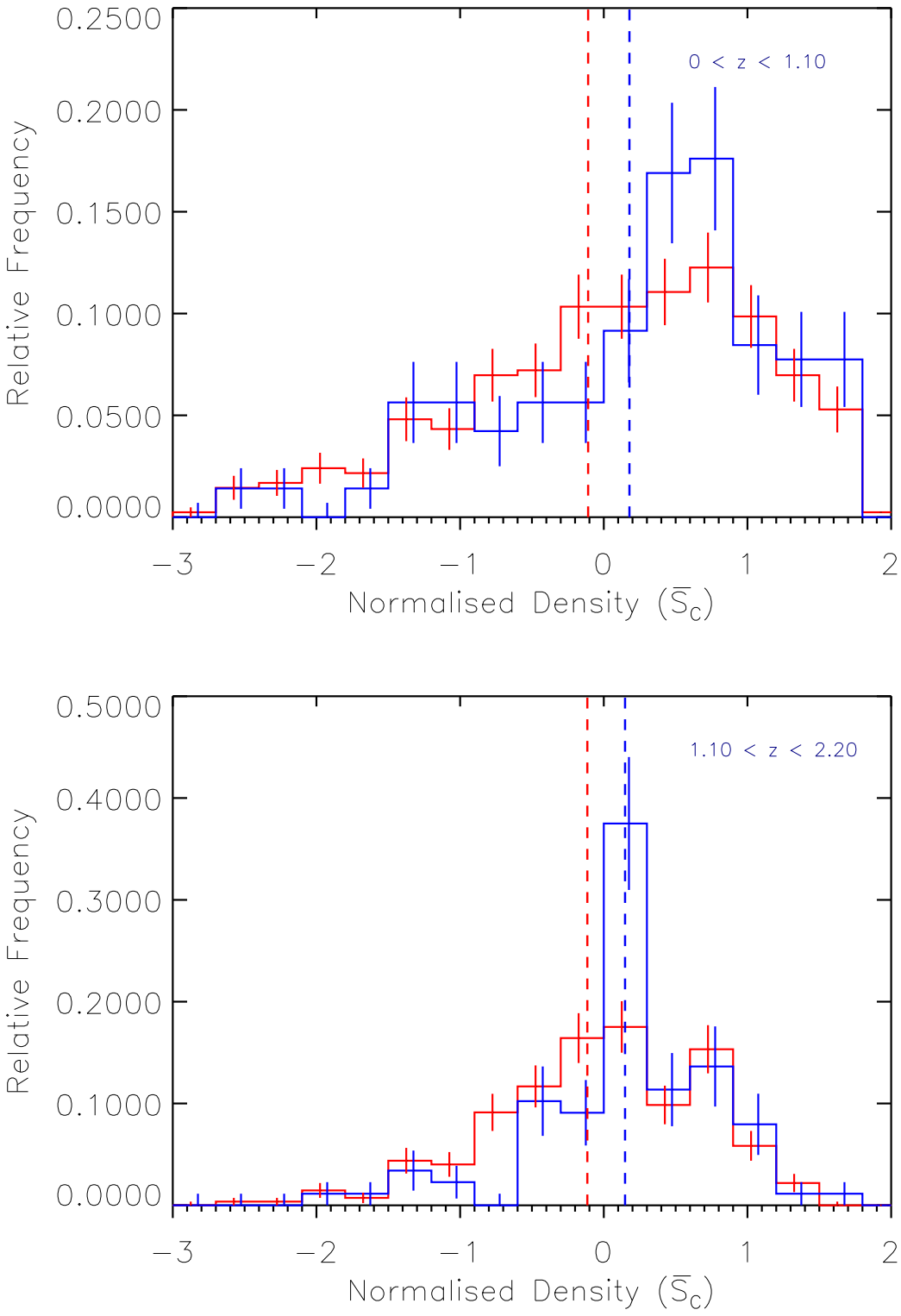

Figure 5.7: Normalized histograms that show the full matched sample binned in Redshift $0 \leq z < 1.10$ and $1.10 \leq z < 2.20$ (*Top* and *Bottom*) respectively, showing a continued separation between the $\bar{S}_c$ distributions of the NIR (*red*) and Radio (*blue*) sample and that this increases with redshift from 2.1σ to 3.4σ significance.

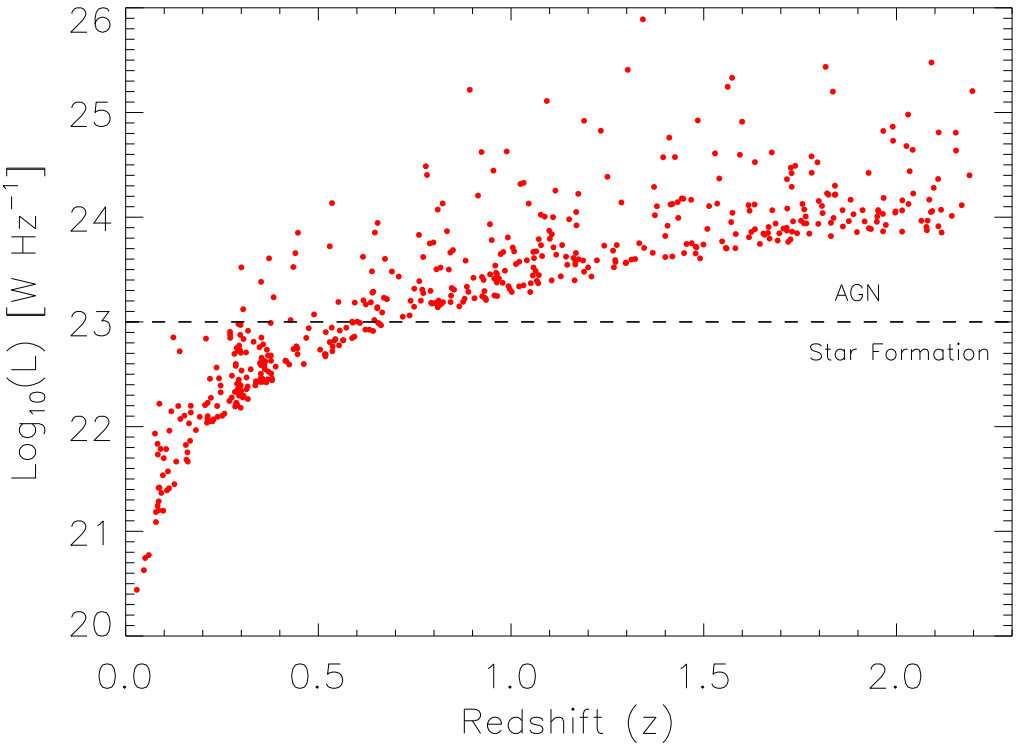

FIGURE 5.8: The rest frame luminosity versus redshift plot of my total radio sample divided at $L = 10^{23}$ W Hz^{-1} (*dashed line*), with AGN considered the dominant radio source above this luminosity (403 objects) and star formation below (175 objects).

Figure 5.9. Applying KS- and MWU-tests to the cross-matched samples revealed, once more, that the cross-matching resulted in two samples that are consistent with being from the same underlying distribution in terms of their colour, magnitude and redshift distributions. When applied to the normalised density distributions these statistical tests returned a KS probability of 1.25×10^{-5}, indicating a significant difference at the 4.5σ level, and a MWU probability of 8.48×10^{-4}, indicating a 3.4σ difference between their mean values. These mean values are (-20.99 ± 10.37) $\times 10^{-2}$ and (17.46 ± 6.04) $\times 10^{-2}$ for NIR and Radio-AGN respectively, and thus it is the radio emission (AGN) that are found to favour the most dense regions. All statistical results are presented in table Table 5.3 and histograms of the density distribution comparison is displayed in Figure 5.10.

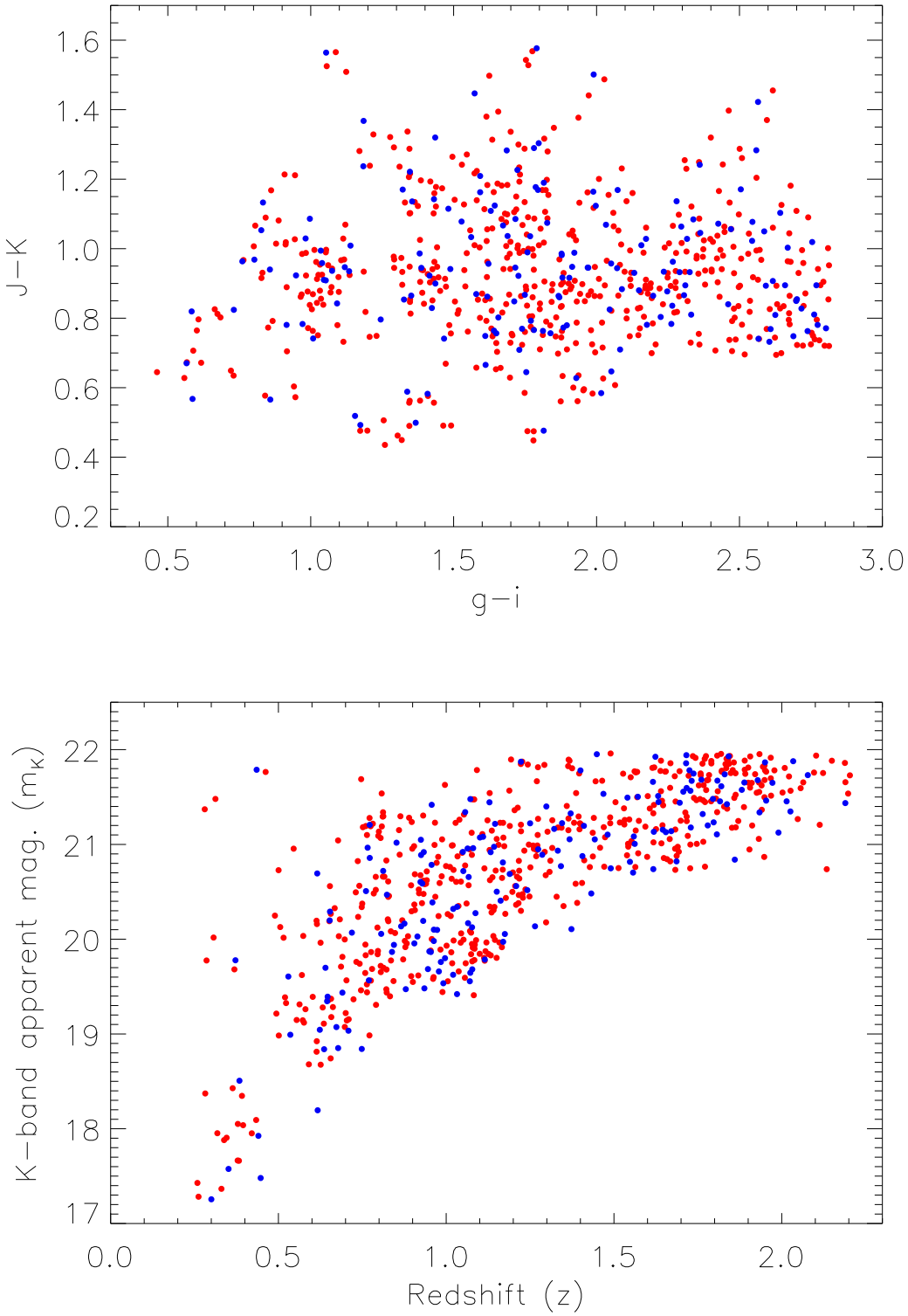

Figure 5.9: *Top*: The $g - i$ versus $J - K$ colour-matched NIR sample (*red*) with the $L > 10^{23}$ W Hz^{-1} (AGN dominated) matched Radio (*blue*) sources, numbering 498 and 166 respectively. *Bottom*: The redshift versus K_S-band apparent magnitude for the same matched samples.

TABLE 5.3: Two sample and two-dimensional KS- and MWU-test results for the cross-matched 498 NIR objects and 166 $L > 10^{23}$ W Hz^{-1} (AGN dominated) radio sources across the redshift range ($0.3 < z < 2.2$). The two density distributions are different at the 4.5σ level from KS tests, with the means of the distributions different at the 3.4σ level from MWU tests.

Distributions Compared			KS Probability	MWU Probability
$z_{(NIR)}$	versus	$z_{(Radio)}$	0.707	0.433
$(g-i)_{NIR}$	versus	$(g-i)_{Radio}$	0.986	0.487
$(J-K)_{NIR}$	versus	$(J-K)_{Radio}$	0.878	0.270
$m_{K(NIR)}$	versus	$m_{K(Radio)}$	0.593	0.155
$(\bar{S}_c)_{NIR}$	versus	$(\bar{S}_c)_{Radio}$	1.25×10^{-5}	8.48×10^{-4}
$(g-i, J-K)_{NIR}$	versus	$(g-i, J-K)_{Radio}$	0.743	-
$(g-i, z)_{NIR}$	versus	$(g-i, z)_{Radio}$	0.740	-
$(J-K, z)_{NIR}$	versus	$(J-K, z)_{Radio}$	0.741	-
$(m_K, z)_{NIR}$	versus	$(m_K, z)_{Radio}$	0.594	-
$(g-i, m_K)_{NIR}$	versus	$(g-i, m_K)_{Radio}$	0.844	-
$(J-K, m_K)_{NIR}$	versus	$(J-K, m_K)_{Radio}$	0.527	-
$(g-i, \bar{S}_c)_{NIR}$	versus	$(g-i, \bar{S}_c)_{Radio}$	6.45×10^{-4}	-
$(J-K, \bar{S}_c)_{NIR}$	versus	$(J-K, \bar{S}_c)_{Radio}$	4.08×10^{-3}	-
$(m_K, \bar{S}_c)_{NIR}$	versus	$(m_K, \bar{S}_c)_{Radio}$	5.07×10^{-4}	-
$(z, \bar{S}_c)_{NIR}$	versus	$(z, \bar{S}_c)_{Radio}$	1.94×10^{-3}	-

5.4.2 Environments of Star Formation Radio Emission

From my full Radio sample I found 175 galaxies with radio $L < 10^{23}$ W Hz^{-1}, and whose radio emission is therefore considered to be dominated by star formation (hereafter my Radio-SF sample). After once more cross-matching in colour, magnitude and redshift parameter space with the NIR sample, I found 93 NIR and 31 Radio-SF cross-matched objects across a redshift range $0.16 < z < 0.56$, and these matched samples are displayed in Figure 5.11. Application of KS- and MWU-tests to these cross-matched

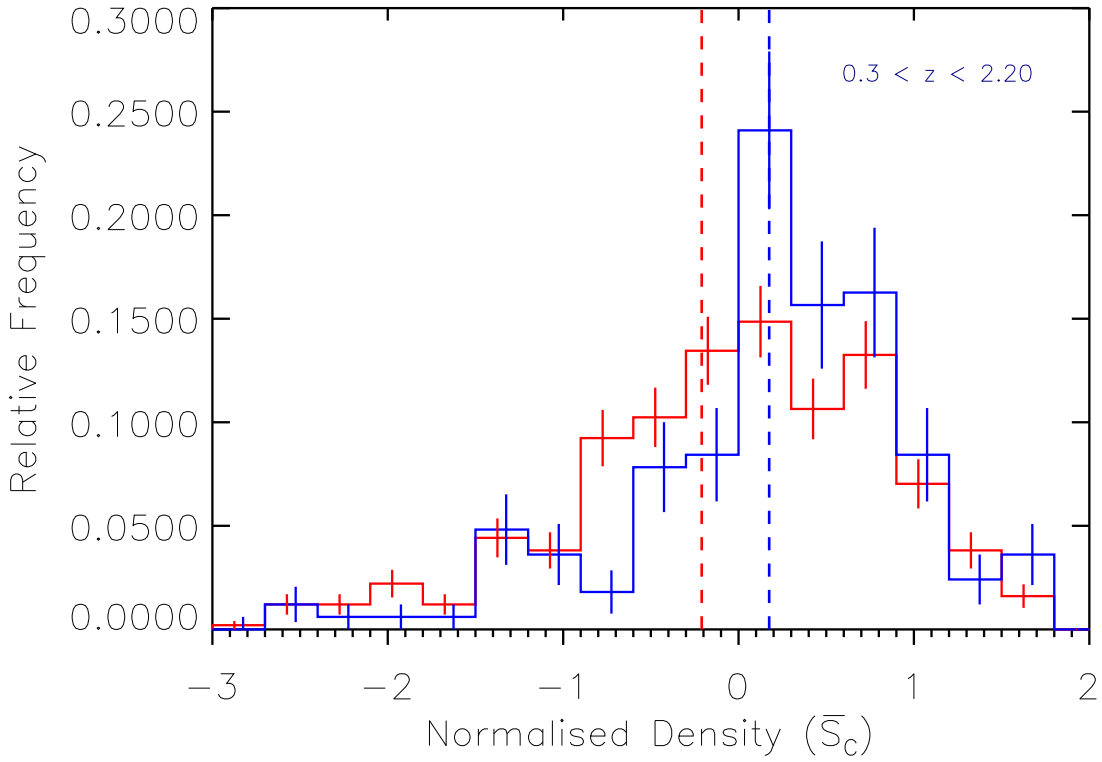

Figure 5.10: Normalised histogram of both environmental density ($\bar{S}_c$) distributions of the cross-matched NIR (*red*) and the $L > 10^{23}$ W Hz^{-1} (AGN dominated) Radio (*blue*) populations (498 and 166 objects respectively) across the redshift range $0.3 \leq z < 2.2$. The Radio data favours generally overdense regions (positive $\bar{S}_c$ values), with the mean of its distribution at (17.46 ± 6.04) x 10^{-2} (*blue dashed line*), this is contrasted against the mean of the NIR distribution at (-20.99 ± 10.37) x 10^{-2} (*red dashed line*). A KS-tests between these two distributions returned a probability value of 1.25×10^{-5} indicating that they are significantly different at the 4.5σ level, while a MWU test returned a probability of 8.48×10^{-4} indicating a significant difference between their mean values at the 3.4σ level.

samples, again reveal that, in terms of their cross-matched parameters, they are consistent with the same underlying distribution. As shown in Table 5.4, their density distributions are significantly different at the 2.7σ level from a KS probability of 8.36×10^{-3} and their means are significantly different at the 3σ level from a MWU probability of 2.98×10^{-3}. With mean values of $(-7.62 \pm 12.67) \times 10^{-2}$ and 0.41 ± 0.27 for the NIR and Radio-SF samples respectively, it is again clear that the radio emission (as a tracer of star formation) also favour overdense regions. The normalised histograms of both density distributions are displayed in Figure 5.12.

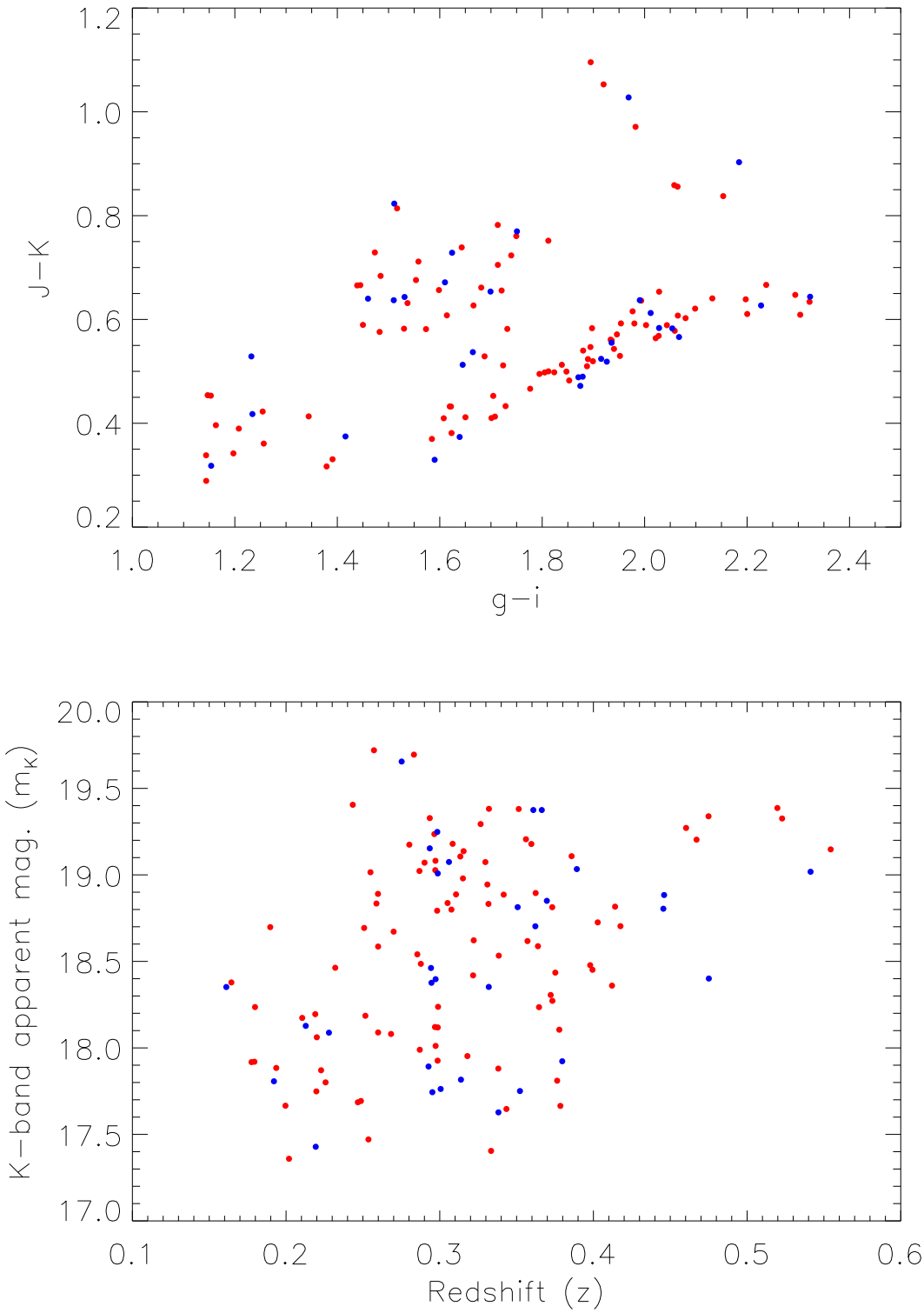

FIGURE 5.11: *Top*: The $g - i$ versus $J - K$ colour-matched NIR sample (*red*) with the $L < 10^{23}$ W Hz^{-1} (SF dominated) matched Radio (*blue*) sources, numbering 93 and 31 respectively. *Bottom*: The redshift versus K_S-band apparent magnitude for the same matched samples.

Table 5.4: Two sample and two-dimensional KS- and MWU-test results for the cross-matched 93 NIR objects and 31 $L < 10^{23}$ W Hz^{-1} (SF dominated) radio sources across the redshift range ($0.16 < z < 0.56$). The two density distributions are different at the 2.7σ level from KS tests, with the means of the distributions different at the 3σ level from MWU tests.

Distributions Compared			KS Probability	MWU Probability
$z_{(NIR)}$	versus	$z_{(Radio)}$	0.314	0.208
$(g-i)_{NIR}$	versus	$(g-i)_{Radio}$	0.975	0.483
$(J-K)_{NIR}$	versus	$(J-K)_{Radio}$	0.975	0.392
$m_{K(NIR)}$	versus	$m_{K(Radio)}$	0.806	0.245
$(\bar{S}_c)_{NIR}$	versus	$(\bar{S}_c)_{Radio}$	$8.36\times\ 10^{-3}$	$2.98\times\ 10^{-3}$
$(g-i, J-K)_{NIR}$	versus	$(g-i, J-K)_{Radio}$	0.926	-
$(g-i, z)_{NIR}$	versus	$(g-i, z)_{Radio}$	0.603	-
$(J-K, z)_{NIR}$	versus	$(J-K, z)_{Radio}$	0.516	-
$(m_K, z)_{NIR}$	versus	$(m_K, z)_{Radio}$	0.274	-
$(g-i, m_K)_{NIR}$	versus	$(g-i, m_K)_{Radio}$	0.846	-
$(J-K, m_K)_{NIR}$	versus	$(J-K, m_K)_{Radio}$	0.487	-
$(g-i, \bar{S}_c)_{NIR}$	versus	$(g-i, \bar{S}_c)_{Radio}$	0.050	-
$(J-K, \bar{S}_c)_{NIR}$	versus	$(J-K, \bar{S}_c)_{Radio}$	0.041	-
$(m_K, \bar{S}_c)_{NIR}$	versus	$(m_K, \bar{S}_c)_{Radio}$	0.031	-
$(z, \bar{S}_c)_{NIR}$	versus	$(z, \bar{S}_c)_{Radio}$	0.041	-

5.5 Discussion

By applying my VT algorithm to a sample of VLA observed radio selected galaxies out to $z < 2.2$, I have shown that a significant correlation with environment exists. This is such that galaxies with radio emission are found to predominantly favour overdensities at a 4σ significance, on individual galaxy scale environments, across the entire radio sample. This is in comparison to near-infrared and optically observed galaxies, from a combination of VIDEO and CFHTLS observations, which are found to predominantly favour underdense regions on the same scales.

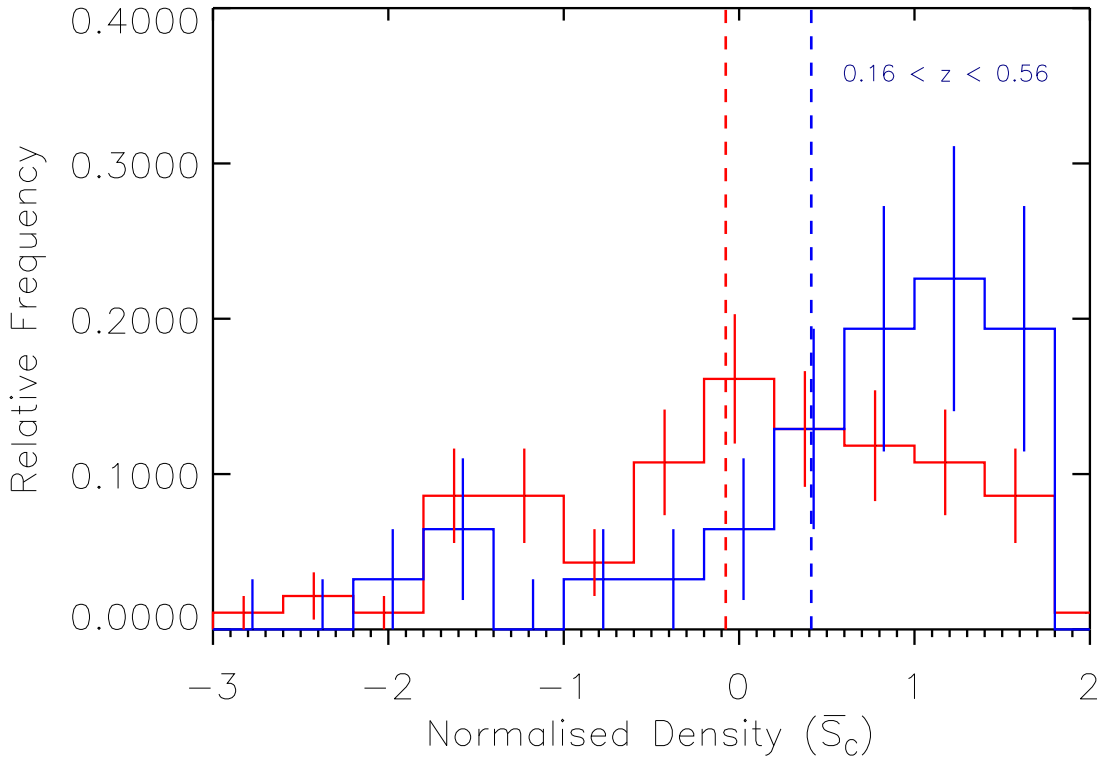

FIGURE 5.12: Normalised histogram of both environmental density ($\bar{S}_c$) distributions of the cross-matched NIR (*red*) and the $L < 10^{23}$ W Hz^{-1} (SF dominated) Radio (*blue*) populations (93 and 31 objects respectively) across the redshift range $0.16 \leq z < 0.56$. The Radio data favours generally overdense regions (positive $\bar{S}_c$ values), with the mean of its distribution at 0.41 ± 0.27 (*blue dashed line*), this is contrasted against the mean of the NIR distribution at (-7.62 ± 12.67) x 10^{-2} (*red dashed line*). A KS-tests between these two distributions returned a probability value of 8.36×10^{-3} indicating that they are significantly different at the 2.7σ level, while a MWU test returned a probability of 2.98×10^{-3} indicating a significant difference between their mean values at the 3σ level.

When dividing into high- and low-redshift bins and repeating the density comparison, I find that the same radio-density correlation remains between my NIR and Radio samples and that there is improved significance in the higher redshift bin, increasing from 2.1σ to 3.4σ from KS tests. This trend may be understood if one considers that AGN form predominantly in high density environments at high redshift due to the galaxy interaction processes believed to be necessary to trigger accretion (i.e major mergers) as described in Section 5.1. Over time the gas available for accretion onto the SMBH will decrease, either through accretion, star formation or AGN feedback effects. Thus, towards the local universe, AGN are primarily found in group and field

regions rather than the most dense cluster regions, where gas for accretion remains (e.g. Silverman et al. 2009c; Bradshaw et al. 2011). This may therefore explain the reduced significance between my NIR and Radio samples in my lower redshift bin.

Considering that it is established that the origin of radio emission from galaxies can be produced via both star formation and AGN emission, I split my radio sample into sub-samples that represent both of these radio contributions according to the radio luminosity cut ($L = 10^{23}$ W Hz^{-1}) defined in Chapter 1. I then repeat the analysis on each of these sub-samples to compare the radio-emission–density relation of each.

My higher radio luminosity sub-sample, defined as having $L > 10^{23}$ W Hz^{-1} which constitute radio emission via AGN synchrotron emission, forms the majority of the radio population consisting of 403 of the 578 Radio sources. From Figure 5.8, it is clear that applying a luminosity cut removes the lowest redshift objects from the analysis, thus the minimum redshift of the Radio-AGN sample is $z \sim 0.3$. After applying the colour, magnitude and redshift cross-matching with the NIR sample, this reduces further to 166 Radio-AGN sources, as shown in Figure 5.9. Statistical comparisons between the non-radio emitting and Radio-AGN sample show significant differences in their densities at the 4.5σ level (Table 5.3), with the Radio-AGN sample favouring more dense regions as measured on individual galaxy scales. This result is in agreement with previous studies of the relationship between AGN and environmental density, discussed in Section 5.1, which postulate an environmental mechanism (such as major mergers) as the catalyst for triggering rapid accretion onto the central black hole and generating AGN in the densest regions.

My lower radio-luminosity sub-sample, with $L < 10^{23}$ W Hz^{-1}, of which the detected radio is defined as being predominantly from star formation related synchrotron emission, consisted of 175 of my initial sample of 578 radio sources. By introducing the luminosity cut, these objects represented the lowest redshift objects in my initial radio sample with a maximum redshift of $z \sim 0.56$. This is a result of the fact that radio luminosities of star formation generated radio emission have been shown to be $\gtrsim 3$ orders of magnitude less luminous than the evidently more powerful and distant AGN (e.g. Seymour et al. 2008; Lacki & Thompson 2010). Applying the same cross-matching in

colour, magnitude and redshift with the NIR sample resulted in 31 Radio-SF objects, as shown in Figure 5.11. Despite this small number of sources, statistical comparisons between the non-radio and Radio-SF samples returned a significant difference at the 2.7σ level from KS-tests and a further significant difference of 3σ between their mean values, with the Radio-SF sources favouring overdense regions (Table 5.4).

This result may, at first, seem to be contrary to the established SFR-density correlations found in the literature and in earlier chapters within this thesis. However, it is evident that there are a number of constraints associated with observing star formation generated radio emission; namely the small contribution to the total bolometric luminosity that this radio emission provides (as described in Chapter 1). Considering these limitations in comparison to AGN generated star formation, these sources are expected to trace predominantly galaxies with the highest rates of star formation and thus the most radio emission. As it is well established that the most massive galaxies in the local universe are found in the densest regions, this result is expected. In other words, my Radio-SF sample is representative of the most overdense outliers of my FIR density distribution from the analysis in Chapter 3, shown in Figure 3.6. In addition, it is important to note that the luminosity cut imposed to separate AGN and star forming origins of radio emission, is not a perfect selection. Therefore the small Radio-SF sample may be contaminated with some AGN, further influencing the density comparison.

This radio AGN contamination issue, in addition to the small number of detectable star formation generated radio galaxies, should be resolved by the next generation of radio telescopes (e.g. LOFAR). These are expected to reach many orders of magnitude deeper than current observations such that AGN will no longer be the dominant source of radio emission, which will instead be dominated by star forming galaxies (e.g. Seymour et al. 2008; Padovani et al. 2009).

6

Summary, Conclusions & Future Work

In this thesis, I have studied the relationship between the environmental densities of galaxies and their associated properties by developing a novel approach to measuring galaxy environments on individual galaxy scales, using Voronoi tessellations. I have investigated the relationship between star formation rate and environmental density out to intermediate ($z \sim 0.5$) redshifts and have compared my results to predictions from semi-analytic models. I then used isothermal dust temperatures to establish relations with environment across that same redshift range. In Chapter 5, I extended my study of galaxy environments to high ($z \sim 2$) redshifts and investigated density relations associated with active galactic nuclei and radio selected star forming galaxies. The main results from these investigations are summarised below.

6.1 A New Method of Environmental Measure

In Chapter 2 of this thesis, I began by discussing the different kinds of environmental measures used throughout the literature, describing the differences between and advantages of local density measures over cluster finding techniques. I introduced Voronoi tessellations as an alternative to the more widely used Nth-nearest neighbour method and compared the two techniques by applying them individually to the same mock catalogue. I have shown that both techniques are adept at returning the density distributions of galaxies and that there is a strong (although non-linear) correlation between their returned densities, with a Spearman's rank correlation coefficient of 0.961 at a $> 5\sigma$ level. This comparison showed that the Nth-nearest neighbour (using $N = 5$ to correspond with the majority of recent studies) has a greater dynamic range in the densest regions where the Voronoi technique is shown to saturate. Conversely, Voronoi tessellations are found to be better suited to less dense regions, and are found to trace the intermediate density resolution much better than the nearest-neighbour method.

I have shown that the resolution of the nearest-neighbour method is strongly dependent on the selection of N. Where the number of associated satellite galaxies is greater than the chosen value of N (i.e. the most overdense regions), the measured density is found to increase with increasing N. However, where the number of associated satellites is smaller than N (i.e. the most underdense regions), the method begins to lose resolution by assigning unrelated satellite galaxies as part of the primary cluster. Voronoi tessellations do not suffer from such resolution issues as the density is established on individual galaxy scales. Following this, I compared each method's ability to reproduce the established mass-density relation, using virial halo masses extracted from the same mock catalogue. This showed that Voronoi tessellations produced a much tighter correlation than the nearest-neighbour method, with less scatter associated with the density values returned.

I described in detail the structure of the VT algorithm; incorporating redshift sampling, Monte-Carlo realisations and normalisation to account for differences in uniformity and number density. The analyses presented in this thesis have shown my VT

algorithm to work well across multiple data-sets of both wide- and narrow-fields and out to high redshifts. With its ability to return normalised environmental densities on individual galaxy scales, requiring only positional and redshift information, this technique is limited only by the accuracies of redshift information and completeness of the sample.

6.2 Environments of Far-Infrared Selected Galaxies

Analysis of the Herschel Science Demonstration Phase Field:

In Chapter 3, I described the comparison between the environmental and star formation properties of far-infrared detected and non–far-infrared detected galaxies out to $z \sim 0.5$. With optical spectroscopy and photometry obtained from the GAMA 9hr survey (DR1 data) and SDSS, with 250μm far-infrared observations from the H-ATLAS SDP, I have applied the technique of Voronoi tessellations to analyse the environmental densities of individual galaxies. This sample was then normalized to account for differences in the population density and uniformity across the redshift range due to the flux-limit of the survey and the increasing volume sampled with increasing redshift. The environmental densities of my Optical and FIR catalogues were compared by initially matching the samples in multi-dimensional colour, magnitude and redshift space ($g-r$, $r-i$, m_r & z) selecting a matched population of the Optical sources numbering three times that of the FIR distribution, in order to obtain a robust comparison over $0 < z \leq 0.5$.

I have shown that objects with far-infrared detected emission, and levels of star formation $> 5\,\mathrm{M}_{\odot}\,\mathrm{yr}^{-1}$, reside in less dense environments than galaxies not detected at far-infrared wavelengths, in agreement with numerous previous studies. KS- and MWU-tests applied to these two distributions returned probabilities indicating a significant difference at the 3.5σ and 4.5σ levels respectively. The significance of the separation between the cross-matched Optical and FIR galaxy samples also increased with redshift, with a 2.2σ difference in the lower redshift bin ($0 < z \leq 0.25$) and a 3.3σ difference in the higher redshift bin ($0.25 < z \leq 0.50$), with the far-infrared detected galaxies again residing in less dense environments in both bins. By calculating the

SFR of each FIR galaxy, I found an increasing separation between the Optical and FIR density distributions with increasing SFR. For SFR $= 0 - 15\,\mathrm{M_{\odot}yr^{-1}}$, I found a significant difference of 2.6σ from both KS- and MWU-tests; for SFR $= 15-30\,\mathrm{M_{\odot}yr^{-1}}$, I found a significant difference of 2.7σ from KS- and 3.8σ from MWU-tests; and for SFR $> 30\,\mathrm{M_{\odot}yr^{-1}}$, I found a significant difference of 3.3σ from KS- and 4.8σ MWU-tests. Although it is noted that I cannot distinguish redshift effects from luminosity effects in the flux-density limited sample.

I then examined the influence of dust reddening within the FIR samples on my results by comparing the $r - K$ distributions of K-band selected sub-samples of the Optical and FIR populations (obtained from UKIDSS). From this comparison I found the FIR sample to be significantly redder than the Optical sample in this colour space with a $> 5\sigma$ significance. As these samples were previously matched in m_r, the noted difference in K-band magnitude indicates that this reddening of the FIR sample has resulted in an underestimation of their r-band magnitudes and subsequently their masses. Accounting for this reddening therefore removes the mass underestimation in my FIR sample and increases the separation between my density distributions, acting to make my results more significant. This was shown by cross-matching these K-band selected Optical and FIR sub-samples in $r-K$, m_K & z space and repeating the density analysis. As expected, the removal of reddening improved the significance of the separation between Optical and FIR galaxies to $> 5\sigma$.

Finally, I applied my analysis to synthetic light-cones generated from SAMs of Guo et al. (2011), finding qualitatively similar behaviour for the SFR and environmental density relations over the whole redshift distribution. This was despite several assumptions made within the SAM with regards to treatments of AGN feedback; the mass ratio between major and minor mergers; ISM heating by old stars; and gas stripping processes. In particular, the SAM prevents ram-pressure stripping from having any impact on the cold gas content of galaxies. Guo et al. (2011) acknowledge that this is unrealistic as would lead to passive S0 galaxies retaining significant gas and dust which should otherwise have been removed. However, even with this prescription, my results still qualitatively agree with the SAM. I have suggested therefore, that ram-pressure

stripping is not the principal mechanism responsible for the observed difference in the environmental densities of the far-infrared-detected galaxies and those without detectable far-infrared emission. I also found substantial differences between the redshift distributions of both my observed and SAM far-infrared samples. Overall this provides interesting indications on how recipes for star formation need to be modified within SAMs to improve their ability to model the observed universe.

Analysis of the Herschel Phase-One fields:

In Chapter 4, I expanded my analysis of the SFR-density relation across a much larger sample of galaxies over three fields out to $z \sim 0.5$, again using optical spectroscopy from both the SDSS and GAMA (DR1 data) surveys with additional photometric data derived from a combination of SDSS and UKIDSS-LAS imaging. In this chapter my optical data was selected to match the regions covered by the full H-ATLAS Phase-One far-infrared observations across its 9hr, 12hr and 15hr fields, each covering $\sim 14 \times 5$ deg. I again used Voronoi tessellations to measure the normalised environmental densities of these galaxies, on individual scales, normalised to account for differences in uniformity and population density across the redshift range. Furthermore, to achieve an accurate comparison between my Optical and FIR samples, following Chapter 3, I cross-matched my Optical and FIR samples in colour, magnitude and redshift parameter space ($g-r$, $r-i$, m_r & z) before comparison. I have applied my statistical analysis to all three Phase-One fields individually which, due to the increased number of objects available, has produced a more robust analysis of the SFR-density relation than in the SDP analysis of Chapter 3. Combining these fields increases the robustness of these results further still.

It is shown that, once more, objects with far-infrared detected emission reside in less dense environments than galaxies not detected at far-infrared wavelengths, in agreement with my analysis of the SDP field in Chapter 3. The significance of the separation between the Optical and FIR samples is found to be at the $> 5\sigma$ level when these fields are combined. In further agreement with the trends found in Chapter 3, the significance of the separation between the Optical and FIR samples increases with

increasing redshift in all three Phase-One fields. With the Phase-One fields combined, this difference ranges from no difference in the lower bin ($0 < z \leq 0.25$) to the $> 5\sigma$ level in the higher bin ($0.25 < z \leq 0.50$). In both cases, objects with far-infrared detected emission reside in less dense environments. Once more examining the influence of dust reddening on my results, I again found the FIR samples to be significantly redder than the Optical sample in $r - K$ colour space with a $> 6\sigma$ significance for all fields. Removing the reddening and repeating the density analysis again improved the significance of the separation between Optical and FIR galaxies in all fields to $> 5\sigma$.

Finally, introducing isothermal dust temperatures for the far-infrared sample and comparing these to their environmental densities, revealed significant trends such that the coldest sources resided in the densest regions. This correlation is found to be significant at the $> 2.1\sigma$ level for the individual fields and at the 3.9σ level for the combined field from KS-tests. I therefore concluded that the observed far-infrared emission in these densest regions are the product of ISM heating by the old stellar populations that are predominant in the densest galaxies. In addition, I have also shown that removal of dust reddening increases the statistical difference between the hot and cold samples of the combined FIR fields, from the 3.9σ to the 4.7σ level.

Context and Future Work:

The measured correlations between environment and far-infrared emission, found in both Chapters 3 and 4, support the numerous previous studies that have also suggested that the presence of star formation in a galaxy is negatively correlated with the density of its environment (e.g. Dressler 1980; Postman & Geller 1984; Dressler et al. 1997; Domínguez et al. 2001; Goto et al. 2003; Kauffmann et al. 2004; O'Mill et al. 2008; Lee et al. 2010). My analysis of the H-ATLAS fields has shown that this SFR-density correlation holds on individual galaxy scales out to $z \sim 0.5$ and that, with the established accuracy of the VT method, the physical mechanisms behind the truncation of star formation in these dense regions (discussed in Chapter 1) must have influence on these individual scales as well as on larger scales. In addition, the use of far-infrared observations mean my results are not affected by uncertainties associated

with extinction.

It is clear that by cross-matching only K-band selected objects accounts for the dust reddening associated with the FIR samples and improves the significance of the density comparisons. However, I have not exclusively used these objects throughout this analysis as the number of objects with K-band identification is much less than the number identified in the g, r and i bands, which represent the most sensitive optical bands over the survey regions used. Therefore this work could be extended by the inclusion of K_S-band near-infrared data obtained from the VISTA-VIKING survey, which aims to obtain a total of $1,500$ deg^2 Z, Y, J, H and K_S observations incorporating the 9hr, 12hr and 15hr GAMA fields used in this thesis. As shown by Fleuren et al. (2012), these observations have already obtained reliable far-infrared counterparts across the H-ATLAS Phase-One 9hr field. Noting that Voronoi tessellations are a reliable and accurate method of calculating the environmental densities for individual galaxies, in comparison to earlier methods, this new data will allow for the analysis of the SFR-density relation to be achieved to a greater degree of accuracy across the H-ATLAS fields.

In addition, I could extend on this wide and shallow analysis by incorporating the deep far-infrared observations of the *Herschel* Multi-tired Extragalactic Survey (HerMES; Oliver et al. 2012), which has obtained 250μm far-infrared observations to low flux densities and much higher redshifts than H-ATLAS observations ($z \lesssim 3$), across a multitude of survey fields. This would therefore allow for my star formation-density analysis from Chapters 3 and 4 to be continued to these high redshifts, allowing for this correlation to be traced across the epoch of peak star formation activity in the universe.

6.3 Environments of Radio Selected Galaxies

In Chapter 5, I used a much smaller yet deeper sample of galaxies, across 1 deg^2 and out to $z \sim 2$, to investigate the environmental dependence of radio sources. I applied my VT algorithm to a combination of near-infrared and optical photometry from the

VISTA-VIDEO and CFHTLS-D1 observations, which were then cross-matched in ($g-i$, $J-K$) colour, m_K magnitude and redshift against 1.4 GHz VLA radio observations.

Across the entire radio sample, galaxies with radio detected emission are found to reside in more overdense environments in comparison to non-radio detected galaxies at a 4σ significance level from KS-tests. The mean of these normalised density distributions are shown to be different at the 3σ level. Splitting the full radio sample into redshift bins and repeating the analysis returned the same trends with density in both bins, such that radio emission is found to trace the most overdense regions. The significance of the separation between radio and non-radio detected sources increased with increasing redshift bin, from 2.1σ ($0 < z < 1.10$) to 3.4σ ($1.10 < z < 2.20$). I then divided my radio sample to investigate environmental dependence on both radio detected star formation and radio detected AGN individually, based upon a luminosity cut of $L = 10^{23}$ W Hz^{-1}. The same trends with environment are displayed by my Radio-AGN sample ($L > 10^{23}$ W Hz^{-1}) which favour overdense regions at the 4.5σ level from KS-tests and 3.4σ level from MWU-tests. At lower radio luminosities, my Radio-SF sample ($L < 10^{23}$ W Hz^{-1}) also displayed a significant trend towards overdense regions in comparison to my non-radio detected sample, at the 2.7σ level from KS-tests and 3.0σ from MWU-tests.

Context and Future Work:

The measured correlations between galaxy environments and whether they are detected in the radio, are in agreement with earlier work that has suggested such a relationship (e.g. Best et al. 2005; Mauch & Sadler 2007; Hickox et al. 2009). For my higher radio-luminosity (AGN) galaxy sub-sample, the improved significance of the separation between radio and non-radio selected galaxies, found at low and high redshifts, is indicative of the changes in accretion rate that drives AGN activity over cosmic time. This can be understood by considering that at high redshifts, AGN form predominantly in the densest regions due to galaxy interaction processes (i.e. major mergers) that are believed to trigger accretion, as discussed. Over time this gas is depleted and the accretion rate falls, lowering the radio-loud activity in the densest regions in the local

universe, in agreement with observations (e.g. Silverman et al. 2009c; Bradshaw et al. 2011).

For my lower radio-luminosity (star forming) galaxy sub-sample, the same trends with density are found. This, at first, appears to be contrary to my previous results, where I have shown star formation to prefer underdense regions. However, this can be reconciled by considering the constraints associated with observations of star formation generated radio emission. As discussed, it has been shown that radio luminosities of star formation generated radio emission are lower than the evidently more powerful and distant AGN. This is in addition to the low contribution of star formation generated radio emission to the overall bolometric luminosity in star forming galaxies. This has the overall effect of only the brightest and most massive radio-emitting star forming galaxies being observed, and thus there is a bias towards overdense regions where these galaxies are expected to reside. This bias towards overdensity is increased further by that fact that the luminosity selection used to separate AGN from star forming galaxies is not a perfect selection and open to AGN contamination in the low-luminosity sample.

This analysis of the relation between environment and radio-selected star forming galaxies can be extended by the next generation of low-frequency, deep radio surveys (e.g. LOFAR) which are expected to reach many orders of magnitude deeper than current observations. With increased sensitivity, these observations will have the ability to probe low-luminosity star forming galaxies via radio emission out to high redshifts while rapidly reducing the radio-loud AGN contamination. Although radio-quiet AGN will still make a significant contribution (e.g. Jarvis & Rawlings 2004; Simpson et al. 2006; Smolčić et al. 2009). These improved radio observations will also increase the number of radio detected sources available for comparison with environment and thus will dramatically improve the robustness of any statistical tests applied.

As the deep far-infrared observations of HerMES has obtained 250μm observations across the total XMM-VIDEO fields, including the 1 deg^2 field used in this analysis, I could compare my calculated density map of the 1 deg^2 field to this data to extend my initial star formation-density analysis to $z \sim 2$. In addition, these far-infrared and radio observations can be used together to apply an accurate separation between the

radio detected AGN and star forming galaxies. This would therefore reduce the AGN contaminants from my star forming sample, improving the accuracy of my comparison. As introduced in Section 1.6.4, a strong positive linear correlation exists between the radio and far-infrared emission of galaxies at all redshifts, as shown by a number of studies (e.g. de Jong et al. 1985; Helou et al. 1985; Condon 1992; Garrett 2002; Jarvis et al. 2010). This therefore indicates that the radio continuum emission must also trace the SFR of a galaxy. As shown by Hardcastle et al. (2013), this far-infrared–radio correlation (FIRC) can be used to define a reasonably good separation between the radio emitting AGN and star forming galaxies by applying a cut in the ratio between the far-infrared and radio luminosity; defined from Virdee et al. (2013) as being 1.3, where the ratio (q_{250}) is defined as:

$$q_{250} = \log_{10}(L_{250}/L_{1.4}) \ , \tag{6.1}$$

where L_{250} and $L_{1.4}$ are the 250μm and 1.4GHz radio luminosities respectively. Figure 6.1, taken from Hardcastle et al. (2013), shows the FIRC for a sample of galaxies detected at 250μm and 1.4GHz, where asterisk symbols indicate Herschel detections at 2σ or better. Of these detections, galaxies identified as star-forming are labelled as black asterisks (SF); galaxies corresponding to the expected spectra of low-excitation radio galaxies (LERGs) are labelled as blue asterisks (Aa); high-excitation, narrow-line radio galaxies (HERGs, or NLRGs) as green asterisks (Ae); and broad-line objects as red asterisks (AeB). The magenta lines represent the expected mean FIRC as well as the upper and lower boundaries of the dispersion in the relationship. The orange line represents the $q_{250} = 1.3$ cut-off, such that where $q_{250} > 1.3$ galaxies are considered part of the star forming population. Application of this FIRC cut, rather than a single cut in the radio luminosity at $L = 10^{23}$ W Hz^{-1}, would therefore reduce the contamination of AGN, while including the brightest star forming galaxies that would otherwise have been removed from my sample.

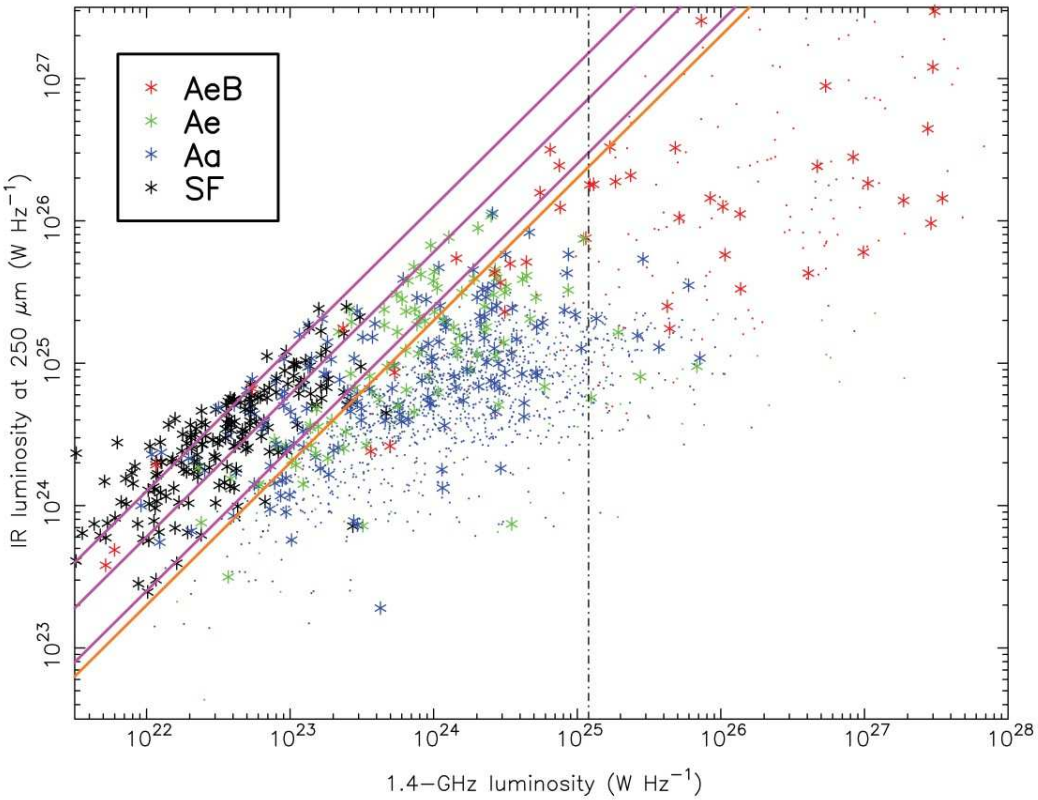

Figure 6.1: 250μm luminosity against 1.4GHz radio luminosity for a sample of objects taken from Hardcastle et al. (2013), where asterisks represent Herschel detections at $> 2\sigma$. Asterisk colours correspond to the emission-line classes: LERGs (*blue*); HERGs or NLRGs (*green*); broad-line objects (*red*); and star-forming galaxies (*black*). The solid magenta lines indicate the expected FIRC for star-forming objects, $q_{250} = 1.78$, and the approximate scatter about this relation, $1.4 < q250 < 2.1$ (from Jarvis et al. 2010). The solid orange line shows the adopted SF cut at $q_{250} = 1.3$, and the dotdashed vertical line shows the nominal FRI/FRII break luminosity. Figure from Hardcastle et al. (2013).

A

Appendices

As discussed throughout this thesis, in comparison to the photometric redshift errors present in the majority of my data, my chosen redshift slicing ($\Delta z = 0.01$), applied through each 3D MC realisation, may be acting to flatten my overall density distribution. Therefore, the impact of my redshift slice selection on these density values should be investigated. In this appendix, I repeat my density analysis of the SDP field from Chapter 3, increasing the width of my redshift binning from $\Delta z = 0.01$, for three separate analyses at $\Delta z = 0.05$, $\Delta z = 0.10$ and $\Delta z = 0.20$. The results of these analyses are outlined and discussed below.

A.1 An Investigation of the Impact of Δz on $\bar{S}_c$

A.1.1 With Redshift Slices of $\Delta z = 0.05$

Increasing the size of my applied redshift slicing from $\Delta z = 0.01$ to $\Delta z = 0.05$, I repeated the comparison between the normalised densities ($\bar{S}_c$) of the Optical and FIR samples, as described between Sections 3.2.1 and 3.2.3. Taking the cross-matched $g-r$, $r-i$, z and m_r samples and applying KS- and MWU-tests, revealed the same probabilities for all combinations of these parameters, as was found when $\Delta z = 0.01$. This was, of course, expected due to the fact that these parameters will not have changed with the increase in redshift slice applied. However, due to the processes involved in the calculating $\bar{S}_c$ within my VT algorithm, as described in Chapter 2, these $\bar{S}_c$ values will be influenced by this increase in the width of the redshift slice. Subsequently the KS- and MWU-tests applied to these cross-matched density distributions revealed different probability values to my original $\Delta z = 0.01$ analysis.

In this analysis, a significant difference remains between the Optical and FIR $\bar{S}_c$ distributions from KS-tests, although this significance itself was reduced from the 3.5σ to the 2.9σ level. MWU tests also reveal a less significant difference, at the 3.7σ level, down from 4.5σ. All probability values are presented in Table A.1, with the identical rows from Table 3.1 removed for clarity. Figure A.1 shows the normalised density distributions of the cross-matched Optical and FIR samples, once more with spectroscopic redshift data plotted as the shaded histograms. The mean densities are $(9.64\pm1.28)\times10^{-2}$ and $(1.98\pm2.04)\times10^{-2}$ for the Optical and FIR samples respectively, confirming that the same result from Chapter 3 is found, such that the SFR (as traced by the FIR sample) predominantly favours underdense regions.

Table A.1: Two sample and two-dimensional KS- and MWU-test results over the full SFR and redshift range ($0 < z \leq 0.5$) when $\Delta z = 0.05$. Where *op* represents Optical (2,706 objects) and *FIR* represents FIR (902 objects). The two density distributions are different at the 2.9σ level from KS-tests, with the means of the distributions different at the 3.7σ level from MWU tests.

Distributions Compared			KS Probability	MWU Probability
$(\bar{S}_c)_{op}$	versus	$(\bar{S}_c)_{FIR}$	4.74×10^{-3}	2.96×10^{-4}
$(g-r, \bar{S}_c)_{op}$	versus	$(g-r, \bar{S}_c)_{FIR}$	0.027	-
$(r-i, \bar{S}_c)_{op}$	versus	$(r-i, \bar{S}_c)_{FIR}$	0.001	-
$(m_r, \bar{S}_c)_{op}$	versus	$(m_r, \bar{S}_c)_{FIR}$	0.024	-
$(z, \bar{S}_c)_{op}$	versus	$(z, \bar{S}_c)_{FIR}$	0.028	-

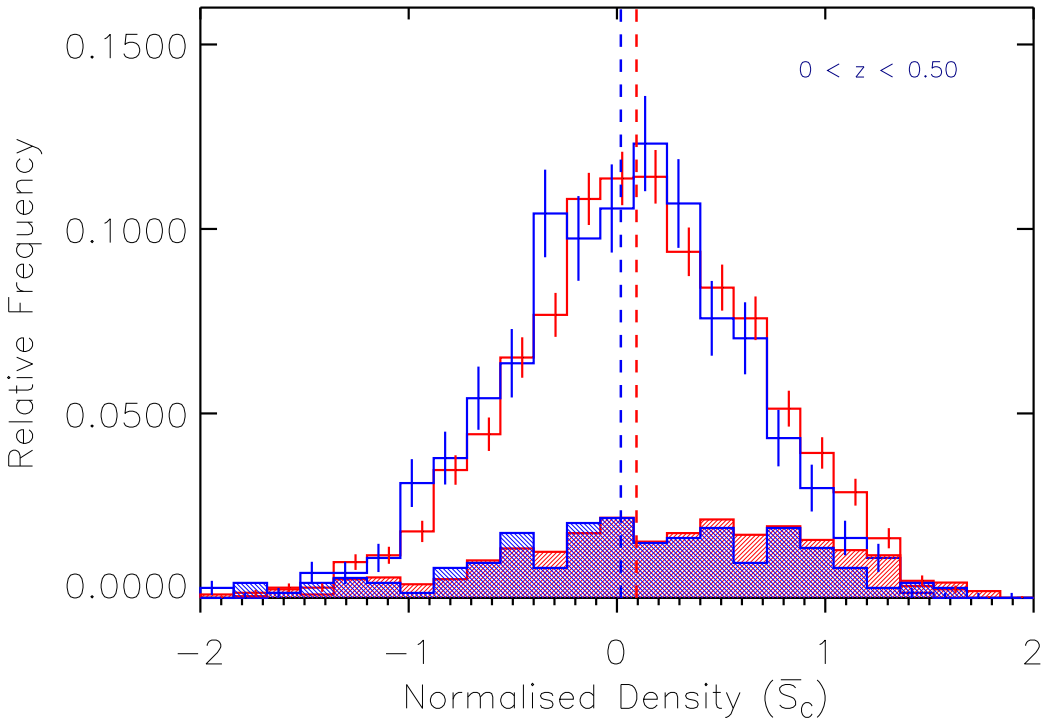

Figure A.1: A normalised histogram showing how the distributions of environmental density ($\bar{S}_c$) of the total Optical (*red*) and FIR (*blue*) populations (2706 and 902 objects respectively) compare with $\Delta z = 0.05$. The FIR data is shifted generally to lower $\bar{S}_c$ values, with the mean of its distribution at $(1.98 \pm 2.04) \times 10^{-2}$ (*blue dashed line*), this is contrasted against the mean of the Optical distribution at $(9.64 \pm 1.28) \times 10^{-2}$ (*red dashed line*).

A.1.2 With Redshift Slices of $\Delta z = 0.10$

I then increased the size of the redshift binning to $\Delta z = 0.10$ and repeated the analysis outlined above. I find that the significance of the difference between the $\bar{S}_c$ distributions of the cross-matched Optical and FIR samples is reduced even further. Applying KS-tests confirmed a significant difference at the 2.6σ level, with MWU-tests revealing a significant difference between the means of these distributions at the 2.8σ level. Once more, all combinations of the cross-matched parameters remain unchanged from the analysis in Chapter 3, and the remaining statistical results are presented in Table A.2. The normalised density distributions of these samples are displayed in Figure A.2, with the mean values for the Optical and FIR samples found at $(8.72 \pm 0.12) \times 10^{-2}$ and $(4.24 \pm 2.20) \times 10^{-2}$ respectively. Despite this evident reduction in the significance of the differences found, the same trend between SFR and density are returned, as found in Chapter 3.

A.1.3 With Redshift Slices of $\Delta z = 0.20$

Finally, I increased the size of my applied redshift binning to $\Delta z = 0.20$ and, once more, repeated the density analysis. With this increased redshift slicing, I again find that the significance of the difference between the $\bar{S}_c$ distributions of the cross-matched Optical and FIR samples has reduced further. As displayed in Table A.3, KS-tests confirmed a difference at the 2.4σ level, with MWU-tests revealing a difference between the means of these distributions at the 2.2σ level. These normalised density distributions are displayed in Figure A.3, with the mean values for the Optical and FIR samples are found at $(5.21 \pm 1.24) \times 10^{-2}$ and $(2.73 \pm 2.03) \times 10^{-2}$ respectively. Again, the same overall trend with density is found such that the FIR sample favours underdensities, in agreement with earlier results.

Table A.2: Two sample and two-dimensional KS- and MWU-test results over the full SFR and redshift range ($0 < z \leq 0.5$) when $\Delta z = 0.10$. Where *op* represents Optical (2,706 objects) and *FIR* represents FIR (902 objects). The two density distributions are different at the 2.6σ level from KS-tests, with the means of the distributions different at the 2.8σ level from MWU tests.

Distributions Compared			KS Probability	MWU Probability
$(\bar{S}_c)_{op}$	versus	$(\bar{S}_c)_{FIR}$	0.011	6.39×10^{-3}
$(g-r, \bar{S}_c)_{op}$	versus	$(g-r, \bar{S}_c)_{FIR}$	0.043	-
$(r-i, \bar{S}_c)_{op}$	versus	$(r-i, \bar{S}_c)_{FIR}$	8.43×10^{-3}	-
$(m_r, \bar{S}_c)_{op}$	versus	$(m_r, \bar{S}_c)_{FIR}$	0.045	-
$(z, \bar{S}_c)_{op}$	versus	$(z, \bar{S}_c)_{FIR}$	0.048	-

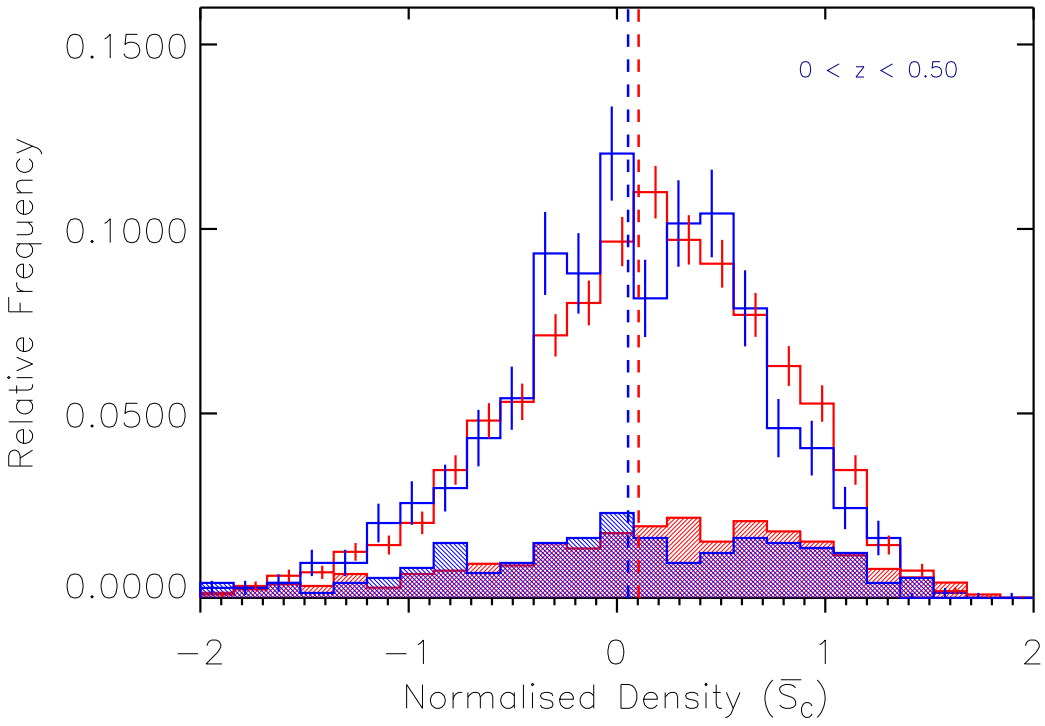

Figure A.2: A normalised histogram showing how the distributions of environmental density ($\bar{S}_c$) of the total Optical (*red*) and FIR (*blue*) populations (2706 and 902 objects respectively) compare with $\Delta z = 0.10$. The FIR data is shifted generally to lower $\bar{S}_c$ values, with the mean of its distribution at $(4.24 \pm 2.20) \times 10^{-2}$ (*blue dashed line*), this is contrasted against the mean of the Optical distribution at $(8.72 \pm 1.41) \times 10^{-2}$ (*red dashed line*).

TABLE A.3: Two sample and two-dimensional KS- and MWU-test results over the full SFR and redshift range ($0 < z \leq 0.5$) when $\Delta z = 0.20$. Where *op* represents Optical (2,706 objects) and *FIR* represents FIR (902 objects). The two density distributions are different at the 2.4σ level from KS-tests, with the means of the distributions different at the 2.2σ level from MWU tests.

Distributions Compared			KS Probability	MWU Probability
$(\bar{S}_c)_{op}$	versus	$(\bar{S}_c)_{FIR}$	0.019	0.031
$(g-r, \bar{S}_c)_{op}$	versus	$(g-r, \bar{S}_c)_{FIR}$	9.85×10^{-3}	-
$(r-i, \bar{S}_c)_{op}$	versus	$(r-i, \bar{S}_c)_{FIR}$	1.88×10^{-3}	-
$(m_r, \bar{S}_c)_{op}$	versus	$(m_r, \bar{S}_c)_{FIR}$	0.045	-
$(z, \bar{S}_c)_{op}$	versus	$(z, \bar{S}_c)_{FIR}$	0.026	-

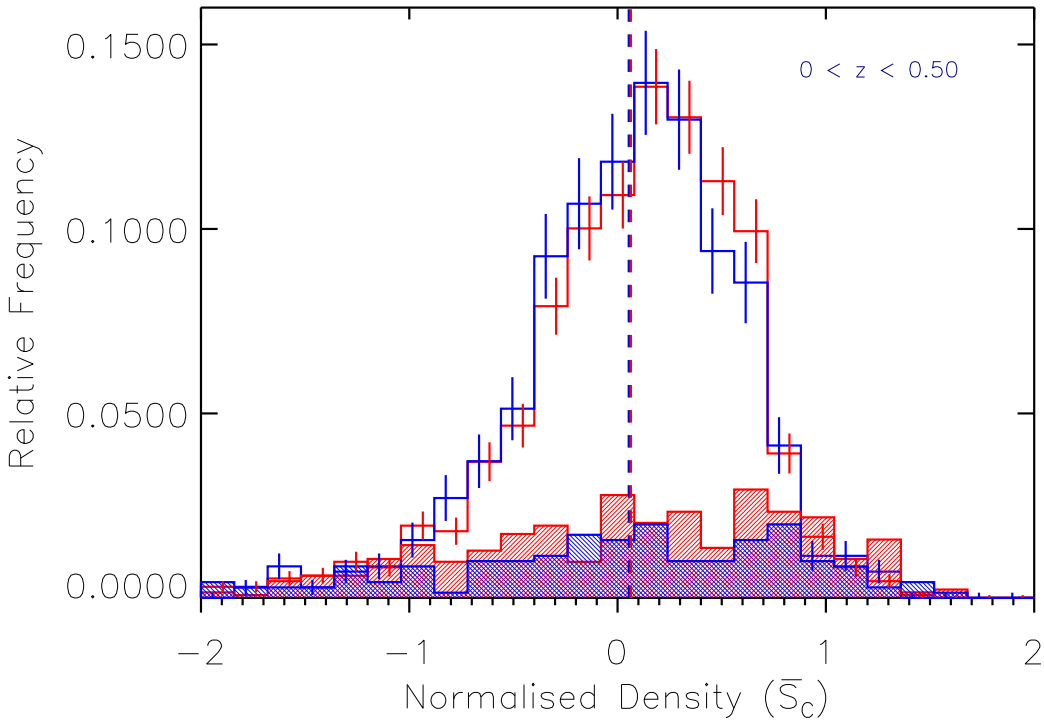

FIGURE A.3: A normalised histogram showing how the distributions of environmental density ($\bar{S}_c$) of the total Optical (*red*) and FIR (*blue*) populations (2706 and 902 objects respectively) compare with $\Delta z = 0.20$. The FIR data is shifted generally to lower $\bar{S}_c$ values, with the mean of its distribution at $(2.73 \pm 2.03) \times 10^{-2}$ (*blue dashed line*), this is contrasted against the mean of the Optical distribution at $(5.21 \pm 1.24) \times 10^{-2}$ (*red dashed line*).

A.1.4 Discussion

As the photometric redshift errors associated with the majority of my data are larger than the initial redshift slicing ($\Delta z = 0.01$), it was suggested that this could lead to my measured density distribution to be flattened. However, this investigation has shown that by increasing the width of the redshift slices, this acts to reduce the significance of the difference found between the Optical and FIR samples. The larger the redshift slice applied, the smaller the significance returned. This suggests, therefore, that applying wider redshift slices actually flattens the density distributions being produced, washing-out the structure. For example, when $\Delta z = 0.20$, two objects that in one particular MC realisation would have initially occupied separate redshift slices when $\Delta z = 0.01$ (and thus contributed separate densities into the calculation), would now appear within the same redshift slice. In this scenario, their very different individual density structure would be diminished by the overall smearing of independent structures within the same redshift slice.

This is supported by the direct comparison of the normalised density distributions produced by my VT algorithm, for different redshift slice widths. When $\Delta z = 0.01$, after 1000 MC realisations, the total distribution is Gaussian in shape, with little spread. Running the same VT algorithm with $\Delta z = 0.05$, for example, produces a much broader, less-Gaussian distribution. Figure A.4 displays the $\Delta z = 0.01$ (*red*) and $\Delta z = 0.05$ (*green*) normalised density distributions, where the difference described is clear. Furthermore, both $\Delta z = 0.10$ and $\Delta z = 0.20$ produce broader and less-Gaussian distributions, similar to $\Delta z = 0.05$, but with larger standard deviations. With such a larger distribution of structure, this would introduce line-of-sight effects that would act to enhance or decrease the overall density measure, but provide much greater scatter. Therefore, my selection of $\Delta z = 0.01$ is actually an appropriate slice width for such analyses as have been conducted in this thesis.

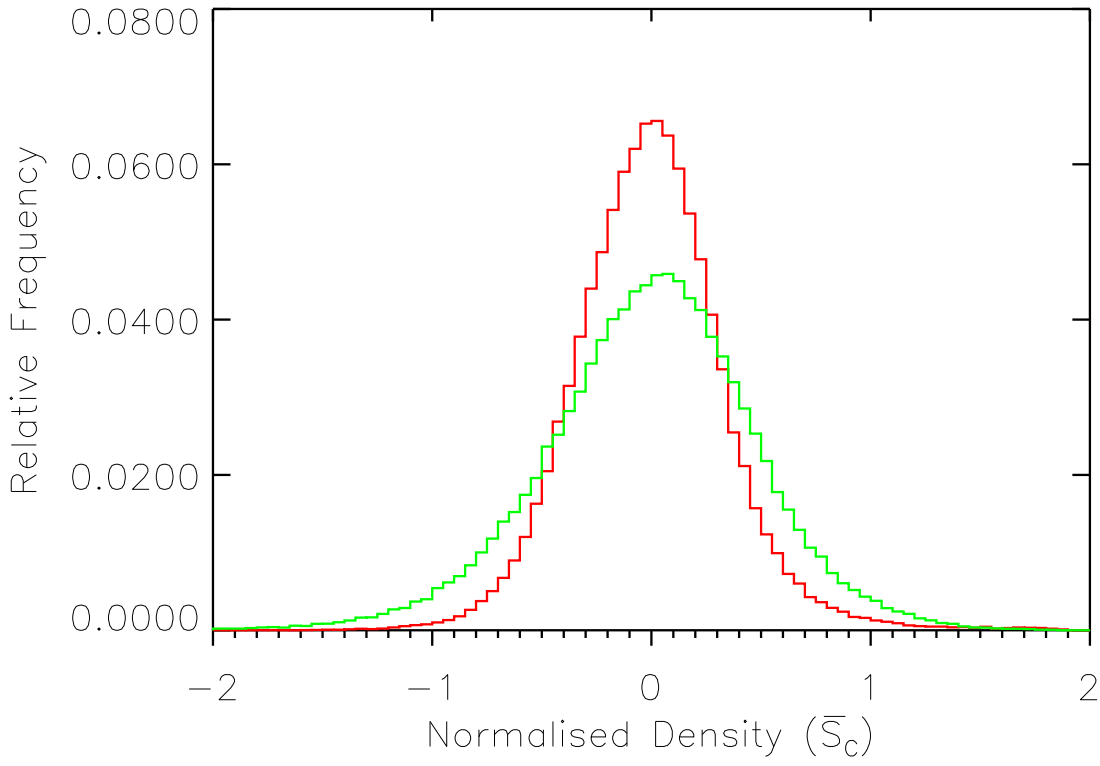

FIGURE A.4: A normalised histogram showing the comparison between the $\Delta z = 0.01$ (*red*) and $\Delta z = 0.05$ (*green*) normalised density distributions. The only difference in the VT code, which produced these two distributions, was the difference in z-bin size applied.

References

Abazajian, K. N., et al. 2009, ApJS, 182, 543

Abraham, R. G., van den Bergh, S., Glazebrook, K., Ellis, R. S., Santiago, B. X., Surma, P., & Griffiths, R. E. 1996, ApJS, 107, 1

Adelberger, K. L. & Steidel, C. C. 2000, ApJ, 544, 218

Appleton, P. N., et al. 2004, ApJS, 154, 147

Aragon-Salamanca, A., Baugh, C. M., & Kauffmann, G. 1998, MNRAS, 297, 427

Arimoto, N. & Yoshii, Y. 1987, A&A, 173, 23

Arnouts, S., Cristiani, S., Moscardini, L., Matarrese, S., Lucchin, F., Fontana, A., & Giallongo, E. 1999, MNRAS, 310, 540

Athanassoula, E. 2003, MNRAS, 341, 1179

Bahé, Y. M., McCarthy, I. G., Crain, R. A., & Theuns, T. 2012, MNRAS, 424, 1179

Baldry, I. K., Balogh, M. L., Bower, R. G., Glazebrook, K., Nichol, R. C., Bamford, S. P., & Budavari, T. 2006, MNRAS, 373, 469

Baldry, I. K., Glazebrook, K., Brinkmann, J., Ivezić, Ž., Lupton, R. H., Nichol, R. C., & Szalay, A. S. 2004, ApJ, 600, 681

Baldry, I. K., et al. 2010, MNRAS, 404, 86

Ball, N. M., Loveday, J., & Brunner, R. J. 2008, MNRAS, 383, 907

Ballo, L., Heras, F. J. H., Barcons, X., & Carrera, F. J. 2012, A&A, 545, A66

Balogh, M., et al. 2004, MNRAS, 348, 1355

Balogh, M. L. & Morris, S. L. 2000, MNRAS, 318, 703

Balogh, M. L., Morris, S. L., Yee, H. K. C., Carlberg, R. G., & Ellingson, E. 1997, ApJL, 488, L75+

Balogh, M. L., Morris, S. L., Yee, H. K. C., Carlberg, R. G., & Ellingson, E. 1999, ApJ, 527, 54

Balogh, M. L., Navarro, J. F., & Morris, S. L. 2000, ApJ, 540, 113

Balogh, M. L., Schade, D., Morris, S. L., Yee, H. K. C., Carlberg, R. G., & Ellingson, E. 1998, ApJL, 504, L75

Bamford, S. P., et al. 2009, MNRAS, 393, 1324

Barnes, J. E. 1988, ApJ, 331, 699

Barnes, J. E. 1992, ApJ, 393, 484

Barnes, J. E. & Hernquist, L. 1992, ARA&A, 30, 705

Barnes, J. E. & Hernquist, L. E. 1991, ApJL, 370, L65

Barnes, K. L., van Zee, L., Côté, S., & Schade, D. 2012, ApJ, 757, 64

Battinelli, P., Capuzzo-Dolcetta, R., Hodge, P. W., Vicari, A., & Wyder, T. K. 2000, A&A, 357, 437

Baugh, C. M., Cole, S., & Frenk, C. S. 1996, MNRAS, 283, 1361

Baum, W. A. 1959, PASP, 71, 106

Bechtold, J., Yee, H. K. C., Elston, R., & Ellingson, E. 1997, ApJL, 477, L29

Becker, R. H., White, R. L., & Helfand, D. J. 1995, ApJ, 450, 559

Bedregal, A. G., Cardiel, N., Aragón-Salamanca, A., & Merrifield, M. R. 2011, MNRAS, 415, 2063

Begeman, K. G. 1989, A&A, 223, 47

Begeman, K. G., Broeils, A. H., & Sanders, R. H. 1991, MNRAS, 249, 523

Bekki, K., Couch, W. J., & Shioya, Y. 2002, ApJ, 577, 651

Bell, E. F. 2003, ApJ, 586, 794

Bell, E. F. & de Jong, R. S. 2000, MNRAS, 312, 497

Bell, E. F., et al. 2006, ApJ, 640, 241

Bell, E. F., et al. 2004, ApJ, 608, 752

Bell, E. F., Zheng, X. Z., Papovich, C., Borch, A., Wolf, C., & Meisenheimer, K. 2007, ApJ, 663, 834

Bendo, G. J., et al. 2012, MNRAS, 419, 1833

Bendo, G. J., et al. 2010, A&A, 518, L65

Bennett, C. L., et al. 2003, ApJS, 148, 1

Bernardi, M., et al. 2003, AJ, 125, 1882

Berrier, J. C., Bullock, J. S., Barton, E. J., Guenther, H. D., Zentner, A. R., & Wechsler, R. H. 2006, ApJ, 652, 56

Best, P. N., Kaiser, C. R., Heckman, T. M., & Kauffmann, G. 2006, MNRAS, 368, L67

Best, P. N., Kauffmann, G., Heckman, T. M., Brinchmann, J., Charlot, S., Ivezić, Ž., & White, S. D. M. 2005, MNRAS, 362, 25

Best, P. N., von der Linden, A., Kauffmann, G., Heckman, T. M., & Kaiser, C. R. 2007, MNRAS, 379, 894

Bigiel, F., Leroy, A., Walter, F., Brinks, E., de Blok, W. J. G., Madore, B., & Thornley, M. D. 2008, AJ, 136, 2846

Blain, A. W., Barnard, V. E., & Chapman, S. C. 2003, MNRAS, 338, 733

Blain, A. W., Chapman, S. C., Smail, I., & Ivison, R. 2004, ApJ, 611, 52

Blandford, R. D. & Rees, M. J. 1974, MNRAS, 169, 395

Bluck, A. F. L., Conselice, C. J., Bouwens, R. J., Daddi, E., Dickinson, M., Papovich, C., & Yan, H. 2009, MNRAS, 394, L51

Bondi, M., et al. 2003, A&A, 403, 857

Bonnell, I. A., Dobbs, C. L., & Smith, R. J. 2013, MNRAS, 430, 1790

Bonoli, S., Marulli, F., Springel, V., White, S. D. M., Branchini, E., & Moscardini, L. 2009, MNRAS, 396, 423

Boselli, A., Gavazzi, G., Donas, J., & Scodeggio, M. 2001, AJ, 121, 753

Bosma, A. 1981, AJ, 86, 1825

Bothun, G. D., Sullivan, III, W. T., & Schommer, R. A. 1982, AJ, 87, 725

Botzler, C. S., Snigula, J., Bender, R., & Hopp, U. 2004, MNRAS, 349, 425

Boulade, O., et al. 2003, in Society of Photo-Optical Instrumentation Engineers (SPIE) Conference Series, Vol. 4841, Society of Photo-Optical Instrumentation Engineers (SPIE) Conference Series, ed. M. Iye & A. F. M. Moorwood, 72–81

Bourne, N., Dunne, L., Ivison, R. J., Maddox, S. J., Dickinson, M., & Frayer, D. T. 2011, MNRAS, 410, 1155

Bouwens, R. J., Illingworth, G. D., Franx, M., & Ford, H. 2007, ApJ, 670, 928

Bower, R. G. 1991, MNRAS, 248, 332

Bower, R. G., Benson, A. J., & Crain, R. A. 2012, MNRAS, 422, 2816

Bower, R. G., Benson, A. J., Malbon, R., Helly, J. C., Frenk, C. S., Baugh, C. M., Cole, S., & Lacey, C. G. 2006, MNRAS, 370, 645

Bower, R. G., Kodama, T., & Terlevich, A. 1998, MNRAS, 299, 1193

Bower, R. G., Lucey, J. R., & Ellis, R. S. 1992a, MNRAS, 254, 601

Bower, R. G., Lucey, J. R., & Ellis, R. S. 1992b, MNRAS, 254, 589

Bradshaw, E. J., et al. 2011, MNRAS, 415, 2626

Brandenberger, R. H. 2001, Brazilian Journal of Physics, 31, 131

Bregman, J. N., Hogg, D. E., & Roberts, M. S. 1992, ApJ, 387, 484

Bregman, J. N., Snider, B. A., Grego, L., & Cox, C. V. 1998, ApJ, 499, 670

Bridge, C. R., et al. 2007, ApJ, 659, 931

Brinchmann, J. & Ellis, R. S. 2000, ApJL, 536, L77

Brodie, J. P. & Huchra, J. P. 1991, ApJ, 379, 157

Brook, C. B., et al. 2011, MNRAS, 415, 1051

Brook, C. B., Kawata, D., Gibson, B. K., & Flynn, C. 2004, MNRAS, 349, 52

Brooks, A. M., et al. 2011, ApJ, 728, 51

Brosch, N., Heller, A., & Almoznino, E. 1998, MNRAS, 300, 1091

Bruzual, G. & Charlot, S. 1993, ApJ, 405, 538

Buat, V., et al. 2010, MNRAS, 409, L1

Buat, V. & Xu, C. 1996, A&A, 306, 61

Bundy, K., Fukugita, M., Ellis, R. S., Targett, T. A., Belli, S., & Kodama, T. 2009, ApJ, 697, 1369

Burton, C. S., et al. 2013, MNRAS, 433, 771

Buson, L. M., et al. 1993, A&A, 280, 409

Butcher, H. & Oemler, Jr., A. 1978, ApJ, 219, 18

Caimmi, R. 2009, Serbian Astronomical Journal, 179, 31

Calzetti, D. & Heckman, T. M. 1999, ApJ, 519, 27

Calzetti, D., Kinney, A. L., & Storchi-Bergmann, T. 1994, ApJ, 429, 582

Carlberg, R. G. 1992, ApJL, 399, L31

Carlberg, R. G., et al. 2000, ApJL, 532, L1

Catinella, B., Haynes, M. P., & Giovanelli, R. 2005, AJ, 130, 1037

Catinella, B., et al. 2010, MNRAS, 403, 683

Cen, R. 2011, ApJ, 741, 99

Chabrier, G. 2003, PASP, 115, 763

Chanial, P., Flores, H., Guiderdoni, B., Elbaz, D., Hammer, F., & Vigroux, L. 2007, A&A, 462, 81

Chapin, E. L., Hughes, D. H., & Aretxaga, I. 2009, MNRAS, 393, 653

Chapman, S. C., Blain, A. W., Smail, I., & Ivison, R. J. 2005, ApJ, 622, 772

Chapman, S. C., Helou, G., Lewis, G. F., & Dale, D. A. 2003, ApJ, 588, 186

Charlot, S., Kauffmann, G., Longhetti, M., Tresse, L., White, S. D. M., Maddox, S. J., & Fall, S. M. 2002, MNRAS, 330, 876

Chiosi, C. & Carraro, G. 2002, MNRAS, 335, 335

Chuter, R. W., et al. 2011, MNRAS, 413, 1678

Cirasuolo, M., et al. 2007, MNRAS, 380, 585

Clements, D. L., Dunne, L., & Eales, S. 2010, MNRAS, 403, 274

Cole, S., Aragon-Salamanca, A., Frenk, C. S., Navarro, J. F., & Zepf, S. E. 1994, MNRAS, 271, 781

Cole, S., Lacey, C. G., Baugh, C. M., & Frenk, C. S. 2000a, MNRAS, 319, 168

Cole, S., Lacey, C. G., Baugh, C. M., & Frenk, C. S. 2000b, MNRAS, 319, 168

Colless, M., et al. 2001, MNRAS, 328, 1039

Condon, J. J. 1992, ARA&A, 30, 575

Condon, J. J., Anderson, M. L., & Helou, G. 1991, ApJ, 376, 95

Condon, J. J., Cotton, W. D., & Broderick, J. J. 2002, AJ, 124, 675

Condon, J. J., Cotton, W. D., Greisen, E. W., Yin, Q. F., Perley, R. A., Taylor, G. B., & Broderick, J. J. 1998, AJ, 115, 1693

Conselice, C. J., Bershady, M. A., Dickinson, M., & Papovich, C. 2003, AJ, 126, 1183

Conselice, C. J., Rajgor, S., & Myers, R. 2008, MNRAS, 386, 909

Conselice, C. J., Yang, C., & Bluck, A. F. L. 2009, MNRAS, 394, 1956

Cooper, M. C., et al. 2007, MNRAS, 376, 1445

Cooper, M. C., Newman, J. A., Madgwick, D. S., Gerke, B. F., Yan, R., & Davis, M. 2005, ApJ, 634, 833

Coppin, K. E. K., et al. 2011, MNRAS, 416, 680

Cortese, L., et al. 2010a, A&A, 518, L63

Cortese, L., Boselli, A., Franzetti, P., Decarli, R., Gavazzi, G., Boissier, S., & Buat, V. 2008, MNRAS, 386, 1157

Cortese, L., et al. 2010b, A&A, 518, L49

Couch, W. J., Ellis, R. S., Sharples, R. M., & Smail, I. 1994, ApJ, 430, 121

Courteau, S. 1997, AJ, 114, 2402

Cowie, L. L., Songaila, A., Hu, E. M., & Cohen, J. G. 1996, AJ, 112, 839

Croton, D. J. 2009, MNRAS, 394, 1109

Croton, D. J., et al. 2006, MNRAS, 365, 11

Cucciati, O., et al. 2010, A&A, 524, A2

da Cunha, E., Charlot, S., & Elbaz, D. 2008, MNRAS, 388, 1595

Daddi, E., et al. 2004, ApJL, 600, L127

Daddi, E., et al. 2007, ApJ, 670, 156

Dalcanton, J. J., Spergel, D. N., & Summers, F. J. 1997, ApJ, 482, 659

Dariush, A., et al. 2011, MNRAS, 418, 64

Das, S., Lochan, K., Sahu, S., & Singh, T. P. 2013, , 88, 085020

Davies, J. I., et al. 2010, A&A, 518, L48

Davies, J. I., et al. 2012, MNRAS, 419, 3505

Davies, R. L., Efstathiou, G., Fall, S. M., Illingworth, G., & Schechter, P. L. 1983, ApJ, 266, 41

Davies, R. L., Sadler, E. M., & Peletier, R. F. 1993, MNRAS, 262, 650

Davis, M., Efstathiou, G., Frenk, C. S., & White, S. D. M. 1985, ApJ, 292, 371

de Jong, R. S. 1996, A&A, 313, 377

de Jong, T., Klein, U., Wielebinski, R., & Wunderlich, E. 1985, A&A, 147, L6

De Lucia, G. & Blaizot, J. 2007, MNRAS, 375, 2

De Lucia, G. & Borgani, S. 2012, MNRAS, 426, L61

De Lucia, G., Springel, V., White, S. D. M., Croton, D., & Kauffmann, G. 2006, MNRAS, 366, 499

de Vaucouleurs, G. 1959, Handbuch der Physik, 53, 275

Dekel, A. & Birnboim, Y. 2006, MNRAS, 368, 2

Del Moro, A., et al. 2013, A&A, 549, A59

Deng, X.-F., Chen, Y.-Q., & Jiang, P. 2011, MNRAS, 417, 453

Devereux, N. A. & Young, J. S. 1990, ApJ, 359, 42

Devriendt, J. E. G., Guiderdoni, B., & Sadat, R. 1999, A&A, 350, 381

Dodelson, S., Gates, E. I., & Turner, M. S. 1996, Science, 274, 69

Domínguez, M., Muriel, H., & Lambas, D. G. 2001, AJ, 121, 1266

Donas, J. & Deharveng, J. M. 1984, A&A, 140, 325

Dorschner, J. & Henning, T. 1995, AAPR, 6, 271

Dressler, A. 1980, ApJ, 236, 351

Dressler, A. & Gunn, J. E. 1983, ApJ, 270, 7

Dressler, A., et al. 1997, ApJ, 490, 577

Dreyer, J. L. E. 1888, MEMRES, 49, 1

Driver, S. P., Allen, P. D., Liske, J., & Graham, A. W. 2007, ApJL, 657, L85

Driver, S. P., et al. 2011, MNRAS, 413, 971

Driver, S. P., Windhorst, R. A., & Griffiths, R. E. 1995, ApJ, 453, 48

Dubinski, J. 1998, ApJ, 502, 141

Dunne, L., Eales, S., Ivison, R., Morgan, H., & Edmunds, M. 2003, Nature, 424, 285

Dunne, L. & Eales, S. A. 2001, MNRAS, 327, 697

Dunne, L., et al. 2011, MNRAS, 417, 1510

Dunne, L., et al. 2009, MNRAS, 394, 1307

Duric, N., Bourneuf, E., & Gregory, P. C. 1988, AJ, 96, 81

Dutta, P., Begum, A., Bharadwaj, S., & Chengalur, J. N. 2010, MNRAS, 405, L102

Dye, S., et al. 2009, ApJ, 703, 285

Dye, S., et al. 2010, A&A, 518, L10

Eales, S., et al. 2010, PASP, 122, 499

Ebeling, H. & Wiedenmann, G. 1993, PRE, 47, 704

Efstathiou, G. & Silk, J. 1983, Fund. Cosmic Phys., 9, 1

Eggen, O. J., Lynden-Bell, D., & Sandage, A. R. 1962, ApJ, 136, 748

Elbaz, D., et al. 2007, A&A, 468, 33

Elbaz, D., et al. 2011, A&A, 533, A119

Eliche-Moral, M. C., González-García, A. C., Aguerri, J. A. L., Gallego, J., Zamorano, J., Balcells, M., & Prieto, M. 2013, A&A, 552, A67

Ellis, R. S. 1997, ARA&A, 35, 389

Ellis, R. S., Smail, I., Dressler, A., Couch, W. J., Oemler, Jr., A., Butcher, H., & Sharples, R. M. 1997, ApJ, 483, 582

Elmegreen, B. G., Elmegreen, D. M., & Hirst, A. C. 2004, ApJ, 612, 191

Emerson, J. P., Sutherland, W. J., McPherson, A. M., Craig, S. C., Dalton, G. B., & Ward, A. K. 2004, The Messenger, 117, 27

Eskridge, P. B., et al. 2000, AJ, 119, 536

Espino-Briones, N., Plionis, M., & Ragone-Figueroa, C. 2007, ApJL, 666, L5

Fabbiano, G. 1989, ARA&A, 27, 87

Faber, S. M., Friel, E. D., Burstein, D., & Gaskell, C. M. 1985, ApJS, 57, 711

Fall, S. M. 2002a, in Astronomical Society of the Pacific Conference Series, Vol. 273, The Dynamics, Structure History of Galaxies: A Workshop in Honour of Professor Ken Freeman, ed. G. S. Da Costa, E. M. Sadler, & H. Jerjen, 289

Fall, S. M. 2002b, in Astronomical Society of the Pacific Conference Series, Vol. 275, Disks of Galaxies: Kinematics, Dynamics and Peturbations, ed. E. Athanassoula, A. Bosma, & R. Mujica, 389–396

Fall, S. M. & Efstathiou, G. 1980, MNRAS, 193, 189

Farouki, R. & Shapiro, S. L. 1981, ApJ, 243, 32

Farouki, R. T. & Shapiro, S. L. 1982, ApJ, 259, 103

Ferguson, A. M. N., Wyse, R. F. G., Gallagher, J. S., & Hunter, D. A. 1998, ApJL, 506, L19

Ferrarese, L., et al. 2006, ApJS, 164, 334

Feruglio, C., et al. 2010, ApJ, 721, 607

Findlay, J. R., Sutherland, W. J., Venemans, B. P., Reylé, C., Robin, A. C., Bonfield, D. G., Bruce, V. A., & Jarvis, M. J. 2012, MNRAS, 419, 3354

Finn, R. A., et al. 2010, ApJ, 720, 87

Fioc, M. & Rocca-Volmerange, B. 1999, A&A, 351, 869

Fixsen, D. J., Dwek, E., Mather, J. C., Bennett, C. L., & Shafer, R. A. 1998, ApJ, 508, 123

Fleuren, S., et al. 2012, MNRAS, 423, 2407

Freedman Woods, D., Geller, M. J., Kurtz, M. J., Westra, E., Fabricant, D. G., & Dell'Antonio, I. 2010, AJ, 139, 1857

Frenk, C. S., White, S. D. M., Davis, M., & Efstathiou, G. 1988, ApJ, 327, 507

Frogel, J. A. 1985, ApJ, 298, 528

Fujita, Y. 2004, PASJ, 56, 29

Fujita, Y. & Nagashima, M. 1999, ApJ, 516, 619

Galametz, M., et al. 2013, MNRAS, 431, 1956

Garcia, A. M. 1993, A&AS, 100, 47

Garnett, D. R. & Shields, G. A. 1987, ApJ, 317, 82

Garrett, M. A. 2002, A&A, 384, L19

Gay, C., Pichon, C., Le Borgne, D., Teyssier, R., Sousbie, T., & Devriendt, J. 2010, MNRAS, 404, 1801

Geach, J. E., Ellis, R. S., Smail, I., Rawle, T. D., & Moran, S. M. 2011a, MNRAS, 413, 177

Geach, J. E., Murphy, D. N. A., & Bower, R. G. 2011b, MNRAS, 413, 3059

Genel, S., Genzel, R., Bouché, N., Naab, T., & Sternberg, A. 2009, ApJ, 701, 2002

Gerhard, O. E. 1981, MNRAS, 197, 179

Gilbank, D. G., et al. 2010, MNRAS, 405, 2419

Giodini, S., et al. 2009, ApJ, 703, 982

Gladders, M. D., Lopez-Cruz, O., Yee, H. K. C., & Kodama, T. 1998, ApJ, 501, 571

Gnedin, N. Y. 2000, ApJ, 542, 535

Gomez, H. L., et al. 2012, ApJ, 760, 96

Gómez, P. L., et al. 2003, ApJ, 584, 210

González-García, A. C., Aguerri, J. A. L., & Balcells, M. 2005, A&A, 444, 803

Goto, T. 2005, MNRAS, 360, 322

Goto, T., Yamauchi, C., Fujita, Y., Okamura, S., Sekiguchi, M., Smail, I., Bernardi, M., & Gomez, P. L. 2003, MNRAS, 346, 601

Gott, III, J. R. & Thuan, T. X. 1976, ApJ, 204, 649

Gottlöber, S., Klypin, A., & Kravtsov, A. V. 2001, ApJ, 546, 223

Goudfrooij, P. 1999, in Astronomical Society of the Pacific Conference Series, Vol. 163, Star Formation in Early Type Galaxies, ed. P. Carral & J. Cepa, 55

Goudfrooij, P., Hansen, L., Jorgensen, H. E., Norgaard-Nielsen, H. U., de Jong, T., & van den Hoek, L. B. 1994, A&AS, 104, 179

Governato, F., et al. 2010, Nature, 463, 203

Governato, F., Gardner, J. P., Stadel, J., Quinn, T., & Lake, G. 1999, AJ, 117, 1651

Granato, G. L., De Zotti, G., Silva, L., Bressan, A., & Danese, L. 2004, ApJ, 600, 580

Griffin, M. J., et al. 2010, A&A, 518, L3

Groves, B., et al. 2012, MNRAS, 426, 892

Grützbauch, R., Conselice, C. J., Varela, J., Bundy, K., Cooper, M. C., Skibba, R., & Willmer, C. N. A. 2011, MNRAS, 411, 929

Gunn, J. E. & Gott, III, J. R. 1972, ApJ, 176, 1

Guo, Q., et al. 2011, MNRAS, 413, 101

Guo, Q., White, S., Li, C., & Boylan-Kolchin, M. 2010, MNRAS, 404, 1111

Halliday, C., Davies, R. L., Kuntschner, H., Birkinshaw, M., Bender, R., Saglia, R. P., & Baggley, G. 2001, MNRAS, 326, 473

Hardcastle, M. J., et al. 2013, MNRAS, 429, 2407

Hashimoto, Y., Oemler, Jr., A., Lin, H., & Tucker, D. L. 1998, ApJ, 499, 589

Hausman, M. A. & Ostriker, J. P. 1978, ApJ, 224, 320

Haynes, M. P., Giovanelli, R., & Chincarini, G. L. 1984, ARA&A, 22, 445

Haynes, M. P., Giovanelli, R., & Kent, B. R. 2007, ApJL, 665, L19

Heckman, T. M., et al. 2005, ApJL, 619, L35

Heller, C. H. & Shlosman, I. 1994, ApJ, 424, 84

Helou, G., Soifer, B. T., & Rowan-Robinson, M. 1985, ApJL, 298, L7

Henriques, B. M. B., White, S. D. M., Lemson, G., Thomas, P. A., Guo, Q., Marleau, G.-D., & Overzier, R. A. 2012, MNRAS, 421, 2904

Hernández-Fernández, J. D., Iglesias-Páramo, J., & Vílchez, J. M. 2012, ApJS, 199, 22

Hernquist, L. 1992, ApJ, 400, 460

Hernquist, L. 1993, ApJ, 409, 548

Herschel, J. F. W. 1864, Royal Society of London Philosophical Transactions Series I, 154, 1

Heyl, J. S., Hernquist, L., & Spergel, D. N. 1994, ApJ, 427, 165

Hickox, R. C., et al. 2009, ApJ, 696, 891

Hildebrand, R. H. 1983, QJRAS, 24, 267

Hill, D. T., et al. 2011, MNRAS, 412, 765

Hinshaw, G., et al. 2007, ApJS, 170, 288

Hirashita, H., Buat, V., & Inoue, A. K. 2003, A&A, 410, 83

Hopkins, A. M. 2004, ApJ, 615, 209

Hopkins, P. F., Cox, T. J., Kereš, D., & Hernquist, L. 2008, ApJS, 175, 390

Hopkins, P. F. & Hernquist, L. 2006, ApJS, 166, 1

Hopkins, P. F., Richards, G. T., & Hernquist, L. 2007, ApJ, 654, 731

Hubble, E. P. 1925, The Observatory, 48, 139

Hubble, E. P. 1926, ApJ, 64, 321

Hubble, E. P. 1936, Realm of the Nebulae

Huchra, J., Davis, M., Latham, D., & Tonry, J. 1983, ApJS, 52, 89

Huchra, J. P. & Geller, M. J. 1982, ApJ, 257, 423

Huchtmeier, W. K. & Richter, O.-G. 1985, A&A, 149, 118

Hughes, T. M. & Cortese, L. 2009, MNRAS, 396, L41

Hunter, D. A. & Elmegreen, B. G. 2004, AJ, 128, 2170

Hunter, D. A., Hawley, W. N., & Gallagher, III, J. S. 1993, AJ, 106, 1797

Hwang, H. S., Elbaz, D., Lee, J. C., Jeong, W.-S., Park, C., Lee, M. G., & Lee, H. M. 2010, A&A, 522, A33

Ibar, E., et al. 2008, MNRAS, 386, 953

Ibar, E., et al. 2010, MNRAS, 409, 38

Icke, V. & van de Weygaert, R. 1987, A&A, 184, 16

Ideue, Y., et al. 2012, ApJ, 747, 42

Ilbert, O., et al. 2006, A&A, 457, 841

Ilbert, O., et al. 2010, ApJ, 709, 644

Immeli, A., Samland, M., Gerhard, O., & Westera, P. 2004, A&A, 413, 547

Ishibashi, W. & Courvoisier, T. J.-L. 2011, A&A, 525, A118

Ivezić, Ž., et al. 2002, in Astronomical Society of the Pacific Conference Series, Vol. 284, IAU Colloq. 184: AGN Surveys, ed. R. F. Green, E. Y. Khachikian, & D. B. Sanders, 137

Ivison, R. J., et al. 2010, A&A, 518, L31

Jansen, R. A., Franx, M., & Fabricant, D. 2001, ApJ, 551, 825

Jarvis, M. J., et al. 2013, MNRAS, 428, 1281

Jarvis, M. J. & Rawlings, S. 2004, New Astronomy Review, 48, 1173

Jarvis, M. J., et al. 2010, MNRAS, 409, 92

Jesseit, R., Naab, T., & Burkert, A. 2005, MNRAS, 360, 1185

Jiang, Y.-F., Ciotti, L., Ostriker, J. P., & Spitkovsky, A. 2010, ApJ, 711, 125

Jimenez, R., Panter, B., Heavens, A. F., & Verde, L. 2005, MNRAS, 356, 495

Jogee, S., et al. 2004, ApJL, 615, L105

Johansson, P. H., Naab, T., & Ostriker, J. P. 2012, ApJ, 754, 115

Johnston, S., et al. 2008, Experimental Astronomy, 22, 151

Jonas, J. L. 2009, IEEE Proceedings, 97, 1522

Kapferer, W., Sluka, C., Schindler, S., Ferrari, C., & Ziegler, B. 2009, A&A, 499, 87

Katz, N. & Gunn, J. E. 1991, ApJ, 377, 365

Katz, N., Hernquist, L., & Weinberg, D. H. 1992, ApJL, 399, L109

Kauffmann, G. 1996, MNRAS, 281, 487

Kauffmann, G. & Charlot, S. 1998, MNRAS, 294, 705

Kauffmann, G., Colberg, J. M., Diaferio, A., & White, S. D. M. 1999, MNRAS, 303, 188

Kauffmann, G. & White, S. D. M. 1993, MNRAS, 261, 921

Kauffmann, G., White, S. D. M., & Guiderdoni, B. 1993, MNRAS, 264, 201

Kauffmann, G., White, S. D. M., Heckman, T. M., Ménard, B., Brinchmann, J., Charlot, S., Tremonti, C., & Brinkmann, J. 2004, MNRAS, 353, 713

Kaviraj, S., et al. 2007, ApJS, 173, 619

Kawata, D. & Mulchaey, J. S. 2008, ApJL, 672, L103

Keel, W. C. 1996, ApJS, 106, 27

Kellermann, K. I., Fomalont, E. B., Mainieri, V., Padovani, P., Rosati, P., Shaver, P., Tozzi, P., & Miller, N. 2008, ApJS, 179, 71

Kennicutt, Jr., R. C. 1989, ApJ, 344, 685

Kennicutt, Jr., R. C. 1998, ARA&A, 36, 189

Kennicutt, Jr., R. C., et al. 2007, ApJ, 671, 333

Kennicutt, Jr., R. C., et al. 2009, ApJ, 703, 1672

Kent, S. M. 1986, AJ, 91, 1301

Kent, S. M. 1987, AJ, 93, 816

Kereš, D., Katz, N., Weinberg, D. H., & Davé, R. 2005, MNRAS, 363, 2

Kewley, L. J., Geller, M. J., & Jansen, R. A. 2004, AJ, 127, 2002

Khalatyan, A., Cattaneo, A., Schramm, M., Gottlöber, S., Steinmetz, M., & Wisotzki, L. 2008, MNRAS, 387, 13

Kiang, T. 1966, ZAP, 64, 433

Kim, R., Strauss, M., Bahcall, N., Gunn, J. E., Lupton, R. H., Vogeley, M. S., Schlegel, D., & the SDSS Collaboration. 2000, in Astronomical Society of the Pacific Conference Series, Vol. 200, Clustering at High Redshift, ed. A. Mazure, O. Le Fèvre, & V. Le Brun, 422

Kim, R. S. J., et al. 2002, AJ, 123, 20

Kimm, T., Devriendt, J., Slyz, A., Pichon, C., Kassin, S. A., & Dubois, Y. 2011, ArXiv e-prints

Kimm, T., et al. 2012, MNRAS, L497

Kirby, E. M., Koribalski, B., Jerjen, H., & López-Sánchez, Á. 2012, MNRAS, 420, 2924

Kitzbichler, M. G. & White, S. D. M. 2007, MNRAS, 376, 2

Koleva, M., Prugniel, P., de Rijcke, S., & Zeilinger, W. W. 2011, MNRAS, 417, 1643

Kormendy, J. & Bender, R. 2012, ApJS, 198, 2

Kormendy, J. & Gebhardt, K. 2001, in American Institute of Physics Conference Series, Vol. 586, 20th Texas Symposium on relativistic astrophysics, ed. J. C. Wheeler & H. Martel, 363

Kovács, A., Chapman, S. C., Dowell, C. D., Blain, A. W., Ivison, R. J., Smail, I., & Phillips, T. G. 2006, ApJ, 650, 592

Kronberger, T., Kapferer, W., Ferrari, C., Unterguggenberger, S., & Schindler, S. 2008a, A&A, 481, 337

Kronberger, T., Kapferer, W., Unterguggenberger, S., Schindler, S., & Ziegler, B. L. 2008b, A&A, 483, 783

Kroupa, P., Tout, C. A., & Gilmore, G. 1990, MNRAS, 244, 76

Kuchinski, L. E., Terndrup, D. M., Gordon, K. D., & Witt, A. N. 1998, AJ, 115, 1438

Kuntschner, H., et al. 2006, MNRAS, 369, 497

Lacey, C. & Cole, S. 1993, MNRAS, 262, 627

Lacki, B. C. & Thompson, T. A. 2010, ApJ, 717, 196

Lambas, D. G., Alonso, S., Mesa, V., & O'Mill, A. L. 2012, A&A, 539, A45

Larson, R. B. 1974a, MNRAS, 166, 585

Larson, R. B. 1974b, MNRAS, 169, 229

Larson, R. B. 1975, MNRAS, 173, 671

Larson, R. B. 1976, MNRAS, 176, 31

Larson, R. B. & Tinsley, B. M. 1978, ApJ, 219, 46

Larson, R. B., Tinsley, B. M., & Caldwell, C. N. 1980, ApJ, 237, 692

Lavery, R. J. & Henry, J. P. 1994, ApJ, 426, 524

Lawrence, A., et al. 2007, MNRAS, 379, 1599

Le Fèvre, O., et al. 2000, MNRAS, 311, 565

Le Floc'h, E., et al. 2005a, ApJ, 632, 169

Le Floc'h, E., et al. 2005b, ApJ, 632, 169

Lee, G.-H., Woo, J.-H., Lee, M. G., Hwang, H. S., Lee, J. C., Sohn, J., & Lee, J. H. 2012, ApJ, 750, 141

Lee, J. H., Lee, M. G., Park, C., & Choi, Y.-Y. 2010, MNRAS, 403, 1930

Lequeux, J., Peimbert, M., Rayo, J. F., Serrano, A., & Torres-Peimbert, S. 1979, A&A, 80, 155

Levine, R., Gnedin, N. Y., & Hamilton, A. J. S. 2010, ApJ, 716, 1386

Lewis, I., et al. 2002, MNRAS, 334, 673

Li, C., Kauffmann, G., Jing, Y. P., White, S. D. M., Börner, G., & Cheng, F. Z. 2006, MNRAS, 368, 21

Lilly, S. J., Le Fevre, O., Hammer, F., & Crampton, D. 1996, ApJL, 460, L1

Lin, L., Patton, D. R., Koo, C. D., Casteels, K., & Hsieh, B. C. 2008, in Astronomical Society of the Pacific Conference Series, Vol. 399, Panoramic Views of Galaxy Formation and Evolution, ed. T. Kodama, T. Yamada, & K. Aoki, 298

Longhetti, M., Bressan, A., Chiosi, C., & Rampazzo, R. 2000, A&A, 353, 917

Longhetti, M., Rampazzo, R., Bressan, A., & Chiosi, C. 1998a, A&AS, 130, 251

Longhetti, M., Rampazzo, R., Bressan, A., & Chiosi, C. 1998b, A&AS, 130, 267

Lonsdale Persson, C. J. & Helou, G. 1987, ApJ, 314, 513

Lotz, J. M., et al. 2008, ApJ, 672, 177

Lotz, J. M., Primack, J., & Madau, P. 2004, AJ, 128, 163

Lynden-Bell, D. 1969, Nature, 223, 690

Mac Low, M. & Ferrara, A. 1999, ApJ, 513, 142

MacArthur, L. A., Courteau, S., Bell, E., & Holtzman, J. A. 2004, ApJS, 152, 175

Madau, P. 1997, in American Institute of Physics Conference Series, Vol. 393, American Institute of Physics Conference Series, ed. S. S. Holt & L. G. Mundy, 481–490

Madau, P., Ferguson, H. C., Dickinson, M. E., Giavalisco, M., Steidel, C. C., & Fruchter, A. 1996, MNRAS, 283, 1388

Madau, P., Pozzetti, L., & Dickinson, M. 1998, ApJ, 498, 106

Magnelli, B., et al. 2012, A&A, 539, A155

Maia, M. A. G., da Costa, L. N., & Latham, D. W. 1989, ApJS, 69, 809

Malumuth, E. M. & Richstone, D. O. 1984, ApJ, 276, 413

Mandelbaum, R., Li, C., Kauffmann, G., & White, S. D. M. 2009, MNRAS, 393, 377

Maraston, C. & Thomas, D. 2000, ApJ, 541, 126

Marconi, A. & Hunt, L. K. 2003, ApJL, 589, L21

Marinoni, C., Davis, M., Newman, J. A., & Coil, A. L. 2002, ApJ, 580, 122

Martin, D. C., et al. 2005, ApJL, 619, L1

Martini, P., Mulchaey, J. S., & Kelson, D. D. 2007, ApJ, 664, 761

Masters, K. L., et al. 2010, MNRAS, 405, 783

Masters, K. L., et al. 2011, MNRAS, 411, 2026

Materne, J. 1978, A&A, 63, 401

Mathews, W. G. & Brighenti, F. 2003, ARA&A, 41, 191

Matsuura, M., et al. 2009, MNRAS, 396, 918

Matthews, L. D. & Gallagher, III, J. S. 2002, ApJS, 141, 429

Matthews, L. D., Gallagher, III, J. S., & van Driel, W. 1999, AJ, 118, 2751

Mauch, T. & Sadler, E. M. 2007, MNRAS, 375, 931

McAlpine, K., Smith, D. J. B., Jarvis, M. J., Bonfield, D. G., & Fleuren, S. 2012, MNRAS, 423, 132

McCarthy, I. G., Schaye, J., Bower, R. G., Ponman, T. J., Booth, C. M., Dalla Vecchia, C., & Springel, V. 2011, MNRAS, 412, 1965

McCarthy, I. G., et al. 2010, MNRAS, 406, 822

McGaugh, S. S. & de Blok, W. J. G. 1997a, ApJ, 481, 689

McGaugh, S. S. & de Blok, W. J. G. 1997b, ApJ, 481, 689

McGee, S. L., Balogh, M. L., Bower, R. G., Font, A. S., & McCarthy, I. G. 2009, MNRAS, 400, 937

McIntosh, D. H., et al. 2005, ApJ, 632, 191

McLure, R. J. & Dunlop, J. S. 2002, MNRAS, 331, 795

Merloni, A. & Heinz, S. 2008, MNRAS, 388, 1011

Merritt, D. 1983, ApJ, 264, 24

Messier, C. 1781, Catalogue des Nébuleuses des amas d'Étoiles (Catalog of Nebulae and Star Clusters), Tech. rep.

Mihos, J. C. 2004, Clusters of Galaxies: Probes of Cosmological Structure and Galaxy Evolution, 277

Mihos, J. C. & Hernquist, L. 1996, ApJ, 464, 641

Miley, G. & De Breuck, C. 2008, AAPR, 15, 67

Miller, C. J., Nichol, R. C., Gómez, P. L., Hopkins, A. M., & Bernardi, M. 2003, ApJ, 597, 142

Mo, H., van den Bosch, F. C., & White, S. 2010, Galaxy Formation and Evolution, ed. Mo, H., van den Bosch, F. C., & White, S.

Mo, H. J., Mao, S., & White, S. D. M. 1998, MNRAS, 295, 319

Monaco, P., Murante, G., Borgani, S., & Dolag, K. 2012, MNRAS, 421, 2485

Moore, B., Katz, N., Lake, G., Dressler, A., & Oemler, A. 1996, Nature, 379, 613

Moore, B., Lake, G., & Katz, N. 1998, ApJ, 495, 139

Moorwood, A. F. M., van der Werf, P. P., Cuby, J. G., & Oliva, E. 2000, A&A, 362, 9

More, S., Kravtsov, A. V., Dalal, N., & Gottlöber, S. 2011, ApJS, 195, 4

Morris, S. L., Hutchings, J. B., Carlberg, R. G., Yee, H. K. C., Ellingson, E., Balogh, M. L., Abraham, R. G., & Smecker-Hane, T. A. 1998, ApJ, 507, 84

Moster, B. P., Somerville, R. S., Maulbetsch, C., van den Bosch, F. C., Macciò, A. V., Naab, T., & Oser, L. 2010, ApJ, 710, 903

Muldrew, S. I., et al. 2012, MNRAS, 419, 2670

Mullaney, J. R., et al. 2012, ApJL, 753, L30

Munshi, F., et al. 2013, ApJ, 766, 56

Murphy, E. J. 2009, ApJ, 706, 482

Naab, T. & Burkert, A. 2003, ApJ, 597, 893

Naab, T., Johansson, P. H., & Ostriker, J. P. 2009, ApJL, 699, L178

Nagashima, M. & Gouda, N. 2001, MNRAS, 325, L13

Nair, P. B. & Abraham, R. G. 2010, ApJL, 714, L260

Nardini, E., Risaliti, G., Salvati, M., Sani, E., Imanishi, M., Marconi, A., & Maiolino, R. 2008, MNRAS, 385, L130

Navarro, J. F. & Benz, W. 1991, ApJ, 380, 320

Navarro, J. F. & Steinmetz, M. 2000, ApJ, 538, 477

Navarro, J. F. & White, S. D. M. 1994, MNRAS, 267, 401

Negroponte, J. & White, S. D. M. 1983, MNRAS, 205, 1009

Neistein, E. & Dekel, A. 2008, MNRAS, 383, 615

Neugebauer, G., et al. 1984, ApJL, 278, L1

Nickerson, S., Stinson, G., Couchman, H. M. P., Bailin, J., & Wadsley, J. 2011, MNRAS, 415, 257

Nipoti, C., Treu, T., Ciotti, L., & Stiavelli, M. 2004, MNRAS, 355, 1119

Noeske, K. G., et al. 2007a, ApJL, 660, L47

Noeske, K. G., et al. 2007b, ApJL, 660, L43

Noguchi, M. 1987, MNRAS, 228, 635

Nolthenius, R. & White, S. D. M. 1987, MNRAS, 225, 505

Nordon, R., et al. 2010, A&A, 518, L24

Oemler, Jr., A. 1974, ApJ, 194, 1

Oemler, Jr., A. 1976, ApJ, 209, 693

Okabe, A., Boots, B., & Sugihara, K. 1992, Spatial tessellations: Concepts and Applications of Voronoi diagrams, ed. Okabe, A., Boots, B., & Sugihara, K.

Okamoto, T., Eke, V. R., Frenk, C. S., & Jenkins, A. 2005, MNRAS, 363, 1299

Okamoto, T., Gao, L., & Theuns, T. 2008, MNRAS, 390, 920

Oliver, S. J., et al. 2012, MNRAS, 424, 1614

O'Mill, A. L., Padilla, N., & García Lambas, D. 2008, MNRAS, 389, 1763

Ostriker, J. P. & Tremaine, S. D. 1975, ApJL, 202, L113

Padovani, P., Mainieri, V., Tozzi, P., Kellermann, K. I., Fomalont, E. B., Miller, N., Rosati, P., & Shaver, P. 2009, ApJ, 694, 235

Padovani, P., Miller, N., Kellermann, K. I., Mainieri, V., Rosati, P., & Tozzi, P. 2011, ApJ, 740, 20

Pappalardo, C., Lançon, A., Vollmer, B., Ocvirk, P., Boissier, S., & Boselli, A. 2010, A&A, 514, A33

Pascale, E., et al. 2011, MNRAS, 415, 911

Pasquali, A., van den Bosch, F. C., Mo, H. J., Yang, X., & Somerville, R. 2009, MNRAS, 394, 38

Patel, H., Clements, D. L., Vaccari, M., Mortlock, D. J., Rowan-Robinson, M., Pérez-Fournon, I., & Afonso-Luis, A. 2013, MNRAS, 428, 291

Patel, S. G., Holden, B. P., Kelson, D. D., Illingworth, G. D., & Franx, M. 2009, ApJL, 705, L67

Patel, S. G., Kelson, D. D., Holden, B. P., Franx, M., & Illingworth, G. D. 2011, ApJ, 735, 53

Patton, D. R., Ellison, S. L., Simard, L., McConnachie, A. W., & Mendel, J. T. 2011, MNRAS, 412, 591

Patton, D. R., et al. 2002, ApJ, 565, 208

Peletier, R. F. & Balcells, M. 1996, AJ, 111, 2238

Peletier, R. F., Davies, R. L., Illingworth, G. D., Davis, L. E., & Cawson, M. 1990, AJ, 100, 1091

Peletier, R. F. & de Grijs, R. 1998, MNRAS, 300, L3

Pelupessy, F. I. & Papadopoulos, P. P. 2009, ApJ, 707, 954

Peng, Y.-j., et al. 2010, ApJ, 721, 193

Pérez-González, P. G., et al. 2005, ApJ, 630, 82

Persic, M., Salucci, P., & Stel, F. 1996, MNRAS, 281, 27

Phillips, M. M., Jenkins, C. R., Dopita, M. A., Sadler, E. M., & Binette, L. 1986, AJ, 91, 1062

Pilbratt, G. L., et al. 2010, A&A, 518, L1

Planck Collaboration. 2006, ArXiv Astrophysics e-prints

Planck Collaboration, et al. 2013, ArXiv e-prints

Poggianti, B. M., et al. 2008, ApJ, 684, 888

Poggianti, B. M., Smail, I., Dressler, A., Couch, W. J., Barger, A. J., Butcher, H., Ellis, R. S., & Oemler, Jr., A. 1999, ApJ, 518, 576

Poggianti, B. M., et al. 2006, ApJ, 642, 188

Poglitsch, A., et al. 2010, A&A, 518, L2

Polletta, M., et al. 2008, A&A, 492, 81

Porciani, C., Magliocchetti, M., & Norberg, P. 2004, MNRAS, 355, 1010

Postman, M., et al. 2005, ApJ, 623, 721

Postman, M. & Geller, M. J. 1984, ApJ, 281, 95

Press, W. H. & Schechter, P. 1974, ApJ, 187, 425

Price, R. & Duric, N. 1992, ApJ, 401, 81

Puget, J.-L., Abergel, A., Bernard, J.-P., Boulanger, F., Burton, W. B., Desert, F.-X., & Hartmann, D. 1996, A&A, 308, L5

Quadri, R. F., Williams, R. J., Franx, M., & Hildebrandt, H. 2012, ApJ, 744, 88

Quinn, T., Katz, N., & Efstathiou, G. 1996, MNRAS, 278, L49

Ramella, M., Boschin, W., Fadda, D., & Nonino, M. 2001, A&A, 368, 776

Ramella, M., Pisani, A., & Geller, M. J. 1997, AJ, 113, 483

Ramella, M., et al. 1999, A&A, 342, 1

Rees, M. J. 1971, Nature, 229, 312

Renzini, A. & Voli, M. 1981, A&A, 94, 175

Richards, E. A. 2000, ApJ, 533, 611

Richards, G. T., et al. 2006, AJ, 131, 2766

Rieke, G. H., et al. 2004, ApJS, 154, 25

Rigby, E. E., et al. 2011, MNRAS, 415, 2336

Roberts, M. S., Hogg, D. E., Bregman, J. N., Forman, W. R., & Jones, C. 1991, ApJS, 75, 751

Roberts, M. S. & Rots, A. H. 1973, A&A, 26, 483

Robertson, B., Bullock, J. S., Cox, T. J., Di Matteo, T., Hernquist, L., Springel, V., & Yoshida, N. 2006, ApJ, 645, 986

Robotham, A. S. G. & Driver, S. P. 2011, MNRAS, 413, 2570

Roediger, E. & Brüggen, M. 2008, MNRAS, 388, 465

Rogstad, D. H. & Shostak, G. S. 1972, ApJ, 176, 315

Rosa-González, D., Terlevich, E., & Terlevich, R. 2002, MNRAS, 332, 283

Rowlands, K., et al. 2012, MNRAS, 419, 2545

Sadler, E. M., et al. 2002, MNRAS, 329, 227

Salim, S., et al. 2007, ApJS, 173, 267

Salpeter, E. E. 1955, ApJ, 121, 161

Salucci, P., Lapi, A., Tonini, C., Gentile, G., Yegorova, I., & Klein, U. 2007, MNRAS, 378, 41

Sambruna, R. M., Gambill, J. K., Maraschi, L., Tavecchio, F., Cerutti, R., Cheung, C. C., Urry, C. M., & Chartas, G. 2004, ApJ, 608, 698

Sambruna, R. M., Gliozzi, M., Tavecchio, F., Maraschi, L., & Foschini, L. 2006, ApJ, 652, 146

Sandage, A. 1961, The Hubble atlas of galaxies

Sandage, A. & Visvanathan, N. 1978, ApJ, 225, 742

Sanders, D. B. & Mirabel, I. F. 1996, ARA&A, 34, 749

Sauvage, M. & Thuan, T. X. 1992, ApJL, 396, L69

Scalo, J. M. 1986, Fund. Cosmic Phys., 11, 1

Scannapieco, C., Tissera, P. B., White, S. D. M., & Springel, V. 2008, MNRAS, 389, 1137

Schiminovich, D., et al. 2010, MNRAS, 408, 919

Schmidt, M. 1959, ApJ, 129, 243

Schmitt, H. R., Calzetti, D., Armus, L., Giavalisco, M., Heckman, T. M., Kennicutt, Jr., R. C., Leitherer, C., & Meurer, G. R. 2006, ApJ, 643, 173

Schombert, J. & Rakos, K. 2009, ApJ, 699, 1530

Schombert, J. M. 1986, ApJS, 60, 603

Schweizer, F. & Seitzer, P. 1992, AJ, 104, 1039

Scoville, N., et al. 2007, ApJS, 172, 1

Sedlmayr, E. 1994, in Lecture Notes in Physics, Berlin Springer Verlag, Vol. 428, IAU Colloq. 146: Molecules in the Stellar Environment, ed. U. G. Jorgensen, 163

Seifert, W. & Scorza, C. 1996, A&A, 310, 75

Sellwood, J. A. 1981, A&A, 99, 362

Seymour, N., et al. 2008, MNRAS, 386, 1695

Shankar, F., Weinberg, D. H., & Miralda-Escudé, J. 2009, ApJ, 690, 20

Sheth, R. K. & Lemson, G. 1999, MNRAS, 305, 946

Silverman, J. D., et al. 2009a, ApJ, 695, 171

Silverman, J. D., et al. 2009b, ApJ, 695, 171

Silverman, J. D., et al. 2009c, ApJ, 696, 396

Simpson, C., et al. 2006, MNRAS, 372, 741

Skillman, E. D., Kennicutt, R. C., & Hodge, P. W. 1989, ApJ, 347, 875

Smith, A. M. & Cornett, R. H. 1982, ApJ, 261, 1

Smith, D. J. B., et al. 2012a, MNRAS, 427, 703

Smith, D. J. B., et al. 2011, MNRAS, 416, 857

Smith, D. J. B., et al. 2013, MNRAS

Smith, G. P., Treu, T., Ellis, R. S., Moran, S. M., & Dressler, A. 2005, ApJ, 620, 78

Smith, M. W. L., et al. 2012b, ApJ, 756, 40

Smith, R., Fellhauer, M., & Assmann, P. 2012c, MNRAS, 420, 1990

Smolčić, V., Zamorani, G., Schinnerer, E., Vla-Cosmos, & Cosmos Collaborations. 2009, in Astronomical Society of the Pacific Conference Series, Vol. 408, The Starburst-AGN Connection, ed. W. Wang, Z. Yang, Z. Luo, & Z. Chen, 116

Smoot, G. F., et al. 1992, ApJL, 396, L1

Snyder, G. F., et al. 2012, ApJ, 756, 114

Soares-Santos, M., et al. 2011, ApJ, 727, 45

Sobral, D., Smail, I., Best, P. N., Geach, J. E., Matsuda, Y., Stott, J. P., Cirasuolo, M., & Kurk, J. 2013, MNRAS, 428, 1128

Somerville, R. S. & Kolatt, T. S. 1999, MNRAS, 305, 1

Somerville, R. S. & Primack, J. R. 1999, MNRAS, 310, 1087

Somerville, R. S., Primack, J. R., & Faber, S. M. 2001, MNRAS, 320, 504

Sommer-Larsen, J., Gelato, S., & Vedel, H. 1999, ApJ, 519, 501

Springel, V., Di Matteo, T., & Hernquist, L. 2005a, MNRAS, 361, 776

Springel, V., et al. 2005b, Nature, 435, 629

Springel, V., White, S. D. M., Tormen, G., & Kauffmann, G. 2001, MNRAS, 328, 726

Stanford, S. A., Eisenhardt, P. R., & Dickinson, M. 1998, ApJ, 492, 461

Stasińska, G., Comte, G., & Vigroux, L. 1986, A&A, 154, 352

Stewart, K. R., Bullock, J. S., Barton, E. J., & Wechsler, R. H. 2009, ApJ, 702, 1005

Stott, J. P., Sobral, D., Smail, I., Bower, R., Best, P. N., & Geach, J. E. 2013, MNRAS, 430, 1158

Strateva, I., et al. 2001, AJ, 122, 1861

Sugerman, B. E. K., et al. 2006, Science, 313, 196

Symeonidis, M., Page, M. J., & Seymour, N. 2011, MNRAS, 411, 983

Symeonidis, M., et al. 2013, MNRAS

Tantalo, R., Chiosi, C., & Bressan, A. 1998, A&A, 333, 419

Taylor, E. N., et al. 2011, MNRAS, 418, 1587

Tekola, A. G., Väisänen, P., & Berlind, A. 2012, MNRAS, 419, 1176

Tempel, E., Tago, E., & Liivamägi, L. J. 2012, A&A, 540, A106

Terlevich, A. I., Caldwell, N., & Bower, R. G. 2001, MNRAS, 326, 1547

Terndrup, D. M., Davies, R. L., Frogel, J. A., Depoy, D. L., & Wells, L. A. 1994, ApJ, 432, 518

Teyssier, R., Moore, B., Martizzi, D., Dubois, Y., & Mayer, L. 2011, MNRAS, 414, 195

Thakar, A. R. & Ryden, B. S. 1996, ApJ, 461, 55

Thomas, D., Maraston, C., Bender, R., & Mendes de Oliveira, C. 2005, ApJ, 621, 673

Thomas, D., Maraston, C., Schawinski, K., Sarzi, M., & Silk, J. 2010, MNRAS, 404, 1775

Tojeiro, R., et al. 2013, MNRAS

Toomre, A. & Toomre, J. 1972, ApJ, 178, 623

Trager, S. C., Faber, S. M., Worthey, G., & González, J. J. 2000, AJ, 119, 1645

Tran, H. D., Tsvetanov, Z., Ford, H. C., Davies, J., Jaffe, W., van den Bosch, F. C., & Rest, A. 2001, AJ, 121, 2928

Trasarti-Battistoni, R. 1998, A&AS, 130, 341

Tremaine, S., et al. 2002, ApJ, 574, 740

Tremonti, C. A., et al. 2004, ApJ, 613, 898

Tsikoudi, V. 1980, ApJS, 43, 365

Tully, R. B. 1980, ApJ, 237, 390

Tully, R. B. 1987, ApJ, 321, 280

Tully, R. B., Mould, J. R., & Aaronson, M. 1982, ApJ, 257, 527

Tully, R. B., Pierce, M. J., Huang, J.-S., Saunders, W., Verheijen, M. A. W., & Witchalls, P. L. 1998, AJ, 115, 2264

Twite, J. W., Conselice, C. J., Buitrago, F., Noeske, K., Weiner, B. J., Acosta-Pulido, J. A., & Bauer, A. E. 2012, MNRAS, 420, 1061

Ueda, Y., Akiyama, M., Ohta, K., & Miyaji, T. 2003, ApJ, 598, 886

Unterborn, C. T. & Ryden, B. S. 2008, ApJ, 687, 976

van Albada, T. S., Bahcall, J. N., Begeman, K., & Sancisi, R. 1985, ApJ, 295, 305

van Breukelen, C. & Clewley, L. 2009, MNRAS, 395, 1845

van Breukelen, C., Clewley, L., & Bonfield, D. 2006a, ArXiv Astrophysics e-prints

van Breukelen, C., et al. 2006b, MNRAS, 373, L26

van de Voort, F., Schaye, J., Booth, C. M., & Dalla Vecchia, C. 2011, MNRAS, 415, 2782

van de Weygaert, R. & Icke, V. 1989, A&A, 213, 1

van den Bosch, F. C., Aquino, D., Yang, X., Mo, H. J., Pasquali, A., McIntosh, D. H., Weinmann, S. M., & Kang, X. 2008, MNRAS, 387, 79

van Dokkum, P. G. 2005, AJ, 130, 2647

van Dokkum, P. G. & Franx, M. 1995, AJ, 110, 2027

van Dokkum, P. G., Franx, M., Fabricant, D., Illingworth, G. D., & Kelson, D. D. 2000, ApJ, 541, 95

van Haarlem, M. P., et al. 2013, A&A, 556, A2

Vika, M., Driver, S. P., Graham, A. W., & Liske, J. 2009, MNRAS, 400, 1451

Virdee, J., et al. 2013, MNRAS, 432, 609

Visvanathan, N. & Sandage, A. 1977, ApJ, 216, 214

Wachter, A., Schröder, K.-P., Winters, J. M., Arndt, T. U., & Sedlmayr, E. 2002, A&A, 384, 452

Wake, D. A., et al. 2011, ApJ, 728, 46

Weil, M. L., Eke, V. R., & Efstathiou, G. 1998, MNRAS, 300, 773

Weinmann, S. M., Kauffmann, G., van den Bosch, F. C., Pasquali, A., McIntosh, D. H., Mo, H., Yang, X., & Guo, Y. 2009, MNRAS, 394, 1213

Welikala, N., Connolly, A. J., Hopkins, A. M., Scranton, R., & Conti, A. 2008, ApJ, 677, 970

Wetzel, A. R., Cohn, J. D., & White, M. 2009, MNRAS, 395, 1376

Whitaker, K. E., et al. 2010, ApJ, 719, 1715

White, S. D. M. 1976, MNRAS, 174, 19

White, S. D. M. 1978, MNRAS, 184, 185

White, S. D. M. & Frenk, C. S. 1991, ApJ, 379, 52

White, S. D. M. & Rees, M. J. 1978, MNRAS, 183, 341

Whitmore, B. C. & Gilmore, D. M. 1991, ApJ, 367, 64

Whitmore, B. C., Gilmore, D. M., & Jones, C. 1993, ApJ, 407, 489

Wijesinghe, D. B., et al. 2012, MNRAS, 3150

Wilkins, S. M., Bunker, A. J., Ellis, R. S., Stark, D., Stanway, E. R., Chiu, K., Lorenzoni, S., & Jarvis, M. J. 2010, MNRAS, 403, 938

Wilkins, S. M., Bunker, A. J., Lorenzoni, S., & Caruana, J. 2011, MNRAS, 411, 23

Willmer, C. N. A., et al. 2006, ApJ, 647, 853

Willmer, C. N. A., Rieke, G. H., Le Floc'h, E., Hinz, J. L., Engelbracht, C. W., Marcillac, D., & Gordon, K. D. 2009, AJ, 138, 146

Wilson, C. D., Madore, B. F., & Freedman, W. L. 1990, AJ, 99, 149

Winters, J. M., Le Bertre, T., Jeong, K. S., Nyman, L.-Å., & Epchtein, N. 2003, A&A, 409, 715

Wirth, G. D., Koo, D. C., & Kron, R. G. 1994, ApJL, 435, L105

Woods, D. F. & Geller, M. J. 2007, AJ, 134, 527

Worthey, G., Faber, S. M., Gonzalez, J. J., & Burstein, D. 1994, ApJS, 94, 687

Worthey, G. & Ottaviani, D. L. 1997, ApJS, 111, 377

Wyder, T. K., et al. 2007, ApJS, 173, 293

Yang, M., Greve, T. R., Dowell, C. D., & Borys, C. 2007, ApJ, 660, 1198

York, D. G., et al. 2000, AJ, 120, 1579

Young, J. S., Allen, L., Kenney, J. D. P., Lesser, A., & Rownd, B. 1996, AJ, 112, 1903

Young, J. S. & Knezek, P. M. 1989, ApJL, 347, L55

Zaritsky, D., Kennicutt, Jr., R. C., & Huchra, J. P. 1994, ApJ, 420, 87

Zasov, A. V. & Khoperskov, A. V. 2008, Astronomy Letters, 34, 739

Zhu, G., Blanton, M. R., & Moustakas, J. 2010, ApJ, 722, 491